THE UNIFICATION OF MASS FLUX AND HIGHER-ORDER CLOSURE IN THE SIMULATION OF BOUNDARY LAYER TURBULENCE

by Cara-Lyn Lappen

David A. Randall, Principal Investigator

Colorado State University

DEPARTMENT OF ATMOSPHERIC SCIENCE

PAPER NO. **679**

THE UNIFICATION OF MASS FLUX AND HIGHER-ORDER CLOSURE IN THE SIMULATION OF BOUNDARY LAYER TURBULENCE

by

Cara-Lyn Lappen

Research supported by the
National Atmospheric and Space Administration
under Grant number NAG1-1701
and the National Science Foundation
under Grant number OPP-9504246

Department of Atmospheric Science
Colorado State University
Fort Collins, CO

July 1999

Atmospheric Science Paper No. 679

ABSTRACT

THE UNIFICATION OF MASS FLUX WITH HIGHER-ORDER CLOSURE IN THE SIMULATION OF BOUNDARY-LAYER TURBULENCE

Typically in large-scale models, cloud schemes vary depending on the type of convection. Separate schemes are used for planetary boundary layer (PBL) processes, shallow and deep cumulus convection, and stratiform clouds. Individually, these schemes may work well in their respective regimes. However, these regimes are not always distinct. Often, two or more of the regimes coexist (e.g., the "stratocumulus-to-cumulus" transition region, "cumulus-under-stratus", and stratocumulus "decoupling"). Large-scale models tend to poorly represent the total effect of clouds in these multiple-cloud regimes. (Randall et al., 1998). The conventional distinction between the boundary layer and the cumulus layer is based on the assumption that they are physically distinct layers. However, this is not always the case. For example, shallow cumulus clouds may be considered to exist completely within the planetary boundary layer (PBL) or they may be regarded as starting in the PBL but terminating above it. Deeper cumulus clouds often originate within the PBL but also can originate aloft. Thus, the distinction between the two layers clearly reflects holes in our understanding. In order to realistically simulate the global hydrologic cycle, energy budget and large-scale circulation, it is imperative that large-scale models accurately represent clouds. Thus, there is a need to unify the approaches that these models take towards representing clouds and the boundary layer.

This study is the first attempt to overcome the dependence of cloud and boundary-layer parameterizations on the type of convection. I present a method to combine the concepts of mass-flux closure (MFC) and "standard" higher-order closure (HOC) into one unified theory which is consistent with both formulations. The model that I will describe combines the two approaches in such a manner that the MFC equations are term-by-term consistent with the terms of "conventional" HOC equations. For this new closure method, the only prognostic variables are the second and third moments of the vertical velocity, all second-order vertical fluxes, and mean

quantities. Variances and all other higher-order moments are diagnosed in terms of an updraft area fraction, a convective mass flux and the differences in properties between the updraft and downdraft.

This new closure method is called "Assumed Distribution Higher-Order Closure" (ADHOC). The name is directly reflective of the approach. I assume a "tophat" distribution similar to that used in current mass-flux models (the "assumed distribution"), in which all mean quantities and higher-moment statistics are written in terms of an updraft-downdraft decomposition. I then take plume equations describing the updraft and downdraft mean states and derive higher-order closure "plume" equations (the "higher-order closure" part). Some new things are discovered and some new techniques are introduced in this model. For example, an interesting result of the term-by-term analogy between the two systems (MFC and HOC) is that the lateral mass exchange terms in ADHOC are directly related to the dissipation terms of the HOC equations. I provide a new "ADHOC-specific" parameterization for these lateral mass exchange terms in the spirit of this discovery. In addition, I add a subplume-scale turbulence scheme to the model to directly address the issue of the inherent "scale-inconsistency" between HOC and MFC closure equations.

Results from this model are compared with observations and with those obtained using large-eddy simulation models. The model is run with a variety of tropical, sub-tropical, and high-latitude cases. These cases include cloud-free convection, stratocumulus, two types of shallow non-precipitating cumulus, and Arctic stratus. These results are discussed in detail and conclusions are drawn as to the strengths and weaknesses of this new closure method when applied to the various regimes.

ACKNOWEDGEMENTS

I would like to express my sincere appreciation to Dr. David Randall, my advisor, for his patience, understanding, and instruction during my Ph.D. work. His moral and technical support was absolutely critical to the success of this work. I would also like to thank my husband Jon, whose unending support during the last four years enabled me to get beyond every difficulty I endured. Finally, I would like to thank my office mates, Kevin Schaeffer and Michael Kelly for putting up with me, especially during the last few months of this work.

This research was funded by the National Aeronautics and Space Administration under Grant No. NAG1-1701, by the National Science Foundation under Grant No. OPP9504246, and by the Jet Propulsion Laboratory under Subcontract #950700/NASA TO#RF256.

Table of Contents

List of Acronyms

AB:	Adams-Bashforth
ADHOC:	Assumed-Distribution HOC
AMTEX:	Air Mass Transformation Experiment
ASTEX:	Atlantic Stratocumulus Experiment
AS74:	Arakawa and Schubert, 1974
ASC:	Arctic stratus clouds
ATEX:	Atlantic Trade-wind Experiment
A76:	André et al., 1976
BA86:	Bougeault and André, 1986
BL:	Boundary layer
BMRC:	Bureau of Meteorology Research Centre (Melbourne, Australia)
BOMEX:	Barbados Oceanographic and Meteorological Experiment
CBL:	Convective boundary layer
CCM3:	Community Climate Model (from NCAR)
CSU:	Colorado State University
CTEI:	Cloud-top entrainment instability
Cu:	Cumulus
C86:	Curry, 1986
DNS:	Direct numerical simulation
ECMWF:	European Center for Medium Range Weather Forecasts
FIRE:	First ISCCP Regional Experiment
GEWEX:	Global Energy and Water Cycle Experiment
GCM:	General Circulation Model
GCSS:	GEWEX Cloud System Study
GR90:	Gregory and Rowntree, 1990
HOC:	Higher-order closure
ISCCP:	International Satellite Cloud Climatology Project
ITCZ:	Intertropical Conversion Zone
KNMI:	Royal Netherlands Meteorological Instititute
LCL:	Lifting condensation level
LES:	Large-eddy simulation
LW:	Long wave
MBL:	Marine boundary layer
MFC:	Mass-flux closure
MPI:	Max-Planck-Institut für Meteorologie (Madrid, Spain)
MSc:	Marine stratocumulus
MTF:	Mean Turbulent Field models
MY82:	Mellor and Yamada, 1982
NCAR:	National Center for Atmospheric Research
PDF:	Probability density function
PBL:	Planetary boundary layer
PS:	Plume scale
RB86:	Raymond and Blyth, 1986
RH:	Relative humidity

RSM:	Randall, Shao, and Moeng, 1992
Sc:	Stratocumulus
ScTBL:	Stratocumulus-topped PBL
SC95:	Siebesma and Cuijpers, 1995
SH96:	Siebesma and Holtslag, 1996
SK96:	Smith and Kao, 1996
SGS:	Sub-grid scale
SHEBA:	Surface Heat and Energy Budget of the Arctic
SPS:	Subplume scale
SST:	Sea-surface temperature
SW:	Short wave
TKE:	Turbulent kinetic energy
TOA:	Top of atmosphere
TWBL:	Trade-wind boundary layer
T89:	Tiedtke, 1989
UCLA:	University of California, Los Angeles
UKMO:	United Kingdom Meteorological Office
UW:	University of Washington
WD:	Willis-Deardorff laboratory convection experiment
WVU:	West Virginia University
1-D:	One-dimensional
2-D:	Two-dimensional
3-D:	Three-dimensional

Chapter I: Introduction

Turbulence is a broad, rather obscure term that can refer to many different aspects of nature. Even the term "atmospheric turbulence" (turbulence within the earth's environment), which is more specific, lacks clarity and requires a more definitive interpretation. In general, there are no preset "rules" which delineate turbulent and non-turbulent atmospheric regimes. Therefore, atmospheric turbulence must be defined within the context of individual studies. More specifically, the confusion with regard to the definition of "atmospheric turbulence" can be avoided if the following questions (among others) are addressed apriori: Is turbulent motion defined on a scale basis? Can it be described in terms of its intensity level? Is the turbulence being viewed from a one-dimensional, two-dimensional, or three-dimensional perspective? Are clouds considered turbulence? Which levels of the atmosphere will be considered?

This thesis is a study of turbulence and thus needs to be clarified in terms of these concepts. The range of turbulent scales which I will address include those which characterize the atmospheric boundary layer (PBL)[1]. Turbulent eddies in this regime range in size from the smallest dissipative scales to those which span the entire boundary layer (on the order of a few kilometers). While I may at times refer to larger scales (e.g., scales on the order of deep cumulus convection), these larger scales are not specifically included in the definition of turbulence in this thesis. I will not restrict the definition of turbulence based on intensity considerations. Thus, I consider the only "non-turbulent" state to be one of zero motion. In addition, while clouds are not typically considered turbulence, they are an integral part of its definition in this study. Finally, I will only consider turbulence from a one-dimensional perspective.

---

[1]. The PBL is the region of the atmosphere through which one can detect the effects of surface-generated turbulence. The depth of the PBL is an indication of the strength of the boundary-layer turbulence. This includes turbulence generated by moisture, energy and momentum exchanges between the surface and the atmosphere, as well as that produced by turbulent entrainment into the PBL from the free atmosphere.

PBL turbulence can be studied using observations and/or numerical models. Ideally, both should be used; observations being a critical component in the development of new parameterizations in numerical models. Two of the most common ways to parameterize turbulence in the atmospheric boundary layer include mass-flux and higher-order closure (MFC and HOC respectively). Each of these methods have been successfully applied to specific types of regimes. In mass-flux models, quantities are typically represented using an "updraft-downdraft" decomposition (or more generally, quantities are described in terms of a area-weighted average of their values in rising and subsiding air; see Section II-E). Thus, these models have enjoyed continued success in regions where the distinction between rising and subsiding motion is clear (e.g., tropical cumulus convection).

Higher-order closure, on the other hand, has typically been applied to describe turbulence only in the PBL, whether clear or cloudy. The HOC equations are assumed to represent ensembled-averages and thus, inherently include all scales of turbulent motion. I believe that one weakness of HOC is the assumption that the small- and large-scale eddies can both be represented by a single set of parameterizations. Despite this weakness, HOC has successfully been used to describe some types of PBL turbulence (see Section II-D for more details on HOC).

Due to the success of these two approaches, both MFC and HOC schemes have separately been incorporated into large-scale models to represent various turbulent processes. However, in these models, the regimes in which these closure perform best are not always distinguishable. For example, general circulation models (GCMs) currently use separate schemes for planetary boundary layer (PBL) processes, shallow and deep cumulus (Cu) convection, and stratiform clouds (Fig. 1). As discussed, these schemes may individually work well in their respective regimes. However, these regimes are not always distinct. Often, two or more may coexist. For example, in the stratocumulus-to-cumulus transition region, cloud-top entrainment instability (CTEI; Lilly, 1968; Randall, 1980; Deardorff, 1980) may act to break up a stratocumulus (Sc) deck. Figure 1 shows the region in which this occurs. This results in a combination of shallow Cu and Sc clouds. The process by which this occurs is as follows: entrainment at cloud top mixes warm, dry inversion air into the PBL. While this would tend to warm the air at the PBL top, it is offset by the cooling which results from evaporation of cloud drops. In many situations, the cooling outweighs the warming (the criterion for this is called the "CTEI criterion"; Randall, 1980; Deardorff, 1980; Siems et. al., 1990). Cooling at cloud top drives downward motion which increases turbulence, and the turbulence, in turn, increases entrainment. This is a positive feedback which, over time, may lead to the breakup of solid cloud decks.

Two other phenomena which can lead to multiple cloud regimes are "cumulus-under-stratus" and "stratocumulus decoupling". These two processes are often connected. Stratocumulus decoupling can occur either from solar absorption within the cloud or from evaporation of drizzle below the cloud (Nicholls, 1984; Brost et al., 1982; Betts, 1990). As the cloud heats from solar absorption, it may become warmer than the subcloud layer, resulting in stable layer between the two. This stable layer decouples the cloud and the subcloud layers. Drizzle can cause the same effect if it falls into the subcloud layer, evaporates and cools. Here, the decoupling is caused by cooling the below the cloud. After decoupling, air near the bottom of the subcloud layer has a lower lifting condensation level (LCL) than air in the upper cloud layer (Betts, 1990). Thus, any surface heating or subcloud condensation results in cumulus clouds forming at the lower LCL. These Cu clouds can grow into the Sc layer above, resulting in cumulus-under-stratus (Betts, 1990; Paluch and Lenschow, 1991, Krueger et. al., 1995).

GCMs tend to poorly represent the total effect of clouds in these multiple-cloud regimes (Randall et al., 1998). The conventional distinction between the boundary layer and the cumulus layer is based on the assumption that they are physically distinct layers. However, this is not always the case. For example, shallow Cu clouds may be considered to exist completely within the PBL or they may be regarded as starting in the PBL but terminating above it. Deeper cumulus clouds often originate within the PBL but also can originate aloft. Thus, the distinction between the two layers clearly reflects holes in our understanding. In order to realistically simulate the global hydrologic cycle, energy budget and large-scale circulation, it is imperative that GCMs accurately represent clouds. Thus, there is a need to unify the approaches that GCMs take towards representing clouds and the boundary layer.

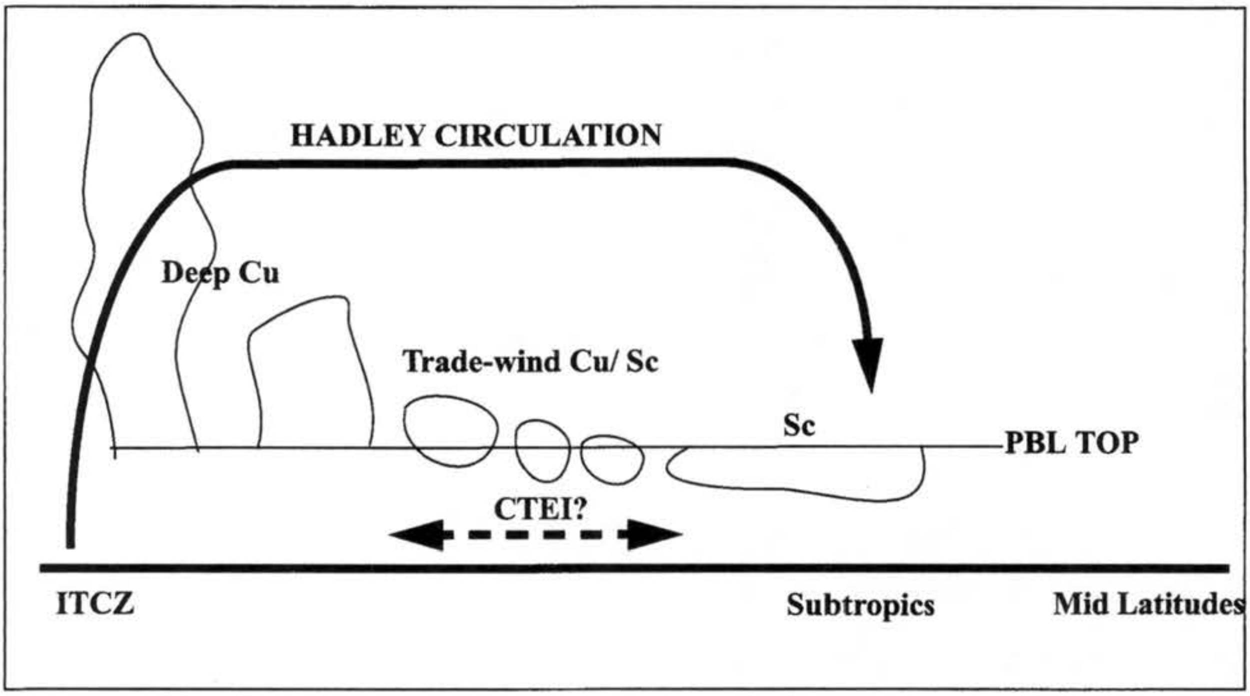

Figure 1: Idealized picture of typical cloud transitions from the tropics to the mid-latitudes. Deep cumulus (Cu) convection occurs near the Intertropical convergence zone (ITCZ). Stratocumulus (Sc) occur in the mid-latitudes. In between, there is a transition region with broken Sc and shallow, trade-wind Cu. The dotted line represents the region where cloud-top entrainment instability (CTEI) is active (Randall, 1976).

All GCMs employ this modular approach. To illustrate this, I will briefly describe the representation of PBL turbulence and clouds in three different GCMs: the Colorado State University GCM (CSU GCM), the European Center for Medium Range Weather Forecasts model (ECMWF GCM), and the National Center for Atmospheric Research Community Climate Model (CCM3). The schemes used in these models are summarized in Table 1.

Table 1: Comparison of GCM cloud and boundary layer parameterizations

GCM	*PBL turbulence scheme*	*Deep Cumulus scheme*	*PBL clouds*	*PBL entrainment*
CSU GCM	Mixed-layer with a modified σ coordinate (Suarez et al., 1983)	Modified Arakawa-Schubert (Randall and Pan, 1993)	Stratocumulus only- diagnosed based on saturation criterion at the PBL top	Diagnosed from a predicted bulk turbulent kinetic energy
ECMWF GCM	First-order closure closed with either a non-local diffusion scheme, a local diffusion scheme with a Richardson number dependence or with Monin-Obukhov functions	Bulk mass-flux scheme (Tiedtke, 1989). Scheme considers deep, shallow, and mid-level clouds.	Shallow convection scheme (Tiedtke et al., 1988)	Represented with an entrainment velocity parameterization (Deardorff, 1976)
NCAR CCM3	First-order closure scheme closed with a non-local vertical diffusion scheme for temperature and humidity (Holtslag and Boville, 1993) and a local scheme for momentum.	Plume ensemble approach developed by Zhang and McFarlane (1995).	Parameterized frontal clouds, tropical low clouds, and marine subtropical stratus	Implicitly treated with a non-local PBL diffusion scheme (Holtslag and Boville, 1993)

In the CSU GCM, the boundary-layer scheme is based on a mixed-layer approach (a simplified first-order closure scheme[2]), following Deardorff (1972) and Lilly (1968). With this approach, conserved quantities are considered vertically homogeneous and a jump condition is assumed across the PBL top (for a more detailed description of mixed-layer models, see Section II-D-2a; Ball, 1960; Lilly, 1968; Randall, 1976; Benoit, 1976). The entrainment rate (in the CSU GCM) at the top of the mixed layer is diagnosed from a predicted bulk turbulent kinetic energy (TKE). Cumulus clouds are assumed to originate at or above the PBL top (Fig. 1). They communicate their presence to the PBL by draining mass and reducing the PBL depth. Only surface and entrainment fluxes, advection, and radiation can effect properties of the PBL. Clouds within the PBL are stratocumulus clouds and are diagnosed by checking a saturation criterion at the PBL top. Shallow cumulus clouds, which exist solely within the PBL (Fig. 1), are not represented.

In CCM3, the boundary-layer scheme used is a first-order closure scheme which involves both local and non-local[3] closures (see Fig. 3; Holtslag and Boville, 1993). The PBL cloud formation schemes are empirical, involving the relative humidity (RH) and large-scale subsidence for frontal and tropical low clouds, and the RH, inversion strength, and PBL depth for subtropical stratus clouds. In CCM3, PBL clouds do not directly affect any parameterized turbulent process. Clouds however, can indirectly affect the PBL depth by altering the thermodynamic profiles of the mean state. Penetrative convection originating near the surface is parameterized using the Zhang and McFarlane (1995) deep convection scheme, along with Hack's (1994) moist convective scheme included for shallow cumulus convection and for convective clouds originating aloft. Like Arakawa-Schubert (1974), the Zhang-McFarlane and Hack parameterizations are based on the

---

2. HOC models are classified according to their "closure level", which determines which moments get predicted (or diagnosed) and which need to be parameterized. The simplest form of HOC is first-order closure, in which all turbulence statistics except the mean state are parameterized. In second-order closure, statistics higher than the second moments are parameterized, etc. For a more complete description, see Sections II-B and II-C.

3. Local and non-local refer to the type of transport in the PBL. Local transport occurs when the flux of a quantity is related to local vertical gradients of that quantity. In local transport, information can flow in both directions due to a single process. This is known as "down-gradient diffusion" and occurs in shear driven, stable boundary layers. Non-local transport occurs when fluxes are related to the overall gradient within the entire boundary layer. In this case, information moves in one direction only, often a direction that is opposite to the local gradients. This type of transport occurs in boundary layers where convection is dominant. Further discussion is given later.

concept of a cumulus mass flux, and use buoyancy closures. Neither the CSU GCM or the NCAR CCM3 includes parameterizations of the effects of deep convection on the surface fluxes.

Finally, the ECMWF GCM uses a first-order closure PBL scheme with a mix of vertical diffusion parameterizations; the surface layer fluxes are diagnosed with Monin-Obukhov similarity functions (Monin and Obukhov, 1954) and the upper-air fluxes are determined using either a local Richardson-number-dependent diffusion scheme or a non-local diffusion scheme (Troen and Mahrt, 1986) depending on whether the boundary layer lapse rate is stable or unstable respectively. Cumulus convection is parameterized by a bulk mass-flux scheme which is described by Tiedtke (1989). The model allows deep, shallow, and mid-level convection. The type of convection is determined by the intensity of the cloud-base mass flux. There are separate ways to determine the cloud base mass flux for each of the three convection types. Each of the three convective types affects the PBL in a different manner. For clouds that exist entirely within the PBL, the non-local diffusion PBL scheme treats cloud-top entrainment implicitly (Kiehl et. al., 1996).

Shallow clouds, which exist entirely within the PBL, are handled in a different manner. In these clouds, entrainment at cloud top must be parameterized within the context of the first-order boundary-layer scheme. As previously discussed, this tends to be unreliable. In the ECMWF GCM, the entrainment flux of any variable at cloud top is represented as the product of an entrainment velocity (Deardorff, 1976) and the jump in value of the quantity between the dry level just above the cloud and the cloud layer just below it. The entrainment velocity is represented in terms of the average buoyancy flux in the mixed layer, the long wave radiative flux divergence, and the jump in the virtual static energy at cloud top (ECMWF Users Guide, 1998).

Some common threads in each of the GCMs discussed above as well as in most other GCMs, are the simplicity of the PBL scheme (first-order closure in most cases), the separate treatment of different cloud types, and the lack of a reliable method to determine the entrainment rate-something that is critical to the evolution of both cloudy and clear PBLs.

In any model, the best parameterization is one that combines simplicity with accuracy. In GCMs however, there is a constant struggle between the two, and often the need for simplicity wins out over the desire for a highly sophisticated, more accurate parameterization. For example, observational results indicate a need for flexible cloud-top and cloud-base heights. The number of cloud types then increases as the square of the number of layers (Ding and Randall, 1998). This level of complexity is troublesome in GCMs. Likewise, current PBL schemes used in GCMs usually employ simple first-order closure which is known to be inadequate in many instances (e.g., thin PBL clouds that cannot be resolved with current vertical grid spacing). At present, the only HOC used in a GCM is a "level 2.5" scheme [In a "level 2.5" scheme, the turbulence kinetic energy is the only prognosed higher-order moment (Mellor and Yamada, 1974)]. GCMs from the Center for Climate System Research in Japan, the Center for Ocean-Land-Atmosphere Studies in Maryland, and the Geophysical Fluid Dynamics Laboratory in New Jersey all use variants of the level 2.5 scheme of Mellor and Yamada (1982; MY82). A modified MY82 scheme is used in the Goddard Laboratory for Atmospheres GCM (Helfand and Labraga, 1988). The inclusion of this minimal form of HOC tends to represent the boundary-layer processes in GCMs well (Miyakoda and Sirutis, 1977). More sophisticated higher-order closure schemes for the PBL have been considered too complex for use in GCMs.

In order to improve GCM simulations of cloud and boundary-layer processes, we need to directly address the following two issues:

- How do we achieve increased accuracy in GCMs without making parameterizations too complex to be used in practice?
- How can we combine cloud and PBL processes (two highly complex components of GCMs) so that they are no longer artificially separated?

In this thesis, I will describe a model which addresses the second of these issues, and I will lay out a framework to generalize this approach for use in GCMs. The theoretical basis of the model is the unification of HOC (a PBL scheme; see Sections II-C and II-D) and mass-flux parameterizations (a cloud scheme; see Section II-E). The hope here is that by combining the two, I can minimize the complexity of the approach and allow for a more sophisticated and accurate treatment of boundary-layer processes and clouds in GCMs.

The thesis is set up as follows: In Chapter II, I will discuss the history of atmospheric turbulence modeling as it relates to the definition of turbulence discussed above. This will include a description of both MFC and HOC parameterizations and a summary of their strengths and weakness as applied to various regimes. In Chapter III, I the current model is described in detail. This will include a background discussion of the work which motivated the idea of a "unified" approach. In Chapter IV, I show results from the simulations of a variety of PBL regimes. These include cloud-free convection, stratocumulus, trade-wind cumulus, and Arctic stratus. I will discuss the strengths and weaknesses of the approach as applied to each of these regimes. Finally, in Chapter V, I provide a summary and conclusions.

Chapter II: Scientific Background

II-A: Early history of turbulence modeling

Atmospheric scientists have used statistical methods to study turbulent flow for more than a century now. In 1894, Reynolds formulated the idea of separating fluid flow into mean and fluctuating parts. It was this keen foresight that became the foundation for more than a century of work in turbulence parameterizations. It wasn't until three decades later that the pioneering work of Reynolds was finally recognized and explored. In 1921, Geoffrey Taylor recognized the importance of the second-order terms that Reynolds discussed in the mean state velocity equations. Shortly after, Keller and Friedman (1924) came to an unpleasant realization: A full statistical description of turbulence requires an infinite set of equations. This became known as the closure problem (described in detail in Section II-B) and today still remains one of the unsolved problems of classical physics.

Since 1924, most of the theoretical work done on turbulence dynamics has been devoted to overcoming the closure problem. The focus of research in this area took two distinct paths: understanding the large-scale turbulent flow (scales on the order of the overall flow) and understanding the small-scale flow. The distinction between these two regimes is clear if the scales are well-separated. The large scale flow depends on flow boundaries and external forcing while the small-scale flow, to a large extent, possesses a universal character.

The earliest closure theories focused on the large-scale flow. They were semi-empirical and were based on an analogy between turbulent chaos and molecular chaos. Their fundamental concepts include the mixing length (analogous to the mean free path of molecules), the intensity of turbulence (analogous to the root-mean-square velocity of molecules), and the coefficients of turbulent viscosity, thermal conductivity, and diffusion. These semi-empirical theories provided a method to diagnose the Reynolds stress (second-moment velocity correlations) in terms of the mean flow velocity.

Although major interest in the small-scale component of the flow would not come for another 15 years, Lewis Richardson (as early as 1922) put forth some penetrating ideas on the physical mechanism of turbulent mixing in large Reynolds number flows, and with that he was the first to address the role of the small-scale component. In 1922, Richardson described turbulence as a hierarchy of eddies. His view of turbulence was the following: Turbulent eddies are produced at the largest scales and successively lose their energy to smaller and smaller eddies through a process which is now called an energy cascade. Eventually, the scale of the eddy is so small that viscous dissipation converts the kinetic energy of the eddy into heat. It is of interest to note that, although Richarson's ideas were strictly qualitative, they have clearly withstood the test of time. More than 75 years later, we still consider this view of turbulence correct.

The next big discovery came in the 1930s from Geoffrey Taylor. He introduced the concept of "homogeneous and isotropic turbulence" and demonstrated the usefulness of looking at turbulent flow from this angle (Taylor, 1935). While it was common knowledge that real turbulence is not homogeneous or isotropic, Taylor recognized that the small-scale component of the flow includes a statistical regime which *is* homogeneous and isotropic. In addition, looking at turbulence in this manner has allowed us to simplify and more easily understand its complex governing equations. This revolutionary view was one of the most valuable steps in our progress towards understanding the nature of turbulence. Even today, 65 years later, any discussion of turbulence begins with the homogeneous and isotropic turbulence equations.

The next decade revived the ideas of Richardson. Kolmogorov (1941) added to both the qualitative and the empirical ideas of Richardson and Taylor. He noted that, as eddies break down into successively smaller scales, they become less and less affected by the mean flow. Thus, since the mean flow has an influence on the orientation of turbulence, these small scales are not oriented and can be considered homogeneous and isotropic. From this, Kolmogorov argued that the statistical regime of such small scales, in high Reynolds number flows, can be fully described with only two parameters: the mean dissipation rate, ε, and the coefficient of viscosity, υ. He further hypothesized that, in between this small scale and the largest scales, there is an inertial subrange through which energy is simply transferred. In this inertial subrange, the flow is effected only by ε. This work became the basis for all developments in the theory of the local structure of turbulence in the 1940s and 1950s.

The advent of computers put the early theories of turbulence to a new test. Due to the transient nature of turbulence in the atmosphere, it is extremely difficult to measure. Thus, numerical simulations of turbulence have emerged as a critical tool for understanding the development and evolution of turbulent flow. Since the 1920s, scientists have recognized that, in order to properly model atmospheric turbulence, they need to address three basic closure problems: the pressure-velocity correlations, the dissipation, and the higher-order moments that appear as transport terms in lower moment equations. The ground-breakers with these three closure parameterizations were Kolmogorov (1942) for dissipation, Rotta (1951) for the pressure terms, and Prandtl (1925) for the transport terms. The fact that we still use some form of all three of these early theories in turbulence models of the 1990s is a true tribute to the pioneering minds of these three men.

Almost fifty years after Reynold's discovery, Kolmogorov (1942) and Prandtl and Wieghardt (1945) formulated the first semi-heuristic turbulence models. These models served as the basis for what was to become known as Mean Turbulent Field (MTF) models. MTF models ranged in complexity from those that predicted all components of the Reynolds stress tensor to those that just predicted the turbulence kinetic energy. In 1951, Rotta advanced the field of turbulence closure modeling with his return-to-isotropy hypothesis for the pressure terms. This theory could be applied to the turbulent kinetic energy equation as well as the directional components of the Reynolds stress tensor.

Since 1951, the focus of turbulence research has shifted. The advent of computers fueled interest in the development of turbulence parameterizations specifically for numerical models. The sophistication of closure parameterizations (see next Section) has grown tremendously in response to the available technology. Thus, the next few sections of history will focus on parameterization development.

II-B: The closure problem

At the very core of atmospheric turbulence modeling is the turbulence closure problem. Perhaps no other concept so concisely describes the level of complexity and uncertainty that comes with trying to understand smaller and smaller scales in the atmosphere. The basic concept is that the number of unknowns in the set of equations for turbulent flow is larger than the number of equations. When equations are included for these unknowns, they contain even more new unknowns (Stull, 1988; described in detail below). Thus, for any finite set of these equations, the description of turbulence is not *closed*; a complete statistical description of turbulence requires an infinite set of equations (Keller and Friedman, 1924). Higher-order closure modeling involves parameterizing the unknowns in terms of the knowns in order to "close" the system of equations. The highest moment determines the level of closure. Zeroth-order closure implies that the mean wind, temperature, humidity, and other mean quantities are parameterized directly as functions of space and time (Stull, 1988). First-order closure predicts only the mean state, and second-order closure predicts the mean state and the second moment statistics, etc...

We can best describe the closure problem by beginning with the equation for the time rate of change of the mean state of a quantity. In this example, I will use the total horizontal wind, U_i

$$\frac{\partial U_i}{\partial t} + U_j\frac{\partial U_i}{\partial x_j} = -\delta_{i3}\left[g - \left(\frac{\theta'_v}{\overline{\overline{\theta}}_v}\right)g\right] - f_c\varepsilon_{ij3}U_i - \frac{1}{\rho}\frac{\partial p}{\partial x_i} + \nu\frac{\partial^2 U_i}{\partial x_j^2} \quad ; \tag{1.1}$$

here $g = 9.8\,\mathrm{m\,s^{-1}}$ is the acceleration due to gravity, p is the pressure, ρ is the density of air, ν is the kinematic viscosity; $\theta_v = \theta(1 + 0.61 r_v - r_L)$ is the virtual potential temperature, θ is the potential temperature, r_v is the vapor mixing ratio, r_L is the liquid water mixing ratio, and f_c is the coriolis parameter.

We can derive a prognostic equation for $\overline{U}_i$ by Reynolds averaging (1.1),

$$\frac{\partial \overline{U}_i}{\partial t} + \overline{U}_j\frac{\partial \overline{U}_i}{\partial x_j} = -\delta_{i3}\left[g - \left(\frac{\theta'_v}{\overline{\overline{\theta}}_v}\right)g\right] - f_c\varepsilon_{ij3}\overline{U}_i - \frac{1}{\rho}\frac{\partial}{\partial x_i}\overline{p} + \nu\frac{\partial^2 \overline{U}_i}{\partial x_j^2} - \frac{\partial}{\partial x_j}\overline{u_i'u_j'} \quad , \tag{1.2}$$

where "barred" quantities represent mean state values and "primed" quantities represent perturbations from the mean state values (i.e., $U_i = \overline{U}_i + u_i'$). Upon examination of (1.2), we see that in trying to predict the mean east-west wind, we have a new unknown; namely, $\overline{u'_iu_j'}$. Thus, in trying to predict an unknown, we develop a prognostic equation which contains more unknowns. In this example, we have one equation and two unknowns. Thus, the problem is not solved.

One way around this is to then try and derive a prognostic equation for the new unknown. This can be done by subtracting (1.2) from (1.1), leaving an equation for $U - \overline{U}$ or u'. We then combine this equation with the perturbation continuity equation to get a prognostic equation for the new unknown $\overline{u'_iu_j'}$,

$$\frac{\partial}{\partial t}\overline{u'_i u'_k} + \overline{U}_j \frac{\partial}{\partial x_j}\overline{u'_i u'_k} = \tag{1.3}$$

$$-\overline{u'_i u'_j}\frac{\partial \overline{U}_k}{\partial x_j} - \overline{u'_j u'_k}\frac{\partial \overline{U}_i}{\partial x_j} - \frac{\partial}{\partial x_j}\overline{u'_i u'_j u'_k} + \delta_{k3}\left(\frac{\overline{u'_i \theta'_v}}{\overline{\theta}_v}\right)g + \delta_{i3}\left(\frac{\overline{u'_k \theta'_v}}{\overline{\theta}_v}\right)g +$$

$$f_c[\varepsilon_{kj3}\overline{u'_i u'_j} + \varepsilon_{ij3}\overline{u'_k u'_j}] - \frac{1}{\rho}\left[\frac{\partial}{\partial x_i}\overline{p'u'_k} + \frac{\partial}{\partial x_k}\overline{p'u'_i} - \overline{p'\left(\frac{\partial u'_i}{\partial x_k} + \frac{\partial u'_k}{\partial x_i}\right)}\right] +$$

$$\nu \frac{\partial^2}{\partial x_j^2}\overline{u'_i u'_k} - 2\nu \frac{\overline{\partial u'_i \partial u'_k}}{\partial x_j^2}$$

The terms in (1.3) represent (from left to right) storage, advection by the mean flow, shear production (2 terms), transport, buoyancy (2 terms), coriolis effects (2 terms), pressure transport and diffusion, molecular diffusion, and viscous dissipation.

It is obvious that we have just made our problem worse. We have created even more unknowns that we don't know (e.g., $\overline{u'_i \theta'_v}$, $\overline{p'u'_i}$, $\overline{u'_i u'_j u'_k}$, and $\frac{\overline{\partial u'_i \partial u'_k}}{\partial x_j^2}$). Following this pattern, we can see that if we try to predict these new unknowns again, we will continue to make the ratio of unknowns to equations larger. The basic unknowns are the higher moment transport terms (e.g., $\overline{u'_i u'_j u'_k}$ in Eq. 1.3), pressure correlations (e.g., $\overline{p'u'_i}$), buoyancy fluxes (e.g., $\overline{u'_i \theta'_v}$), and dissipation terms (e.g., $\frac{\overline{\partial u'_i \partial u'_k}}{\partial x_j^2}$). A similar effect can be found in any second moment prognostic equation. Another example is Eq. 1.4 for the heat flux $\overline{u_i'\theta'}$,

$$\frac{\partial}{\partial t}\overline{u'_i\theta'} + \overline{U}_j\frac{\partial}{\partial x_j}\overline{u'_i\theta'} = \tag{1.4}$$

$$-\overline{u'_j\theta'}\frac{\partial \overline{U}_i}{\partial x_j} - \overline{u'_iu'_j}\frac{\partial}{\partial x_j}\bar{\theta} - \frac{\partial}{\partial x_j}\overline{u'_iu'_j\theta'} + \delta_{i3}\left(\frac{\overline{\theta'\theta'_v}}{\overline{\theta_v}}\right)g +$$

$$f_c[\varepsilon_{ij3}\overline{u'_j\theta'}] - \frac{1}{\rho}\left[\frac{\partial}{\partial x_i}\overline{p'\theta'} - \overline{p'\left(\frac{\partial}{\partial x_i}\theta'\right)}\right] +$$

$$\nu\frac{\partial^2}{\partial x_j^2}\overline{u'_i\theta'} - 2\nu\frac{\overline{\partial u'_i \partial\theta'}}{\partial x_j^2} - \left(\frac{1}{\rho C_p}\right)\overline{u'_i\frac{\partial Q'_j}{\partial x_j}} ,$$

where Q' is the perturbation radiative flux, and $C_p = 1004\ \mathrm{J\ kg^{-1}\ K^{-1}}$ is the specific heat of air at constant pressure. The terms in (1.4) represent (from left to right) storage, advection by the mean flow, gradient production (2 terms), transport, buoyancy, pressure transport and diffusion, molecular diffusion, viscous dissipation, and radiation.

So, the question arises as to how to stop the number of unknowns from multiplying. Obviously, in order to do this we need to parameterize the unknowns in terms of quantities that we already known so that we can bring the number of equations and unknowns into balance. However, there is no obvious place to stop. Two things determine the stopping place: (1) the amount of computer power available, and (2) the accuracy that one desires. The cost of predicting higher-order terms is that simulation takes longer to complete. If in fact the prediction of higher-order terms make the solution more accurate, is the increase in accuracy worth cost of the added computation time?

In addition to choosing the order of closure, one must also decide which parameterizations to use for the unknown terms. Closure parameterizations abound in the literature. The next few sections are devoted to this topic.

II-C: Higher-order closure parameterizations

Equations 1.3 and 1.4 both represent prognostic equations for second-order turbulence moments (For a complete list of first- and second-order turbulence closure equations, see Appendix A). As I showed in the last section, each of the turbulence equations has more than one unknown term. In (1.3), the unknowns that must be parameterized are the transport, buoyancy, pressure, and dissipation terms. Similar unknowns exist in (1.4) with the additional unknown of the turbulent radiative flux. In this next few sections, I will review a few of the more common parameterizations for second- and third-order closure modeling, describe the history of their use, and comment on their advantages and disadvantages.

II-C-1: Pressure terms

The pressure transport and diffusion terms which appear in Eqs. 1.3-1.4 appear in the equation for any turbulent moment which involves a component of the wind. The literature abounds with ideas on how to parameterize these terms (Rotta, 1951; Lilly, 1967, Crow, 1968; Deardorff, 1973; Launder, 1975; Zeman, 1981). Prior to 1980, many turbulence modelers believed that the pressure transport terms were small and they often neglected them (Hanjalic and Launder, 1972; Mellor, 1973; André et. al., 1978). However, during this time period, some argued that the effect was significant (Wyngaard, 1978; Zeman and Lumley, 1976). Wyngaard and Coté (1971) measured shear and buoyant production, turbulent transport, and dissipation in the unstable surface layer. Their results showed that a substantial imbalance resulted. Nothing else but the unmeasured pressure transport could have accounted for this imbalance, and they argued for the importance of retaining it in models. In another observational study, McBean and Elliott (1975) confirmed that the pressure transport is a source of kinetic energy in the unstable surface layer.

By 1990, most agreed that neglect of the pressure terms is a serious error, especially in the surface or inversion regions of the boundary layer where the air is forced to rapidly slow down (Canuto, 1992; Fig. 2). It is currently believed that, the convergence air as a downdraft approaches the surface creates high pressure, which acts to slows the air down. Conversely, updraft air near the surface creates a low pressure wake behind it which works to inhibit the air from leaving. The manner in which these pressure terms act is to convert vertical momentum into horizontal momentum. In fact, the original ideas for the parameterization of these terms were based on pressure "redistributing" momentum among the velocity components. This process is shown in

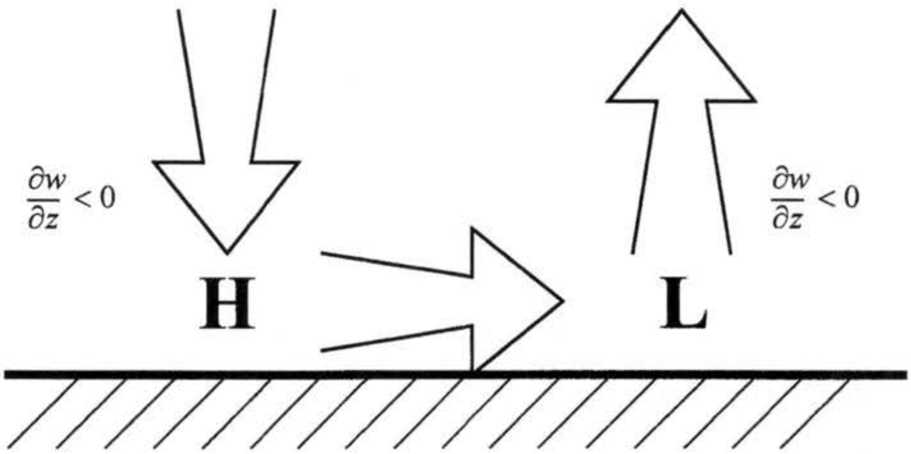

Figure 2: Schematic showing the pressure-induced motions that results from updraft and downdraft flows near the surface.

Fig. 2.

We call the last part of the pressure term in the turbulent momentum equation (Eq. 1.3) the "return-to-isotropy" term. We call the analogous terms in the wind-scalar-type equations (Eq. 1.4) "pressure-scalar transport" terms. A parameterization for the return-to-isotropy term was suggested by Rotta (1951). Equation 1.3 represents a 3x3 matrix system. Rotta noted that if one adds term the last part of the pressure term for the three equations that make up the trace of this matrix ($\overline{u'u'}$, $\overline{v'v'}$, and $\overline{w'w'}$), they sum to zero. Thus, this term does not contribute to the total turbulence kinetic energy $TKE \times 2 = \overline{u'u'} + \overline{v'v'} + \overline{w'w'}$. However, in any one component of the trace, this term is not zero. Thus, the function of this term must be to redistribute energy among the three components in a manner such that the net change over all three is zero. He postulated that it must return anisotrophic turbulence to isotropy through energy redistribution. Thus, Rotta coined the term "return-to-isotropy" and made the term proportional to the level of anisotropy of the turbulence.

The parameterization that Rotta developed is

$$\overline{p'\left(\frac{\partial u'_i}{\partial x_k}+\frac{\partial u'_k}{\partial x_i}\right)} = -C\frac{q}{l}\left(\overline{u'_iu'_k}-\delta_{ij}\frac{q^2}{3}\right) ; \tag{1.5}$$

where $q = \overline{u'^2_i}$ and l is the dissipation length scale (Bougeault and André, 1986). The forcing produced by this term will always be toward isotropy. For example, if $\overline{u'u'}$ contains more than its share of one-third of the velocity variance ($TKE \times 2$ or q^2), then the right-hand side of (1.5) is negative and it will act to decrease $\overline{u'u'}$ (Eq. 1.3). This means that if $\overline{u'u'}$ is too big, it will decrease and if $\overline{u'u'}$ is too small, it will increase. This force, acting on all three components of the TKE simultaneously will force the motion toward an isotropic state.

This parameterization was used by itself for many years in many turbulence models. However, does this simple parameterization tell the whole story? Purely turbulent interactions comprise the Rotta parameterization. If one takes one component of the perturbation velocity equation ($\frac{\partial}{\partial t}u'$, $\frac{\partial}{\partial t}v'$, or $\frac{\partial}{\partial t}w'$) and takes the divergence of this equation, there will be a term $\nabla^2 p'$.

Solving for this term, one gets a Poisson equation which describes the factors that can have an effect on turbulent pressure perturbations in the atmosphere,

$$\frac{1}{\rho_0}\nabla^2 p' = -\left(\overline{\frac{\partial u'_i \partial u'_k}{\partial x_k \partial x_i}} - \overline{\frac{\partial u'_i \partial u'_k}{\partial x_k \partial x_i}}\right) - 2\frac{\partial \overline{U}_i \partial u'_k}{\partial x_k \partial x_i} + \beta g \frac{\partial}{\partial x_3}\theta' \; ; \tag{1.6}$$

where ρ_0 is the density of air, $\beta = \frac{g}{\theta_0}$ is the buoyancy coefficient, and θ_0 is a reference potential temperature, typically taken as 300 K. This Poisson equation shows that turbulent pressure perturbations arise from three sources:

- turbulent-turbulent (non-linear) interactions
- Mean Shear-turbulent effects (linear)
- Buoyancy- turbulent effects (linear)

The terms in (1.6) represent "slow" and "rapid" effects that pressure perturbations can have on turbulence. The first of these terms (representing turbulent-turbulent interactions) is the part that Rotta parameterized. It is a non-linear term that has become known as the "slow" part of the pressure effect. The "slow" here referring to the indirect effect this term has on the turbulence. (first the turbulence field gets distorted, and then this term acts to restore the order). This is in contrast to the linear shear and buoyancy terms [second and third terms on the right-hand side of (1.6)] which represent the "rapid" part of the effect. The "rapid" effects are so-named due to the instant or "rapid" effect on the anisotropy of the turbulence that occurs when buoyancy or shear is generated in an isotropic turbulent field.

If mean shear or buoyancy effects are important contributors to the pressure effects, then the Rotta parameterization for the pressure covariance term is incomplete. Launder (1975) believed that this was the case and he was among the first to parameterize these "rapid" pressure effects. The mean strain generations [the second term on the right-hand side of (1.6)] was the first "rapid" part they considered. Ironically, Naot et al. (1970) originally proposed using this term as a replacement for the Rotta parameterization. Later, both Lumley and Khajeh Nouri (1973) and Launder, Reece, and Rodi (1975) used it as an addition to Rotta's term. Finally, Launder (1975) noted that, if one accepts that mean-strain generation should be an included effect, then one should also include the buoyancy generation term from (1.6). The final form that he adopted and that others most-often use is:

$$\overline{p'\left(\frac{\partial u'_i}{\partial x_k}+\frac{\partial u'_k}{\partial x_i}\right)} = -C_1\frac{q}{l}\left(\overline{u'_iu'_k}-\delta_{ij}\frac{q^2}{3}\right)-C_2\left(P_{ij}-\frac{2}{3}\delta_{ij}P\right) , \tag{1.7}$$

$$\text{where } P_{ij} = -\left\{\overline{u'_iu'_k}\frac{\partial\overline{U}_j}{\partial x_k}+\overline{u'_ju'_k}\frac{\partial\overline{U}_i}{\partial x_k}\right\}-\beta\{\overline{u'_iT'}g_j+\overline{u'_jT'}g_i\} , \tag{1.8}$$

$$P = -\left\{\overline{u'_iu'_k}\frac{\partial\overline{U}_i}{\partial x_k}+\beta\overline{u'_iT'}g_i\right\} , \tag{1.9}$$

$C_1 = 2.0$, and $C_2 = 0.6$.

As noted previously, these second-order pressure-covariance terms also appear in any prognostic equation which involves a component of velocity. Thus, there is also a pressure covariance term to deal with when predicting any $\overline{u'_i\psi'}$ (where ψ is any scalar). In general, most modelers have neglected this term in the turbulent scalar equations. However, for similar reasons that I described for the momentum-pressure covariances, there is controversy about its importance-especially in the surface layer. Mellor (1973) extended the Rotta parameterization to include the pressure terms found in the equations of scalar fluxes, $\overline{u'_i\psi'}$ (see Appendix A). It is interesting to note that in the case of a scalar flux, the last term in (1.5) is zero since $\delta_{ij} = 0$. What remains in this equation is

$$\frac{\partial}{\partial t}\overline{u'_i\psi'} \sim -C\frac{q}{Lx}\overline{u'_i\psi'} \quad . \tag{1.10}$$

This is basically a dissipation term (Section II-C-3), where $\frac{q}{Lx}$ is the dissipation time scale. Thus, we see that if we keep the Rotta parameterization in the scalar flux equations, the effect is to dissipate the flux. This is logical if you consider that a flux is a vector (directional) quantity. A flux may only be isotropic only if it is equal to zero. Thus, the "return-to-isotropy" parameterization of Rotta must take the form of a dissipation.

Finally, in the triple moment equations, the pressure terms are either modeled as dissipation or neglected completely. The discussion of the handling of the pressure terms in the current model explored in Section III-H. Next, I will talk about diffusion and transport parameterizations in HOC.

II-C-2: Diffusion and Transport

The earliest thoughts on atmospheric turbulent diffusion were that it was analogous to molecular diffusion (Donaldson, 1973). Molecular diffusion is affected by two things; the gradient of the diffusing quantity and a molecular diffusivity constant, μ. This constant is a function of the fluid and thus depends on the temperature and pressure (and thus the density) of the fluid. Thus, molecular diffusion is parameterized as

$$\frac{\partial}{\partial z}\overline{w'\psi'} = \frac{1}{\rho}\frac{\partial}{\partial z}\mu\frac{\partial\psi}{\partial z} \quad . \tag{1.11}$$

The quantity μ/ρ is represented by the symbol ν and is called the molecular diffusivity.

If we suppose that turbulent diffusion behaves in a similar manner, we arrive at the simplest and perhaps least accurate parameterization for turbulent diffusion used in atmospheric models; down-gradient diffusion (also called K-theory):

$$\frac{\partial}{\partial z}\overline{w'\psi'} = \frac{1}{\rho}\frac{\partial}{\partial z}K\frac{\partial\psi}{\partial z} \; ; \tag{1.12}$$

here K, the eddy diffusivity, is different for momentum and heat (dry or moist). There are many problems inherent in trying to make atmospheric turbulence analogous to molecular turbulence. Most stem from the fundamental differences in the scales on which these phenomenon occur. Molecular diffusion is a "small eddy" phenomenon; it happens only on small scales. In the atmosphere, boundary-layer turbulent eddies can be very large and the associated fluxes are often counter-gradient (Deardorff, 1966; Wyngaard and Coté, 1974; Zeman and Lumley, 1976). For example, on a clear, convective day, surface heating may be communicated to the top of the PBL with a single large eddy (Fig. 3). This "non-local" transport occurs despite any sections of the ambient atmosphere where the potential temperature locally increases with height. Another example of "non-local" transport (see footnote, page 9) is cumulus convection. A down-gradient diffusion parameterization for transport in the either of these convective regimes is clearly inaccurate; it would cause transport to be too slow and, in places, in the wrong direction. In general, the larger the eddy, the less realistic the down-gradient diffusion assumption.

In addition, the diffusivity constant in atmospheric turbulence is a function of the flow (not of the fluid as is the case in molecular diffusion). More mixing takes place with more turbulence; thus, K must be parameterized in terms of the shear and the stability of the flow at each level. Typical parameterizations of K have ranged from constant values (the least accurate) to complex

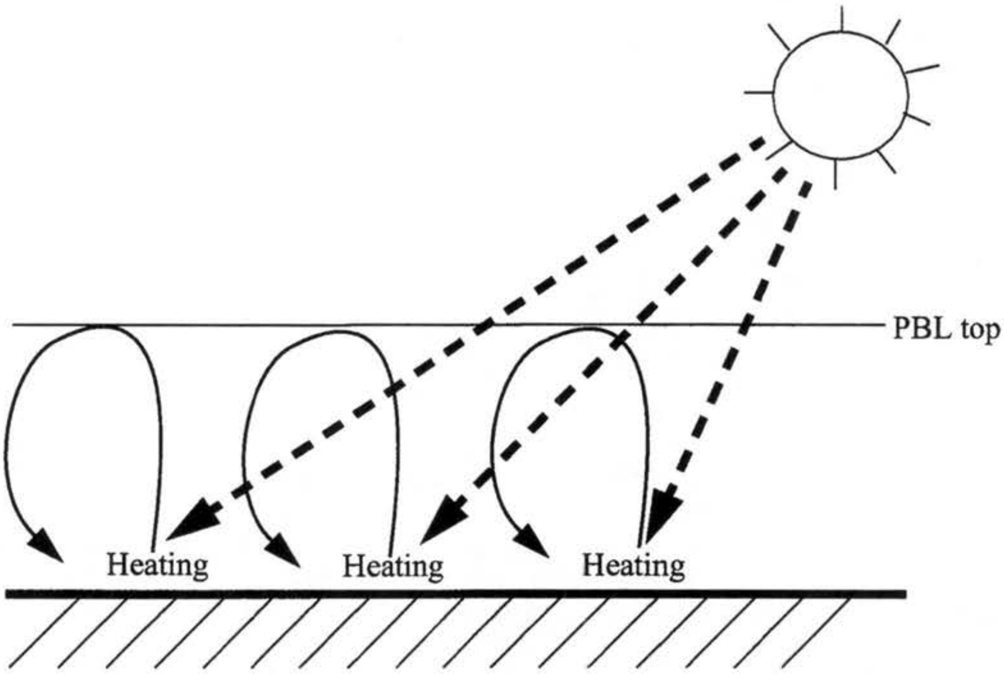

Figure 3: Schematic showing the generation of large convective eddies in the boundary layer, which are initiated from strong surface heating. In such a regime, "non-local" transport is dominant and local down-gradient relationships are invalid (i.e., the flow will persist in the direction shown regardless of the background ambient temperature gradient).

functions of the inertial and convective stability of the atmosphere (e.g., Bhumralkar, 1975; Louis, 1979). The need to parameterize K in (1.12) adds a level of complexity and uncertainty to the seemingly simple mathematical form for diffusion. Another uncertain aspect of K-theory parameterizations is the ratio of K between heat (K_h)and momentum (K_m). It is typically assumed that

$$\frac{K_h}{K_m} = 1.35 \qquad (1.13)$$

(Stull, 1988) for neutral conditions.

Attempts were made to modify K-theory to "non-local" conditions in order to better parameterize turbulent diffusion. There is no shortage of ideas in the literature as to how this should be done. Examples include the following:

1. the addition of a "counter-gradient" term (Eq. 1.14); γ in (1.14) represents the "non-local" part of the transport (Deardorff, 1966; Mailhot and Benoit, 1982; Therry and Lecarreré, 1983; Troen and Mahrt, 1986; Holtslag and Moeng, 1991);
2. transilient turbulence theory [mixing occurs between *any* combination of two levels at once-adjacent or not; this mixing occurs in different parameterized ratios which depend on the turbulent structure and the different layer proximity (Stull, 1988)];
3. spectral diffusivity theory (assumes that K varies with the size of the eddy and spectrally decomposes the diffusion equations; Berkowicz et. al., 1979).

$$\overline{w'\psi'} = -K\left(\frac{\partial\psi}{\partial z} - \gamma\right) \tag{1.14}$$

The plethora of ways to parameterize K in the literature is a testimony to the fact no one approach has met with great success. Literally dozens of revisions have been proposed since the original analogy with molecular diffusion. All have failed to produce a parameterization which can be universally applied to the full range of atmospheric turbulent states. However, not all first-order closure models use this K-theory or one of its variants. One of the simplest first-order closure models is a mixed-layer model (discussed in detail in Sections II-D-1 and II-D-2a). These models determine the structure of the PBL from only the surface and entrainment fluxes. Thus, the properties of the PBL are determined "non-locally". While this simple model represents non-local effects, it is unable to be used in boundary layers where "local" effects are dominant (e.g., is shear-driven PBLs).

While the inclusion of counter-gradient effects allows "non-local" transport to be considered in the parameterization of fluxes, no such parameterization exists for the corresponding "flux-like" (third moment) terms in the second-order closure equations. In parameterizing the third moments, more than two-thirds of models currently use a simple down-gradient diffusion assumption with varying formulae for the eddy diffusivity (a form analogous to Eq. 1.12; Moeng and Wyngaard, 1989). This is a staggering figure considering the evidence which exists that shows how poorly this parameterization can perform. This fact alone boldly exposes the biggest weakness of turbulence modeling in the atmosphere: the representation of the transport process. In large-scale models for which lower-order schemes are adopted, often a modified form of *K*-theory is chosen to represent fluxes [e.g., the K-profile model of Troen and Mahrt (1986) in the National Center for Atmospheric Research (NCAR) Community Climate Model (CCM3); K-Richardson-number-dependent model based on Louis (1979) in the European Center for Medium Range Weather Forecasts model (ECMWF)].

Surely, a more realistic way to represent diffusion could greatly improve the accuracy of turbulence simulations in all atmospheric boundary-layer models. The combined MFC/HOC model described in this thesis may provide a solution (Section III-A).

II-C-3: Dissipation

Dissipation is a form of damping for turbulence, acting to prevent any turbulent moment from getting too large. It is always a sink. It appears in any given turbulence closure equation as a correlation of the gradients of the components of the moment times a kinematic (or thermal in the case of temperature and moisture) viscosity (ν), and is often given the symbol ε:

$$\frac{\partial}{\partial u}\overline{u_i'u_k'} \sim -2\nu\overline{\left(\frac{\partial}{\partial x_j}u_i'\right)\left(\frac{\partial}{\partial x_j}u_k'\right)} = 2\varepsilon \ . \tag{1.15}$$

A natural way to parameterize a process whose sole job is to prevent turbulence build-up is to make it proportional to the negative value of what it supposed to dissipate:

$$\frac{\partial}{\partial u}\overline{u_i'u_k'} \sim -2\nu\overline{\left(\frac{\partial}{\partial x_j}u_i'\right)\left(\frac{\partial}{\partial x_j}u_k'\right)} = -C\frac{\overline{u_i'u_k'}}{\tau} . \tag{1.16}$$

In this way, the bigger the turbulent moment, the larger the restoring force.

With this natural parameterization, we must decide how to determine the dissipation time scale (τ), or equivalently a dissipation length scale (Lx). If a model predicts the TKE and if the length over which a given eddy will mix can be estimated, then it is trivial to diagnose the dissipation time scale,

$$\tau = \frac{Lx}{\sqrt{e}} ; \tag{1.17}$$

here $e = TKE$. Turbulence modelers have followed two paths in attempts to represent accurately the effects of turbulent dissipation. The first is to predict either the dissipation or a turbulent length scale directly,

$$\frac{\partial \varepsilon}{\partial t} = \frac{C_3 \varepsilon}{e} \cdot \left(-\overline{w'u'}\frac{\partial}{\partial z}\overline{U} - \overline{w'v'}\frac{\partial}{\partial z}\overline{V} + \frac{g}{C_p T_v}\overline{w's'_v}\right) - \frac{C_4 \varepsilon}{\tau} + C_5 \frac{\partial}{\partial z}K\frac{\partial \varepsilon}{\partial z} \tag{1.18}$$

(Langland and Liou, 1996; Beljaars et al., 1987; Detering and Etling, 1985), and the second is to diagnostically determine one of these quantities. In (1.5), w is the vertical velocity, $s_v = C_p T_v + gz$ is the virtual dry static energy, $T_v = T(1 + 0.61 r_v - r_L)$ is the virtual temperature, T is the actual temperature, and z is height.

The original version of current model (which was purely a second-order closure scheme with no mass flux) used (1.18) to predict the dissipation. That version obtained a dissipative time scale by simply dividing the TKE by the dissipation. This time scale was in turn used to dissipate all turbulent moments. Regardless of the turbulent situation that I was trying to represent, this formulation produced a boundary layer top which was too high. In very stable layers (e.g., the inversion at the PBL top), the turbulence should die out immediately and, in the absence of any upper level source, should be zero above this height. The dissipation, parameterized in this manner, was not able to kill the turbulence on a time scale close to that observed. Other modelers have encountered similar difficulties. Canuto (1992) adopted the work of Weinstock (1987) and directly addressed this problem.

Canuto (1992) used a prognostic equation for the dissipation, but added to it a stability-adjusted correction term which increased this dissipation rate in stable layers. This is analogous to decreasing the dissipation time scale, τ (see Eq. 1.19). Canuto's formulation can be written as

$$\tau_p = \tau(1 + C_w N^2 \tau^2)^{-1} , \qquad (1.19)$$

where N^2 is the square of the Brunt-Vaisala frequency, τ is the unadjusted turbulent time scale (equal to twice the TKE divided by the dissipation). $C_w = 0.04$ if $N^2 > 0$, and $C_w = 0$ if $N^2 \le 0$.

In the original "higher-order closure only" version of the current model, the addition of (1.19) helped to decrease the inversion height by dissipating the turbulence within the inversion more quickly. However, the modeled turbulence at and above the PBL top still did not die to zero. With the increased dissipation in the stable layers still unable to completely kill the turbulence, there was a clear inconsistency between the turbulence that the model is produced and what the model was "capable" of dissipating. The inconsistency is related to the choice of constants in the prognostic dissipation scheme (1.18) verses those used in the HOC equations.

We can see this with the following analysis: Each term in the prognostic dissipation scheme (Eq. 1.18) is identical to the terms in the *TKE* equation, only multiplied by a constant and divided by a dissipation time scale (i.e., in order from left to right, there are shear, buoyancy, dissipation, and diffusion; each multiplied by a constant and the time scale, ε/e).Thus, there is a direct connection between the TKE and dissipation in the model. The only two ways dissipation would not be able to keep pace with production are if the dissipation time scale is too big or if the constants in (1.18) are too small. The implementation of the Canuto stability-correction decreased the time scale but did not alleviate the discrepancy in the constants.

In order to help understand why the inconsistency exists, it is helpful to know the origins of the equation itself. Both the TKE and the dissipation equations (Eq. 1.19) are derived directly from the Navier-Stokes equations (For a complete derivation, see Hanjalic and Launder, 1972 and Lumley, 1978.). These equations start with the same basic physics and thus, it is easy to see how the subsequent addition of inconsistent constants would cause problems. If this inconsistency between what the model can produce and what the model can dissipate becomes too large (through these constants), the dissipation cannot keep up and turbulence will not die out in the time that it should. I believe that this was in fact the problem I had with the early "HOC-only" version of the model.

In addition to this discrepancy, there are other problems with using a prognostic dissipation scheme. Equation 1.18 employs *K*-theory for the diffusion of the dissipation. As I discussed in Section II-C-2, the choice of down-gradient diffusion (*K*-theory) is not optimal. I initially chose the diagnostic length scale approach following Bougeault and André (1986). In a later version of the model, I used a modified form of the length scale (see Chapter III).

Blackadar (1962) was the first to use a diagnostic length scale to determine the dissipation rate. In the Blackadar scheme, the turbulent length scales which appear in the different HOC equations are all assumed to be proportional to one master length scale. This master length scale (known as the "Blackadar formula") is

$$L = \frac{\kappa z}{1 + \frac{\kappa z}{L_0}} , \tag{1.20}$$

where L_0 is an asymptotic length scale given by

$$L_0 = \alpha \frac{\int_0^{z_i} qz dz}{\int_0^{z_i} q dz} , \tag{1.21}$$

z_i is the PBL height, $q = \sqrt{2 \times TKE}$, α is an empirically-determined constant, and $\kappa = 0.4$ is the Von Karman constant.

The Blackadar formula was used for years in HOC models. In 1984, Moeng and Randall found that spurious oscillations occurred near cloud top in third-order closure models which used this formulation. This discovery motivated the work of Bougeault and André (1986; BA86) who discovered a weakness in the Blackadar formulation. They noted that (1.20) reached an asymptotic value in the *middle* of the PBL and above. They argued that, at the top of the PBL, where a strong capping inversion (which acts likes a rigid lid) can often exist, the characteristic length scale of turbulent eddies should be small, as it is in the surface layer. Thus, they developed a new formulation designed to insure that the dissipation length scale is small (i.e., the dissipation is large) near the PBL top (or in any other stable regime).

The BA86 scheme is represented by (1.22)-(1.24). This scheme, which diagnoses the turbulent length scale, is used in conjunction with the predicted TKE to determine a dissipation time scale (Eq. 1.17). The scheme is represented by three equations:

$$\int_{z}^{(Z+L_{up})} \beta\{\bar{s}_v(z'') - \bar{s}_v(z)\} dz'' = \bar{e}(z) \ , \tag{1.22}$$

$$\int_{(Z+L_{down})}^{Z} \beta\{\bar{s}_v(z) - \bar{s}_v(z'')\} dz'' = \bar{e}(z) \text{ (where } \ Z - L_{down} \geq 0\text{)}, \tag{1.23}$$

and

$$\frac{1}{Lx} = 0.5 \cdot \left(\frac{1}{L_{up}} + \frac{1}{L_{down}}\right); \tag{1.24}$$

here s_v is the virtual dry static energy, β is the buoyancy parameter, Lx is the turbulent length scale, z is height, and the subscripts "up" and "down" refer to the directions of moving parcels.

In (1.22)-(1.23), the dissipation length scale is a function of the harmonic average of the upward and downward "free paths" of a parcel. The idea behind (1.22)-(1.24) is simple and logical; (1.22) says that the turbulent length scale at any height for an upward-moving parcel is equal to the distance that the parcel can travel (given its initial TKE and the environmental static stability) until it reaches its level of neutral buoyancy. Equation 1.23 says the same thing for a parcel moving in the downward direction. Finally (1.24) says that the total turbulent length scale is equal to the harmonic average of the calculated upward and downward length scales. The reason that Bougeault chose a harmonic average (Eq. 1.24) is that the shortest length scale will be the one that dominates the dissipation rate. Thus, we see that, if the TKE is small or a parcel resides in a very stable environment, the total turbulent length scale, Lx, will be small and the turbulence will dissipate very quickly.

In the original "higher-order closure only" version of the current model, I chose to use the scheme of BA86 for these reasons. It is designed to dissipate turbulence very quickly in stable regions, and thus directly solves the problem I was having with prognostic dissipation. This method had been used by others with much success (Steve Krueger, personal communication). The current version of the model (the unified PBL/mass-flux model) uses a more sophisticated scheme for dissipation, which is based on BA86. This scheme is discussed in detail in Section III-G.

As a final note of interest, many HOC models neglect the dissipation of fluxes, covariances, and third-moments (Mellor and Yamada, 1982; MY82). The basis for neglecting these terms relates to the form of the molecular dissipation in the HOC equations. For example, in the equation for a flux $\overline{w'h'}$ (here h is any variable), the dissipation rate takes the form

$$\frac{\partial}{\partial t}\overline{w'h'} \sim -\nu\overline{\frac{\partial}{\partial z}w'\frac{\partial}{\partial z}h'} \ . \tag{1.25}$$

We see that the dissipation depends on the averaged correlation between the spatial derivatives of w' and h'. Previous higher-order closure models have neglected this dissipation on the basis that sometimes the product is positive and sometimes it is negative so that the average of the product is close to zero.

I argue that, while neglect of these terms is valid for the very small scales (where true molecular dissipation occurs), HOC is an ensemble-averaged system which describes all scales of turbulent motion with a single set of statistics. On the larger scales, this cancellation will, in general, not occur. What may in fact "rescue" the HOC models which neglect such terms is the manner in which they parameterize the pressure terms in these equations. The Rotta (1951) part of the pressure parameterization (see Section II-C-1) resembles dissipation (Eq. 1.5); it takes the same form as the last term in Eq. 1.16 with a different constant of proportionality. Since uncertainty exists regarding the values of the constants in these pressure terms, the chosen constants themselves may have been adjusted to represent the sum of the pressure effects and the true dissipation. This is discussed further in Section IV-A.

II-C-4: Third-order closure parameterizations

Many turbulence modelers turned to third-order closure in the hope that, by predicting higher-moment statistics, the resulting theory would be more accurate for the lower-order terms. The big challenge in third-order closure modeling is the parameterization of the fourth-order terms. The first third-order closure models were developed by Donaldson (1973), Wyngaard et al. (1974), and Lumley and Khajeh-Nouri (1974), among others. In these studies, the third-order correlations are modeled with the use of ad hoc gradient-diffusion assumptions. Such a modeling technique requires the use of many unknown constants, only a portion of which can be obtained from measurements in simple turbulent flows (Andre et al., 1976).

Another example of a closure technique employed by third-order closure models in the quasi-normal approximation (Millionshchikov, 1941). In this technique, the fourth-order correlations are related to the second-order correlations by assuming that the velocity is a Gaussian random variable;

$$\overline{w'w'w'w'} = 3\overline{w'w'} \cdot \overline{w'w'} \quad . \tag{1.26}$$

Unfortunately, it was found that the quasi-normal approximation often leads to the development of negative energies (Ogura, 1962a,b). This deficiency in the quasi-normal approximation is a direct result of excessive growth of the third-order correlations (Orszag, 1970). The function of the fourth-order terms is to limit the build-up of the third-order correlations (through the transport process). When the quasi-normal approximation is used, this term no longer acts as a "transport" term, and the third-order correlations can unrealistically increase at a given level. As a result of this, André et al. (1976) implemented the quasi-normal approximation in his third-order closure model with an additional restriction: the "clipping approximation". The "clipping approximation" is based on the fact that the triple correlations between fluctuations of turbulent quantities must satisfy realizability conditions derived from generalized Schwartz' inequalities (Blanchet, 1970). André et al. (1976) literally cut (or "clipped") the third-order correlations in situations where these realizability conditions were not met. By "clipping" these terms, they were able to prevent the build-up of the third-order correlations and maintain internal consistency (realizability) with the other turbulent moments. A major advantage of the "plume model" described in Chapter III is that there are *no* realizability issues and thus, there is no need to use André's "clipping" approximation. The reasons for this will be discussed in Chapter III.

The pressure and dissipation terms in the third-moment equations of closure models are typically handled in a manner similar to those in the second-moment equations. The pressure terms are modeled with an extension of the "return-to-isotropy" hypothesis (see Section II-C-1). For third-order correlations whose "trace" (or isotropic part) is zero, a simple dissipation-like form is assumed for the pressure terms (this "return-to-zero" approach is used since these quantities have no isotropic part). For third-order correlations whose isotropic part is non-zero, the pressure term is typically split into a "trace-free" redistribution term and a "source" term, the former being modeled as a "return-to-isotropy" term and the latter being taken as proportional to its isotropic part (André et al., 1978; Canuto, 1992).

The dissipation (or molecular) terms of the third-moment equations are usually modeled assuming isotropy for dissipative scales. With this approach, the dissipation term is neglected in the equations of naturally isotropic higher-moments (e.g., $\overline{w'w'w'}$; André et al., 1978). As we will see in Chapter III, the dissipation terms in the current study are never neglected.

II-D: Application of HOC to atmospheric boundary layers

Turbulence in the atmospheric boundary layer is strikingly different under convective (buoyancy-driven turbulence) and stably stratified (shear-driven turbulence) conditions. Thus, atmospheric boundary layer studies have typically focused on one or the other of these two regimes. Early atmospheric boundary layer research focused exclusively on closures developed for shear flows. It wasn't until the 1970's when the recognition grew that these closures were inadequate to describe regimes in which convection plays a dominant role. Thus, the focus of atmospheric boundary layer modeling shifted in the 1970's and 1980's toward closure techniques to represent buoyantly-driven turbulence.

Observations, however, show that almost all atmospheric boundary layers exhibit some combination of both shear and buoyancy. Thus, it is clearly necessary, to accurately model the PBL, that we develop closure techniques that are universal and bridge the gap between these two regimes. It is instructive, however, to study different turbulent regimes in isolation before attempting to understand them in combination. In this section, I will review some of these studies with a focus on the convective PBL.

II-D-1: Modeling the dry convective PBL

The simplest type of closure is first-order closure. Models using this closure retain the prognostic equations only for the mean state variables. To close the system, one needs to parameterize the turbulent fluxes in terms of the mean state. As mentioned previously, these terms are typically parameterized with a form of down-gradient diffusion (K-theory) and the closure problem becomes parameterizing the eddy diffusivity, K.

All early boundary layer models used a form of K-theory closure to parameterize fluxes.

However, in 1966, Deardorff observed that the heat flux within the convective PBL is often counter-gradient. By the mid 1970s, the recognition grew from both observational and modeling studies (Wyngaard and Coté 1974; Zeman and Lumley, 1976) that "local" closure techniques such as down-gradient diffusion are insufficient to describe these regimes. Thus, the focus of atmospheric boundary layer modeling shifted in the 1970s and 1980s toward the development of closure techniques to represent buoyantly-driven turbulence. Luckily, by 1972, the statistics of the convective PBL were very well understood and documented (Deardorff, 1972). Thus, the task to model this regime seemed less formidable. Three basic approaches were taken to model convection.

The first and perhaps most extensively used approach was to simply adapt *K*-theory parameterizations to represent the convective PBL. The various modifications differed tremendously and met with varied levels of success. One method was to add a counter-gradient term as a "non-local" (see footnote, page 9; Fig. 3) correction to the eddy diffusivity parameterization. Deardorff (1972) was the first to propose this correction. Twenty years later, modelers are still developing new forms for this counter-gradient term as well as other parameterizations for non-local eddy diffusion (Holtslag and Moeng, 1991; Abdella and McFarlane, 1996) (see Section II-C-2).

An alternative type of first-order closure, in which it is unnecessary to have knowledge of an eddy diffusivity, is mixed-layer (or "bulk") models. These models have been successfully applied to the dry convective PBL because they inherently represent "non-local" closure (Ball, 1960; Deardorff, 1972; Schubert, 1979). Mixed-layer models assume vertical homogeneity of conserved quantities and a jump condition across the PBL top (Ball, 1960; Lilly, 1968; Randall, 1976; Benoit, 1976). They are simplified first-order closure schemes. In mixed-layer models, the boundary layer is typically one layer and the turbulent fluxes in the PBL are computed from only the surface flux and the entrainment rate. Thus, the properties of the PBL are determined "non-locally". Many modelers used mixed-layer models in conjunction with a mass-flux model to simulate the dry convective PBL (e.g., Wang and Albrecht, 1990).

The second approach was to predict the higher-moment statistics. The interest in second-order (and higher) closure grew directly from advances in computer technology. Prior to this, the only method to test parameterizations was observations. Since it was already difficult to measure the fluxes (to test first-order closure), no one even speculated about parameterizing even higher moments. Thus, second-order closure techniques have been used only since the early 1970s in turbulence calculations. Many of its initial applications were to shear flows (Donaldson, 1971; Hanjalic and Launder, 1972; Naot, Shavit and Wolfshtein, 1972). Donaldson (1973) was one of the first to apply it to PBL modeling.

Models of dry convection typically use second-order closure techniques that fall within one of the hierarchy of models described by Mellor and Yamada (1974). The second-order approach predicts the fluxes and thus alleviates the need to use K-theory to diagnose them. Lumley and Khajeh-Nouri (1974) summarized the thinking on higher-order closure at the time when they said: "If a crude assumption for second moments predicts first moments adequately, perhaps a crude assumption for third moments will predict the second moments adequately." While this may be true, it was soon discovered that second-order closure also had problems in the convective PBL. These problems arose from the fact that modelers still employed down-gradient approximations; albeit this time, for the triple moments (Wyngaard and Coté, 1974; Lewellen and Teske, 1976; Yamada and Mellor, 1975) (see Section II-C-2).

For the purpose of evaluating higher-order closure parameterizations of convective turbulence, atmospheric modelers most often use data from either the Wangara experiment or the Willis Deardorff (laboratory) convection experiment. (Wyngaard and Coté, 1974; Pielke and Mahrer, 1975; André et al., 1978, Willis and Deardorff, 1974; André et al., 1976). Yamada and Mellor

(1975) were among the first to simulate the Wangara experiment with second-order closure. The gross behavior of the simulated PBL agreed with observations. However, the model underpredicted the mixed-layer depth and the downward heat flux at the mixed-layer top. In addition, it predicted a slightly unstable (instead of neutral) mixed layer. The failure of this model, and others like it, to simulate convection was due to the down-gradient diffusion assumption for the third moments (André et al., 1976a,b; Zeman and Lumley, 1976; Lewellen and Teske, 1976; see Section II-C-2). We see a similar deficiency (Monin and Yaglom, 1971) even in models that use improved semi-empirical diffusion theories [e.g., the mixing length approach (Prandtl, 1925); the Smagorinski (1963) formulation]. As a result, scientist turned to third-order closure models whose assumptions were exclusively "tailored" to convectively-driven turbulence.

Hanjalic and Launder (1972) proposed a more advanced scheme for the third moments. They employed an eddy-damped quasi-Gaussian approximation to the third moments;

$$\overline{u'_i u'_j u'_k} = \frac{C}{\tau}\left(\overline{u'_i u'_l}\frac{\partial}{\partial x_l}\overline{u'_j u'_k} + \overline{u'_k u'_l}\frac{\partial}{\partial x_l}\overline{u'_i u'_j} + \overline{u'_j u'_l}\frac{\partial}{\partial x_l}\overline{u'_k u'_i}\right) . \tag{1.27}$$

Lumley and Khajeh-Nouri (1974) extended this method and Zeman and Lumley (1976) were the first to successfully apply it to thermal convection. This approach was adapted and also used successfully in the HOC models of Sun and Ogura (1980), Chen and Cotton (1983), and Finger and Schmidt, (1986).

While the third-order closure technique of Zeman and Lumley did improve the results, André et al. (1976a,b) proposed a different third-order closure technique to simulate convection. This technique used no diffusion assumptions for the third moments. André closed the system by using a quasi-normal approximation for the fourth-order terms (Millionshchikov, 1941; Section II-C-4). The use of this approximation produced excessive growth of the third-order correlations which resulted in negative values of the energy density (Orszag, 1970) (The function of fourth-order moments is to prevent the build-up of the third-order moments. The quasi-normal form for these terms was not able to prevent this build-up). Thus, André clipped the third-order moments in order to force "realizability" with the other equations (the "clipping" approximation; Section II-C-4). This clipping provided the needed damping of the third-order moments. André had great success with this technique in simulating both the Wangara experiment (André et al., 1978) and the Willis-Deardorff laboratory convection experiment (André et al., 1976b). While this third-order model greatly improved the simulations of convectively-driven turbulence, it was not without problems. Some problems arose from the new pressure and dissipation terms contained in these higher-order equations (Section II-C-4). The other major drawback is that, in practice, it was too complex for use in a three-dimensional model.

In the 1980s, several high-resolution parametrization schemes for modeling the CBL were proposed (Wang and Albrecht, 1990). Among these are the large-eddy exchange model that Blackadar (1979) developed (which is now successfully incorporated into the Penn. State- NCAR Mesoscale Model; Zhang and Anthes, 1982, the transilient turbulence model that Stull described (Stull, 1984), the integral closure method of Fiedler (1984), and the "two-stream" model of Chatfield and Brost (1987; a "two stream" model is the same as a "mass-flux" model). A common feature of these models is the recognition that non-local transport is the dominant mode of turbulent mixing in the CBL (Section II-C-2).

The next decade revived some older approaches. Canuto et al. (1994) decided to modify the Zeman-Lumley (1976) approach. He noted that simulations based on their approach had several weaknesses including a diffuse inversion interface, temperature variance profiles that did not match observations, a negative turbulent kinetic energy flux near the surface and underpredicted horizontal root-mean-square (rms) velocities. Canuto et al. (1994) attributed these problems to two factors: an unnecessarily complex dissipation equation and crude algebraic expressions for the third moment terms in which several needed terms were neglected (specifically neglected were the contribution of the mean temperature gradient and the explicit dependence on buoyancy of $w'\overline{u}'^2$ and $w'\overline{v}'^2$). Thus, Canuto changed the Zeman- Lumley formulation by including the terms that they neglected and simplifying their dissipation equation. He proved that his model was more robust and less sensitive to changes in the model constants. His model was very successful at reproducing the results of the Willis-Deardorff laboratory experiments.

II-D-2: Modeling the cloudy PBL

The challenge of representing clouds in already complex turbulence models is formidable. Clouds complicate and completely change the turbulent structure of the PBL through interactions with surface, radiation, and large-scale processes. These interactions depend on properties which vary greatly from case to case; liquid water content and drop size distributions, the presence of ice, fractional cloud cover, and the dynamics of turbulence within the cloud. Large scale conditions such as mean subsidence, and temperature and humidity profiles also alter the degree to which clouds affect PBL turbulence. Finally, cloud effects on PBL turbulence can vary enormously with the type of surface and the degree of surface homogeneity.

What makes the inclusion of clouds even more complex are the feedbacks they induce. For example, not only do surface turbulent fluxes affect the formation and longevity of clouds, but clouds also affect the surface fluxes. Other feedbacks include "cloud-radiation" (Ramanathan, 1989; Lee, 1997) and "cloud-mesoscale" effects (Soong, 1980; Miller, 1995). In the "cloud-radiation" feedback, an increase in cloud cover changes the amount of radiation which reaches the surface (shortwave is decreased, while longwave is increased for low clouds). This, in turn, changes the surface sensible and latent heat fluxes, which in turn determine the quantity of moisture which is available in produce more clouds or refuel the old ones. An example of the cloud-mesoscale feedback occurs in cumulus clouds. In the updraft of the cloud, the condensation and evaporation of cloud liquid drops and the vertical thermodynamic fluxes redistribute the heat and moisture. This in-cloud heating and moistening initiates mesoscale circulations with the clear, relatively unchanged air surrounding the updrafts. These mesoscale circulations change the surface sensible and latent heat fluxes, which in turn, alters the available moisture for the cloud.

I will briefly summarize the most prominent research in HOC modeling in the cloudy PBL for three different regimes: stratocumulus, trade-wind cumulus, and Arctic stratus. This section will not cover the simulation of these regimes with MFC which will be discussed in Section II-E-1.

II-D-2a: Stratocumulus-topped PBLs

Stratocumulus clouds are both locally and globally important (for a detailed discussion of these clouds and their local and global effects, see Section IV-D). Most investigations of the stratocumulus-topped PBL have evolved from Lilly's (1968) mixed-layer approach. For this application, mixed-layer models have had much success (Randall and Suarez, 1984; Turton and Nicholls, 1987; Bechtold et al., 1996). The first Global Energy and Water Cycle Experiment (GEWEX) Cloud System Study (GCSS) workshop showed that these "bulk" models produce reasonable results in climate studies, but are not reliable in mesoscale and small-scale models (Bechtold et al., 1996). The major shortcoming of bulk models is their inability to predict the evolution of the PBL in situations where (1) "local" transport dominates (e.g., shear-driven boundary layers) or (2) the PBL is not well-mixed (an additional drawback of mixed-layer model is that they do not contain enough information by themselves to diagnose and account for partial cloudiness; however, this effect is not extremely important in the stratocumulus regime). To overcome this deficiency, many cloud modelers looked toward second-order closure to model the stratocumulus-topped PBL.

To apply the second-order closure approach to the *cloudy* PBL, one should change the second moment equations as follows: Instead of predicting higher-moment statistics for potential temperature (or virtual potential temperature) and vapor mixing ratios, one should use variables which are conserved under both moist and dry and adiabatic processes (i.e., equivalent potential temperature and total water mixing ratio). In addition, one must relate buoyancy (including liquid water effects) statistics to the predicted thermodynamic relationships. What further complicates the matter is that, in partly cloudy regions (such as cumulus regimes), the buoyancy statistics no longer relate in a straightforward manner to the conserved thermodynamic statistics. Existing theories surrounding this relationship are often disputed (Randall, 1987). A further complication in modeling cloudy boundary layers is the need to include radiative effects (since they represent a source of TKE) in the mean and turbulent equations.

In a cloudy PBL regime, statistics such as the variances and covariances of the equivalent potential temperature and total water mixing ratio are important to determine the cloud amount and fractional cover (Somméria and Deardorff, 1977). This means that second-order closure modelers must employ a level-four[4] Mellor-Yamada scheme (or higher) if they wish to diagnose such features. Early studies that applied such schemes to the stratocumulus-topped PBL included Oliver et al. (1978) and Moeng and Arakawa (1980). In general, however, these level-four Mellor-Yamada models tended to underpredict entrainment fluxes. As discussed in the previous section, I attribute this to the use of a down-gradient assumption for the third-order moments. Due to the importance of entrainment fluxes in the stratocumulus-topped PBL, many cloud modelers abandoned second-order schemes and turned to third-order closure (Chen and Cotton, 1983; Moeng and Randall, 1984; Krueger, 1988).

---

4. A level-four Mellor Yamada scheme refers to a higher-order closure model in which all second moments are predicted (Mellor and Yamada, 1974).

II-D-2b: Trade-wind cumulus PBLs

Since deep cumulus convection is not a PBL-only phenomenon, I will limit this discussion to trade-wind and shallow cumulus convection. Shallow cumulus clouds often occur over the tropical and subtropical oceans. A major importance of these clouds is their large radiative impact on the global energy budget. Diagnostic model studies of the tropical cloud populations (Nitta, 1975; Yanai et al., 1976) in both the disturbed and undisturbed troposphere have showed that the role of trade-wind PBL cloud processes is to cool and moisten the upper part of the PBL, thereby maintaining the trade wind inversion and providing a moist environment for the deeper clouds (Betts, 1975; Hanson, 1981; for a detailed discussion of trade-wind cumulus clouds, see Section IV-C).

Currently, there exist four types of models to represent the trade-wind boundary layer (Bechtold, 1995): three-dimensional (3-D) Large eddy Simulation (LES) models (Somméria, 1976; Cuijpers and Duynkerke, 1993; Schumann and Moeng, 1991) which resolve cumulus updrafts explicitly (see Section IV-A-1), two-dimensional (2-D) cloud ensemble models (Krueger, 1988; Krueger and Bergeron, 1994) which cover a mesoscale domain, one-dimensional (1-D) HOC models which make use of a sub-grid scale condensation scheme (Bougeault, 1981a,b), and mixed-layer or bulk models (Betts, 1973; Albrecht, 1979; Randall et al., 1992) where the boundary layer is typically one layer and the turbulent fluxes in the PBL are computed from only the surface flux and the entrainment rate. The most successful methods for modeling this regime are the LES since they explicitly resolve the updrafts. Somméria (1976), using a 3-D LES, performed the first successful simulation of the trade-wind PBL. Although he noted several deficiencies, he was able to simulate in a realistic manner the Puerto Rico Field Experiment's observations (Pennell and LeMone, 1974). Later, Asai and Nakamura developed a 2-D version of this model and successfully applied it to the Air Mass Transformation Experiment (AMTEX) data. Other successful LES simulations of the trade-wind cumulus regime include that of Siebesma and Cuijpers (1995).

One-dimensional turbulence closure models, which parameterize both the convective circulations and the small scale turbulence, typically have difficulties modeling cumulus clouds. This is because "conventional" closures make use of the assumption that turbulence is nearly isotropic and nearly Gaussian (Lumley, 1978), whereas cumulus regimes are highly non-isotropic and non-Gaussian. Thus, in order to simulate the trade-wind cumulus regime accurately, these models must be modified. For example, Bougeault (1981a) developed a special turbulence condensation scheme with the help of the LES results of Somméria (1976) for a 1-D higher-order closure simulation of the trade-wind PBL. Bechtold (1995) developed an level 1.5 scheme in which he linearly interpolated between the Gaussian turbulence profiles and a distribution with known constant positive skewness. In this scheme, however, he *tuned* the skewness to a "trade-wind-specific" value. One-dimensional mass-flux models applied to the trade-wind PBL also "tuned" their models to be "trade-wind-specific" (see Section II-E-1).

Krueger and Bergeron (1994) noted that 2-D cloud ensemble models currently contain the minimum level of complexity to simulate the trade-wind cumulus boundary layer without special tuning. Two cloud ensemble models have had great success in modeling this regime: Sun and Ogura (1980; a second-order closure scheme) and Krueger and Bergeron (1994; a third-order closure scheme).

II-D-2c: Arctic Stratus Clouds

Arctic stratus clouds (ASC) can significantly affect the global energy balance. These clouds modify not only the surface radiation balance, but also the vertical structure of the boundary layer and thus the surface sensible and latent heat and momentum fluxes. Large discrepancies exist between GCM simulations and observed cloudiness in the Arctic (Lappen, 1996). An understanding of how cloud properties will change in a warmer climate is currently one of the key problems in climate modeling. Because of the unique thermodynamic and radiative environment in the

Arctic, conclusions drawn for the lower latitudes regarding cloud feedback processes may be inappropriate over the Arctic Ocean (McInnes and Curry, 1995; see Section IV-E). As a result of all this, there is a big push in the modeling and observational communities to study Arctic stratus and develop Arctic-specific parameterizations (for a detailed discussion of ASCs and their local and global effects, see Section IV-E).

Up to this point, only closure models have simulated the turbulent small-scale structure of Arctic stratus. Herman and Goody (1976) and Forkel and Wendling (1986) applied a first-order closure model to a multi-layered cloudy boundary layer (type II). These simple models had limited capacity to represent the turbulent structure of the PBL however. Mixed-layer models (simplified first-order closure models; see Section IV-B and IV-D) have also been applied to the Arctic (Busch et al., 1982; Randall et al., 1985; Ebert, 1984), although they also have not had much success. Mixed-layer models, as currently formulated have limited applicability to Arctic stratus for the following reasons: (1) they fail to describe the typical laminated structure of ASC (i.e., clouds which may form throughout the lower troposphere and in the presence of either large-scale ascending or descending motion; and (2) mixed layer models cannot describe clouds occurring in the stable boundary layer, or in the case consisting of a stable layer underlying an elevated mixed layer (Curry et. al., 1988).

McInnes and Curry (1995) examined multiple-layer clouds with a level-three second-order closure scheme (only the TKE and the thermodynamic variances are predicted). Even with this level of complexity, they found that simulated variances and fluxes of temperature and humidity were far too small when compared with observations. Finger and Wendling (1990) used a more sophisticated level-four second-order closure (all second moments are predicted) to model the case of a cloud-topped mixed-layer (type I) and had good results. These studies, as well as others, suggest that a minimum of level-four second-order closure is needed to fully capture the turbulent processes that occur within Arctic stratus.

II-E: Mass-Flux Closure

Mass-flux closure is a very attractive method for solving the closure problem (Section II-B). It involves minimal assumptions and works for a large range of conditions. The idea was pioneered by Arakawa (1969), who developed mass-flux parameterizations and applied them to deep cumulus convection. In the late 1960s and early 1970s, boundary-layer parameterizations (e.g., K-theory, mixed-layers, HOC) and mass-flux schemes (e.g., Arakawa, 1969; Arakawa and Schubert, 1974; Simpson and Wiggert, 1969) were simultaneously (but independently) being developed. Later, many researchers combined the two by generalizing the cumulus mass-flux approach to the PBL, thus developing more refined mass-flux methods that included both cloudy and clear regimes. The motivation for this work was fueled by the need for more sophisticated parameterizations to more accurately represent turbulent convection and clouds in PBL simulations. These models, which required the use of both boundary-layer and mass-flux schemes, were the first models to pull MFC into the framework of a boundary-layer model.

Initially, only the simpler boundary-layer parameterizations were used in these models. For example, mixed-layer models were combined with mass-flux models to simulate the dry, convective (Wang and Albrecht, 1990), and cloudy (Betts, 1976 and Albrecht, 1979) PBLs (these models will be discussed in the next section). Later, Randall et al. (1992; RSM) provided a potential framework to pull mass-flux parameterizations into a more sophisticated PBL model; a HOC model (this paper is reviewed in Section III-A). The current work adds another level of sophistication to the ideas of RSM; it completely unifies HOC and MFC into a single system of equations which satisfies both formulations (see Chapter III).

II-E-1: Application of MFC to atmospheric boundary layers

As discussed, Arakawa (1969) pioneered the development of mass-flux models to study cumulus convection. The concept was suggested by the realization that, in order to satisfy mass continuity, compensating downdrafts must fill the space between the buoyant thermals in a convective regime. Within the "classical" mass-flux framework, all dynamic and thermodynamic quantities are represented with tophat[5] profiles (Figs. 4-5). Using tophat distributions, Arakawa was able to partition the cumulus regime into two components; updrafts and the environment surrounding updrafts. He then parameterized the turbulent fluxes as the product of a convective mass flux (M_c) and the difference in a quantity's value between the updraft and the environment using

$$\overline{w'h'} = M_c(h_{up} - h_e) \tag{2.1}$$

(A derivation of this equation is given in Section III-A). A fundamental assumption used in (2.1) (written here for a single cloud type) is that "large eddies" (eddies whose scales are comparable to or larger than the depth of the PBL) account for most of the turbulent transport in the convective boundary layer (CBL). Later, many researchers generalized this approach to include the PBL and developed more refined mass-flux parameterizations that can be applied to both cloudy and clear regimes (Betts, 1973,1983; Albrecht, 1979; Hanson, 1981; Randall, 1987; Wang and Albrecht, 1986, 1990). Because the distinction between updraft and environment is not as clear for the dry convective and stratocumulus-topped boundary layers, many of these researchers generalized Arakawa's "updraft-environment" tophat profile to an updraft-downdraft decomposition.

Betts (1976) was the first to apply a convective mass-flux representation of fluxes to the subcloud layer undergoing dry convection. He generalized Arakawa's parameterization (Eq. 2.1) by replacing h_e with h_{dn}; the value of h in a convective downdraft. Thus, the flux of h is written as

---

5. A tophat profile is a probability distribution function which consists only of two delta functions. Thus, a quantity represented by a top hat profile has 100% probability of having one of two possible values. In a mass-flux model, the two allowed states of a variable are its updraft and the downdraft values.

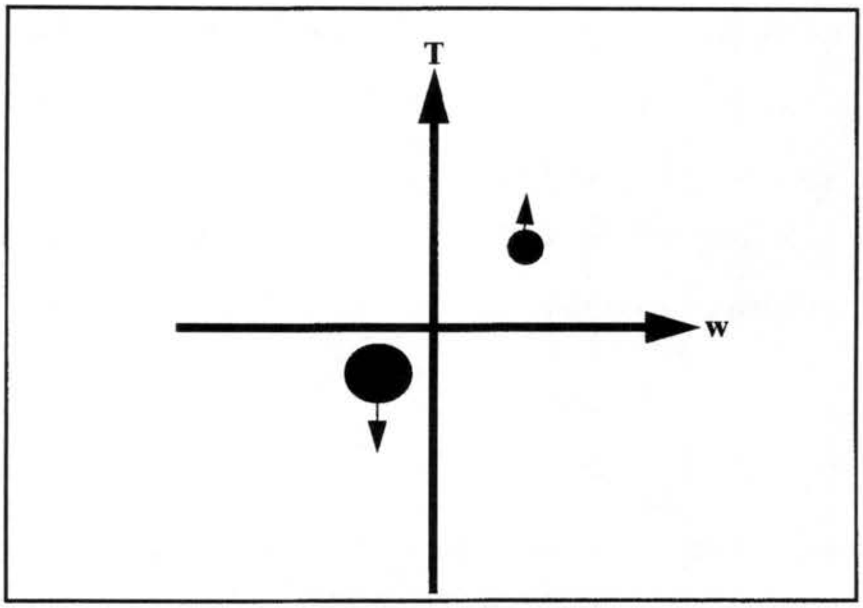

Figure 4: Tophat joint probability density function for the vertical velocity (w) and the temperature (T). The two black dots represent the two possible states for these variables (e.g., updrafts and downdrafts). The size of the dots are indicative of the area occupied by a given state in a particular regime. For example, in the above picture, we have a cumulus regime, where the downdrafts occupy a larger area than the narrow updrafts.

$$\overline{w'h'} = M_c(h_{up} - h_{dn}) \quad . \tag{2.2}$$

The fundamental assumption in (2.2) is that the plumes account for most of the turbulent transport in the CBL [subsequent studies have shown that (2.2) actually represents only 60% of the total flux (Businger and Oncley, 1990; Young, 1988a; Schumann and Moeng, 1991; Wyngaard and Moeng, 1992; de Laat and Duynkerke, 1998]. Using observations, Nicholls and Lemone (1980), Greenhut et al. (1982), and Greenhut and Khalsa (1987) confirmed that this formula can be applied to the CBL. Other observational studies (Lenschow and Stephens, 1980; Crum et al., 1987, Young, 1988a,b) have advanced our understanding of the dynamics of thermals in the CBL and have helped modelers incorporate (2.2) into numerical models (Wang and Albrecht, 1986;

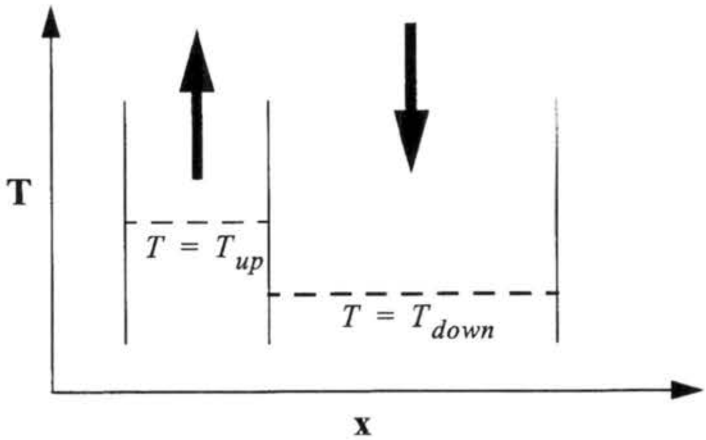

Figure 5: A schematic of the updraft/downdraft decomposition of temperature in a tophat PDF. The up arrow represents the updraft and the down arrow represents the downdraft. T_{up} and T_{down} are the temperature in the updraft and downdraft respectively.

Chatfield and Brost, 1987).

Despite the observational evidence, it wasn't until this decade when (2.2) was used in a numerical model to simulate dry convection (Wang and Albrecht, 1990). In this model, Wang and Albrecht used prognostic equations only for the mean vertical quantities in the updraft and downdraft. They used (2.2) to close the equations. They found that this computationally simple model was able to simulate the observed CBL better than mixed-layer models. The major improvement over a mixed-layer model was the fact that it allowed for an explicit representation of additional processes (beyond just surface and entrainment fluxes) that control gradients of conserved variables (i.e., internal mixing and lateral mixing between updraft and downdraft elements). Due to the success of a mass-flux parameterization in studying dry convection, Wang and Albrecht postulated that a unified cloud and PBL model could be developed with such an approach.

Mass-flux models applied to the cloudy PBL are also abundant in the literature. As discussed, the challenge of representing clouds in already complex turbulence models is formidable (see Section II-D-2). Due to the complexity of cloud regimes, atmospheric modelers have typically focused on either the dry PBL or a regime that contains only one cloud type. For example, Arakawa (1969), Arakawa and Schubert (1974), Betts (1975), and Ooyama (1971) built models specifically designed to study cumulus; Lilly (1968) and Betts (1976) constructed models whose parameterizations were specific to stratocumulus; and Wang and Albrecht (1990) and André et al. (1978) examined only the dry PBL. I will briefly summarize some key research in mass-flux modeling of clear convective and cloudy PBLs. The discussion of cloudy regimes involves only two cloud types: stratocumulus and trade-wind cumulus (both convective regimes).

As discussed above, the applicability of mass-flux models to non-convective regimes has been documented in numerous observational studies. Despite this fact, no attempts have been made to apply them to non-convective conditions. In the HOC/MFC plume model described in this thesis (Chapter III), I attempt this task in the simulation of Arctic stratus clouds (Section IV-E). To my knowledge, there have been no attempts to use mass-flux parametrization for Arctic stratus clouds. The main reason for this is that mass-flux models were developed for convective situations; a property not inherent to Arctic stratus. In addition, the traditional method to employ a mass-flux model is in conjunction with a mixed-layer model. In general, a mixed-layer model is not representative of the Arctic subcloud layer.

Mass-flux models have met with some success in modeling the stratocumulus-topped PBL (ScTBL). Penc and Albrecht (1987) postulated and confirmed (using observations) that a mass-flux approach, which had been used successfully for cumulus convection (Betts, 1973; Arakawa and Schubert, 1974), was also useful for describing stratocumulus. Taking data from the NCAR Electra which flew off the coast of California in June 1976, they showed that (2.2) could be used to describe the ScTBL. This was further confirmed recently by deLaat and Duynkerke (1998) using data from the Atlantic Stratocumulus Experiment (ASTEX).

Despite these observations, however, very few cloud modelers have used the mass-flux approach to model the ScTBL. The few studies that have used this method all employ mixed-layer models, along with the mass-flux parametrization (e.g., Wang and Albrecht, 1986). As discussed, mixed-layer models are inherently deficient at predicting the evolution of the PBL in situations where the boundary layer is not well mixed (see Section II-D-1). As a solution, Randall et al. (1992) developed a combination HOC/MFC (reviewed in Section III-A). The plume modeled developed for this thesis work also directly addresses this weakness (Chapter III).

Mass-flux schemes have also been used in conjunction with mixed-layer models in simulating the trade-wind cumulus layer (Hanson, 1981; Betts, 1976; Albrecht, 1979). One-dimensional turbulence closure models, which parameterize both the convective circulations (with mass-flux parameterizations) and the small-scale turbulence (with a PBL model), typically have difficulties modeling cumulus clouds (Section II-D).

Thus, in order to simulate the trade-wind cumulus regime accurately, these models must be modified. For example, Albrecht (1979) combined a mixed-layer model for the subcloud layer with a convective mass-flux model and a cumulus parameterization for the cloud layer. This bulk model contained constants which were *tuned* for the trade-wind PBL. Betts (1976) used a similar approach. A major weakness of this approach is this tuning which is greatly situation-dependent. Currently no model with higher than first-order closure has been used in conjunction with a mass-flux model. The inherent deficiencies of first-order closure were discussed in Section II-D. As a result of the deficiencies surrounding first-order closure, there are some questions that mass-flux models have been unable to answer: What determines the mass flux from the mixed layer into cumulus clouds? How does the cumulus ensemble affect the mixed-layer turbulence? How can we parameterize the mixing between the cumulus ensemble and its environment?

The current model is the first mass-flux model able to address some of these issues. It is able to do so because it also makes use of our knowledge of the higher-moment statistics. The model is based on a unification of HOC and MFC, and thus combines the knowledge of convection and PBL turbulence, which is encoded in these closures individually. As discussed, RSM pioneered the concept of this unification. In the next section, I review their work; in Chapter III, I will describe the derivation of the plume model unified equations; and in Chapter IV, I will discuss the simulation of two different trade-wind cases; the Barbados Oceanographic and Meteorological Experiment (BOMEX; Section IV-C-2) and the Atlantic Trade-wind Experiment (ATEX; Section IV-C-3), as well a simulation of stratocumulus from the Atlantic Stratocumulus Experiment (ASTEX; Section IV-D-1), Arctic stratus from the Surface Heat and Energy Budget of the Arctic and First International Satellite Cloud Climatology Project (ISCCP) Regional Experiment (SHEBA/FIRE; Section IV-E-1), and pure convection based on the Willis-Deardorff water tank experiment (WD; Section IV-B).

In the next chapter, I will describe the current model in great detail. I will call the unified method "Assumed-distribution higher-order closure" (ADHOC). This name directly describes the approach; I assume a tophat distribution (see footnote, page 50; Fig. 4,5) to describe thermodynamic and dynamic quantities (the "assumed distribution"), and I predict $\overline{w'w'}$, $\overline{w'w'w'}$, and vertical fluxes by inserting these distributions (where possible) into the terms in these HOC equation (the "higher-order closure"). The resulting predicted values are used to diagnose the parameters describing the tophat distribution (Eqs. 3.7-3.10).

Chapter III: ADHOC

Currently, the biggest application for mass-flux models is GCMs. As discussed in Chapter I, cloud schemes employed by many GCMs vary depending on the type of convection. To overcome this dependence, RSM formulated a new hybrid PBL model that combined the concepts of HOC with MFC (Section III-A). With ADHOC, I have taken the RSM approach much further. The model that I will describe combines the two approaches in such a manner that the MFC equations are term-by-term consistent with the terms of "conventional" HOC equations. This eliminates some major disadvantages of the RSM approach used by itself (Section III-A-1b).

Some new things are discovered and some new techniques are introduced in this model. For example, an interesting result of the term-by-term analogy between the two systems (MFC and HOC) is that the lateral mass exchange terms in ADHOC are directly related to the dissipation terms of the HOC equations (Section III-G). I provide a new "ADHOC-specific" parameterization for these lateral mass exchange in the spirit of this discovery. In addition, I add a subplume-scale (SPS) turbulence scheme to the mass-flux model to directly address the issue of the inherent "scale-inconsistency" of HOC and MFC closure equations (Section III-I). The basic setup of this chapter is as follows: in Section III-A, I review the work of Randall, Shao, and Moeng (1992), on which the current work is based; in Sections III-B to III-F, I derive the equations of the model and prove that they are term-by-term consistent with HOC; in Section III-G, I describe the new dissipation scheme; in Section III-I, I explain the use of the SPS scheme; in Section III-J, I discuss the special issues surrounding momentum in the context of ADHOC; in Sections III-K and III-L, I outline the model logic and boundary conditions; and in Section , I summarize ADHOC equations and parameterizations.

III-A: Randall, Shao, and Moeng, 1992

Schubert (1979) nailed the problem when he said that "A model is needed that is capable of handling situations in which the cloud base lies either above or below the top of the mixed layer...". Sixteen years later, RSM took the first step toward that end and, perhaps in this thesis, I take the second. As discussed in the previous section, most mass-flux models are used in conjunction with a *separate* mixed-layer PBL model. In RSM, these models are referred to as "bulk mass-flux models". A major shortcoming of these models is their mixed-layer assumption, which does not allow us to accurately represent the detailed structure of the PBL or to accurately determine the entrainment rates at the PBL top- things which are critical for predicting the evolution of PBL (Section II-D-2a). In addition, with the mass-flux approach, a method is needed to determine the updraft area fraction (σ) and the mass flux (M_c). No existing bulk mass-flux model includes a physically based method to determine these quantities. Finally, for applications in general circulation models (GCMs), there is a need to unify PBL and mass-flux models into one internally consistent system (discussed extensively in Chapter I).

The cloud schemes employed by many GCMs vary depending on the type of convection (see Chapter I). For cumulus convection, many employ mass-flux models, while for stratocumulus and dry convective PBLs, most use a *K*-theory parameterization. To date, no large-scale model has ever incorporated a mass-flux model without an accompanying *separate* PBL model. To overcome these deficiencies, RSM formulated a PBL model that combines the ideas of HOC with mass-flux. In that paper, they proposed a theoretical framework for building a hybrid PBL model that can be applied to *all* types of boundary layers and cloudy atmospheres.

In the spirit of previous mass-flux models, RSM adopted a "tophat" probability density function (PDF; see footnote, page 50; Figs. 4-5) to describe the mean-state and turbulent fluxes in the atmosphere (Eq. 2.2). In that paper, they derive expressions similar to (2.2) for *all* higher-order terms (e.g., variances, other covariances, and third-order and higher moments). Thus, they show that all higher-moment term can be represented as various combinations of a convective mass flux and the difference in properties between updrafts and downdrafts. This has immediate appeal for the "closure" problem (Section II-B) as one can represent higher-order moments with these formulations, alleviating the need for diffusion parameterizations (Section II-C-2).

As an example, suppose that h is some intensive property of a system (potential temperature, mixing ratio, etc.). With mass flux, we can represent the mean value of h, $\bar{h}$, as in Eq. 3.1, where σ is the fractional area covered by the updrafts and h_{up} and h_{down} are the values of h in the updraft and downdraft respectively. [Throughout the literature, there are many different definitions of σ (RSM, Table 1). Currently, it is most often defined as the fractional area with vertical velocities > 0)]. This representation sets the mean value of h equal to an area-weighted average of its two components,

$$\bar{h} = \sigma h_{up} + (1-\sigma) h_{down} \ . \tag{3.1}$$

We also define a convective mass flux,

$$M_c = m\sigma(1-\sigma)(w_{up} - w_{down}) \ ; \tag{3.2}$$

where m is the density, σ is the fractional updraft area, $1-\sigma$ is the fractional downdraft area, and $(w_{up} - w_{down})$ is the difference in the vertical velocity between the updraft and downdraft. M_c has units of mass divided by the product of area and time (mass flux).

The idea of MFC is that we can use (3.1)-(3.2) to represent any higher-moment statistic. For example, we can derive an expression for the vertical flux of h by replacing $\bar{h}$ with $\overline{w'h'}$, in (3.1). We then use $h'_{up} = h_{up} - \bar{h}$ and $h'_{down} = h_{down} - \bar{h}$, do the same for vertical velocity perturbations (w'_{up} and w'_{down}), and multiply it out to get the "mass-flux formula" for $\overline{w'h'}$:

$$
\begin{aligned}
m\overline{w'h'} &= m[\sigma \cdot w'_{up}h'_{up} + (1-\sigma) \cdot w'_{down}h'_{down}] \\
&= m[\sigma \cdot (w_{up} - \overline{w}) \cdot (h_{up} - \overline{h})] + m[(1-\sigma) \cdot (w_{down} - \overline{w}) \cdot (h_{down} - \overline{h})] \\
&= m\sigma(1-\sigma)(w_{up} - w_{down})(h_{up} - h_{down}) \\
&= M_c(h_{up} - h_{down})
\end{aligned}
\tag{3.3}
$$

One can follow the same procedure to obtain expressions for variances,

$$m\overline{h'h'} = m\sigma(1-\sigma)(h_{up} - h_{down})^2 \ . \tag{3.4}$$

or any higher-order turbulent moments,

$$m\overline{w'h'h'} = m\sigma(1-\sigma)(1-2\sigma)(w_{\mathrm{up}} - w_{\mathrm{dn}})(h_{\mathrm{up}} - h_{\mathrm{dn}})^2 \ ; \tag{3.5}$$

$$m\overline{w'h'h'h'} = m\sigma(1-\sigma)(1-3\sigma+3\sigma^2)(w_{\mathrm{up}} - w_{\mathrm{dn}})(h_{\mathrm{up}} - h_{\mathrm{dn}})^3 \ . \tag{3.6}$$

To get a better feel for the meaning of the mass-flux parameterizations, let's look at the variance transport equation (Eq. 3.5); if $\sigma = 0$, we have no variance transport which makes sense since this means that there are no updrafts. If $\sigma < 0.5$, then $m\overline{w'h'h'} > 0$ and we have upward variance transport ($w_{up} - w_{down} > 0$ by definition). As an example, suppose that h represents temperature and that we have a heated surface. Then, $\overline{h'^2}$ will be large and turbulence will transfer heat away from the surface. If this occurs, we will observe an upward transport of h, and according to (3.5), this will occur if σ is less than 1/2. Such would be the case in a clear convective PBL. We can use similar reasoning for a PBL with cloud-top radiative cooling to show that σ must be less than 1/2 for this case.

As an example of the usefulness of this approach, we can use the expressions (3.1)-(3.3) to diagnostically determine any higher-moment terms that appear in the turbulence closure equations (provided that we know σ and M_c). This includes transport terms which have traditionally been poorly represented with down-gradient diffusion (one of the biggest weaknesses in "traditional" HOC; see Section II-C-2). So far, we have learned that given σ, M_c, and the updraft and downdraft properties of any variable, we can solve the closure problem by using (3.3)-(3.6) to diagnostically determine any higher turbulent moment of that variable. The next logical question is, how do we determine σ and M_c?

The method is both simple and elegant. In (3.1), (3.4), and (3.5), we replace h with w everywhere. In doing so, we are left on the right-hand side with 3 equations and 3 unknowns, w_{up}, w_{dn}, and σ. Solving this system of equations, we get

$$\sigma = \frac{1}{2} - \frac{S_w}{2\sqrt{4+S_w^2}} \; ; \tag{3.7}$$

$$M_c = \rho\sigma(1-\sigma)(w_{up} - w_{down}) = \frac{m\sqrt{\overline{w'}^2}}{\sqrt{4+S_w^2}} \; ; \tag{3.8}$$

$$w_{up} = \overline{w} + \frac{(1-\sigma)}{M_c}\overline{w'w'} ; \tag{3.9}$$

and

$$w_{down} = \overline{w} - \frac{\sigma}{M_c} \overline{w'w'} \; ; \tag{3.10}$$

where

$$S_w = skewness = \frac{\overline{w'^3}}{(\overline{w'^2})^{\frac{3}{2}}} \; . \tag{3.11}$$

Now, we see that provided that we know $\overline{w'^2}$ and $\overline{w'^3}$, we can diagnose both σ and M_c. Two things are apparent here; first, we need to know $\overline{w'^2}$ and $\overline{w'^3}$ (I will come back to this point); and second, we need to know all the vertical fluxes. The second point is not so obvious so I will explain it further: Lets take as an example, the flux, $\overline{w'h'}$. If we look at (3.3), we see that once we know M_c, we need to know the difference between h_{up} and h_{down} to determine $\overline{w'h'}$ (or visa-versa). In addition, once we know h_{up}, h_{down}, σ, and M_c, we can use (3.4)-(3.6) to diagnose any higher-order moment involving these two variables and the system is truly "closed". A schematic of this logic is shown in Fig. 6.

From the discussion above, we see that the success of this method *requires* the knowledge of certain higher-moment statistics; namely, $\overline{w'^2}$, $\overline{w'^3}$, and the vertical flux of any model variable. RSM proposed using HOC equations to determine these quantities. Thus, we see how this method is a first step toward combining HOC and MFC into one model. In the description of ADHOC in Chapter III, I use two thermodynamic variables; one for heat and one for moisture. In order to apply the approach described here in such a model, we require four higher-order closure equations, plus equations for the mean state (I am not considering horizontal momentum here for rea-

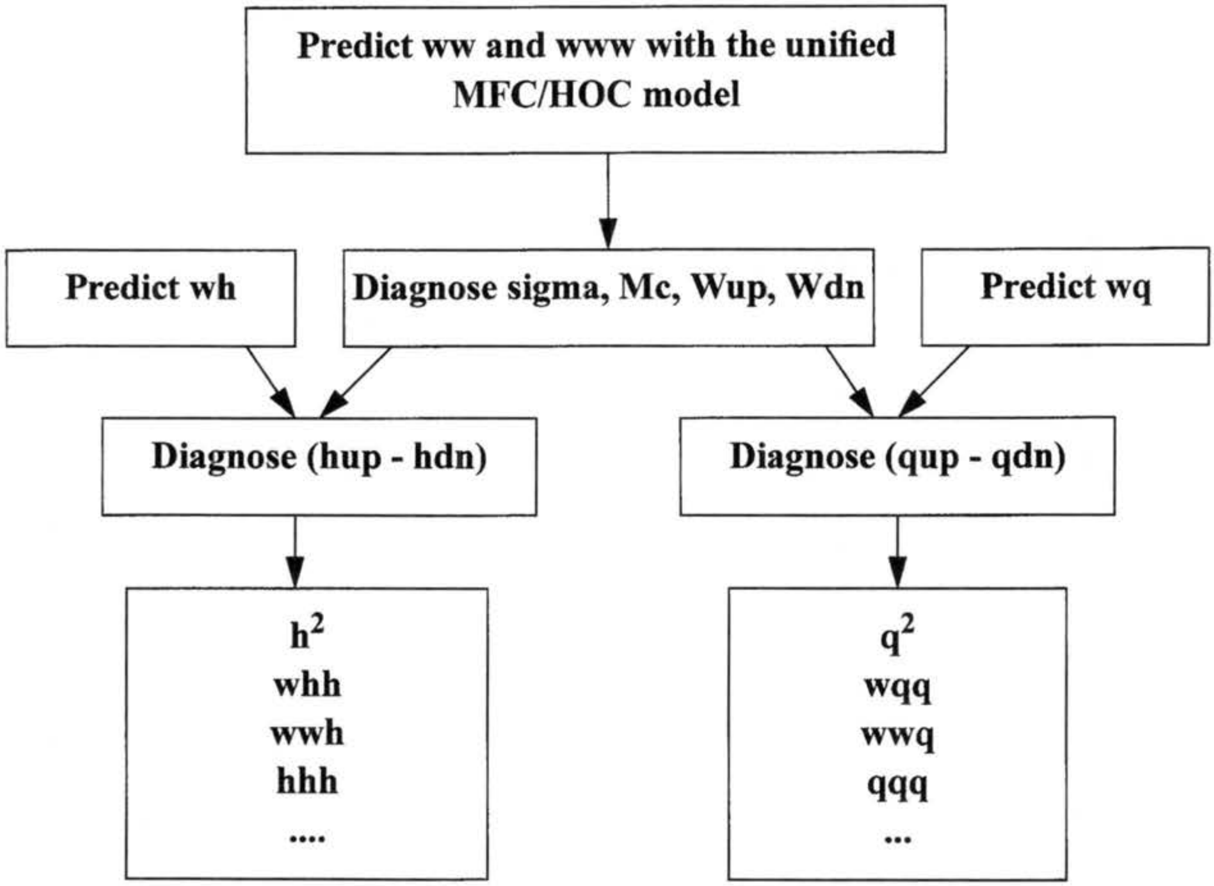

Figure 6: Model logic of ADHOC, which is based on RSM. We use $\overline{w'w'}$ and $\overline{w'w'w'}$ to predict sigma, M_c, w_{up}, and w_{down} using (3.7)-(3.10). We then predict the flux of a variable and use (3.3)to diagnose the difference in properties of the variable between the updraft and downdraft. Finally, we use equations of the form (3.4)-(3.6) to diagnose any higher moment in which we wish to know.

sons which will be discussed in Section III-J). In addition, we use one basic assumption for all other higher-moments; the assumption that variables can be represented with an updraft-downdraft decomposition ("tophat" probability density function).

In a "conventional" third-order closure model that has two thermodynamic variables, there are ten higher-moment equations to be solved (Stull, 1988); there is no guarantee that the closure assumptions will be consistent among the equations, and many more closure assumptions are needed. The advantages of MFC over conventional HOC are quite clear. There are also disadvantages to this approach. Both will be discussed in greater detail in Section III-A-1.

As a final note, I'd like to discuss the skewness introduced in Eqs. 3.7-3.8 and defined in Eq. 3.11. Knowledge of the skewness of the vertical velocity gives us keen insight into the nature of the flow. From it, we can learn about the structure of the turbulence, the nature of the diffusion, and the transport of energy in a convective boundary layer (Moeng and Rotunno, 1990). As an example, let's look at the derived formula for σ (Eq. 3.7). This formula guarantees that $0 < \sigma < 1$. If $\sigma < 0.5$, (3.7) implies that $S_w > 0$. Thus, positive skewness is associated with narrow updrafts (e.g., for trade-wind cumulus). In the limit $\sigma \to 0$, the skewness goes to positive infinity. Thus, we see that the larger the skewness, the closer we get to the tropical cumulus regime. Similarly, if $\sigma > 0.5$, $S_w < 0$ and we see that negative skewness is associated with slow, broad updrafts (and narrow rapid downdrafts). This may be the case if cloud top radiative cooling drives turbulence (e.g., for stratocumulus).

The skewness involves $\overline{w'w'}$ and $\overline{w'w'w'}$. Thus, if we just predict (or measure) these two quantities, we can determine the skewness and get specific insight into the atmospheric regime in which we are working (i.e., we will know σ and have insight into the vertical fluxes). This is useful with atmospheric observations where often radar measurements are taken and the moments of the vertical velocity can be calculated (e.g., Frisch et al., 1995).

RSM showed that a combined MFC/HOC model is possible. By combining the two approaches, the resulting equations can incorporate all of the concepts in both of the original systems. Thus, theoretically, the RSM equations should approach both those of HOC and MFC when specific limits are imposed. RSM analyzed the variance equation of the mass-flux model and demonstrated this. For example, they showed that, under simplified conditions (σ and M_c independent of height), the variance equation of an arbitrary scalar reduces to a down-gradient diffusion formula when σ is close to 1/2. This is what one would expect since, in this limiting case, the vertical motion is weak and local transport dominates. This assumption is used in HOC. They also showed that, under the same simplified conditions and with $\sigma << 1$, the variance equation reduces to the "compensating subsidence" formula that is well-known in cumulus (mass-flux) parameterizations (Arakawa and Schubert, 1974). The fact that the theory does not break down in these limiting cases reflects the versatility of the approach, and lays a potential framework for a unified PBL-cumulus model. In Chapter III, I show a detailed analysis of these limiting cases using the ADHOC variance equation without the simplifying assumption that σ and M_c independent of height.

In this thesis, I have taken the RSM approach considerably further. I use a plume model to derive prognostic equations for higher-moment statistics, based on (3.1)-(3.6). I show that this higher-order plume model is exactly consistent with "conventional" HOC equations so that if I write the terms of the HOC equations with the definitions (3.1)-(3.6), I have an exact term-by-term correspondence. Some interesting new concepts fall out of this analysis. The derivation and discussion of this is described in detail in Chapter III.

III-A-1: Advantages and disadvantages of RSM closure

In this section, I will review the major advantages and disadvantages of the RSM method. As mentioned, this method is significantly extended in the current model (called ADHOC). Thus, the advantages and disadvantages of the RSM method also include ADHOC (ADHOC has additional advantages which will be discussed later). An important thing to keep in mind here is that these advantage and disadvantages vary in importance from regime to regime. Thus, the level of success of the RSM method (or the more-advanced ADHOC discussed in Chapter III) depends highly on the type of boundary-layer regime simulated; dry, stratocumulus-topped, shallow cumulus, stratus-topped, etc. In Chapter IV, simulations of these varied regimes are described. In that section, the importance of the advantages and disadvantages as applied to specific PBL regimes will be clarified.

III-A-1a: Advantages

Perhaps the biggest advantage of the RSM MFC is its simplicity; few prognostic equations are required, minimal assumptions are needed, and quantities are expressed with simple diagnostic formulas which are functions of the updraft/downdraft properties of the flow and a convective mass flux (Eqs. 3.1-3.6). In addition, this method provides us with the first "physically-based" method to determine σ and M_c. No existing bulk mass-flux model includes a physically-based method to determine these quantities.

The logic of the model is also simple. As discussed, the model must predict $\overline{w'w'}$, $\overline{w'w'w'}$, and the flux of any model variable. These values are then used to determine σ and M_c. We use M_c and the fluxes to determine the difference in properties between the updraft and downdraft for all model variables. Finally, we can use the difference in properties between the updrafts and downdrafts, along with σ, to determine *any* other moment (Fig. 6). A huge advantage of this method is that it insures consistency among all higher moments of the flow (they are all computed from the same "tophat" probability density function (see footnote on page 50; Figs. 4-5). This alleviates the problem of realizability and assumptions like the "quasi-normality" (Section II-C-4) and "the clipping approximation: (Section II-C-4) are not needed.

Another advantage of this whole process is that the system of HOC equations is "closed" (with regard to the higher moments which appear; this does not solve the pressure and dissipation closure problem). We do not need a method to parameterize transport, and thus we eliminate a big weakness of "conventional" HOC models (Section II-C-2). As I discussed in Section II-C-2, the down-gradient diffusion parameterization currently used in many HOC models can be highly inaccurate; most notably in the convective boundary layer where non-local transport dominates (see footnote, page 9; Fig. 3). The terms that are parameterized with down-gradient in HOC are, in reality, *transport* terms; they do not represent diffusion. The RSM method gracefully solves the closure problem and, in the process, allows transport terms to be represented as they naturally appear in the actual equations; as higher-moments terms (e.g., third moments in the second-order equations and second moments in the mean state equations). For clarity, (3.12) and (3.13) show the old and the new methods to represent the transport term (respectively) that appears in the equation for $\overline{w'h'}$.

$$\frac{\partial}{\partial z}\overline{w'w'h'} = -\frac{\partial}{\partial z}K\frac{\partial}{\partial z}\overline{w'h'} \tag{3.12}$$

$$\frac{\partial}{\partial z}\overline{w'w'h'} = \frac{\partial}{\partial z}m\sigma(1-\sigma)(1-2\sigma)(h_{up}-h_{down})(w_{up}-w_{down})^2 \tag{3.13}$$

Another manner in which to view the advantage that the mass-flux representation of the fluxes has over diffusion (especially in the convective PBL) is as follows: With diffusion, transport occurs level-by-level and information flows simultaneously both upwards and downwards in the boundary layer. With MFC, information either flows up (if σ is small) or down (if σ is large). It is similar to advection in that information flows in whatever direction the "velocity" is pointing. We can say that local transport is diffusive, while non-local transport (like that described by MFC) is advective. In a convective boundary layer (where σ is very small), the transport is clearly not diffusive. Thus, the representation of higher-moment transport terms with MFC is likely more realistic than with diffusion closure.

In addition, that there are *no* realizability issues with this approach and thus, there is no need to use André's "clipping" or the quasi-normal approximation (see Section II-C-4). The reason for this is that I am already assuming a joint distribution for all the mean quantities and I compute higher moments directly from these distributions. As long as the moments are computed from a single set of internally consistent joint distributions, they are guaranteed to be consistent with each other. In this manner, the fourth-order terms are represented exactly as "transport" term and thus, they naturally acts to prevent the build-up of the third-order correlations.

One final advantage of the MFC method is its inherent ability to represent partial cloudiness. Many turbulence models allow for any one grid cell to be either cloudy *or* clear. In reality, completely clear or uniformly cloudy skies are rare occurrences. Thus, models that represent a grid box in this fashion will undoubtedly have large errors in the diagnosed buoyancy and liquid water fluxes. These errors will feed back on the turbulence equations and produce more errors. Buoyancy fluxes are computed in the RSM model from the same diagnostic relationships as the other higher moments (Eqs. 3.1-3.6) and thus they are direct functions of the area-weighted updraft and downdraft temperature and humidity profiles.

More sophisticated HOC models use a subgrid-scale (SGS) condensation scheme (e.g., Somméria and Deardorff, 1976) to represent the effects of partial cloudiness (Yamada and Mellor, 1979; Banta and Cotton, 1980). These SGS schemes assume a joint-normal distribution for the temperature and total water mixing ratios. Although the inclusion of SGS parameterization improves the treatment of cloud processes in these models, they still make assumptions about the distribution of thermodynamic quantities. As pointed out by Bougeault (1981; 1982), these distributions can vary a great deal from a normal distribution. For example, in a field of scattered cumuli, the distribution of thermodynamic quantities is highly skewed due to the presence of narrow cloudy updrafts (that have properties that are very different from the mean) and broad, clear downdrafts (that have properties which are quite close to the mean). Highly skewed distributions are the foundation for mass-flux models, which use tophat probability distribution functions (PDFs). Thus, the mass-flux model concept was applied by Randall (1987) to diagnose buoyancy and liquid water fluxes in partially cloud layers. The results of his study were strongly at odds with those of Somméria and Deardorff (1976). Bougeault also examined the highly skewed case and showed the distribution of the thermodynamic variable and the vertical velocity to be bimodal (the tophat approach used by Randall (1987) is a special type of bimodal distribution in which each "mode" is a delta function; Figs. 4-5). The RSM approach alleviates the need for "distribution" assumptions in clouds. The buoyancy statistics calculated with (3.1)-(3.6) are an exact representation of the environment simulated in the model.

III-A-1b: Disadvantages

As I discussed in the previous section, the RSM method provides a method to "solve" the closure problem. However, this method also has drawbacks. Ironically, the most obvious drawback is also one of its strengths; the fact that we assume a simple tophat profile for all variables in the model. This assumption makes the model simple, but is a crude simplification of reality. With a tophat profile, there are only two values for a parameter at a given height; an updraft and a downdraft value. In the atmosphere, many more states exist for a thermodynamic or dynamic quantity at a given height. A more realistic assumption would be to include multiple categories of updrafts and downdrafts (i.e., a broader PDF) for the thermodynamic and dynamic properties of the system. These additional categories, while complicating the system of equations, would more accurately represent the real atmosphere.

Another disadvantage of the mass-flux system is the uncertainty that surrounds its applicability to momentum. In a way, the MFC equations are naturally suited for the thermodynamic quantities such as heat and moisture. To explain this, lets examine the flux of temperature in a convective boundary layer; this flux can be viewed as a covariance between perturbations of vertical velocity and temperature. In a convective boundary layer, these two quantities will be correlated in both the updrafts and downdrafts (surface heating or cloud-top cooling directly drives vertical motion). In between the updrafts and downdrafts, both the vertical velocity and temperature perturbations are small. Thus, the partitioning of the vertical velocity and temperature into their updraft and downdraft components and formulating fluxes based on this partitioning, naturally and accurately represents the real atmosphere. However, one can not always use a similar argument for the momentum fluxes. Horizontal momentum fluxes may tend to be largest where the vertical velocity is smallest (in between the updrafts and downdrafts), especially near the top and bottom of the layer. It is uncertain whether the mass-flux partitioning, which is based on the high degree of covariance between quantities, will be an accurate representation of momentum transport in the real atmosphere. This issue is discussed more in Section III-J and is depicted in Fig. 14.

The RSM approach has a couple of other disadvantages as well. As I mentioned in the previous section, an advantage of the mass-flux approach is that it guarantees that all the mass-flux-diagnosed terms will be consistent with the prognosed values of $\overline{w'w'w'}$ and $\overline{w'w'}$. However, in order for the RSM system to be implemented, I also need to predict the vertical fluxes of all thermodynamic quantities in the model. If one uses "conventional" HOC equations to do this, there is nothing which guarantees that the fluxes will be consistent with $\overline{w'w'w'}$ and $\overline{w'w'}$, or that $\overline{w'w'w'}$ and $\overline{w'w'}$ will be consistent with each other. I must use assumptions that are used in "conventional" HOC to obtain these quantities. While RSM suggests that HOC equations be used to predict these quantities, other methods could be used in practice. ADHOC is one such method; in Chapter III, I will describe a method to predict these quantities in a manner which guarantees their consistency.

Finally, there is one last disadvantage to the RSM method. While it solves the "closure" problem by diagnosing higher-moments, it is not a panacea for all closure parameterization problems; even with this approach, I still need to parameterize the pressure covariance terms as well as dissipation. It does not eliminate the need for these additional assumptions. However, in the current model, I use a new parameterization for the dissipation that is in the "spirit" of the mass-flux approach. In addition, in Appendix B, I will also describe a possible "plume-type" approach for the pressure terms.

III-B: Framework

Following RSM, I distinguish between the rising and sinking subregions of a grid cell. Accordingly, I divide each grid cell into two sub-regions, denoted by subscripts "up" and "dn," with areas A^i_{up}, and A^i_{dn}, respectively. Here the superscript i denotes the grid cell under consideration. Subscripts are used to denote a sub-region. I assume that

$$A^i_{\mathrm{up}} + A^i_{\mathrm{dn}} = A^i . \tag{3.14}$$

Here A^i (no subscript) is the total area of the grid cell. The two sub-regions can exchange mass, and in addition each sub-region in grid cell i can exchange mass with neighboring grid cells. I denote mass exchanges inside the cell (hereafter "intra-cell") by E, and mass exchanges with neighboring cells (hereafter "inter-cell") by F.

Consider an arbitrary intensive variable h, and let S_h denote the source or sink of h. One can write the following budget equations for grid box i:

$$\frac{\partial}{\partial t}(m^i h^i{}_{\mathrm{up}} A^i{}_{\mathrm{up}}) = D^i A^i h^i{}_{\mathrm{dn}} - E^i A^i h^i{}_{\mathrm{up}}$$
$$- \sum_{i'} F^{i+i'}{}_{\mathrm{up}} \hat{h}^{i+i'}{}_{\mathrm{up}} - \frac{\partial}{\partial z}(m^i w^i{}_{\mathrm{up}} h^i{}_{\mathrm{up}} A^i{}_{\mathrm{up}}) + m^i (S_h)^i{}_{\mathrm{up}} A^i{}_{\mathrm{up}} , \tag{3.15}$$

$$\frac{\partial}{\partial t}(m^i h^i{}_{\mathrm{dn}} A^i{}_{\mathrm{dn}}) = D^i A^i h^i{}_{\mathrm{up}} - E^i A^i h^i{}_{\mathrm{dn}}$$
$$- \sum_{i'} F^{i+i'}{}_{\mathrm{dn}} \hat{h}^{i+i'}{}_{\mathrm{dn}} - \frac{\partial}{\partial z}(m^i w^i{}_{\mathrm{dn}} h^i{}_{\mathrm{dn}} A^i{}_{\mathrm{dn}}) + m^i (S_h)^i{}_{\mathrm{dn}} A^i{}_{\mathrm{dn}} . \tag{3.16}$$

Here I have used the shorthand

$$\frac{E^i}{A^i} = E^i{}_{\mathrm{dn,up}} \tag{3.17}$$

and

$$\frac{D^i}{A^i} = E^i{}_{\mathrm{up,dn}} , \tag{3.18}$$

where E^i is the lateral mass exchange from the sinking air into the rising air and D^i is the lateral mass from the rising air into the sinking air. Here m^i is the density of the air in grid cell i. I ignore density differences between the updrafts and downdrafts, except for buoyancy effects which I discuss later. The quantities E and F have units of density times velocity times length; here the length in question is the distance along the relevant boundary (Fig. 7). Note that the scheme that I chose for the lateral mass exchange terms is "upstream". In principle, however, one is free to choose another scheme for these terms.

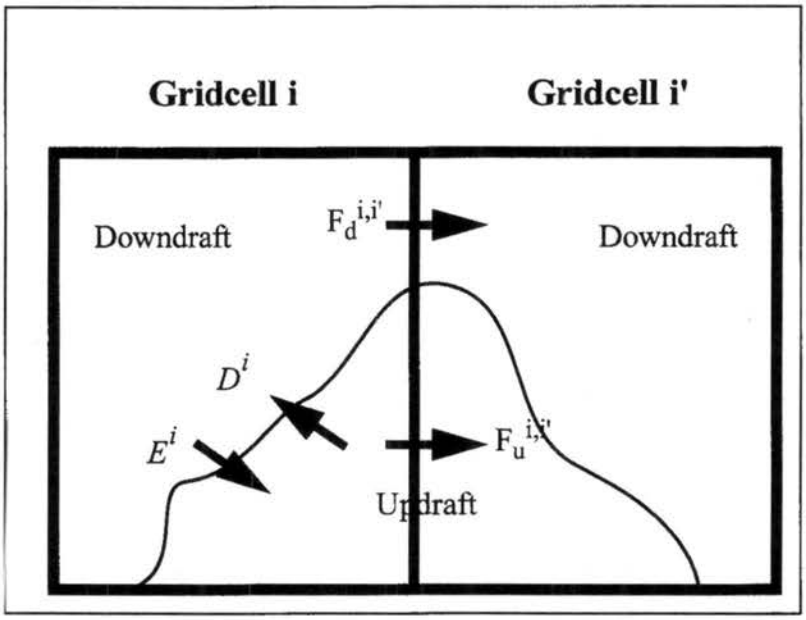

Figure 7: Relationship among E, D, and F terms in ADHOC.

When I add (3.15) and (3.16), all of the E terms cancel out, because they represent intra-cell exchanges, but the F terms survive because they represent inter-cell exchanges. I obtain

$$A^i\frac{\partial}{\partial t}(m^i\bar{h}^i) = -\sum_{i'} F^{i+i'}{}_{\mathrm{up}}\hat{h}^{i+i'}{}_{\mathrm{up}} - \sum_{i} F^{i+i'}{}_{\mathrm{dn}}\hat{h}^{i+i'}{}_{\mathrm{dn}} - A^i\frac{\partial}{\partial z}(m^i\overline{wh}^i) + m^i\overline{(S_h)}^i A^i \quad , \qquad (3.19)$$

where

$$\bar{h}^i A^i = h^i{}_{\mathrm{up}}A^i{}_{\mathrm{up}} + h^i{}_{\mathrm{dn}}A^i{}_{\mathrm{dn}} , \qquad (3.20)$$

$$\overline{mwh}^i A^i = m^i w^i{}_{\mathrm{up}}h^i{}_{\mathrm{up}}A^i{}_{\mathrm{up}} + m^i w^i{}_{\mathrm{dn}}h^i{}_{\mathrm{dn}}A^i{}_{\mathrm{dn}} , \qquad (3.21)$$

and

$$\overline{(S_h)}^i A^i = (S_h)^i_{\text{up}} A^i_{\text{up}} + (S_h)^i_{\text{dn}} A^i_{\text{dn}}. \tag{3.22}$$

In (3.19), I take into account that A^i is independent of time and height.

The continuity equations corresponding to (3.15)-(3.19) can be obtained by setting $h \equiv 1$ and $S_h = 0$:

$$\frac{\partial}{\partial t}(m^i A^i_{\text{up}}) = E^i A^i - D^i A^i - \sum_{i'} F^{i+i'}_{\text{up}} - \frac{\partial}{\partial z}(m^i w^i_{\text{up}} A^i_{\text{up}}), \tag{3.23}$$

$$\frac{\partial}{\partial t}(m^i A^i_{\text{dn}}) = D^i A^i - E^i A^i - \sum_{i'} F^{i+i'}_{\text{dn}} - \frac{\partial}{\partial z}(m^i w^i_{\text{dn}} A^i_{\text{dn}}), \tag{3.24}$$

$$A^i \frac{\partial m^i}{\partial t} = -\sum_{i'} (F^{i+i'}_{\text{up}} + F^{i+i'}_{\text{dn}}) - A^i \frac{\partial}{\partial z}(m^i \overline{w}^i). \tag{3.25}$$

To obtain (3.25), I have used

$$A^i \overline{w}^i = w^i_{\text{up}} A^i_{\text{up}} + w^i_{\text{dn}} A^i_{\text{dn}}, \tag{3.26}$$

where $\overline{w}^i$ is the area-averaged vertical velocity. Eqs. (3.23)-(3.24) govern the time change of the mass or area within each sub-region. Eq. (3.25) is the continuity equation for a whole grid cell.

For convenience, define

$$\sigma^i \equiv \frac{A^i_{\text{up}}}{A^i}. \tag{3.27}$$

Using (3.14) and (3.27), I find that

$$1-\sigma^i = \frac{A^i{}_{\mathrm{dn}}}{A^i}. \tag{3.28}$$

With this definition of σ^i, I can show, using (3.26), that

$$w^i{}_{\mathrm{up}} = \overline{w}^i + (1-\sigma^i)(w^i{}_{\mathrm{up}} - w^i{}_{\mathrm{dn}}), \tag{3.29}$$

$$w^i{}_{\mathrm{dn}} = \overline{w}^i - \sigma^i(w^i{}_{\mathrm{up}} - w^i{}_{\mathrm{dn}}) \quad , \tag{3.30}$$

and

$$\begin{aligned} \overline{mwh}^i &= m^i w^i{}_{\mathrm{up}} h^i{}_{\mathrm{up}} \sigma^i + m^i w^i{}_{\mathrm{dn}} h^i{}_{\mathrm{dn}} (1-\sigma^i) \\ &= m^i \overline{w}^i \overline{h}^i + M^i{}_{\mathrm{c}}(h^i{}_{\mathrm{up}} - h^i{}_{\mathrm{dn}}) \quad . \end{aligned} \tag{3.31}$$

In (3.31), $m^i\overline{w}^i$ is the "large-scale" mass flux, and

$$M^i{}_{\mathrm{c}} \equiv m^i \sigma^i (1-\sigma^i)(w^i{}_{\mathrm{up}} - w^i{}_{\mathrm{dn}}) \tag{3.32}$$

is the convective mass flux. Each of these mass fluxes contributes to the total vertical flux of any quantity.

By combining (3.23)-(3.25) and (3.31) with (3.15)-(3.19), I can derive "advective forms" of the budget equations for h:

$$m^i A^i{}_{\mathrm{up}} \frac{\partial h^i{}_{\mathrm{up}}}{\partial t} = E^i A^i (h^i{}_{\mathrm{dn}} - h^i{}_{\mathrm{up}}) - \sum_{i'} F^{i+i'}{}_{\mathrm{up}} (\hat{h}^{i+i'}{}_{\mathrm{up}} - h^i{}_{\mathrm{up}})$$
$$- m^i A^i{}_{\mathrm{up}} w^i{}_{\mathrm{up}} \frac{\partial h^i{}_{\mathrm{up}}}{\partial z} + m^i (S_h)^i{}_{\mathrm{up}} A^i{}_{\mathrm{up}} , \tag{3.33}$$

$$m^i A^i{}_{\mathrm{dn}} \frac{\partial h^i{}_{\mathrm{dn}}}{\partial t} = D^i A^i (h^i{}_{\mathrm{up}} - h^i{}_{\mathrm{dn}}) - \sum_{i'} F^{i+i'}{}_{\mathrm{dn}} (\hat{h}^{i+i'}{}_{\mathrm{dn}} - h^i{}_{\mathrm{dn}})$$
$$- m^i A^i{}_{\mathrm{dn}} w^i{}_{\mathrm{dn}} \frac{\partial h^i{}_{\mathrm{dn}}}{\partial z} + m^i (S_h)^i{}_{\mathrm{dn}} A^i{}_{\mathrm{dn}} , \tag{3.34}$$

$$A^i m^i \frac{\partial \bar{h}^i}{\partial t} = - \sum_{i'} F^{i+i'}{}_{\mathrm{up}} (\hat{h}^{i+i'}{}_{\mathrm{up}} - \bar{h}^i) - \sum_{i} F^{i+i'}{}_{\mathrm{dn}} (\hat{h}^{i+i'}{}_{\mathrm{dn}} - \bar{h}^i)$$
$$- A^i m^i \bar{w}^i \frac{\partial \bar{h}^i}{\partial z} - A^i \frac{\partial}{\partial z} [M^i{}_{\mathrm{c}} (h^i{}_{\mathrm{up}} - h^i{}_{\mathrm{dn}})] + m^i \overline{(S_h)}^i A^i \quad . \tag{3.35}$$

III-C: Intra-cellular exchanges of mass

As discussed, D^i represents air moving from the rising area to the sinking area, and similarly E^i represents air moving from the sinking area to the rising area. With these definitions,

$$D^i \geq 0 \text{, and } E^i \geq 0 . \tag{3.36}$$

Note that D^i is *not* equal to minus E^i. The two mass exchange processes can occur independently and simultaneously within each grid cell.

Intra-cell fluxes *between sub-regions of the same type* ("sub-sub-regions") are neglected here, so that, for instance, flows between two clear portions of the same grid cell are assumed to have no effect on quantities of interest. In effect I assume that all subregions *of the same type*, within a given cell, have identical properties, so that exchanges among them are irrelevant.

A full discussion of the parameterization of E^i and D^i is given in Section III-G.

III-D: Inter-cellular exchanges of mass

I assume that when air flows across cell walls, between neighboring grid cells, *it always moves between sub-regions of like type*, so that, for example, air can travel from the rising sub-regions of grid box i to the rising sub-regions of grid box $i + i'$, but not from the rising sub-region of grid box i to the sinking sub-region of grid box $i + i'$. The rationale is that it would be quite unlikely for the boundary of a sub-region to coincide exactly with the wall of a grid cell.

To minimize the number of symbols, I adopt the notation $F^{i+i'}{}_{\mathrm{up}}$ to denote the flow of mass *outward from* grid box i *to* neighboring grid box $i + i'$, in this case between the rising sub-regions of each. Corresponding conventions are used with $F^{i+i'}{}_{\mathrm{dn}}$. This is why the F terms appear with minus signs on the right-hand sides of (3.15) - (3.19). The Fs can have either sign.

$\sum_{i'} F^{i+i'}{}_{\mathrm{up}}$ represents the net flow of air from the rising region in one cell to the rising regions of the surrounding cells. Similarly, $\sum_{i'} F^{i+i'}{}_{\mathrm{dn}}$ represents the flow of air from the sinking region in one cell to the sinking regions of the surrounding cells. Summations such as $\sum_{i'} F^{i+i'}{}_{\mathrm{up}} \hat{h}^{i+i'}{}_{\mathrm{up}}$ represent exchanges between grid box i and all neighboring grid boxes. The "hat" symbol, as in $\hat{h}^{i+i'}$, denotes an interpolated value on a cell wall.

I assume that

$$F^{i+i'}{}_{\mathrm{dn}} = \hat{m}^{i+i'} v^{i+i'}{}_{\mathrm{dn}} l^{i+i'}{}_{\mathrm{dn}}, \tag{3.37}$$

where $\hat{m}^{i+i'}$ is an interpolated mass variable, defined on the cell wall, $v^{i+i'}{}_{\mathrm{dn}}$ is the outward normal velocity component along the cell wall, and $l^{i+i'}{}_{\mathrm{dn}}$ is the distance occupied by sinking air, along the cell wall. Note that I distinguish between the horizontal velocities in the updrafts and downdrafts; such differences are associated with the vertical flux of horizontal momentum. Similarly, I assume that

$$F^{i+i'}{}_{\mathrm{up}} = \hat{m}^{i+i'} v^{i+i'}{}_{\mathrm{up}} l^{i+i'}{}_{\mathrm{up}}. \tag{3.38}$$

I require that

$$l^{i+i'}{}_{\mathrm{up}} + l^{i+i'}{}_{\mathrm{dn}} = l^{i+i'}, \tag{3.39}$$

where $l^{i+i'}$ is the total length of the cell wall. This simply means that the updrafts and downdrafts together fill the entire the cell wall. I assume that

$$l^{i+i'}{}_{\mathrm{up}} = l^{i+i'} \hat{\sigma}^{i+i'}, \tag{3.40}$$

$$l^{i+i'}{}_{\mathrm{dn}} = l^{i+i'} (1 - \hat{\sigma}^{i+i'}), \tag{3.41}$$

where

$$\hat{\sigma}^{i+i'} \equiv \frac{\hat{A}^{i+i'}{}_{\mathrm{up}}}{\hat{A}^{i+i'}}, \tag{3.42}$$

$$1-\hat{\sigma}^{i+i'} = \frac{\hat{A}^{i+i'}{}_{\mathrm{dn}}}{\hat{A}^{i+i'}}, \tag{3.43}$$

and $\hat{A}^{i+i'}{}_{\mathrm{up}}$, $\hat{A}^{i+i'}{}_{\mathrm{dn}}$, and $\hat{A}^{i+i'}$ are suitably interpolated "edge" values of the corresponding areas. In view of (3.39) and (3.43), I must require that

$$\hat{A}^{i+i'}{}_{\mathrm{up}} + \hat{A}^{i+i'}{}_{\mathrm{dn}} = \hat{A}^{i+i'}. \tag{3.44}$$

Because I enforce (3.14), the requirement (3.44) is automatically met by either upstream or centered interpolation of the fractional areas, and also by any linear combination of upstream and centered interpolations. Note that $\hat{\sigma}^{i+i'}$ is *not* the average of the neighboring cell center values of σ.

Substitution of (3.40) - (3.41) into (3.37) - (3.38) gives

$$F^{i+i'}{}_{\mathrm{up}} = \hat{m}^{i+i'} v^{i+i'}{}_{\mathrm{up}} l^{i+i'} \hat{\sigma}^{i+i'}, \tag{3.45}$$

$$F^{i+i'}{}_{\mathrm{dn}} = \hat{m}^{i+i'} v^{i+i'}{}_{\mathrm{dn}} l^{i+i'} (1-\hat{\sigma}^{i+i'}). \tag{3.46}$$

Substitution of (3.45)-(3.46) into (3.25), and use of (3.44), leads to

$$\begin{aligned} A^i \frac{\partial m^i}{\partial t} &= -\sum_{i'} \hat{m}^{i+i'} v^{i+i'}{}_{\mathrm{up}} l^{i+i'} \hat{\sigma}^{i+i'} - \sum_{i'} \hat{m}^{i+i'} v^{i+i'}{}_{\mathrm{dn}} l^{i+i'} (1-\hat{\sigma}^{i+i'}) - A^i \frac{\partial}{\partial z}(m^i \overline{w}^i) \\ &= -\sum_{i'} \hat{m}^{i+i'} v^{i+i'} l^{i+i'} - A^i \frac{\partial}{\partial z}(m^i \overline{w}^i) \quad . \end{aligned} \tag{3.47}$$

To obtain the second equality, I have used

$$v^{i+i'} = v^{i+i'}{}_{\mathrm{up}}\hat{\sigma}^{i+i'} + v^{i+i'}{}_{\mathrm{dn}}(1-\hat{\sigma}^{i+i'}). \tag{3.48}$$

Eq. (3.47) is just what one would expect from the large-scale point of view. On the other hand, Eqs. (3.45)-(3.46) imply a subplume-scale flux across cell walls. To see this, substitute (3.45)-(3.46) into (3.19), to obtain

$$\begin{aligned} & A^i\frac{\partial}{\partial t}(m^i\bar{h}^i) \\ &= -\sum_{i'}\hat{m}^{i+i'}v^{i+i'}{}_{\mathrm{up}}l^{i+i'}\hat{\sigma}^{i+i'}\hat{h}^{i+i'}{}_{\mathrm{up}} - \sum_{i'}\hat{m}^{i+i'}v^{i+i'}{}_{\mathrm{dn}}l^{i+i'}(1-\hat{\sigma}^{i+i'})\hat{h}^{i+i'}{}_{\mathrm{dn}} \\ &\quad - A^i\frac{\partial}{\partial z}(m^i\bar{w}^i\bar{h}^i) - A^i\frac{\partial}{\partial z}[M^i{}_{\mathrm{c}}(h^i{}_{\mathrm{up}} - h^i{}_{\mathrm{dn}})] + m^i\overline{(S_h)}^iA^i \\ &= -\sum_{i'}\hat{m}^{i+i'}v^{i+i'}l^{i+i'}\hat{h}^{i+i'} - G^{i+i'}(h) \\ &\quad - A^i\frac{\partial}{\partial z}(m^i\bar{w}^i\bar{h}^i) - A^i\frac{\partial}{\partial z}[M^i{}_{\mathrm{c}}(h^i{}_{\mathrm{up}} - h^i{}_{\mathrm{dn}})] + m^i\overline{(S_h)}^iA^i \quad , \end{aligned} \tag{3.49}$$

where

$$\hat{h}^{i+i'} = \hat{h}^{i+i'}{}_{\mathrm{up}}\hat{\sigma}^{i+i'} + \hat{h}^{i+i'}{}_{\mathrm{dn}}(1-\hat{\sigma}^{i+i'}), \tag{3.50}$$

and

$$
\begin{aligned}
G^{i+i'}(h) \equiv& \sum_{i'} \hat{m}^{i+i'} v^{i+i'}{}_{\mathrm{up}} l^{i+i'} \hat{\sigma}^{i+i'} \hat{h}^{i+i'}{}_{\mathrm{up}} + \sum_{i'} \hat{m}^{i+i'} v^{i+i'}{}_{\mathrm{dn}} l^{i+i'} (1-\hat{\sigma}^{i+i'}) \hat{h}^{i+i'}{}_{\mathrm{dn}} \\
&- \sum_{i'} \hat{m}^{i+i'} v^{i+i'} l^{i+i'} \hat{h}^{i+i'} \\
=& \sum_{i'} \hat{m}^{i+i'} v^{i+i'}{}_{\mathrm{up}} l^{i+i'} \hat{\sigma}^{i+i'} \hat{h}^{i+i'}{}_{\mathrm{up}} + \sum_{i'} \hat{m}^{i+i'} v^{i+i'}{}_{\mathrm{dn}} l^{i+i'} (1-\hat{\sigma}^{i+i'}) \hat{h}^{i+i'}{}_{\mathrm{dn}} \\
&- \sum_{i'} \hat{m}^{i+i'} v^{i+i'}{}_{\mathrm{up}} l^{i+i'} \hat{\sigma}^{i+i'} \hat{h}^{i+i'} - \sum_{i'} \hat{m}^{i+i'} v^{i+i'}{}_{\mathrm{dn}} l^{i+i'} (1-\hat{\sigma}^{i+i'}) \hat{h}^{i+i'} \\
=& \sum_{i'} \hat{m}^{i+i'} v^{i+i'}{}_{\mathrm{up}} l^{i+i'} \hat{\sigma}^{i+i'} (\hat{h}^{i+i'}{}_{\mathrm{up}} - \hat{h}^{i+i'}) \\
&+ \sum_{i'} \hat{m}^{i+i'} v^{i+i'}{}_{\mathrm{dn}} l^{i+i'} (1-\hat{\sigma}^{i+i'}) (\hat{h}^{i+i'}{}_{\mathrm{dn}} - \hat{h}^{i+i'}) \\
=& \sum_{i'} \hat{m}^{i+i'} (v^{i+i'}{}_{\mathrm{up}} - v^{i+i'}) l^{i+i'} \hat{\sigma}^{i+i'} (\hat{h}^{i+i'}{}_{\mathrm{up}} - \hat{h}^{i+i'}) \\
&+ \sum_{i'} \hat{m}^{i+i'} (v^{i+i'}{}_{\mathrm{dn}} - v^{i+i'}) l^{i+i'} (1-\hat{\sigma}^{i+i'}) (\hat{h}^{i+i'}{}_{\mathrm{dn}} - \hat{h}^{i+i'}) \\
&+ \sum_{i'} \hat{m}^{i+i'} v^{i+i'} l^{i+i'} \hat{\sigma}^{i+i'} (\hat{h}^{i+i'}{}_{\mathrm{up}} - \hat{h}^{i+i'}) \\
&+ \sum_{i'} \hat{m}^{i+i'} v^{i+i'} l^{i+i'} (1-\hat{\sigma}^{i+i'}) (\hat{h}^{i+i'}{}_{\mathrm{dn}} - \hat{h}^{i+i'}) \\
=& \sum_{i'} \hat{m}^{i+i'} (v^{i+i'}{}_{\mathrm{up}} - v^{i+i'}) l^{i+i'} \hat{\sigma}^{i+i'} (\hat{h}^{i+i'}{}_{\mathrm{up}} - \hat{h}^{i+i'}) \\
&+ \sum_{i'} \hat{m}^{i+i'} (v^{i+i'}{}_{\mathrm{dn}} - v^{i+i'}) l^{i+i'} (1-\hat{\sigma}^{i+i'}) (\hat{h}^{i+i'}{}_{\mathrm{dn}} - \hat{h}^{i+i'}) \ .
\end{aligned}
\tag{3.51}
$$

represents a subplume-scale flux of the form $\overline{v'h'}$, which arises from the indicated differences in h and v. To obtain the final equality in (3.51) I have used

$$
\begin{aligned}
&\sum_{i'} \hat{m}^{i+i'} v^{i+i'} l^{i+i'} \hat{\sigma}^{i+i'} (\hat{h}^{i+i'}{}_{\mathrm{up}} - \hat{h}^{i+i'}) + \\
&\sum_{i'} \hat{m}^{i+i'} v^{i+i'} l^{i+i'} (1-\hat{\sigma}^{i+i'}) (\hat{h}^{i+i'}{}_{\mathrm{dn}} - \hat{h}^{i+i'}) = 0 \ .
\end{aligned}
\tag{3.52}
$$

III-E: Second and third moments

In this section, I derive the second- and third-moment equations, starting from the equations for the updraft and downdraft properties. I will do this for $\overline{w'h'}$, $\overline{w'w'}$, and $\overline{w'w'w'}$. I will show that the resulting equations are term-by-term consistent with the "standard" HOC equations for these moments:

$$\frac{\partial}{\partial t}\overline{w'h'} = -\frac{1}{m}\frac{\partial}{\partial z}m\overline{w'w'h'} - \overline{w'w'}\frac{\partial}{\partial z}\bar{h} + \frac{g}{C_pT_o}\overline{h'S_v'} - \frac{1}{m}\overline{h'\frac{\partial p'}{\partial z}} - \varepsilon_{wh} \tag{3.53}$$

$$\frac{\partial}{\partial t}\overline{w'w'} = -\frac{1}{m}\frac{\partial}{\partial z}m\overline{w'w'w'} + 2\frac{g}{C_pT_o}\overline{w'S_v'} - \varepsilon_{ww} - \frac{2}{m}\overline{w'\frac{\partial p'}{\partial z}} \tag{3.54}$$

and

$$\frac{\partial}{\partial t}\overline{w'w'w'} = -\frac{1}{m}\frac{\partial}{\partial z}m\overline{w'w'w'w'} + \frac{3}{m}\overline{w'^2}\frac{\partial}{\partial z}\left(m\overline{w'^2}\right) + 3\frac{g}{C_pT_o}\overline{w'S_v'} - \varepsilon_{www} - \frac{3}{m}\overline{w'^2\frac{\partial p'}{\partial z}} \tag{3.55}$$

In the above equations, w is the vertical velocity, h is an arbitrary intensive variable, $C_p = 1004\,\mathrm{J\,kg^{-1}\,K^{-1}}$, $g = 9.8\,\mathrm{m\,s^{-1}}$, T_o is a reference temperature, $S_v = C_pT_v + gz - L_vR_L$ is the virtual liquid water static energy, T_v is the virtual temperature, z is the height, $L_v = 2.52 \times 10^6\,\mathrm{J\,kg^{-1}}$, R_L is the liquid water mixing ratio, ε_x is the dissipation of x, and p is the pressure.

The "plume" forms that I seek for these moments are the RSM forms outlined in Eqs. (3.3)-(3.6). To derive these second- and third-moment "plume" equations, I begin by expanding the RSM form of $\overline{w'w'}$ (Eq. 3.3 with h replaced by w). For simplicity here, I drop the subscripts,

i.

$$\frac{\partial}{\partial t}[\sigma(1-\sigma)(w_{\mathrm{up}}-w_{\mathrm{dn}})^2] = (w_{\mathrm{up}}-w_{\mathrm{dn}})^2(1-2\sigma)\frac{\partial \sigma}{\partial t} + 2\sigma(1-\sigma)(w_{\mathrm{up}}-w_{\mathrm{dn}})\frac{\partial}{\partial t}(w_{\mathrm{up}}-w_{\mathrm{dn}}) \quad , \tag{3.56}$$

$$\frac{\partial}{\partial t}[\sigma(1-\sigma)(w_{\mathrm{up}}-w_{\mathrm{dn}})(h_{\mathrm{up}}-h_{\mathrm{dn}})] = (w_{\mathrm{up}}-w_{\mathrm{dn}})(h_{\mathrm{up}}-h_{\mathrm{dn}})(1-2\sigma)\frac{\partial \sigma}{\partial t} + {} + \sigma(1-\sigma)\frac{\partial}{\partial t}[(w_{\mathrm{up}}-w_{\mathrm{dn}})(h_{\mathrm{up}}-h_{\mathrm{dn}})] \quad , \tag{3.57}$$

and

$$\frac{\partial}{\partial t}[\sigma(1-\sigma)(1-2\sigma)(w_{\mathrm{up}}-w_{\mathrm{dn}})^3] = (w_{\mathrm{up}}-w_{\mathrm{dn}})^3[6\sigma^2-6\sigma+1]\frac{\partial \sigma}{\partial t} + 3\sigma(1-\sigma)(1-2\sigma)(w_{\mathrm{up}}-w_{\mathrm{dn}})^2\frac{\partial}{\partial t}(w_{\mathrm{up}}-w_{\mathrm{dn}}) \quad . \tag{3.58}$$

From (3.33) and (3.34), I can derive an equation for the time change of the updraft-downdraft difference, $h_{\mathrm{up}}-h_{\mathrm{dn}}$:

$$\frac{\partial}{\partial t}(h_{\mathrm{up}}-h_{\mathrm{dn}}) = -\left(\frac{E}{\sigma}+\frac{D}{1-\sigma}\right)\frac{(h_{\mathrm{up}}-h_{\mathrm{dn}})}{m} - w_{\mathrm{up}}\frac{\partial h_{\mathrm{up}}}{\partial z} + w_{\mathrm{dn}}\frac{\partial h_{\mathrm{dn}}}{\partial z} (S_h)_{\mathrm{up}} - (S_h)_{\mathrm{dn}} \quad . \tag{3.59}$$

Here I have neglected terms involving F, on the grounds that advection by the mean flow is negligible in the second- and third-moment equations which I are currently working to derive.

We can write an essentially identical equation for the vertical velocity difference:

$$\begin{aligned}\frac{\partial}{\partial t}(w_{\text{up}} - w_{\text{dn}}) &= -\left(\frac{E}{\sigma} + \frac{D}{1-\sigma}\right)\frac{(w_{\text{up}} - w_{\text{dn}})}{m} \\ &\quad -\frac{1}{2}\frac{\partial}{\partial z}[(w_{\text{up}})^2 - (w_{\text{dn}})^2] \\ &\quad + [(S_w)_{\text{up}} - (S_w)_{\text{dn}}] \quad .\end{aligned} \tag{3.60}$$

Section III-H explains how I treat the pressure terms which contribute to $(S_w)_{\text{up}} - (S_w)_{\text{dn}}$.

From (3.59) and (3.60) I can form a prognostic equation for $(w_{\text{up}} - w_{\text{dn}})(h_{\text{up}} - h_{\text{dn}})$:

$$\begin{aligned}\frac{\partial}{\partial t}[(w_{\text{up}} - w_{\text{dn}})(h_{\text{up}} - h_{\text{dn}})] &= \\ &-2\left(\frac{E}{\sigma} + \frac{D}{1-\sigma}\right)\frac{(w_{\text{up}} - w_{\text{dn}})(h_{\text{up}} - h_{\text{dn}})}{m} \\ &-\frac{(h_{\text{up}} - h_{\text{dn}})}{2}\frac{\partial}{\partial z}[(w_{\text{up}})^2 - (w_{\text{dn}})^2] \\ &+ (w_{\text{up}} - w_{\text{dn}})\left[-w_{\text{up}}\frac{\partial h_{\text{up}}}{\partial z} + w_{\text{dn}}\frac{\partial h_{\text{dn}}}{\partial z}\right] \\ &+ (h_{\text{up}} - h_{\text{dn}})[(S_w)_{\text{up}} - (S_w)_{\text{dn}}] \\ &+ (w_{\text{up}} - w_{\text{dn}})[(S_h)_{\text{up}} - (S_h)_{\text{dn}}] \quad .\end{aligned} \tag{3.61}$$

This immediately carries over to

$$\begin{aligned}\frac{\partial(w_{\text{up}} - w_{\text{dn}})^2}{\partial t} &= -2\left(\frac{E}{\sigma} + \frac{D}{1-\sigma}\right)\frac{(w_{\text{up}} - w_{\text{dn}})^2}{m} \\ &\quad -(w_{\text{up}} - w_{\text{dn}})\frac{\partial}{\partial z}[(w_{\text{up}})^2 - (w_{\text{dn}})^2] \\ &\quad + 2(w_{\text{up}} - w_{\text{dn}})[(S_w)_{\text{up}} - (S_w)_{\text{dn}}] \quad .\end{aligned} \tag{3.62}$$

Using the identity $\frac{\partial A^3}{\partial t} = 3A^2\frac{\partial A}{\partial t}$, we can write

$$\begin{aligned}\frac{\partial(w_{\mathrm{up}} - w_{\mathrm{dn}})^3}{\partial t} &= -3\left(\frac{E}{\sigma} + \frac{D}{1-\sigma}\right)\frac{(w_{\mathrm{up}} - w_{\mathrm{dn}})^3}{m} \\ &-\frac{3}{2}(w_{\mathrm{up}} - w_{\mathrm{dn}})^2\frac{\partial}{\partial z}[(w_{\mathrm{up}})^2 - (w_{\mathrm{dn}})^2] \\ &+ 3(w_{\mathrm{up}} - w_{\mathrm{dn}})^2[(S_w)_{\mathrm{up}} - (S_w)_{\mathrm{dn}}] \quad .\end{aligned} \tag{3.63}$$

I now recast the continuity equations for the updrafts and downdrafts, making use of the definition of σ, neglecting terms involving F (on the grounds that the plume-scale mass-flux convergences and divergences are much larger than those of the large scale), and, in the spirit of the anelastic approximation, also neglecting the tendency of m:

$$\frac{\partial\sigma}{\partial t} = \frac{E-D}{m} - \frac{1}{m}\frac{\partial}{\partial z}(mw_{\mathrm{up}}\sigma), \tag{3.64}$$

$$\frac{\partial}{\partial t}(1-\sigma) = \frac{D-E}{m} - \frac{1}{m}\frac{\partial}{\partial z}[mw_{\mathrm{dn}}(1-\sigma)]. \tag{3.65}$$

We would like to combine (3.64) and (3.65) into a symmetrical form. Multiply (3.65) by σ, and subtract the result from $(1-\sigma)$ times (3.64), to obtain

$$\frac{\partial\sigma}{\partial t} = \left(\frac{E-D}{m}\right) - \frac{1}{m}\frac{\partial}{\partial z}(M_{\mathrm{c}}) - \overline{w}\frac{\partial\sigma}{\partial z}. \tag{3.66}$$

Here I have made use of (3.26) and (3.32). In deriving the second- and third-moment equations, I neglect the effects of the mean vertical velocity [this is consistent with my earlier neglect of the F terms in (3.59), (3.64), and (3.65)], so that I approximate (3.66) by

$$\frac{\partial\sigma}{\partial t} = \left(\frac{E-D}{m}\right) - \frac{1}{m}\frac{\partial M_{\mathrm{c}}}{\partial z} \quad . \tag{3.67}$$

Now I assemble the various pieces to form the second- and third-moment equations, beginning with the equation for the vertical velocity variance,

$$\begin{aligned}\frac{\partial}{\partial t}[\sigma(1-\sigma)(w_{\mathrm{up}}-w_{\mathrm{dn}})^2] &= (w_{\mathrm{up}}-w_{\mathrm{dn}})^2(1-2\sigma)\frac{\partial\sigma}{\partial t} \\ &+ 2\sigma(1-\sigma)(w_{\mathrm{up}}-w_{\mathrm{dn}})\frac{\partial}{\partial t}(w_{\mathrm{up}}-w_{\mathrm{dn}}) \quad .\end{aligned} \tag{3.68}$$

Using (3.62), (3.64), and (3.65), we can write (3.68) as

$$\begin{aligned}\frac{\partial}{\partial t}[\sigma(1-\sigma)(w_{\mathrm{up}}-w_{\mathrm{dn}})^2] &= (w_{\mathrm{up}}-w_{\mathrm{dn}})^2(1-2\sigma)\frac{\partial\sigma}{\partial t} \\ &+ 2\sigma(1-\sigma)(w_{\mathrm{up}}-w_{\mathrm{dn}})\frac{\partial}{\partial t}(w_{\mathrm{up}}-w_{\mathrm{dn}}) \\ &= (w_{\mathrm{up}}-w_{\mathrm{dn}})^2(1-2\sigma)\left[\left(\frac{E-D}{m}\right) - \frac{1}{m}\frac{\partial M_{\mathrm{c}}}{\partial z}\right] \\ &- \frac{2\sigma(1-\sigma)(w_{\mathrm{up}}-w_{\mathrm{dn}})^2}{m}\left(\frac{E}{\sigma} + \frac{D}{1-\sigma}\right) \\ &- \sigma(1-\sigma)(w_{\mathrm{up}}-w_{\mathrm{dn}})\frac{\partial}{\partial z}[(w_{\mathrm{up}})^2 - (w_{\mathrm{dn}})^2] \\ &+ 2\sigma(1-\sigma)(w_{\mathrm{up}}-w_{\mathrm{dn}})[(S_w)_{\mathrm{up}} - (S_w)_{\mathrm{dn}}] \quad .\end{aligned} \tag{3.69}$$

Collecting terms, multiplying through by m, and using the definition of M_{c}, we obtain

$$\frac{\partial}{\partial t}[m\sigma(1-\sigma)(w_{\mathrm{up}}-w_{\mathrm{dn}})^2] = -(w_{\mathrm{up}}-w_{\mathrm{dn}})^2(E+D)$$

$$-M_{\mathrm{c}}\frac{\partial}{\partial z}[(w_{\mathrm{up}})^2-(w_{\mathrm{dn}})^2]-(w_{\mathrm{up}}-w_{\mathrm{dn}})^2(1-2\sigma)\frac{\partial M_{\mathrm{c}}}{\partial z} \tag{3.70}$$

$$+2M_{\mathrm{c}}[(S_w)_{\mathrm{up}}-(S_w)_{\mathrm{dn}}] \ .$$

Using

$$\begin{aligned}(w_{\mathrm{up}})^2-(w_{\mathrm{dn}})^2 &= (w_{\mathrm{up}}-w_{\mathrm{dn}})(w_{\mathrm{up}}+w_{\mathrm{dn}}) \\ &= (w_{\mathrm{up}}-w_{\mathrm{dn}})[2\overline{w}+(1-2\sigma)(w_{\mathrm{up}}-w_{\mathrm{dn}})] \\ &\cong (1-2\sigma)(w_{\mathrm{up}}-w_{\mathrm{dn}})^2 \ ,\end{aligned} \tag{3.71}$$

we can rewrite (3.70) as

$$\begin{aligned}\frac{\partial}{\partial t}[m\sigma(1-\sigma)(w_{\mathrm{up}}-w_{\mathrm{dn}})^2] &= -(w_{\mathrm{up}}-w_{\mathrm{dn}})^2(E+D) \\ &-\frac{\partial}{\partial z}[M_{\mathrm{c}}(1-2\sigma)(w_{\mathrm{up}}-w_{\mathrm{dn}})^2] \\ &+2M_{\mathrm{c}}[(S_w)_{\mathrm{up}}-(S_w)_{\mathrm{dn}}] \ .\end{aligned} \tag{3.72}$$

We can identify the terms on the right-hand side of (3.72) as dissipation, transport, and the effects of sources and sinks associated with buoyancy, pressure forces, and small-scale mixing. Dissipation is associated with mass exchanges between the updraft and downdraft. Additional dissipation can enter through the mixing terms included on the third line.

I now perform a similar analysis for the flux equation. This time we expect to find gradient production, in addition to dissipation, transport, and the source-sink terms. The starting point is

$$\frac{\partial}{\partial t}[\sigma(1-\sigma)(w_{up}-w_{dn})(h_{up}-h_{dn})] = (w_{up}-w_{dn})(h_{up}-h_{dn})(1-2\sigma)\frac{\partial\sigma}{\partial t} + \sigma(1-\sigma)\frac{\partial}{\partial t}[(w_{up}-w_{dn})(h_{up}-h_{dn})] \ . \tag{3.73}$$

Using (3.61), (3.64), and (3.65), we can write (3.73) as

$$\begin{aligned}\frac{\partial}{\partial t}[\sigma(1-\sigma)(w_{up}-w_{dn})(h_{up}-h_{dn})] &= (w_{up}-w_{dn})(h_{up}-h_{dn})(1-2\sigma)\frac{\partial\sigma}{\partial t} \\ &\quad + \sigma(1-\sigma)\frac{\partial}{\partial t}[(w_{up}-w_{dn})(h_{up}-h_{dn})] \\ &= (w_{up}-w_{dn})(h_{up}-h_{dn})(1-2\sigma)\left[\left(\frac{E-D}{m}\right)-\frac{1}{m}\frac{\partial M_c}{\partial z}\right] \\ &\quad -2\sigma(1-\sigma)\left(\frac{E}{\sigma}+\frac{D}{1-\sigma}\right)\frac{(w_{up}-w_{dn})(h_{up}-h_{dn})}{m} \\ &\quad -\sigma(1-\sigma)\frac{(h_{up}-h_{dn})}{2}\frac{\partial}{\partial z}[(w_{up})^2-(w_{dn})^2] \\ &\quad +\sigma(1-\sigma)(w_{up}-w_{dn})\left[-w_{up}\frac{\partial h_{up}}{\partial z}+w_{dn}\frac{\partial h_{dn}}{\partial z}\right] \\ &\quad +\sigma(1-\sigma)(h_{up}-h_{dn})[(S_w)_{up}-(S_w)_{dn}] \\ &\quad +\sigma(1-\sigma)(w_{up}-w_{dn})[(S_h)_{up}-(S_h)_{dn}] \ . \end{aligned} \tag{3.74}$$

Collecting terms, multiplying through by m, using the definition of M_c, and using (3.71), we obtain

$$
\begin{aligned}
&\frac{\partial}{\partial t} m\sigma(1-\sigma)(w_{\rm up}-w_{\rm dn})(h_{\rm up}-h_{\rm dn}) \\
&\quad = -(E+D)(w_{\rm up}-w_{\rm dn})(h_{\rm up}-h_{\rm dn}) \\
&\quad -(m\sigma)(1-\sigma)\frac{(h_{\rm up}-h_{\rm dn})}{2}\frac{\partial}{\partial z}[(1-2\sigma)(w_{\rm up}-w_{\rm dn})^2] \\
&\quad -(w_{\rm up}-w_{\rm dn})(h_{\rm up}-h_{\rm dn})(1-2\sigma)\frac{\partial M_{\rm c}}{\partial z} \\
&\quad + M_{\rm c}\left[-w_{\rm up}\frac{\partial h_{\rm up}}{\partial z}+w_{\rm dn}\frac{\partial h_{\rm dn}}{\partial z}\right] \\
&\quad + m\sigma(1-\sigma)(h_{\rm up}-h_{\rm dn})[(S_w)_{\rm up}-(S_w)_{\rm dn}] \\
&\quad + M_{\rm c}[(S_h)_{\rm up}-(S_h)_{\rm dn}] \ .
\end{aligned}
\tag{3.75}
$$

At this point it is apparent that the dissipation term of this flux equation is exactly analogous to that of the vertical velocity variance equation. By analogy with (3.71), we write

$$
\begin{aligned}
&-w_{\rm up}\frac{\partial h_{\rm up}}{\partial z}+w_{\rm dn}\frac{\partial h_{\rm dn}}{\partial z} \\
&\quad = -[\overline{w}+(1-\sigma)(w_{\rm up}-w_{\rm dn})]\frac{\partial h_{\rm up}}{\partial z} \\
&\quad + [\overline{w}-\sigma(w_{\rm up}-w_{\rm dn})]\frac{\partial h_{\rm dn}}{\partial z} \\
&\quad \cong -(w_{\rm up}-w_{\rm dn})\left[(1-\sigma)\frac{\partial h_{\rm up}}{\partial z}+\sigma\frac{\partial h_{\rm dn}}{\partial z}\right] \ .
\end{aligned}
\tag{3.76}
$$

Substitution gives

$$\begin{aligned}
&\frac{\partial}{\partial t} m\sigma(1-\sigma)(w_{\text{up}}-w_{\text{dn}})(h_{\text{up}}-h_{\text{dn}}) \\
&= -(E+D)(w_{\text{up}}-w_{\text{dn}})(h_{\text{up}}-h_{\text{dn}}) \\
&-m\sigma(1-\sigma)\frac{(h_{\text{up}}-h_{\text{dn}})}{2}\frac{\partial}{\partial z}[(1-2\sigma)(w_{\text{up}}-w_{\text{dn}})^2] \\
&-(w_{\text{up}}-w_{\text{dn}})(h_{\text{up}}-h_{\text{dn}})(1-2\sigma)\frac{\partial M_{\text{c}}}{\partial z} \\
&-M_{\text{c}}(w_{\text{up}}-w_{\text{dn}})\left[(1-\sigma)\frac{\partial h_{\text{up}}}{\partial z}+\sigma\frac{\partial h_{\text{dn}}}{\partial z}\right] \\
&+m\sigma(1-\sigma)(h_{\text{up}}-h_{\text{dn}})[(S_w)_{\text{up}}-(S_w)_{\text{dn}}] \\
&+M_{\text{c}}[(S_h)_{\text{up}}-(S_h)_{\text{dn}}] \quad .
\end{aligned} \tag{3.77}$$

We now write

$$\begin{aligned}
(1-\sigma)\frac{\partial h_{\text{up}}}{\partial z}+\sigma\frac{\partial h_{\text{dn}}}{\partial z} &= \frac{\partial}{\partial z}\bar{h}-\frac{\partial}{\partial z}\bar{h}+(1-\sigma)\frac{\partial h_{\text{up}}}{\partial z}+\sigma\frac{\partial h_{\text{dn}}}{\partial z} \\
&= \frac{\partial}{\partial z}\bar{h}-\frac{\partial}{\partial z}[\sigma h_{\text{up}}+(1-\sigma)h_{\text{dn}}]+(1-\sigma)\frac{\partial h_{\text{up}}}{\partial z}+\sigma\frac{\partial h_{\text{dn}}}{\partial z} \\
&= \frac{\partial}{\partial z}\bar{h}-\sigma\frac{\partial h_{\text{up}}}{\partial z}-(1-\sigma)\frac{\partial h_{\text{dn}}}{\partial z}+(1-\sigma)\frac{\partial h_{\text{up}}}{\partial z}+\sigma\frac{\partial h_{\text{dn}}}{\partial z}-(h_{\text{up}}-h_{\text{dn}})\frac{\partial\sigma}{\partial z} \\
&= \frac{\partial}{\partial z}\bar{h}+(1-2\sigma)\frac{\partial}{\partial z}(h_{\text{up}}-h_{\text{dn}})-(h_{\text{up}}-h_{\text{dn}})\frac{\partial\sigma}{\partial z} \quad .
\end{aligned} \tag{3.78}$$

The factor of $\frac{\partial}{\partial z}\bar{h}$ which has emerged here will give us the gradient production term. We also need:

$$
\begin{aligned}
& m\sigma(1-\sigma)\frac{(h_{\mathrm{up}}-h_{\mathrm{dn}})}{2}\frac{\partial}{\partial z}[(1-2\sigma)(w_{\mathrm{up}}-w_{\mathrm{dn}})^2] \\
&= m\sigma(1-\sigma)(1-2\sigma)(h_{\mathrm{up}}-h_{\mathrm{dn}})(w_{\mathrm{up}}-w_{\mathrm{dn}})\frac{\partial}{\partial z}(w_{\mathrm{up}}-w_{\mathrm{dn}}) \\
&\quad -m\sigma(1-\sigma)(w_{\mathrm{up}}-w_{\mathrm{dn}})^2(h_{\mathrm{up}}-h_{\mathrm{dn}})\frac{\partial\sigma}{\partial z} \\
&= M_{\mathrm{c}}(h_{\mathrm{up}}-h_{\mathrm{dn}})\left[(1-2\sigma)\frac{\partial}{\partial z}(w_{\mathrm{up}}-w_{\mathrm{dn}})-(w_{\mathrm{up}}-w_{\mathrm{dn}})\frac{\partial\sigma}{\partial z}\right] \quad .
\end{aligned}
\tag{3.79}
$$

Substitution of (3.78) and (3.79) into (3.77) gives

$$
\begin{aligned}
& \frac{\partial}{\partial t}m\sigma(1-\sigma)(w_{\mathrm{up}}-w_{\mathrm{dn}})(h_{\mathrm{up}}-h_{\mathrm{dn}}) \\
&= -(E+D)(w_{\mathrm{up}}-w_{\mathrm{dn}})(h_{\mathrm{up}}-h_{\mathrm{dn}}) \\
&\quad -M_{\mathrm{c}}(h_{\mathrm{up}}-h_{\mathrm{dn}})\left[(1-2\sigma)\frac{\partial}{\partial z}(w_{\mathrm{up}}-w_{\mathrm{dn}})-(w_{\mathrm{up}}-w_{\mathrm{dn}})\frac{\partial\sigma}{\partial z}\right] \\
&\quad -(w_{\mathrm{up}}-w_{\mathrm{dn}})(h_{\mathrm{up}}-h_{\mathrm{dn}})(1-2\sigma)\frac{\partial M_{\mathrm{c}}}{\partial z} \\
&\quad -M_{\mathrm{c}}(w_{\mathrm{up}}-w_{\mathrm{dn}})\left[\frac{\partial}{\partial z}\bar{h}+(1-2\sigma)\frac{\partial}{\partial z}(h_{\mathrm{up}}-h_{\mathrm{dn}})-(h_{\mathrm{up}}-h_{\mathrm{dn}})\frac{\partial\sigma}{\partial z}\right] \\
&\quad +m\sigma(1-\sigma)(h_{\mathrm{up}}-h_{\mathrm{dn}})[(S_w)_{\mathrm{up}}-(S_w)_{\mathrm{dn}}] \\
&\quad +M_{\mathrm{c}}[(S_h)_{\mathrm{up}}-(S_h)_{\mathrm{dn}}] \quad .
\end{aligned}
\tag{3.80}
$$

Collecting terms, we obtain

$$
\begin{aligned}
&\frac{\partial}{\partial t} m\sigma(1-\sigma)(w_{\mathrm{up}}-w_{\mathrm{dn}})(h_{\mathrm{up}}-h_{\mathrm{dn}}) \\
&\quad = -(E+D)(w_{\mathrm{up}}-w_{\mathrm{dn}})(h_{\mathrm{up}}-h_{\mathrm{dn}}) \\
&-\frac{\partial}{\partial z}(1-2\sigma)(w_{\mathrm{up}}-w_{\mathrm{dn}})M_{\mathrm{c}}(h_{\mathrm{up}}-h_{\mathrm{dn}}) \\
&\quad -M_{\mathrm{c}}(w_{\mathrm{up}}-w_{\mathrm{dn}})\frac{\partial}{\partial z}\bar{h} \\
&+m\sigma(1-\sigma)(h_{\mathrm{up}}-h_{\mathrm{dn}})[(S_w)_{\mathrm{up}}-(S_w)_{\mathrm{dn}}] \\
&\quad +M_{\mathrm{c}}[(S_h)_{\mathrm{up}}-(S_h)_{\mathrm{dn}}] \quad .
\end{aligned}
\tag{3.81}
$$

Here we see both the transport term and the gradient production term. The very last term is the one which represents the effects of sources and sinks of h (such as subplume mixing discussed in Section III-I) on the flux. The second-last term, which involves sources and sinks of the vertical velocity, contributes the important buoyancy term of the flux equation. It also represents the effects on the flux of the subplume mixing of the vertical velocity. The latter effects are probably negligible. Both of these "source" terms also represent the pressure effects.

Finally, to complete the discussion of second moment terms, I show the ADHOC equation for the variance, $\overline{h'^2}$,

$$
\begin{aligned}
&\frac{\partial}{\partial t} m\sigma(1-\sigma)(h_{\mathrm{up}}-h_{\mathrm{dn}})^2 \\
&\quad = -(E+D)(h_{\mathrm{up}}-h_{\mathrm{dn}})^2 \\
&-\frac{\partial}{\partial z}[M_{\mathrm{c}}(1-2\sigma)(h_{\mathrm{up}}-h_{\mathrm{dn}})^2] \\
&\quad -M_{\mathrm{c}}(h_{\mathrm{up}}-h_{\mathrm{dn}})\frac{\partial}{\partial z}\bar{h} \\
&\quad +2M_{\mathrm{c}}[(S_h)_{\mathrm{up}}-(S_h)_{\mathrm{dn}}] \quad .
\end{aligned}
\tag{3.82}
$$

However, it is important to note that this equation is not explicitly used in ADHOC [In ADHOC, I diagnose $\overline{h'^2}$ using the RSM formulas (see Section III-A)]. In other words, in ADHOC, Eq. 3.82 will be implicitly satisfied provided that the source terms of (3.81) and (3.70) are consistently formulated. However, this does not include the pressure terms [which are contained in the source terms of (3.81) and (3.70)] because they are not included in thermodynamic variance equations, such as Eq. 3.82.

Finally, I work out the equation for the third moment of the vertical velocity:

$$\begin{aligned}\frac{\partial}{\partial t}[\sigma(1-\sigma)(1-2\sigma)(w_{\mathrm{up}}-w_{\mathrm{dn}})^3] &= (w_{\mathrm{up}}-w_{\mathrm{dn}})^3[6\sigma^2-6\sigma+1]\frac{\partial\sigma}{\partial t}\\ &+3\sigma(1-\sigma)(1-2\sigma)(w_{\mathrm{up}}-w_{\mathrm{dn}})^2\frac{\partial}{\partial t}(w_{\mathrm{up}}-w_{\mathrm{dn}})\end{aligned} \tag{3.83}$$

$$\begin{aligned}\frac{\partial}{\partial t}[\sigma(1-\sigma)(1-2\sigma)(w_{\mathrm{up}}-w_{\mathrm{dn}})^3] &= (w_{\mathrm{up}}-w_{\mathrm{dn}})^3[6\sigma^2-6\sigma+1]\frac{\partial\sigma}{\partial t}\\ &+3\sigma(1-\sigma)(1-2\sigma)(w_{\mathrm{up}}-w_{\mathrm{dn}})^2\frac{\partial}{\partial t}(w_{\mathrm{up}}-w_{\mathrm{dn}})\\ &= (w_{\mathrm{up}}-w_{\mathrm{dn}})^3[6\sigma^2-6\sigma+1]\left[\left(\frac{E-D}{m}\right)-\frac{1}{m}\frac{\partial M_{\mathrm{c}}}{\partial z}\right]\\ &-\frac{3\sigma(1-\sigma)(1-2\sigma)(w_{\mathrm{up}}-w_{\mathrm{dn}})^3}{m}\left(\frac{E}{\sigma}+\frac{D}{1-\sigma}\right)\\ &-\frac{3}{2}\sigma(1-\sigma)(1-2\sigma)(w_{\mathrm{up}}-w_{\mathrm{dn}})^2\frac{\partial}{\partial z}[w_{\mathrm{up}}{}^2-w_{\mathrm{dn}}{}^2]\\ &+3\sigma(1-\sigma)(1-2\sigma)(w_{\mathrm{up}}-w_{\mathrm{dn}})^2[(S_w)_{\mathrm{up}}-(S_w)_{\mathrm{dn}}]\ .\end{aligned} \tag{3.84}$$

Collecting terms, multiplying through by m, using the definition of M_c, and using (3.71), we obtain

$$
\begin{aligned}
&\frac{\partial}{\partial t}[m\sigma(1-\sigma)(1-2\sigma)(w_{\mathrm{up}}-w_{\mathrm{dn}})^3] \\
&\quad = (w_{\mathrm{up}}-w_{\mathrm{dn}})^3 E\left[3\left(\sigma-\frac{1}{2}\right)-\frac{1}{2}\right] \\
&\quad + (w_{\mathrm{up}}-w_{\mathrm{dn}})^3 D\left[3\left(\sigma-\frac{1}{2}\right)+\frac{1}{2}\right] \\
&-(w_{\mathrm{up}}-w_{\mathrm{dn}})^3[6\sigma^2-6\sigma+1]\frac{\partial}{\partial z}[m\sigma(1-\sigma)(w_{\mathrm{up}}-w_{\mathrm{dn}})] \\
&-\frac{3}{2}m\sigma(1-\sigma)(1-2\sigma)(w_{\mathrm{up}}-w_{\mathrm{dn}})^2\frac{\partial}{\partial z}[(1-2\sigma)(w_{\mathrm{up}}-w_{\mathrm{dn}})^2] \\
&\quad + 3(1-2\sigma)M_{\mathrm{c}}(w_{\mathrm{up}}-w_{\mathrm{dn}})[(S_w)_{\mathrm{up}}-(S_w)_{\mathrm{dn}}] \ .
\end{aligned}
\tag{3.85}
$$

Here something new and different happens with the entrainment and detrainment terms. Such new behavior is not too surprising because we know that entrainment and detrainment modify σ directly, and that $[m\sigma(1-\sigma)(1-2\sigma)(w_{\mathrm{up}}-w_{\mathrm{dn}})^3]$ is closely related to σ. As Fig. 8 shows,

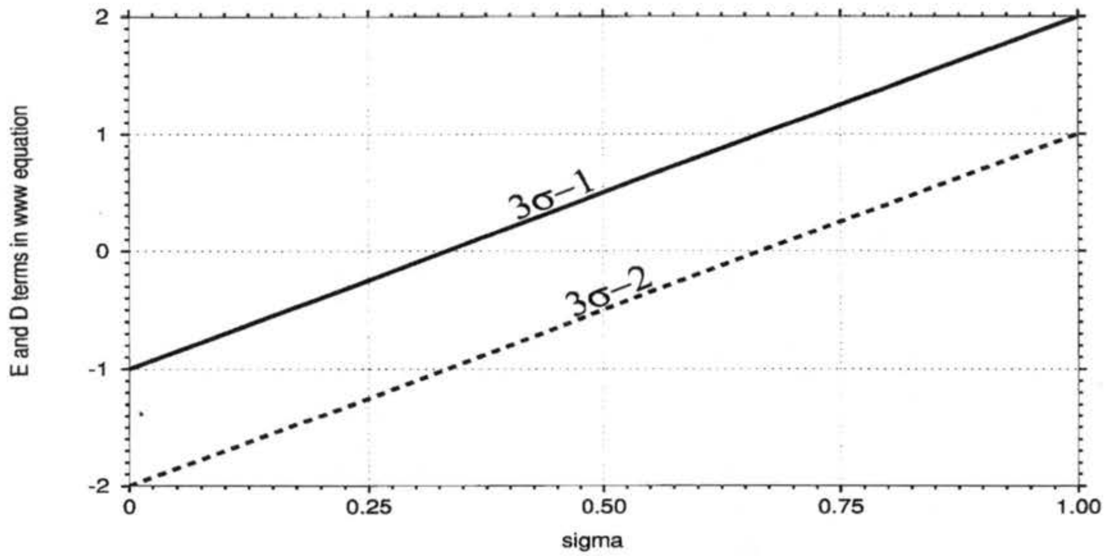

Figure 8: The horizontal axis is sigma. The upper and lower slanting lines are plots of 3σ - 1 and 3σ -2, respectively.

mass exchange in either direction tends to increase $[m\sigma(1-\sigma)(1-2\sigma)(w_{\mathrm{up}}-w_{\mathrm{dn}})^3]$ if $\sigma > \frac{2}{3}$. This means that when $[m\sigma(1-\sigma)(1-2\sigma)(w_{\mathrm{up}}-w_{\mathrm{dn}})^3]$ becomes sufficiently negative to produce large σ, the mass exchange terms will act to damp $[m\sigma(1-\sigma)(1-2\sigma)(w_{\mathrm{up}}-w_{\mathrm{dn}})^3]$ back towards zero. Similarly, mass exchange in either direction tends to decrease $[m\sigma(1-\sigma)(1-2\sigma)(w_{\mathrm{up}}-w_{\mathrm{dn}})^3]$ if $\sigma < \frac{1}{3}$. This means that when $[m\sigma(1-\sigma)(1-2\sigma)(w_{\mathrm{up}}-w_{\mathrm{dn}})^3]$ becomes sufficiently positive to produce small values of σ, mass exchange in either direction tends to damp $[m\sigma(1-\sigma)(1-2\sigma)(w_{\mathrm{up}}-w_{\mathrm{dn}})^3]$ back towards zero. The mass exchange terms do, therefore, act somewhat like dissipation terms in the equation for the third moment of the vertical velocity.

In order for the standard HOC and the ADHOC equations for $\overline{w'w'w'}$ to be consistent, the terms on the third and fourth lines of the right-hand side of (3.85) must combine to make the two terms in the $\overline{w'w'w'}$ standard HOC equation that involve vertical derivatives:

$$\frac{\partial}{\partial t}m\overline{w'w'w'} \sim -\frac{\partial}{\partial z}m\overline{w'w'w'w'} + 3\overline{w'w'}\frac{\partial}{\partial z}m\overline{w'w'} \ . \tag{3.86}$$

These are transport and gradient-production terms, respectively. We can show that

$$\begin{aligned} m\overline{w'w'w'w'} &= m[\sigma(w_{\mathrm{up}}-\overline{w})^4 + (1-\sigma)(w_{\mathrm{dn}}-\overline{w})^4] = \\ &m\sigma(1-\sigma)[1-3\sigma+3\sigma^2](w_{\mathrm{up}}-w_{\mathrm{dn}})^4 \ . \end{aligned} \tag{3.87}$$

From (3.87), it follows that

$$\frac{\partial}{\partial z} m\overline{w'w'w'w'} = \frac{\partial}{\partial z} m[\sigma(w_{\mathrm{up}} - \overline{w})^4 + (1-\sigma)(w_{\mathrm{dn}} - \overline{w})^4] = \tag{3.88}$$

$$m(w_{\mathrm{up}} - w_{\mathrm{dn}})^4[-12\sigma^3 + 18\sigma^2 - 8\sigma + 1]\frac{\partial\sigma}{\partial z} +$$

$$m(w_{\mathrm{up}} - w_{\mathrm{dn}})^3 4\sigma(1-\sigma)[3\sigma^2 - 3\sigma + 1]\frac{\partial}{\partial z}(w_{\mathrm{up}} - w_{\mathrm{dn}}) +$$

$$\sigma(1-\sigma)[1 - 3\sigma + 3\sigma^2](w_{\mathrm{up}} - w_{\mathrm{dn}})^4\frac{\partial m}{\partial z} \quad .$$

We can also show that

$$3\overline{w'w'}\frac{\partial}{\partial z} m\overline{w'w'} = 6m\sigma^2(1-\sigma)^2(w_{\mathrm{up}} - w_{\mathrm{dn}})^3\frac{\partial}{\partial z}(w_{\mathrm{up}} - w_{\mathrm{dn}}) \tag{3.89}$$

$$+ 3m\sigma(1-\sigma)(1-2\sigma)(w_{\mathrm{up}} - w_{\mathrm{dn}})^4\frac{\partial\sigma}{\partial z} +$$

$$3\sigma^2(1-\sigma)^2(w_{up} - w_{dn})^4\frac{\partial m}{\partial z} \quad .$$

If we add the negative of (3.88) to (3.89), we get

$$-\frac{\partial}{\partial z}m\overline{w'w'w'w'} + 3\overline{w'w'}\frac{\partial}{\partial z}m\overline{w'w'} = \tag{3.90}$$

$$-m(w_{up}-w_{dn})^4[-12\sigma^3+18\sigma^2-8\sigma+1]\frac{\partial\sigma}{\partial z}$$

$$-m(w_{up}-w_{dn})^3 4\sigma(1-\sigma)[3\sigma^2-3\sigma+1]\frac{\partial}{\partial z}(w_{up}-w_{dn})$$

$$-\sigma(1-\sigma)[1-3\sigma+3\sigma^2](w_{up}-w_{dn})^4\frac{\partial m}{\partial z}$$

$$+6m\sigma^2(1-\sigma)^2(w_{up}-w_{dn})^3\frac{\partial}{\partial z}(w_{up}-w_{dn})$$

$$+3m\sigma(1-\sigma)(1-2\sigma)(w_{up}-w_{dn})^4\frac{\partial\sigma}{\partial z}$$

$$+3\sigma^2(1-\sigma)^2(w_{up}-w_{dn})^4\frac{\partial m}{\partial z} =$$

$$-m(w_{up}-w_{dn})^4[(1-2\sigma)(1-6\sigma+6\sigma^2)]\frac{\partial\sigma}{\partial z}$$

$$-m(w_{up}-w_{dn})^3 4\sigma(1-\sigma)[3\sigma^2-3\sigma+1]\frac{\partial}{\partial z}(w_{up}-w_{dn})$$

$$-\sigma(1-\sigma)[1-3\sigma+3\sigma^2](w_{up}-w_{dn})^4\frac{\partial m}{\partial z}$$

$$+6m\sigma^2(1-\sigma)^2(w_{up}-w_{dn})^3\frac{\partial}{\partial z}(w_{up}-w_{dn})$$

$$+3m\sigma(1-\sigma)(1-2\sigma)(w_{up}-w_{dn})^4\frac{\partial\sigma}{\partial z}$$

$$+3\sigma^2(1-\sigma)^2(w_{up}-w_{dn})^4\frac{\partial m}{\partial z}$$

$$= -m(w_{up}-w_{dn})^4(1-2\sigma)\{[6\sigma^2-6\sigma+1]-3\sigma(1-\sigma)\}\frac{\partial\sigma}{\partial z}$$

$$-m(w_{up}-w_{dn})^3\sigma(1-\sigma)\{[6\sigma^2-6\sigma+1]+3(1-2\sigma)^2\}\frac{\partial}{\partial z}(w_{up}-w_{dn})$$

$$-\sigma(1-\sigma)[6\sigma^2-6\sigma+1](w_{up}-w_{dn})^4\frac{\partial m}{\partial z}.$$

To check whether this form emerges from (3.85), we expand the relevant terms of (3.85), as follows:

$$
\begin{aligned}
&-(w_{up}-w_{dn})^3[6\sigma^2-6\sigma+1]\frac{\partial}{\partial z}[m\sigma(1-\sigma)(w_{up}-w_{dn})] \\
&-\frac{3}{2}m\sigma(1-\sigma)(1-2\sigma)(w_{up}-w_{dn})^2\frac{\partial}{\partial z}[(1-2\sigma)(w_{up}-w_{dn})^2] \\
&= -m(w_{up}-w_{dn})^4(1-2\sigma)[6\sigma^2-6\sigma+1]\frac{\partial\sigma}{\partial z} \\
&-m(w_{up}-w_{dn})^3\sigma(1-\sigma)[6\sigma^2-6\sigma+1]\frac{\partial}{\partial z}(w_{up}-w_{dn}) \\
&-\sigma(1-\sigma)[6\sigma^2-6\sigma+1](w_{up}-w_{dn})^4\frac{\partial m}{\partial z} \\
&+3m(w_{up}-w_{dn})^4\sigma(1-\sigma)(1-2\sigma)\frac{\partial\sigma}{\partial z} \\
&-3m(w_{up}-w_{dn})^3\sigma(1-\sigma)(1-2\sigma)\frac{\partial}{\partial z}(w_{up}-w_{dn}) \\
&= -m(w_{up}-w_{dn})^4(1-2\sigma)\{[6\sigma^2-6\sigma+1]-3\sigma(1-\sigma)\}\frac{\partial\sigma}{\partial z} \\
&-m(w_{up}-w_{dn})^3\sigma(1-\sigma)\{[6\sigma^2-6\sigma+1]+3(1-2\sigma)^2\}\frac{\partial}{\partial z}(w_{up}-w_{dn}) \\
&-\sigma(1-\sigma)[6\sigma^2-6\sigma+1](w_{up}-w_{dn})^4\frac{\partial m}{\partial z}\ .
\end{aligned}
\tag{3.91}
$$

Inspection shows that (3.90) and (3.91) match exactly, and thus the third and fourth lines on the right-hand side of (3.85) correspond exactly to the terms in (3.86).

So, up to this point, there are two main insights from this analysis. First, the entrainment and detrainment terms act as dissipation in the second-moment equations, but they act rather differently in the equation for the third moment of the vertical velocity. Second, the SPS fluxes will contribute a term in the prediction equations for the large-eddy fluxes. This term is probably quite important, especially when clouds are present. In Sections III-G-III-I, I will explain in detail how ADHOC handles these terms. In the next section, I will examine the ADHOC equations derived here [using an analysis similar to that of RSM (see Section III-A)] and show how they specifically encompass both HOC and MFC within a single framework.

III-F: Limiting cases of the ADHOC equations

To derive the ADHOC equations in the last section, I used took known budget equations for updraft and downdraft quantities (e.g., Eqs. 3.15-3.16), and from them, derived prognostic equations for higher-moment statistics written in terms of the mass-flux formulas of RSM (Section III-A). I then showed that these equations are exactly consistent with those of "conventional" HOC equations. Thus, the ADHOC equations derived in Section III-E should encompass the information contained in both HOC and MFC. The purpose of this section is to demonstrate that this is true.

I start by examining two limiting cases; $\sigma = 1/2$ and $\sigma << 1$. It is logical to wonder what happens in the ADHOC equations as σ approaches either of these limits. In the former case ($\sigma = 1/2$), the mean vertical motion is weak and local transport dominates. Thus, local assumptions (like diffusion) should work well. Is ADHOC capable of representing this? In the latter case ($\sigma << 1$), we approach the limit of deep cumulus convection. Do the ADHOC formulations reduce to known cumulus parameterizations (e.g., Arakawa and Schubert, 1974) in this limiting case? Answering these questions can help us evaluate the limitations of the approach. Below, I will answer these questions and show that ADHOC is capable of representing both of these situations.

To explain this, I consider some limiting cases of the variance equation (Eq. 3.82) written in the "mass-flux framework"

$$\frac{\partial}{\partial t}\overline{h'^2} = -2\frac{M_c(h_{up}-h_{dn})}{m}\frac{\partial}{\partial z}\bar{h} - \frac{1}{m}\frac{\partial}{\partial z}[M_c(1-2\sigma)(h_{up}-h_{dn})^2] - (E+D)(h_{up}-h_{dn})^2 \quad (3.92)$$

Assuming a quasi-steady state and using Eq. 3.3 and the relationship

$$
(h_{up} - h_{dn})^2 = \left(\frac{\overline{w'h'}}{M_c}\right)^2 , \tag{3.93}
$$

we can rewrite (3.92) as

$$
0 = -2\frac{\overline{w'h'}}{m}\frac{\partial}{\partial z}\bar{h} - \frac{1}{m}\frac{\partial}{\partial z}[M_c(1-2\sigma)(h_{up}-h_{dn})^2] - (E+D)\left(\frac{\overline{w'h'}}{M_c}\right)^2 . \tag{3.94}
$$

In the case of $\sigma = 1/2$, I would expect non-local transport (see footnote, page 9; Fig. 3) processes to be unimportant and for down-gradient diffusion to apply. Setting $\sigma = 1/2$ in (3.94), the middle term drops out and we can solve for the flux $\overline{w'h'}$:

$$
m\overline{w'h'} = \frac{-2M_c^2}{E+D}\frac{\partial}{\partial z}\bar{h} . \tag{3.95}
$$

This describes down-gradient diffusion in which the effective eddy diffusivity is represented by

$$
K_{eff} = \frac{2M_c^2}{E+D} . \tag{3.96}
$$

From this exercise, we see that when σ approaches 1/2, the non-local transport term (third-moment) drops out and the remaining terms describe local diffusion, similar to that of a higher-order closure model. Thus, the mass-flux model is able to represent situations in which non-local effects play no role.

It is interesting to note here that more than three decades ago, Deardorff (1966) came to this same conclusion that I did above. He performed this same analysis with the HOC variance equation for the potential temperature, θ. Her determined that, when the triple-correlation transport term is small, and there is nearly steady state conditions, one can solve for the heat flux in terms of the remaining molecular dissipation and radiation term. The conclusion he reached for this situation was that the heat flux is directed down the gradient. Here, I reach the same conclusion, but narrow down the specifics under which it occurs (i.e., I specify that the triple correlation term is equal to zero when $\sigma = 1/2$).

The another limiting case I discussed is that of deep cumulus convection ($\sigma << 1$). To examine this situation, we rewrite (3.94) using (3.93) and the equilibrium assumption

$$-2\overline{w'h'}\frac{\partial}{\partial z}\bar{h} - \frac{1}{m}\frac{\partial}{\partial z}\left[\frac{\overline{w'h'}^2}{M_c}(1-2\sigma)\right] - (E+D)\left(\frac{\overline{w'h'}}{M_c}\right)^2 = 0 . \tag{3.97}$$

In the limit $\sigma << 1$, $1 - 2\sigma \approx 1$. Using this in (3.97), and expanding out the middle term, we get

$$-2\overline{w'h'}\frac{\partial}{\partial z}\bar{h} - \left(\frac{2\overline{w'h'}}{M_c}\right)\frac{\partial}{\partial z}\overline{w'h'} + \left(\frac{\overline{w'h'}}{M_c}\right)^2\frac{\partial M_c}{\partial z} - (E+D)\left(\frac{\overline{w'h'}}{M_c}\right)^2 = 0 . \tag{3.98}$$

Equation (3.98) can be simplified further using the steady state version of 3.67,

$$\frac{\partial M_c}{\partial z} = E - D . \tag{3.99}$$

Using (3.99) in (3.98), we get

$$-2\overline{w'h'}\frac{\partial}{\partial z}\bar{h} - 2\left(\frac{\overline{w'h'}}{M_c}\right)\frac{\partial}{\partial z}\overline{w'h'} - 2D\left(\frac{\overline{w'h'}}{M_c}\right)^2 . \tag{3.100}$$

Here we see that the terms involving E cancel out of the equation. This result means that the total area-averaged $\bar{h}$ (or any other area-weighted mean thermodynamic quantity) does not depend on the lateral mass flow into the updraft. This same result is found in cumulus convection parameterizations (e.g., Arakawa and Schubert, 1974; AS74) and is a result of the fact that air coming into the updraft has the thermodynamic properties of the environmental (non-updraft) air. In the limit of $\sigma << 1$, $\bar{h}$ is very close to the value of h in the environment. Thus, entraining air which contains the environmental value of h into the updraft is roughly equivalent to entraining $\bar{h}$ into the updraft; and entraining $\bar{h}$ into the updraft will not change $\bar{h}$.

Multiplying (3.100) by $-\frac{M_c}{2\overline{w'h'}}$ and solving for $\frac{\partial}{\partial z}\overline{w'h'}$, we get

$$\frac{\partial}{\partial z}\overline{w'h'} = -M_c\frac{\partial}{\partial z}\bar{h} - D(h_{up} - h_{down}) \ . \tag{3.101}$$

Equation 3.101 is quite well-known in the field of cumulus parameterization. The first term represents the effects of "compensating subsidence". It acts to warm and dry the environmental air. The second term describes the effect of cloud detrainment on the environment. It is especially important near cloud top. This same equation was derived by AS74.

We see that the ADHOC framework is able to span quite nicely the limiting cases of "local transport only" ($\sigma = 1/2$) and "non-local transport only" ($\sigma << 1$). The fact that the theory does not break down in these limiting cases illustrates the versatility of the approach, and opens the door to a unified PBL-cumulus model.

It is of interest to note that, using a very different approach, Wyngaard and Weil (1991) obtained a result similar to (3.94). Their Eq. (36) can be written as

$$\frac{\partial}{\partial z}\overline{C} = -\frac{\overline{c'w'}}{K} - \left(\frac{S\sigma_w T_L}{2K}\right)\frac{\partial}{\partial z}\overline{c'w'} \; ; \tag{3.102}$$

where C is a passive, conservative scalar, K is the eddy diffusivity, S is the skewness of the vertical velocity, $\sigma_w = \left(\overline{w'^2}\right)^{1/2}$, and T_L is the Lagrangian integral time scale. This equation contains three terms which are proportional to (in order from left to right) the gradient of the mean scalar, the scalar flux itself, and the scalar-flux divergence. If the last term is negligible, we obtain the down-gradient diffusion formula,

$$\overline{c'w'} = -K\frac{\partial}{\partial z}\overline{C} \; . \tag{3.103}$$

This is analogous to my Eq. 3.95, for the limiting case of $\sigma = 1/2$. If the middle term in (3.102) is negligible, we get

$$\frac{\partial}{\partial z}\overline{c'w'} = -\left(\frac{2K}{S\sigma_w T_L}\right)\frac{\partial}{\partial z}\overline{C} \; . \tag{3.104}$$

This is similar to my Eq. 3.101 (without the detrainment term), for the limiting case of $\sigma << 1$.

III-G: Parameterizations of Lateral Mass Exchanges

A key to accurate simulations with ADHOC is a proper representation of the effects of lateral mixing on the properties of the plume. In ADHOC, the lateral mixing terms are represented by the E and D terms in the mass continuity equations (Eqs. 3.23-3.24). In the last section, I showed that these terms are related to the dissipation terms in the higher-moment equations (Eqs. 3.72, 3.81, and 3.85). In this section, I review previous attempts to parameterize these terms and then describe a new technique that I have developed for use in ADHOC.

III-G-1: Review of previous lateral mass exchange parameterizations

Stommel (1947) was the first to note that cumulus clouds had to be significantly diluted by air from above cloud base in order to explain their internal temperature and liquid water contents (i.e., they had to laterally mix with or "entrain" environmental air). To my knowledge, the earliest documented attempt to parameterize this lateral mass exchange between updrafts and downdrafts (or updrafts and environment) was by Batchelor (1954). He proposed that the lateral mixing velocities between updraft and downdraft are proportional to the updraft velocity. This was followed by the works of Morton (1957), Squire and Turner (1962), and Scorer (1957). Entrainment in these models was represented by empirical laws based on laboratory experiments. All have the essential features that air in the cloud at certain levels comes solely from that level or below. However, Warner (1970, 1971) demonstrated a fundamental problem with this type of model. In particular, he showed that these models could not simultaneously predict the liquid water content and cloud top height of small, non-precipitating cumulus clouds (Raymond and Blyth, 1986; RB86).

Another early concept of cumulus cloud evolution was discussed by Squire (1958). He showed that parcels of dry air, engulfed by a cumulus cloud near cloud top, could descend a considerable distance through a cloud by entraining dry air, which evaporates and cools. This provided an alternative view of dilution in cumulus clouds; vertical mixing. Twenty years later, Telford (1975) and Raymond (1979) designed conceptual models which incorporated this concept. In contrast to the lateral entrainment models, these vertical mixing models assume that air is incorporated into the cloud at cloud top and cloud base, and subsequently moves vertically to its level of neutral buoyancy, where it exits the cloud. The success of these models led to the concept of "buoyancy sorting" first described by RB86.

"Buoyancy sorting" conceptually evolved from the fact that convective updrafts were observed to reach their level of neutral buoyancy as defined by their undiluted ascent (Warner, 1970; Heymsfield et al., 1978; Raymond and Wilkening, 1985). It was proposed that a high degree of intermittent motion, known to occur in higher Reynolds number flows (such as that in cumulus clouds), was responsible for this observation (if turbulence was intermittent in clouds, then perhaps some of the parcels would make it to their level of neutral buoyancy without mixing). If true, cloud top would be defined by those parcels lucky to ascend without a mixing event (RB86). This suggested that mixing takes place as a series of discrete events, rather than in a continuous manner.

RB86 generalized the conceptual model of Telford (1975) to include this concept. In the Telford (1975) model, environmental air was only allowed to enter the cloud at cloud top. In RB86, this was extended to include mixing events at all elevations. They assumed that parcels of low-level air reach a variety of heights before they mix with their environment. The heights at which mixing occurs is uniformly distributed between low levels and the level of undilute neutral buoyancy. The subparcels originating at low levels can mix with their environment in varying proportions at each level. For each proportion, the newly mixed subparcel moves to its level of neutral buoyancy (with respect to the environment) and exits the cloud (i.e., detrainment occurs). This proposed mechanism became known as "buoyancy sorting". In a "buoyancy sorting" model, entrainment events produce locally well-mixed regions of different compositions than the main cloud mass, each of which ascends or descends to their level of neutral buoyancy before being detrained. This model has been further refined and generalized in later studies (e.g., Taylor and Baker, 1991; Kain and Fritsch, 1990).

While many of these models provided the framework for our understanding of the entrainment and detrainment process, these models were not specifically mass-flux models. Mass-flux models used many of these concepts, but developed "mass-flux specific" parameterizations for the entrainment an detrainment events in cumulus clouds. To my knowledge, all current models that use mass-flux formulations for convection parameterize the lateral mixing terms as proportional to the convective mass flux (Turner, 1973; Simpson, 1971):

$$E = \varepsilon M_c \text{ and } D = \delta M_c, \tag{3.105}$$

where

$$\varepsilon = \frac{0.2}{R_{up}} \tag{3.106}$$

and R_{up} is the radius of the updraft (Simpson et. al., 1965; Simpson and Wiggert, 1969), and δ is parameterized differently depending on the model (the parameterization of δ is discussed below).

The schemes most often employed by GCMs are those proposed by Tiedtke (1989; T89), Arakawa and Schubert (1974; AS74), and Gregory and Rowntree (1990; GR90). Entrainment and detrainment schemes in cumulus convection are all based on the work of Arakawa (1969) and many of them are rooted in the ideas put forth by AS74. AS74 assumed that R_{up} is constant with height in a Lagrangian sense, but they did not assume that the cloud is a column-like steady jet as is done in Simpson et. al., 1965. Instead, they assumed that the fractional rate of entrainment (ε in this discussion; λ in AS74) for the *time-averaged* mass flux of a cloud is approximately constant with height. Clouds are assumed to detrain only at their level of neutral buoyancy. In order to satisfy mass continuity, massive detrainment must occur at this level (the cloud mass flux must drop discontinuously to zero there). The idea of detrainment at the level of neutral buoyancy is very similar to the ideas put forth by Bougeault and André (1986) (and used in ADHOC) in which the parameterized dissipation of higher moments is inversely proportional to the neutral buoyancy height of rising (or sinking) parcels (see Section III-G-2b).

Another interesting analogy between ADHOC and AS74 is the relationship between the "assumed distribution" in ADHOC and the fractional entrainment rate (λ) in AS74. AS74 defined different cloud "types" in terms of the level at which the clouds reach their neutral buoyancy and detrain. These cloud "types" were defined in terms of a single parameter, λ, which was called the fractional entrainment rate. Clouds with large λ grew to only low altitudes, while those with small λ were able to reach much higher heights. In this manner, λ determined the "cloud type". Different "cloud types" implicitly represented updrafts of varying strength. This is analogous to ADHOC as follows: if a more realistic PDF is assumed (instead of the tophat PDF currently used), then the PDF would allow for multiple classes of updrafts (i.e., a realistic PDF would contain cumulus clouds of all different strengths along with a slow, broad downdraft). Thus, the "assumed distribution" part of ADHOC is related to the fractional entrainment rate of AS74. However, with the current version of ADHOC, the "assumed distribution" is a tophat PDF (i.e., only one "cloud type" is represented by this distribution).

In T89, E and D are broken down into two parts; a part that includes turbulent exchange of mass along the cloud edges and a part that accounts for organized inflow and outflow at the cloud base and the cloud top respectively. The lateral mass exchange along the cloud edges is represented in Eq. (3.105) with ε and δ parameterized as in Eq. (3.106). In T89, he assumed values for R_{up} and determined that $\varepsilon = \delta = 10^{-4}$ m^{-1} for penetrative and mid-level convection and $\varepsilon = \delta = 3x10^{-4}$ m^{-1} for shallow convection. He also added an "enhancement" factor to increase the lateral mixing within 150 mb of cloud base. The T89 scheme is currently used in the ECMWF model as well as the GCMs at the Max-Planck-Institut für Meteorologie (MPI) in Madrid and at the Bureau of Meteorology Research Centre (BMRC) in Melbourne, Australia. GR90, used in the United Kingdom Meteorological Office (UKMO) GCM, is a scheme similar to T89 with the exception that δ is taken to be $1/3\ \varepsilon$.

Recently, Siebesma and Cuijpers (1995; SC95) and Siebesma and Holtslag (1996; SH96) used LES (Section IV-A-1) to derive profiles of E and D as residuals terms in the ADHOC equations. They did this for shallow cumulus observations collected during the Barbados Oceanographic and Meteorological Experiment (BOMEX). Surprisingly, they discovered that the values for ε and δ used in the above schemes were an order of magnitude too small. In addition, they found that $\delta > \varepsilon$ for a wide range of sensitivity studies. The ranges that they found were $\varepsilon \sim 1.5 - 2.5x10^{-3}$ m^{-1} and $\delta \sim 2.5 - 3.0x10^{-3}$ m^{-1}. In BOMEX, they found that mass-flux schemes which employed T89 (or something similar) were too active.

The physical implications of the modified values of ε and δ are as follows: In T89 and GR90, both the relatively slow lateral mixing and the assumption of equal entrainment and detrainment rates imply a need for large inversion-base detrainment (mass continuity). Both the greater lateral mixing and the larger values of δ implied by SC95 and SH96 facilitate more lateral mass exchange *between* cloud base and the inversion base, and thus require little or no need for massive detrainment at the inversion base. In this way, the inversion is not excessively moistened and cooled by cloud convection. This seems reasonable for shallow cumuli because many shallow clouds do not reach the inversion at all; thus, they should completely detrain before arriving there. In summary, SH96 argue that previous values of ε and δ may be valid for penetrative and mid-level convection, but the larger distribution of cloud types in the category of shallow convection prohibit the use of a single updraft radius to describe them (Eq. 3.106).

In the next section, I describe a new method for determining E and D, which is implemented in ADHOC. Using the ADHOC results from BOMEX (see Section II-D-2b), I compare the SC95 formulas (Eq. 3.105 with the new values of ε and δ) to those I that I obtain using the new approach (Fig. 11).

III-G-2: Parameterization of lateral mass exchange terms in ADHOC

As discussed earlier, a key to using ADHOC in a practical application is to parameterize the lateral mixing (or dissipation) terms, E and D. In ADHOC, the situation is significantly more complex than in previous mass-flux models. This is due to the additional complications that arise from the occurrence of E and D in higher-moment equations and the differing forms that they take in the second- and third-moment equations. Prior attempts to models these terms never dealt with this issue for the simple reasons that previous plume models did not make use of higher-order prognostic equations and that lateral mass exchange terms do not explicitly appear in the ensemble-averaged equations of HOC models. Thus, the new challenge here is to come up with a parameterization for E and D that is physically realistic for both the second- and third-order moment equations.

III-G-2a: Relating Dissipation Time Scales

One simple approach to this problem is to assume that the dissipation time scale for the second moments is proportional to that for the third moments. In doing this, we can obtain two equations ($\overline{w'w'}$ and $\overline{w'w'w'}$) and two unknowns (E and D) as follows: We refer to (3.72) and equate the E and D terms to the dissipation of the $\overline{w'w'}$ as it would appear in the HOC equations, giving

$$-\left(\frac{E+D}{m}\right) = \frac{-\sigma(1-\sigma)}{\tau_{Boug}}. \tag{3.107}$$

Here τ_{Boug} is a dissipation time scale used by Bougeault and André (1986), which is discussed in Section (III-G-2b). We do the same thing for $\overline{w'w'w'}$ (Eq. 3.85), except that we introduce an arbitrary proportionality factor, r, multiplying the dissipation time scale:

$$\frac{E}{m}(3\sigma - 2) + \frac{D}{m}(3\sigma - 1) = -r\frac{\sigma(1-\sigma)(1-2\sigma)}{\tau_{Boug}} . \tag{3.108}$$

Solving (3.107) for $\frac{D}{m}$ and substituting this into (3.108), we obtain the following solutions for E and D:

$$\frac{E}{m} = \frac{\sigma(1-\sigma)}{\tau_{Boug}}[(3\sigma - 1) + r(1 - 2\sigma)] , \tag{3.109}$$

$$\frac{D}{m} = \frac{\sigma(1-\sigma)}{\tau_{Boug}}\{1 - [(3\sigma - 1) + r(1 - 2\sigma)]\} . \tag{3.110}$$

Subtracting (3.110) from (3.109), we form an expression for $E - D$:

$$\frac{E-D}{m} = \frac{\sigma(1-\sigma)}{\tau_{Boug}}(1-2\sigma)(2r - 3) . \tag{3.111}$$

By definition, E and D must be positive. Thus, we need to choose a value for r that meets this condition. In addition, we must choose r so as not to restrict σ. Thus, the value of r that we choose must insure that E and D are positive in the range $0 < \sigma < 1$. What possible values of r meet these conditions? From (3.109), $E > 0$ implies that $\sigma(3 - 2r) > -(r - 1)$. This implies

$$\sigma > \frac{(1-r)}{3-2r} \quad \text{for } r < 3/2 \tag{3.112}$$

and

$$\sigma < \frac{(r-1)}{2r-3} \quad \text{for } r > 3/2. \tag{3.113}$$

For $r = 3/2$, we get $E = D$. This would be analogous to $\varepsilon = \delta$ in the previous discussion, which SC95 showed to be invalid, especially for shallow cumulus convection.

In order to have $0 \le \sigma \le 1$, (3.112) implies that $\frac{1-r}{3-2r} \le 0$ and (3.113) implies that $\frac{r-1}{2r-3} \ge 1$. The first of these conditions is true for all $r \ge 1$, and the second is true for all $r \le 2$. If we repeat this analysis using (3.110) and the assumption that $D > 0$, we find the same restrictions on the value of r. In conclusion, in order to insure that both σ has no restrictions and that D and E are positive, we must choose a value for r in the range

$$1 \le r \le 2 . \tag{3.114}$$

Let's examine what happens if we let $r = 1$. This implies equal time scales for the dissipation of $\overline{w'w'}$ and $\overline{w'w'w'}$. Equations (3.109)-(3.111) become

$$\frac{E}{m} = \frac{\sigma^2(1-\sigma)}{\tau_{Boug}} , \tag{3.115}$$

$$\frac{D}{m} = \frac{\sigma(1-\sigma)^2}{\tau_{Boug}} , \tag{3.116}$$

and

$$\frac{E-D}{m} = \frac{\sigma(1-\sigma)}{\tau_{Boug}}(2\sigma - 1) . \tag{3.117}$$

Equation (3.117), along with (3.67), implies that, in time, narrow updrafts become even narrower and broad updrafts become even broader. In order to see this more clearly, suppose that σ is less than 1/2. In this case, $E-D$ will be negative (Eq. 3.111). Using Eq. (3.67), we see that this implies that σ will decrease with time. Thus, if the updraft is already narrow ($\sigma < 1/2$), it will become even narrower. By a similar line of reasoning, if σ is initially greater than 1/2, the already broad updraft will become even broader. This tendency to push σ towards 0 or 1 seems inappropriate for the lateral mass exchange terms, which we expect to be dissipative in character. we therefore reject $r = 1$. This simple argument indicates that second and third moment turbulence statistics do not dissipate on the same time scale (i.e., $r > 1$).

At the other extreme, we try setting $r = 2$ in Eqs. (3.109)-(3.111). This gives

$$\frac{E}{m} = \frac{\sigma(1-\sigma)^2}{\tau_{Boug}}, \tag{3.118}$$

$$\frac{D}{m} = \frac{\sigma^2(1-\sigma)}{\tau_{Boug}}, \tag{3.119}$$

and

$$\frac{E-D}{m} = \frac{\sigma(1-\sigma)}{\tau_{Boug}}(1-2\sigma). \tag{3.120}$$

Equation (3.120), along with (3.67), implies that, in time, narrow updrafts become broad and broad updrafts become narrow; the opposite of what we got when we assumed equal time scales ($r = 1$). This very "safe" solution always acts to push σ toward 1/2. The choice $r = 2$ acts in the exact manner that I seek; it keeps the solution stable and insures that E and D are always positive. Thus, I choose $r = 2$ as the ratio of the second- to third-moment dissipation time scales.

III-G-2b: The Modified Bougeault Length Scale

In order to fully implement ADHOC, I still need to take this one step further. The parameterization of dissipation has been a weakness of HOC models since their inception. As reviewed earlier, everything from prognostic length scale or dissipation schemes to diagnostic regimes such as that proposed by Bougeault and André (1986; BA86) have been used with varying degrees of success. To fully implement ADHOC as the equations stand, I try a new idea for E and D. It is formulated specifically so that E will be large near the ground and that D will be large near the inversion (Fig. 9).

Before I discuss this idea, it is important for two reasons to briefly review the length scale closure proposed by BA86. First, Bougeault and André's approach is the most widely used formulation in turbulence models today, and second, it provides a nice framework with which to compare the parameterization I propose. In BA86, they argued that there are two dissipation length scales: one for upward moving parcels and one for downward moving parcels. In order to take into account the reduction of the mixing length by the effects of the inversion and the lower boundary, they chose to use a harmonic average of the two to obtain one dissipation mixing length that could be used to dissipate all turbulent moments:

$$\frac{1}{L} = \frac{1}{2}\left(\frac{1}{L_{up}} + \frac{1}{L_{down}}\right) = \frac{1}{2}\frac{(L_{up} + L_{down})}{L_{up}L_{down}} , \tag{3.121}$$

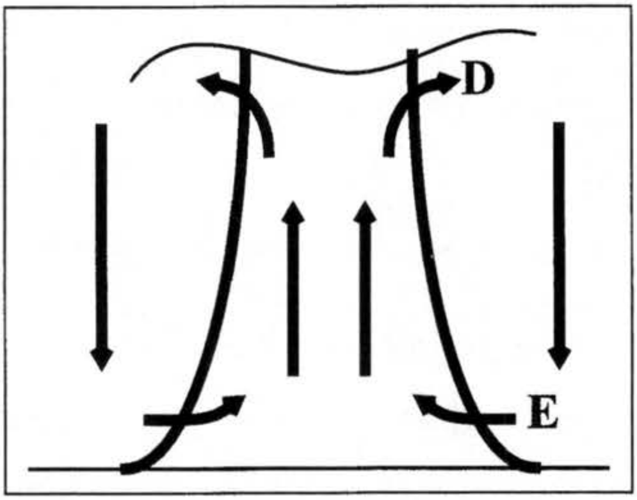

Figure 9: Diagram of an updraft with E and D identified. From this figure, we see that we want E to be large near the ground and D to be large near the top of the boundary layer.

where L_{up} is defined in (1.22), and L_{down} is defined in (1.23). In BA86, the dissipation timescale is diagnosed by dividing this length scale by the square root of the TKE,

$$\tau_{Boug} = \frac{L}{\sqrt{e}} . \tag{3.122}$$

Equations (1.22) and (1.23) say that a parcel with a given amount of TKE will move upward or downward in an environment of a given stability as far as it can before its energy runs out. Of course, the distance it can move is bounded by the surface and the model top. For a complete discussion of this parameterization, see Section II-C-3.

If we look at Fig. 9, we can draw an analogy with the BA86 parameterization. We would like to make E and D as big as possible near the ground and the inversion, respectively, to accurately represent the dissipation that occurs there. Bougeault and André tried to make L_{up} small near the inversion and L_{down} small near the ground to achieve a similar goal. He did this through the use of the harmonic average in which the smallest of the two length scales has the largest effect on the total dissipation length scale.

With this analogy in mind, I make the following proposal for E and D in Eqs. 3.72 and 3.85:

$$E \sim \frac{M_c}{L_{down}} = \frac{m}{\tau_{Boug}} \text{ and } D \sim \frac{M_c}{L_{up}} = \frac{m}{\tau_{Boug}} . \tag{3.123}$$

If one considers L_{up} and L_{down} as the distances a parcel has to travel to reach its level of neutral buoyancy, then (3.123) relates the entrainment and detrainment of parcels traveling in a cloud to their level of neutral buoyancy. The only other paper (to my knowledge) to directly discuss this relationship is that of Lin and Arakawa (1997a,b).

I use a slightly modified version of Eqs. 1.22-1.23 to determine L_{up} and L_{down}; I replace s_v with $s_{v_{up}}$ in (1.22) and $s_{v_{dn}}$ in (1.23) so that the upward (downward) length scale is determined using the updraft (downdraft) sounding instead of the mean state sounding.

Substituting (3.123) into (3.118) and (3.119), and substituting the results of this into (3.72) and (3.85), we get

$$\frac{\partial}{\partial t}\overline{w'w'} \sim -\overline{w'w'}\left(\frac{M_c}{m}\right)\left(\frac{(1-\sigma)L_{up} + \sigma L_{down}}{L_{up}L_{down}}\right), \tag{3.124}$$

$$\frac{\partial}{\partial t}\overline{w'w'w'} \sim \frac{-(w_{\mathrm{up}} - w_{\mathrm{dn}})^3}{m}\left[\sigma(1-\sigma)M_c\left(\frac{(1-\sigma)(2-3\sigma)}{L_{down}} + \sigma\frac{(1-3\sigma)}{L_{up}}\right)\right]. \tag{3.125}$$

We see that (3.124) is similar to the formulation of BA86 except that the velocity scale of importance is $\frac{M_c}{m}$ instead of $\sqrt{e}$. Equation (3.125) is interesting. We see that an increase in the mass-flux (M_c) or a decrease in either turbulent length scale (L_{up} or L_{down}) will increase the rate of dissipation of $\overline{w'w'w'}$. This is how a dissipation parameterization should behave. However, we have a fourth degree σ polynomial in (3.125) which complicates things.

Thus, we need to examine how the "σ part" of this parameterization will effect the overall dissipation of $\overline{w'w'w'}$. It turns out that the complex σ polynomials in (3.125) also act to dissipate $\overline{w'w'w'}$. Since M_c, L_{up}, and L_{down} are all positive, the signs of the σ polynomials will determine the ultimate sign of the this dissipation term. These polynomials are shown in Fig. 10. When $\overline{w'w'w'}$ is large and positive, σ is small (convective regime; see Eq. 3.7), and the complex σ polynomial in both the first and the second term of (3.125) (the E and D terms respectively) are positive. This, combined with the negative sign in front of the dissipation term (and the fact that M_c and the length scales are positive) that will act to decrease $\overline{w'w'w'}$. This is true for all $\sigma < 1/3$. On the other hand, when $\overline{w'w'w'}$ is large and negative (large σ), both of the σ polynomials in (3.125) are negative, tending to increase $\overline{w'w'w'}$ (toward zero). This is true for all $\sigma > 2/3$. In the case where $\overline{w'w'w'}$ is exactly zero ($\sigma = 1/2$), we see that the σ polynomials in (3.125) are opposite sign and will partially (if not completely) cancel. The degree of cancellation of course depends on the relative values of L_{up} and L_{down}. When $\sigma = 1/2$ ($\overline{w'w'w'} = 0$) and $L_{up} = L_{down}$, then the two terms in (3.125) exactly cancel. In this case, we would not expect there to be any dissipation since $\overline{w'w'w'}$ is already zero.

At values in the range $1/3 < \sigma < 2/3$, it is a little less clear whether this parameterization truly acts as a dissipation term. Let's examine this in more detail: If $1/3 < \sigma < 1/2$, we would expect narrow updrafts and a positive $\overline{w'w'w'}$, implying that near the ground, $L_{up} > L_{down}$. If this is the case, then (3.125) says that the second σ term will have the larger effect; the second σ polynomial is that associated with E and the E curve in Fig. 10 is positive in this range. This, along with the negative sign in (3.125), implies that the right-hand side of (3.125) is negative; thus, the positive $\overline{w'w'w'}$ will be dissipated. A similar argument can be used for the range $1/2 < \sigma < 2/3$. Based on this discussion, it appears as if the parameterization shown in Eq. 3.125 will generally act in a manner consistent with its "goal" of dissipating $\overline{w'w'w'}$.

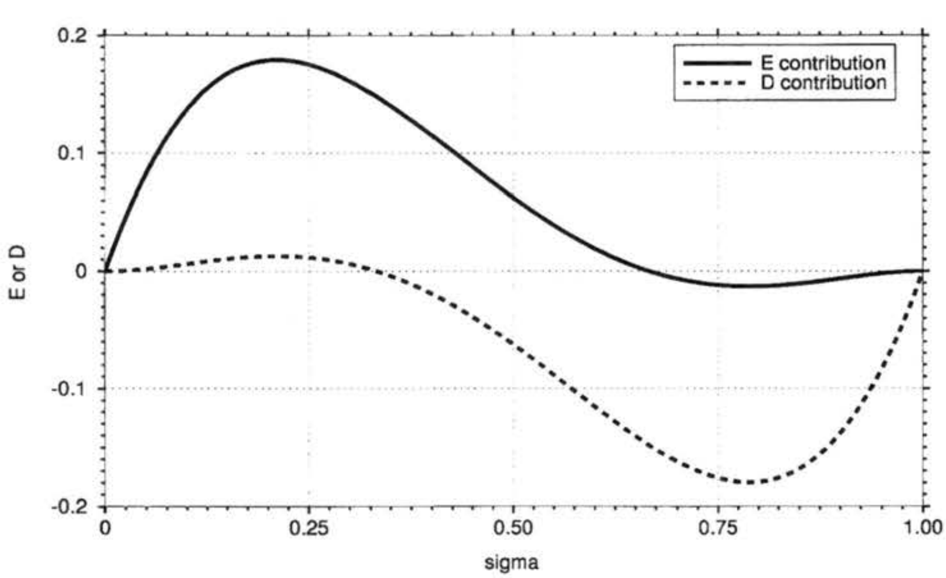

Figure 10: The effect of the sigma polynomials in Eq. 3.125. These plots isolate the effect of the "sigma part" of the E and D terms in the www tendency.

It is clear that this new parameterization for E and D is very different than those discussed in Section III-G-1. Fig. 11 shows the simulated profiles for E and D, along with those computed by ADHOC using the SC95 formulas (Eq. 3.105 with $\varepsilon \sim 1.5 - 2.5x10^{-3}$ m^{-1} and $\delta \sim 2.5 - 3.0x10^{-3}$ m^{-1}). The values calculated (from BOMEX observations) by Esbensen (1978) are also indicated. In general, The SC95 and the ADHOC formulas produce profiles for the lateral mass exchanges which are similar in shape within the cloudy region. However, there are some obvious differences; namely, the SC95 values of E and D are larger than those of ADHOC and they do not affect the region below cloud base.

In ADHOC, mass is exchanged between the updraft and downdraft at all levels, while in SC95, the entrainment and detrainment parameterizations are most active within the cloud. Figure 11 shows that, with the ADHOC parameterization, mass leaves the updraft in the lower part of the boundary layer (large E), while little mass gets recirculated in (small D); with the SC95 parameterization, no updraft mass is lost in this region. Thus, as the "ADHOC" updraft enters the cloudy region, it does not need to detrain mass as quickly as the "SC95" updraft.

The ADHOC formulation has the advantage that it applies to all turbulent masses, whether or not an organized updraft or clouds are present. The SC95 formulas are empirical relationships that were specifically designed for shallow cumulus convection. The difference is subtle but significant; in ADHOC, E and D are not truly "entrainment" and "detrainment" in the "classic" cumulus-parameterization sense; they represent mass flow across the edge of a turbulent mass rather than mass flux across an updraft edge. In the case of shallow cumulus convection, these two regions coincide; however, the ADHOC formulas can be applied even if this is not the case.

Finally, it should be mentioned that the observed values of E and D do not agree with the ADHOC output for either parameterization. It is difficult to compare observed values to those simulated by a model using a highly idealized representation of the observed values (see Section IV-C-2a for a description of the GCSS BOMEX case). We can make some qualitative statements here, however. The observations (which are only for the cloudy regions) show that the entrainment is largest near cloud base and taper to zero by cloud top. The ADHOC parameterization also shows a relative maximum near cloud base which decreases toward cloud top. In addition, both the observed detrainment and the ADHOC detrainment show an increase near cloud top. The BOMEX case, along with some of these issues will be discussed further in Section IV-C-2a.

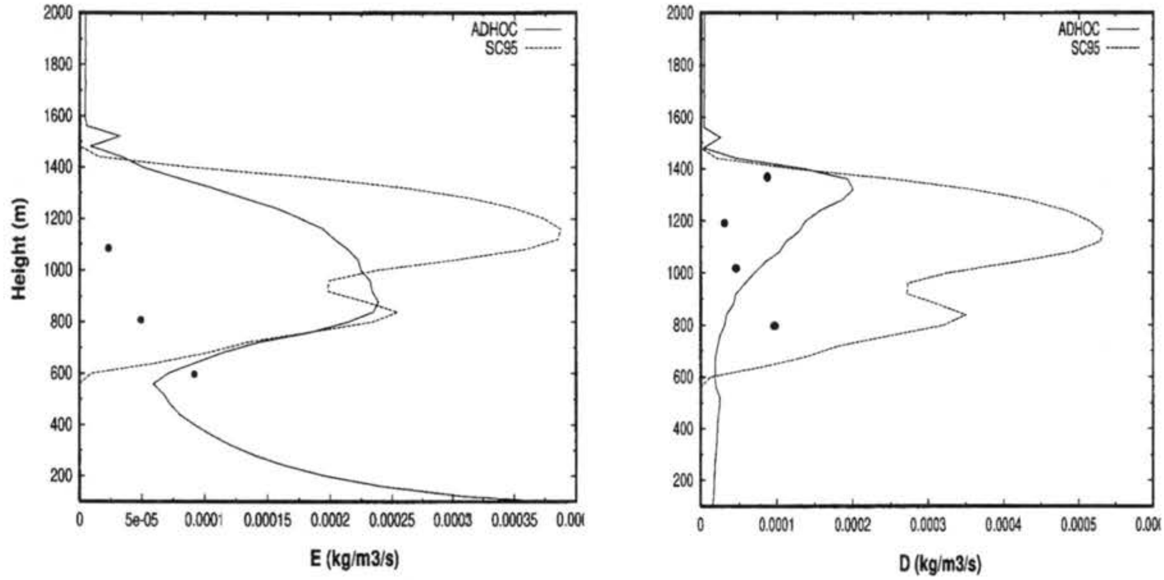

Figure 11: Comparison between the ADHOC and SC95 formulas for the lateral mass exchange terms in the BOMEX simulation. Left: E; Right: D. The dots represent the results of Esbensen (1978) based on BOMEX observations.

III-H: The pressure terms

The pressure terms are one of the most challenging aspects of combining MFC and HOC. Part of this difficulty stems from the huge difference in how these terms have previously been dealt with in each of these closures. The pressure term parameterizations have always been an integral part of HOC models (with the exception of first- order closure models for obvious reasons). On the other hand, in mass-flux models, few have even considered these terms. Thus, in ADHOC, I have a unique challenge to try and make the current HOC pressure parameterizations consistent with the mass-flux model.

In a "standard" HOC model, there are two aspects of the pressure terms to consider; the "slow" part and the "rapid" part (see Section II-C-1). One can see this clearly by examining the Poisson equation that results from taking the divergence of the perturbation velocity equation (Eq. 1.6). The Poisson equation shows that there are three turbulence interactions which can effect the perturbation pressure field; turbulence-turbulence, mean shear-turbulence, and buoyancy-turbulence. In HOC models, all three of these effects are typically parameterized.

However, the pressure terms, which are an integral part of HOC, played little role in previous mass-flux parameterizations. In fact, the only mass flux models to include the pressure effect were from the 1960s (Simpson and Wiggert, 1969; Simpson, 1965). In these papers, a "virtual mass coefficient" was used to reduce the buoyancy in the w_{up} equation. While it was not explicitly stated that the "virtual mass coefficient" was pressure-related, the only thing which can counter the buoyancy term is a pressure gradient force acting on the updraft.

Only two other papers (to my knowledge) address the role of pressure in a mass-flux model, Zhang and Cho (1991a,b) and Wu and Yanai (1994). In the former study, they assumed a specific form for the cloud-kinematic field to obtain the perturbation pressure field. They did not discuss the effects of the cloud-scale pressure field on the parameterization in physical terms. In the latter study, Wu and Yanai assume that the convective-scale pressure perturbations arise from shear-updraft interactions and they formulate a cumulus momentum transport parameterization which includes the convective-scale pressure-gradient force. This pressure-gradient force is related to the vertical wind shear, the cloud mass flux, and the orientation of organized convection. In view of the Poisson equation (Eq. 1.6), Wu and Yanai addressed only the pressure field induced by shear-turbulence interactions (i.e., they did not include the turbulence-turbulence and the buoyancy-turbulence interactions).

In unifying MFC and HOC, with their inherently different methods for dealing with pressure, I face a unique challenge. The pressure effect in the ADHOC equations enters through the vertical velocity "source" terms (e.g., $(S_w)_{\mathrm{up}} - (S_w)_{\mathrm{dn}}$ in Eq. 3.60). In the current version of the model, I use the "standard" HOC parameterizations discussed in Section II-C-1; for the $\overline{u'u'}$, $\overline{v'v'}$, and $\overline{w'w'}$ equations, I use the exact form of (1.7), with l calculated according to Bougeault and André, 1986 (see Section III-G). In the flux equations, I neglect all terms in (1.7) except the first term, which represents the "slow", "return-to-isotropy" part of the effect. This use of this form is understandable if one considers that a vector quantity (such as a flux) is only isotropic if it has zero magnitude. The resulting form used in the ADHOC flux equations is

$$\frac{\partial}{\partial t}\overline{w'x'} = -C\frac{q}{l}\overline{w'x'} \ , \tag{3.126}$$

where x is any variable, $C = 4.85$ for thermodynamic fluxes, and $C = 4.5$ for momentum fluxes. In the $\overline{w'w'w'}$ equation, I use the same form as (3.126) with $C = 6.5$.

Using a "purely" HOC approach in this unified model is not the best choice. With such an approach, the pressure terms in the ADHOC equations cannot be consistent with the mass-flux decomposition (used for all other terms). The task of developing an "ADHOC-consistent" parameterization for the pressure terms is critical for complete unification of MFC and HOC. This fact will become even more clear in Chapter IV, where many of the results exhibit problems in regions where the pressure effects are important (e.g., near the surface and near the inversion). In light of the results in that chapter, a possible approach to modeling these terms in the spirit of ADHOC is proposed in Appendix B. The future direction of this model will undoubtedly be to implement such a scheme and completely unify the last piece of these two closures.

III-I: The subplume-scale terms

Large eddy simulation (LES) models resolve the large eddies and parameterize the small eddies with a subgrid-scale (SGS) scheme (see Section IV-A-1; Deardorff, 1972; Moeng, 1984). The ensemble-averaged statistics in conventional HOC models are *supposed* to represent all scales and thus, have no need for a parameterization of the effects of smaller-scale eddies. Mass-flux models applied to the PBL have typically been used in conjunction with a mixed-layer model (e.g., Wang and Albrecht, 1986) and thus have not been concerned with the small-scale flow.

However, it has been found by Businger and Oncley (1990) for the surface layer and by Young (1988a), Schumann and Moeng (1991), Wyngaard and Moeng (1992), and de Laat and Duynkerke (1998) for the convective boundary layer that the "tophat" contribution to a flux is approximately 60% of the total flux. A theoretical estimate of this contribution, given by Wyngaard and Moeng (1992), is 64% when a Gaussian joint probability density function is assumed between the vertical velocity and any scalar. With an LES model, Siebesma and Cuijpers (1995) showed that large errors occur if the total flux of a quantity is parameterized solely with a tophat decomposition (Eq. 3.3). They determined that, in order to accurately represent the total flux, subplume-scale effects must be considered. Thus, mass-flux models, which use this breakdown and do not include an additional subplume-scale contribution, produce results that have errors. (Note, that these errors may not be in the fluxes themselves but may be manifested in the other properties of the updraft and downdrafts).

In a recent study by Petersen et al. (1999), it was shown that mass-flux schemes for the convective boundary layer are sensitive to the parameterization of the parts of the total flux that are not resolved explicitly by the mass-flux formulas (i.e., the "subplume-scale" fluxes). Petersen et al. (1999) ran several tests with different mass-flux schemes in "stand alone" mode (in which they prescribed the boundary-layer height, updraft area fraction, and convective mass flux) and compared the results to LES models. They concluded that the best performance is obtained with mass-flux schemes that are nearly identical to the exact plume-budget equations. In addition, they showed that, in order to accurately model the lateral mass exchange terms, one must account for gross exchanges between the updrafts and downdrafts (something which I explicitly do in ADHOC; see Section III-G). This study clearly shows that the subplume-scale contributions must be included if one hopes to accurately model the convective PBL with a mass-flux model. Despite all this evidence, Petersen et al. (1999) were the first (to my knowledge) to include subplume-scale effects into a mass-flux model. This current study includes these effects as well, with the exception that the boundary layer height, updraft area fraction, and convective mass flux do not need to be prescribed (RSM provides us with a method to diagnose these quantities from the predicted statistics of the flow (see Section III-A).

In ADHOC, there is a need to include the SPS effects. Using the ADHOC approach, I combine in one set of equations a MFC (an inherently large-eddy scheme) with a HOC model. In order to combine these two approaches so that the equations are consistent scale-wise, there is a need to add small eddy (subplume-scale) motions to the mass-flux equations to obtain realistic results in regions where the motions are inherently small (e.g., near the surface and the inversion; see Fig. 13). What first drew my attention to this fact was the inability of ADHOC to accurately simulate the Willis-Deardorff laboratory convection experiment (WD; Willis and Deardorff, 1974; Section IV-B-1). In these simulations, I found that entrainment near the inversion and mixing near the surface were both too weak; both are regions where small-scale motions dominate. Figure 12 shows the simulated heat flux of WD with and without the implementation of an SPS scheme. At the base of the inversion, the entrainment increases with the use of the SPS scheme. The heat-flux results with the SPS scheme are more representative of those observed (Willis and Deardorff, 1974), as well as those simulated by Large Eddy Simulations (Section IV-A-1; Moeng and Wyngaard, 1989). In addition, the effect of a SPS scheme is also found to be substantial near the surface, where it helps insure that the temperature below the inversion is well-mixed (not shown).

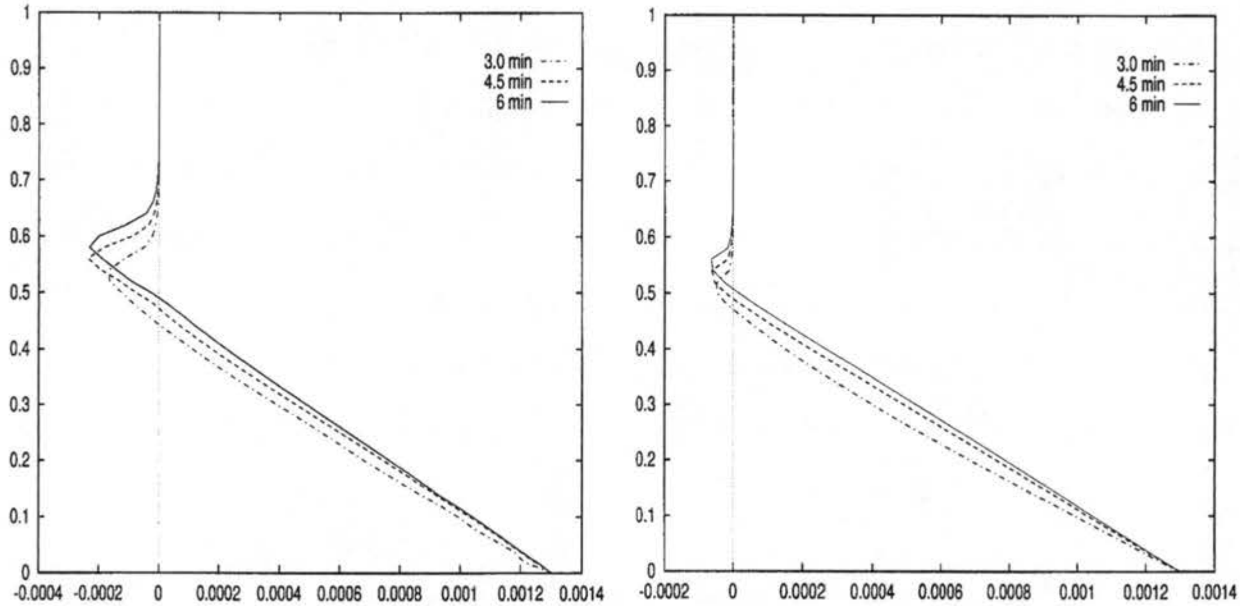

Figure 12: Evolution of the heat flux at 3, 4.5, and 6 minutes into the simulation. Left: subplume-scale (SPS) scheme included; Right: no SPS scheme included. The entrainment is more effective and closer in value to LES and observations with the SGS scheme included. The SPS scheme benefits the near-surface mixing of the temperature as well (not shown).

While the above argument for an SPS scheme is qualitative, the ADHOC equations (derived in Sections III-B to Section III-E) provide some quantitative justification. For example, we see in Eqs. (3.19) (for $\bar{h}$) and (3.81) (for $\overline{w'h'}$) terms that represents the sources and sinks of h such as

$$\frac{\partial}{\partial t} m\bar{h} \sim m\overline{(S_h)} \tag{3.127}$$

and

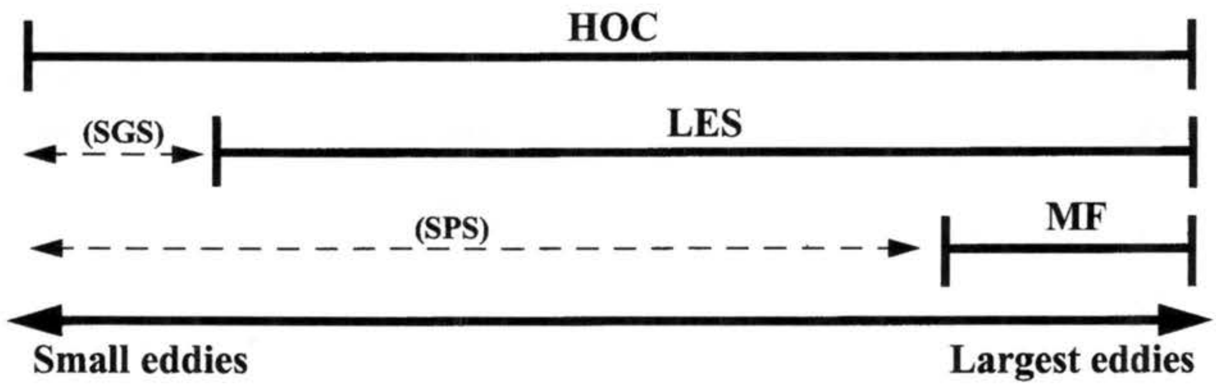

Figure 13: Graphical interpretation of the relevant scales in HOC, LES and mass-flux models (MF). In order to cover all scales of motion, LES models include the smallest scales through the use of a SGS parameterization. In the ADHOC MF model, I need to include a wider range of scales. This is done with the use of a SPS model.

$$\frac{\partial}{\partial t}\overline{w'h'} \sim M_{\mathrm{c}}[(S_h)_{\mathrm{up}} - (S_h)_{\mathrm{dn}}] \ . \tag{3.128}$$

In (3.127), $\overline{(S_h)}$ represents (among other things) the divergence of the SPS flux. In (3.128), $\overline{(S_h)}$ includes the SPS contribution to the flux $\overline{w'h'}$. I can write these contributions as

$$\frac{\partial}{\partial t}m\bar{h} \sim -\frac{\partial}{\partial z}(m\overline{w'h'}_{sps}) \tag{3.129}$$

If we assume that these SPS fluxes are down-gradient, we can write

$$\frac{\partial}{\partial t}\overline{w'h'} \sim M_{\mathrm{c}}\left[\frac{\partial}{\partial z}\left(K_h\frac{\partial\overline{w'h'}_{sps}}{\partial z}\right)_{up} - \frac{\partial}{\partial z}\left(K_h\frac{\partial\overline{w'h'}_{sps}}{\partial z}\right)_{dn}\right] , \tag{3.130}$$

where the subscript "sps" represents the subplume-scale terms; the subscript "up" ("dn") denotes an updraft (downdraft) quantity; and K_h is the SPS eddy diffusivity for heat (which is different for the updraft and downdraft). It is important to note that the *total* SPS eddy flux appears in the mean state equation, while the updraft and downdraft SPS fluxes appear separately in the second-moment equation. Thus, while the symbol $\overline{w'h'}_{sgs}$ appears three times in the above equations, it represents a different quantity each time, as indicated by the subscripts.

I model the SPS terms in ADHOC in a slightly different manner than LES models. The reason is that the ADHOC equations separately require the updraft and downdraft components of the SPS fluxes. I thus use a modified version of the SPS turbulence energy model proposed by Deardorff (1980);

$$\frac{\partial \bar{e}_{sps}}{\partial t} = -\overline{w'u'}_{sps}\frac{\partial U}{\partial z} - \overline{w'v'}_{sps}\frac{\partial V}{\partial z} + \frac{g}{C_p T_0}\overline{w's_v'}_{sps} - \frac{\partial}{\partial z}\overline{[w'(e_{sps} + p'/\rho_0)]} - \varepsilon_{sps} + \varepsilon_{ls} \quad . \quad (3.131)$$

Here, e_{sgs} is the SPS turbulent kinetic energy (TKE); U and V are the mean wind components; p is the pressure; ρ_0 is a reference density; ε_{sgs} is the SPS TKE dissipation; and, ε_{ls} is the large-scale dissipation rate.

In using (3.131), I make two major modifications to the Deardorff (1980) formulation. First, I call the routine *twice* in each timestep; once for the updraft and once for the downdraft. By separating the SPS TKE and fluxes into the updraft and downdrafts, I more accurately represent regions of partial cloudiness (e.g., shallow cumuli) by allowing the SPS turbulence to be stronger in the cloudy updrafts and weaker in the clear downdrafts. Secondly, I include an additional source term, ε_{ls}; the large-scale dissipation rate. By doing this, I assume that the large-scale TKE isn't truly dissipated but merely is "removed" from the large scale. After its "removal", it cascades to the small scales where it appears as a source of SPS TKE. In this manner, I conserve energy and allow the small scale eddies to feed off the large-scale eddies. Even at the surface, where most of the energy should be SPS energy, I do not feed the surface fluxes directly into the SPS TKE. I first feed the large scale and, due to large near-surface dissipation rates, the SPS takes over rapidly.

The closure assumptions that I make to close (3.131) are the down-gradient diffusion assumption

$$[\overline{w'(e_{sps} + p'/\rho_0)}] = -2K_m \frac{\partial \bar{e}_{sps}}{\partial z} \tag{3.132}$$

and the Kolmogorov hypothesis

$$\varepsilon_{sps} = \frac{C e_{sps}^{-3/2}}{l} \tag{3.133}$$

with

$$C = 0.19 + 0.51 \frac{l}{\Delta z} \; . \tag{3.134}$$

I adjust the value of C to 3.9 at the lowest layer due to wall effects (Deardorff, 1980). In (3.134), Δz is the vertical grid spacing and l is the turbulent length scale defined as

$$l = \Delta z \tag{3.135}$$

when the stratification is unstable, and

$$l = 0.76\sqrt{\frac{\bar{e}_{sps}}{\left(\frac{g}{C_pT_0}\frac{\partial s_L}{\partial z}\right)}} \tag{3.136}$$

when the stratification is stable. In the latter case, I impose an upper limit of $l = \Delta z$. Here, s_L is the liquid water static energy defined as

$$s_L = C_pT + gz - L_v r_L, \tag{3.137}$$

where r_L is the liquid water mixing ratio and $L_v = 2.52x10^6$ J kg^{-1}.

Finally, I calculate the eddy diffusivities for momentum and heat using

$$K_m = 0.1l\sqrt{\bar{e}_{sps}} \text{ and } K_h = \left[1 + 2\frac{l}{\Delta z}\right]K_m, \tag{3.138}$$

and use these to calculate $\overline{w'u'}_{sps}$ and $\overline{w'v'}_{sps}$, using a down-gradient assumption. In order to calculate $\overline{w's_v'}_{sps}$, I first write it in terms of the fluxes of the conserved liquid water static energy, $\overline{w's_L'}_{sps}$, and total water mixing ratio, $\overline{w'r_T'}_{sps}$ (which I calculate with a down-gradient assumption). I then combine them as in Randall (1987) to determine $\overline{w's_v'}_{sps}$.

Since the calculation outlined above is done twice in any one timestep (once for the updraft and once for the downdraft), at the end of an iteration, the model has calculated l, K_m, K_h, C, $\bar{e}_{sps}$, and all the SPS fluxes for the updraft and downdrafts separately. The mean state equations (e.g., Eq. 3.129), however, require the total SPS fluxes. Thus, in order to combine the updraft and downdraft fluxes for use in the mean state equations, I use the area-weighted mass-flux formula

$$(\overline{w'x'}_{sps})_{Total} = \sigma(\overline{w'x'}_{sps})_{up} + (1-\sigma)(\overline{w'x'}_{sps})_{dn} \ . \tag{3.139}$$

Finally, in order to implement this scheme, I need to provide a method to partition the large-scale dissipation and mean winds between the updraft and downdraft in Eq. (3.131). In partitioning the dissipation and mean winds, I must ensure that the sum of the area-weighted updraft and downdraft values add up to the total. With this in mind, I choose

$$U_{up} = U_{dn} = U \tag{3.140}$$

and

$$\varepsilon_{up} = \frac{\varepsilon}{2\sigma};\ \varepsilon_{dn} = \frac{\varepsilon}{2(1-\sigma)} \ . \tag{3.141}$$

The reason for using (3.141) instead of a simpler form analogous to (3.140) is that (3.139) has the desired property of stronger (weaker) dissipation in the updraft when σ is small (big).

III-J: Momentum

The success of the RSM method in part depends on a strong correlation between the vertical velocity and the thermodynamic variable of interest (e.g., warm temperatures ($T' > 0$) and rising motion ($w' > 0$) are well-correlated in the convective boundary layer (CBL); thus, this method works well in this regime for higher-moment statistics that involve w's and T's). However, the same correlation is not always found between the vertical velocity the dynamic quantities (zonal and meridional momentum). In a convective boundary layer, mass continuity dictates that u' and

v' are largest *in between* the updraft and downdrafts (where w' is near zero) and are smallest in the centers of the updrafts and downdrafts (where w' is a maximum) (Fig. 14a) This "non-correlation" does not bode well for an accurate determination of the momentum fluxes with the RSM method. In a shear-driven boundary layer, however, the correlation between u' and w' is strong (Fig. 14b), and I may very well be able to use the mass-flux method with accurate results. The only study (which I am aware of) that tested the representation of momentum fluxes with a mass-flux decomposition was that of Khalsa and Greenhut (1985). They showed that this formulation is valid for momentum fluxes in the lower third of the marine boundary layer. However, this study is quite limited in its range of applicability and to we knowledge, has not been shown to be true in other regimes.

One could argue that, given the fact that momentum fluxes are weak (and relatively unimportant) in the convective boundary layer, the "non-correlation" is meaningless. This, combined with the fact that u' and w' are well-correlated in the shear-driven boundary layer, may indicate the RSM could still produce accurate momentum statistics. While this may be true, I have chosen to prognose the momentum fluxes (as I do the thermodynamic fluxes) but use down-gradient diffusion for the third-moment terms to close these equations. The reason why I chose this approach is the well-known fact that down-gradient diffusion can accurately describe shear-driven turbulence (Hanjalic and Launder, 1972; Donaldson, 1973).

Thus, ADHOC predicts $\overline{u'x'}$, $\overline{w'u'}$, $\overline{u'u'}$ (as well as the analogous v' moments; x represents any thermodynamic variable) using the following higher-order closure equations:

$$\frac{\partial}{\partial t}\overline{u'u'} = \frac{\partial}{\partial z}K_m\frac{\partial}{\partial z}\overline{u'u'} - 2\overline{w'u'}\frac{\partial}{\partial z}\bar{u} - \frac{2}{3}\varepsilon - \frac{C_4}{\tau}\left(\overline{u'u'} - \frac{2}{3}\varepsilon\right) + P_{sb} \ , \tag{3.142}$$

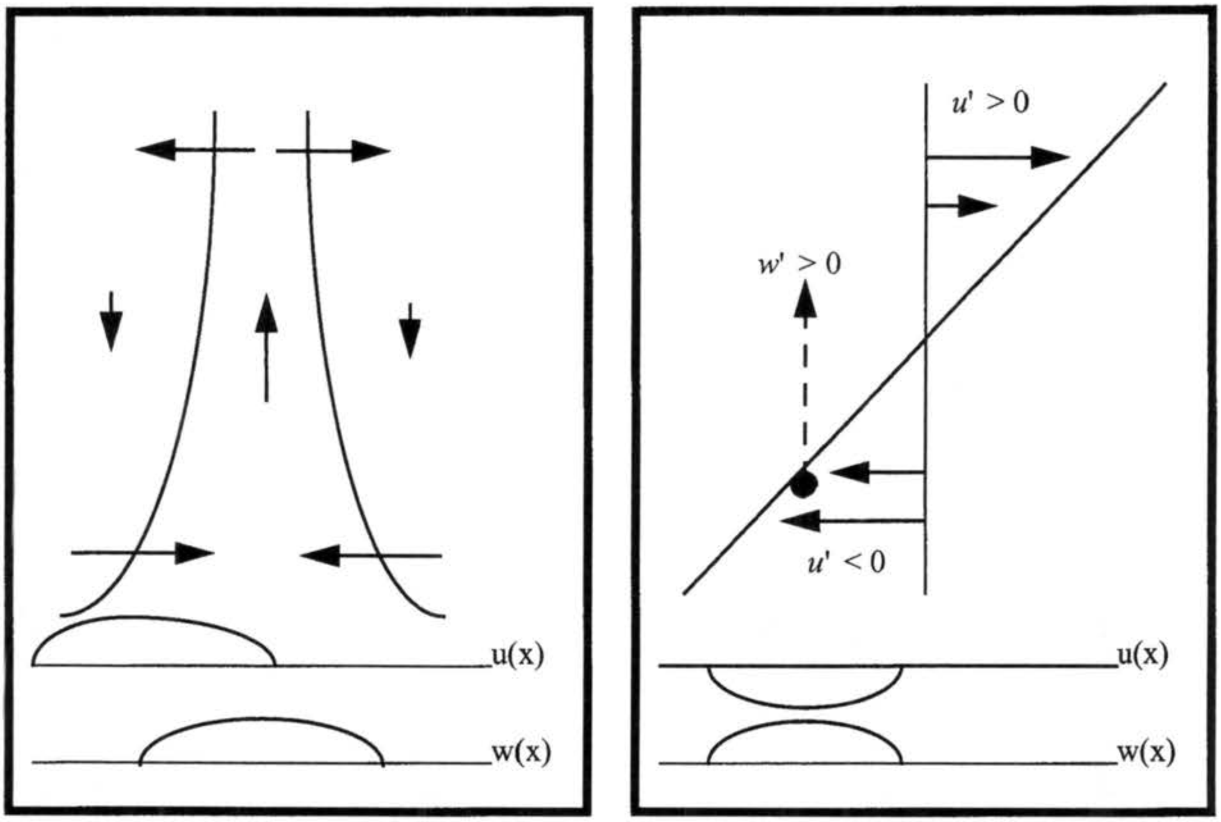

Figure 14: The correlation of w and u in (a) the convective boundary layer and (b) the shear-driven boundary layer. We see that w and u are correlated in (b) but are 90 degrees out of phase in (a).

$$\frac{\partial}{\partial t}\overline{u'x'} = \frac{\partial}{\partial z}K_h\frac{\partial}{\partial z}\overline{u'x}-\overline{w'u'}\frac{\partial}{\partial z}\bar{x}-(1-C_7)\overline{w'x'}\frac{\partial}{\partial z}\bar{u}-\frac{C_6}{\tau}\overline{u'x'} , \tag{3.143}$$

and

$$\frac{\partial}{\partial t}\overline{w'u'} = \frac{\partial}{\partial z}K_m\frac{\partial}{\partial z}\overline{w'u'}-\overline{w'^2}\frac{\partial}{\partial z}\bar{u}+\frac{g}{C_pT_v}\overline{u's_v'}-\frac{C_4}{\tau}\overline{w'u'} . \tag{3.144}$$

Here, the eddy diffusivities for momentum and heat (K_m and K_h) are calculated following Louis (1979); P_{sb} represents the pressure strain and buoyancy effects: $P_{sb} = -C_5\left(P_{uu} - \frac{2}{3}P\right) = \left(\frac{4}{3}C_5 - 2\right)\left(\overline{w'u'}\frac{\partial}{\partial z}\bar{u}\right) - \frac{2}{3}C_5\left(\overline{w'v'}\frac{\partial}{\partial z}\bar{v}\right) - \frac{2}{3}C_5\left(\frac{g}{C_p T_v}\overline{w's_v'}\right)$; $C_4 = 1.75$; $C_5 = 0.3$; $C_6 = 3.75$; $C_7 = 0.33$; ε is the large-scale dissipation rate; $\tau = l/\sqrt{e}$ where l is the Bougeault length scale (Bougeault and André, 1986; see Section II-C-3) and e is the TKE; and $\overline{u's_v'}$ is diagnosed by writing it in terms of $\overline{u's_L'}$ and $\overline{u'r_T'}$ and using the method outlined by Randall (1987).

III-K: Boundary Conditions

In ADHOC, boundary conditions are needed at the surface and at the top of the model domain. The surface fluxes are diagnosed following Louis (1979); however, I must choose which scale the surface forcing will affect, the large scale (i.e., the plume scale; PS) or the SPS. Since the eddies at the surface are inherently "small", it would be logical to put the surface forcing into the SPS. However, numerous tests show that it is not important whether the surface forcing is fed directly into the SPS or into the large scale (or is divided between the two). The model adjusts and the resulting fields are almost identical.

With the exception of the surface fluxes, I set all higher moments (large scale and SPS) to zero at the surface. In addition, at the lower boundary, I need a surface pressure (to integrate the hydrostatic equation) and a skin temperature. Thus, I prescribe a constant or time-varying surface pressure and temperature.

In the first layer above the surface, I predict all mean and second-moment quantities using the standard ADHOC equations. The third moment, $\overline{w'w'w'}$, is also predicted. However, in order to do this, I prescribe $\overline{w'w's'_v}$ in the middle of the first layer according to the surface layer similarity relationship of Moeng and Wyngaard (1989):

$$\overline{w'w's'_v} = 0.3w^* w^* s_v^* \quad \text{if} \quad \overline{w's'_{v\text{-}sfc}} > 0 \tag{3.145}$$

and

$$\overline{w'w's'_v} = 0 \ \text{if} \ \overline{w's'_{v\text{-}sfc}} < 0 \ , \tag{3.146}$$

where w^* is the convective velocity scale and $s^*{}_v = \dfrac{\overline{w's'_{v\text{-}sfc}}}{w^*}$. This is done to insure that $\overline{w'w'w'}$ is positive in the lowest layer of the convective boundary layer. I diagnose all other third moments that appear in the flux prognostic equations using a mass-flux formula analogous to Eq. 3.5. For example,

$$m\overline{w'w'h'} = m\sigma(1-\sigma)(1-2\sigma)(w_{\text{up}} - w_{\text{dn}})^2(h_{up} - h_{dn}) \ . \tag{3.147}$$

Because all of the quantities on the right-hand side of (3.147) are defined at the layer edges and the third moment is defined at the layer center (Fig. 15), I do an arithmetic average of σ, $(h_{up} - h_{dn})$, and $(w_{\text{up}} - w_{\text{dn}})$ between the surface and the top of the first layer. In doing so, I use $(w_{\text{up}} - w_{\text{dn}}) = (h_{up} - h_{dn}) = 0$ and $\sigma = 1/2$ at the surface.

At the model top, I use a "zero-divergence" condition for the second moments and set the fourth moment to zero. In addition, in order to vertically advect into the PBL properties of the free atmosphere, I prescribe either a constant or time-varying free atmospheric values for all the dynamic and thermodynamic variables. Just below the model top, in the middle of the top layer, I predict the mean state quantities as usual using the zero flux gradient condition for the transport term. Thus, the only things that affect the mean state quantities at this level are vertical and horizontal advection. I compute the third moments at this level in an analogous manner to the lowest layer. I use (3.147) and perform an arithmetic average on the quantities on the right-hand side of the equation. However, because of the "zero-divergence" flux boundary condition, the quantities $(h_{up} - h_{dn})$ and $(w_{\mathrm{up}} - w_{\mathrm{dn}})$ at the model top and in the layer below the model top are identical (Eq. 3.3). Since $\overline{w'w'w'}$ must be zero at the PBL top, $\sigma = 1/2$ there (see Eq. 3.7).

III-L: Computational Logic

I implement ADHOC with a choice of a second- or third-order Adams Bashforth time integration scheme (set at run time). The only terms which use an alternate scheme are transport and dissipation [this includes pressure terms that are modeled as dissipation (see Section III-H)]. A complete discussion of the finite difference methods in ADHOC are discussed in Appendix C. I use a staggered grid such that the mean quantities and the triple moments are defined at the middles of the layers, while the second and fourth moments are defined at the layer edges (Fig. 15). This staggering allows the transport and diffusion terms to be finite-differenced without averaging (Krueger, 1985). I discuss these finite difference schemes in greater detail in Appendix C.

The model is forced by the surface fluxes [which are either prescribed or diagnosed following Louis (1979)], temperature and moisture advective tendencies (which must be prescribed), radiative forcing [which is prescribed or calculated via the radiation code of Stephens and Gabriel (1999)], and the geostrophic winds (which are prescribed as constant or time-varying). In addition, the model integrates the hydrostatic equation and updates the pressure and density (every 15 minutes) at the each model level. The vertical coordinate is height. The "temperature-like" variable that I use is the liquid water static energy, s_L.

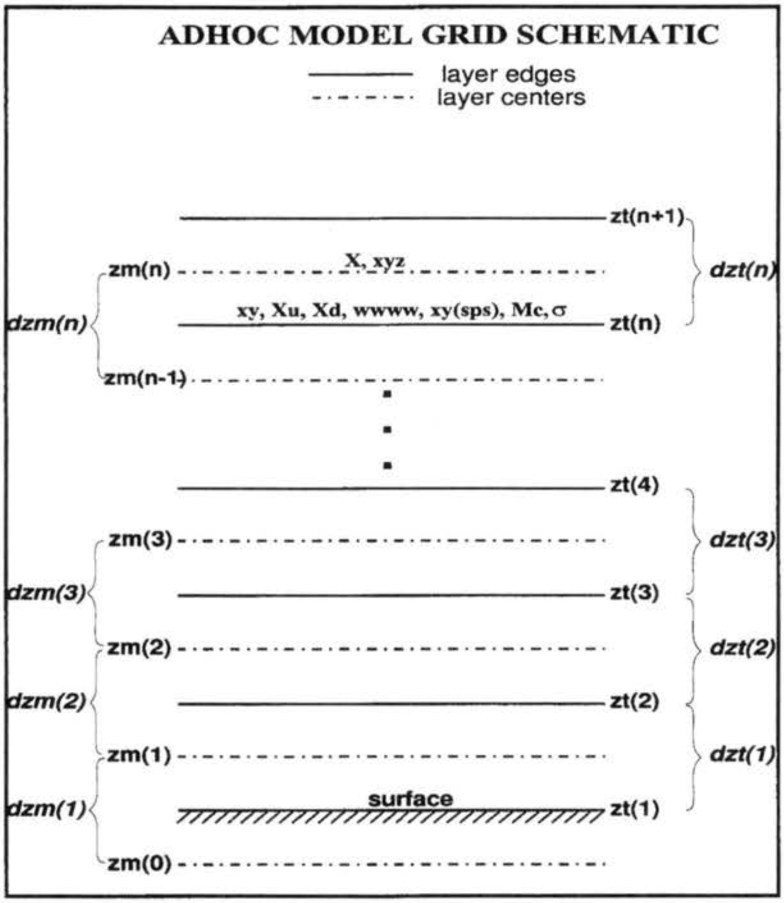

Figure 15: Staggered grid configuration of the model. The mean state and third moments are defined at the layer centers (zm) while the second and fourth moments are defined at the layer edges (zt). In addition, all mass-flux and SPS quantities are defined at the layer edges. Above, small letters represent turbulent quantities and capitals represent the mean state values. x, y, and z are dummy symbols representing any model thermodynamic or dynamic variable.

A flow chart of the model execution is shown in Fig. 16. At the beginning of each timestep, calculate the Adams-Bashforth (AB) weight factors for the previous and current timesteps. During the first run through the code, I simply use a forward timestep. I then integrate the prognostic equations for the mean state, second moments, and $\overline{w'w'w'}$ and I output the *tendencies* of these variables. I then update these variables by adding the AB-weighted tendencies from the current and past timesteps, and time integrating. Then next step is updating the mass-flux

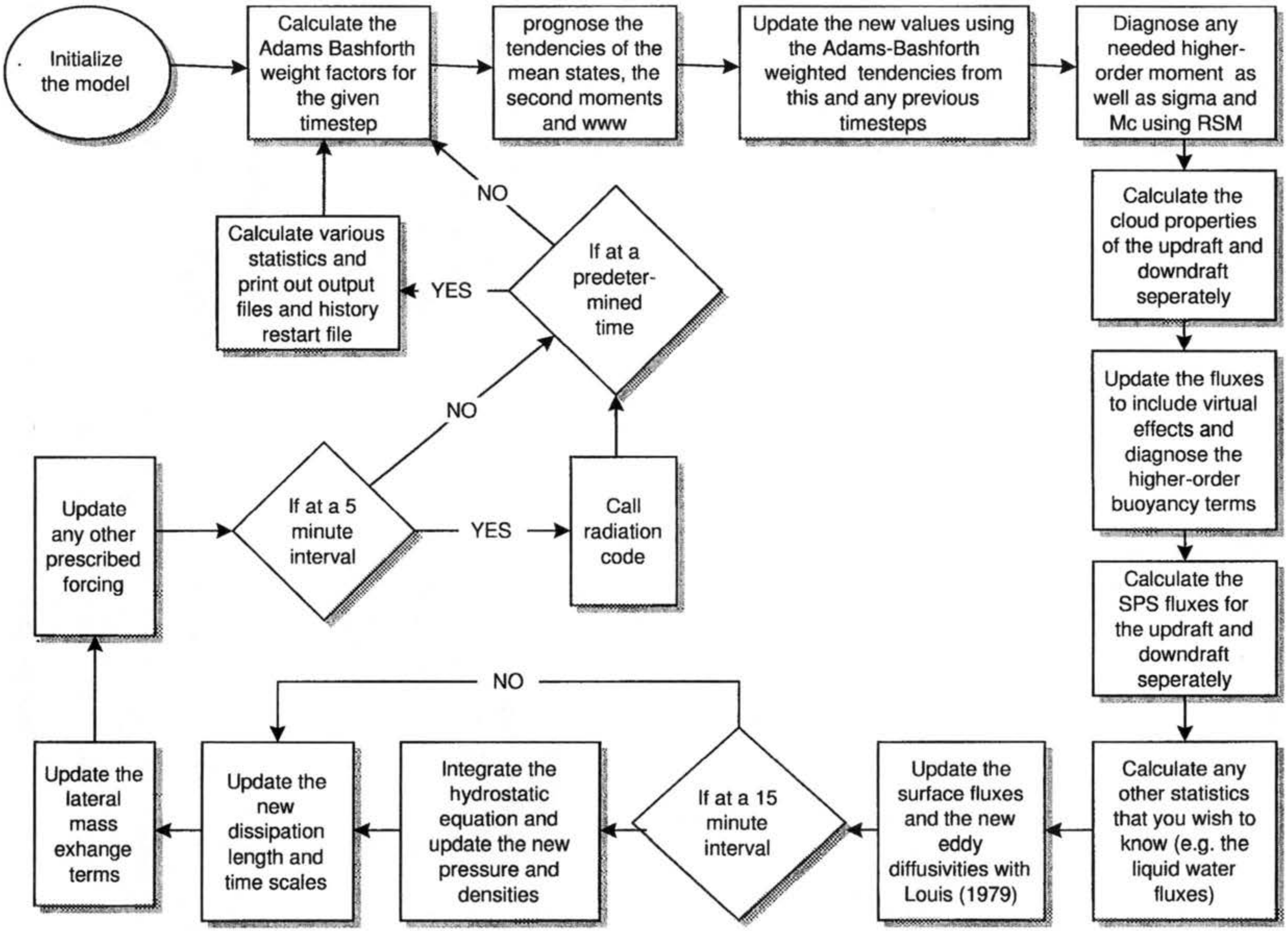

Figure 16: Model Flow Chart

quantities σ and M_c using (3.7) and (3.8) and diagnosing any needed higher-order moments using (3.3)-(3.6). Now, I diagnose the new cloud properties, the SPS fields, and the dissipation time and length scales. I do all this separately for the updraft and the downdraft. Finally, every 15 minutes, I integrate the hydrostatic equation and update the pressure and densities, while every 5 minutes I call the radiation scheme and update the radiative heating/cooling rates. In addition, I write out history restart files and output statistics at predetermined intervals.

Chapter IV: Simulations

IV-A: Introduction

The cases that I will analyzed in this section include the Willis-Deardorff laboratory convection experiment (WD; Willis and Deardorff, 1974; pure convection); the Barbados Oceanographic and Meteorological Experiment (BOMEX; Holland and Rasmusson, 1973; trade-wind cumulus); the Atlantic Trade-wind Experiment (ATEX; Augstein et al., 1973; "upstream" trade-wind cumulus); the Atlantic Stratocumulus Experiment (ASTEX; Bretherton and Pincus, 1995; stratocumulus); and the Surface Heat and Energy Budget of the Arctic (SHEBA; http://sheba.apl.washington.edu; Arctic stratus) and First International Satellite Cloud Climatology Project (ISCCP) Regional Experiment (FIRE). The case setup for each of these simulations is shown in Table 2.

The reason for analyzing five different cases is to understand the limitations of the current version of ADHOC under a wide range of conditions. Certain key physical issues are specific to one "type" of regime. If I hope to truly make the ADHOC approach "regime-independent" (for incorporation into large-scale models), I need to be aware of its strengths and weakness for as many physical situations as possible. It is only through learning about its limitations that I can make the general approach more robust and universal.

In this chapter, I would like to take a "non-traditional" approach by revealing the "punchlines" before the cases and results are discussed. The reason for this is that common themes appear again and again throughout the simulations. Rather than repeat these themes in each section, I'd like to provide a coherent list that readers can reference. In addition, I believe it would be helpful to explain here some universal limitations of the model and then show examples of how these limitations manifest themselves in different regimes. In this manner, readers can understand the foundation of the weaknesses, before they see their actual effects in different regimes. The case-specific severity of the problems will be discussed in the appropriate sections.

One of the most important limitations of the current version of ADHOC relates to its handling of the pressure terms (Section III-H). The pressure terms which appear in the ADHOC equations are parameterized with a "conventional" HOC approach (Section III-H), even in the thermodynamic equations where all other terms are consistent with *both* MFC and HOC. This is particularly bothersome in the thermodynamic flux equations. In these equations, "conventional" HOC models assume that the dissipation term is negligible (the reason for this is explained at the end of Section II-C-3), while at the same time, they assume a "dissipation-like" form for the pressure terms; one that is directly proportional to the actual dissipation. The ADHOC equations clearly demonstrate that the dissipation term of the flux equations is not negligible; it is related to the lateral mass exchange between turbulent updrafts and downdrafts (Section III-G).

Thus, although it is never stated, I believe that the constant of proportionality in the pressure term actually incorporates both the actual dissipation and the pressure effect (i.e., I argue that HOC models unknowingly "rescue" themselves by using a pressure constant which is large enough to incorporate the effects of "true" dissipation). In ADHOC, that fact that we use the "conventional" HOC pressure parameterization (along with its constant of proportionality), and we additionally include the effects of "true" dissipation through the lateral mass exchange terms, we are in reality representing the true dissipation twice. In order to prevent this from occurring, the pressure term constant needs to be reduced. However, it is unclear how much reduction is necessary to remove only the "true-dissipation" part of the term. In addition, the results are highly sensitive to any change in this constant (Fig. 17).

To demonstrate how sensitive the model is to the pressure constant, I performed a simple sensitivity study using WD. The results of this are shown in Fig. 17. We see that changing the pressure constant by a small amount completely changes the amount of entrainment at cloud top, as well as the degree to which the surface layer mixes with the rest of the boundary layer. By cutting the pressure constant in half, I am able to reduce the entrainment to near zero, while increasing the pressure constant by 50% makes the entrainment 2-5 times larger. In the top left figure, we see that mixed-layer temperature gradient (which should ideally be zero), is 2 K when the pressure constant is halved, while it is only 0.3 K when the pressure constant is increased by 50%. In Section III-I, I showed that the inclusion of an SPS scheme in the model greatly improved the results of WD at the surface and near the inversion (Fig. 12). We see here that these results are sensitive to any change in the model parameters at these heights. Other sensitivity tests performed with BOMEX and ATEX also show the sensitivity to the pressure constant (not shown).

This pressure sensitivity is largest at the surface and at the inversion base, where the pressure and dissipation effects are largest. At the surface, the function of the pressure term is to convert vertical momentum into horizontal momentum; what is not converted must be dissipated to insure that the turbulence goes to zero at the surface. At the inversion, the pressure terms have the same job, with the added complication that not all turbulence must completely die at the base of the inversion. Here, part of the turbulence gets converted horizontally (as it does at the surface); a portion gets dissipated; and what is "left over" drives the entrainment process. If the balance between the dissipation and the pressure effect is not properly accounted for, the entrainment will be too weak or too strong. The fact that the dissipation may actually be represented twice in ADHOC reduces the amount of energy "left over" for entrainment. This is the exact problem that is seen again and again in all 5 cases discussed in this chapter.

In Fig. 17, I showed how changing the pressure term constant alone can drastically change the amount of entrainment in WD. In a more complicated situation with clouds, the accurate breakdown of the PBL-top turbulence into that affected by pressure, that affected by dissipation, and that which affects entrainment is even more essential. The evolution of many cloudy regimes is almost completely determined by the degree of entrainment (e.g., stratocumulus, trade-wind

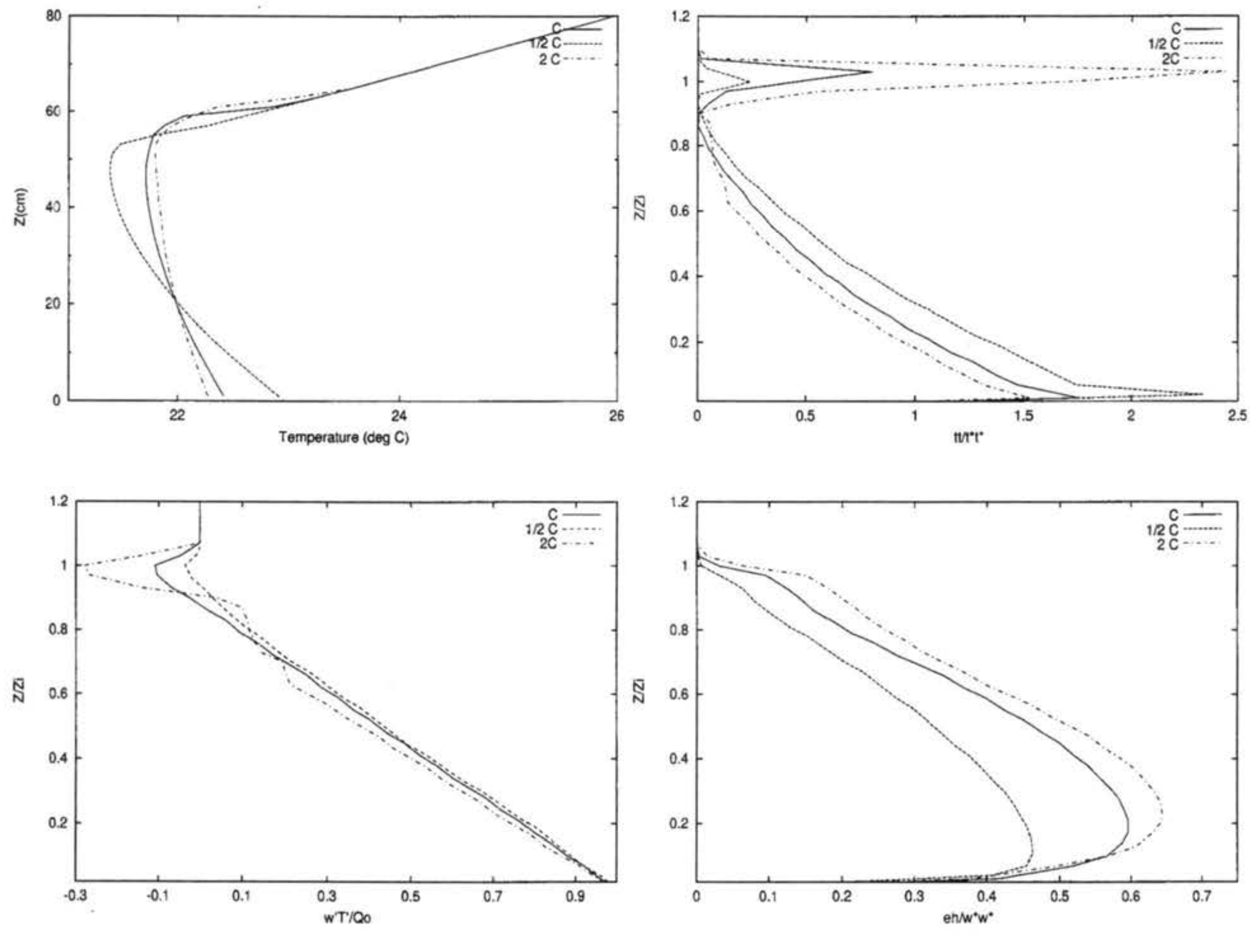

Figure 17: The sensitivity of the WD results to changes in the pressure constant. Dashed-dotted line, pressure constant multiplied by two; dashed line, pressure constant halved; solid line, "conventional" HOC pressure constant. The heat flux is the total (large-scale plus SPS) flux.

cumulus). To help with this problem, I could artificially "tune" the pressure constant so that the regime I am simulating acts in a manner consistent with observations; however, this is clearly not the best method if I wish to make the approach "regime-independent". In general, this problem needs to be solved with the development of an "ADHOC-consistent" pressure parameterization. A possible method to do this is discussed in Appendix B. I will refer to this problem in the proceeding discussions as "the pressure-dissipation problem".

Another limitation of ADHOC, which appears in all 5 of the simulated cases in this chapter, deals with the horizontal momentum terms, which are currently not handled in the same "ADHOC-consistent" manner as the thermodynamic variables and the vertical velocity (Section III-J). Inconsistencies such as this, which appear in the momentum flux and variance equations, naturally make the approach less robust. In the flux equations, momentum transport is parameterized in the same manner as it is in a "conventional" HOC model; by the slow process of diffusion (Section II-C-2). The mass-flux model plays no direct role. Thus, *if* surface heating (or another typically "non-local" process) is responsible for the transport in a specific regime, then the momentum will not be transported and mixed as efficiently as the thermodynamic variables (see footnote, page 9; Fig. 3). Even given enough time, small-scale diffusion will not help transport momentum non-locally. This is a direct result of the timescale differences between diffusion and the large-scale flow; the turbulence which is transported by small-scale diffusion is quickly dissipated or modified by the faster-acting boundary-layer turbulence, before it is able to travel across more than a few layers.

This problem is also applicable in the equations for the momentum variances. The three components of the momentum variance equations ($\overline{u'u'}$, $\overline{v'v'}$, and $\overline{w'w'}$) in HOC models are intricately coupled through both the pressure and dissipation parameterizations. In these equations, isotropy is assumed so that each of these three components is identically affected by pressure and dissipation. "Conventional" HOC models either predict or diagnose a TKE dissipation rate, and using the assumption of local small-scale isotropy (Kolmogorov, 1941), divide the dissipation so that it acts equally on the three components of the variance (Mellor and Yamada, 1982).

However, the larger-scales eddies represented by ADHOC do not dissipate isotropically. This can be seen by examining the form of the dissipation terms (lateral mass exchange terms) in the ADHOC equations; a form that dictates that the dissipation is proportional to both lateral mixing and the difference in properties between the updraft and downdraft components of the higher moment being dissipated (not isotropic assumptions). For example, in the equation for $\overline{w'h'}$, the dissipation term is proportional to the lateral mixing terms (E and D), as well as the updraft/downdraft differences of w and h ($w_{up} - w_{dn}$ and $h_{up} - h_{dn}$; Eq. 3.81). The dissipation in the $\overline{w'w'}$ is represented in the same manner; Eq. 3.72). In ADHOC, this non-isotropic dissipation of the larger eddies feeds the SPS TKE (Section III-I), which in turn dissipates isotropically following Kolmogorov (1941). However, since the horizontal momentum terms are not incorporated into the "ADHOC framework", they dissipate as they would in a "conventional" HOC model. Thus, the assumption of isotropic dissipation in the equations for $\overline{u'u'}$ and $\overline{v'v'}$, and the assumption of non-isotropic dissipation in the equation for $\overline{w'w'}$ are inconsistent. Only the incorporation of the horizontal momentum terms into the ADHOC framework will alleviate this inconsistency. There are problems associated with doing this however (Section III-J), and thus, it is not used in the current version of the model.

Similarly, it is difficult to accurately implement the "return-to-isotropy" assumption for the pressure terms of the momentum variance equations (Rotta, 1951; Section II-C-1) because the equations are formulated with different assumptions ($\overline{w'w'}$ with ADHOC and $\overline{u'u'}$ and $\overline{v'v'}$ with a "conventional" HOC model). For example, the "return-to-isotropy" component of the pressure parameterization appears to be overactive in many instances (e.g., BOMEX; Section IV-C-2b, Fig. 35).

Finally, I can think of one additional weakness in the current version of the model, which is seen in each of the 5 simulated cases. It relates to controlling the "artificial" appearance of turbulence in stable layers. In the context of the mass-flux model, all turbulence evolves with the updraft area fraction, σ, and the convective mass flux, M_c (Chapter III). These quantities, in turn, depend on the vertical velocity statistics, $\overline{w'w'}$ and $\overline{w'w'w'}$ (Eqs. 3.7-3.8) through the skewness, (S_w; Eq. 3.11). In stable layers, $\overline{w'w'}$ and $\overline{w'w'w'}$ are very small. However, the ratio of two small numbers is not always small; thus S_w can become artificially large and σ artificially small in these situations. For example, if $\overline{w'w'} = 1x10^{-8}$ m^2 s^{-2} and $\overline{w'w'w'} = 1x10^{-12}$ m^2 s^{-2}, then the $S_w = 1$ and $\sigma = 0.3$. This value of σ indicates a moderately concentrated updraft, which will initiate turbulence. However, in reality, there is no turbulence since both $\overline{w'w'}$ and $\overline{w'w'w'}$ are practically zero. The "artificial" turbulence generated in this manner causes many stability problems in the inversion layer. Thus, to prevent this situation, I enforce the condition;

$$\text{if } \overline{w'w'} < 1x10^{-4} \text{ m}^2 \text{ s}^{-2}, \text{ then all turbulence} = 0, \qquad (4.1)$$

where "all turbulence" refers to the second and third moments. I believe that this criterion is too strict, and that this may inhibit the initiation of entrainment.

In a stable layer (one not in direct contact with turbulence), this criterion prevents the artificial growth of turbulence. However, any stable layer which *is* in contact with the turbulence (e.g., the layer just above cloud top) needs the freedom to grow slowly if the PBL turbulence dictates that it should. It may be that the slow growth of turbulence due to entrainment is inhibited with the criterion (4.1). However, if I try to relax this constraint to a lower minimum value for $\overline{w'w'}$, instability in the inversion layer causes problems. A better method for extinguishing artificial turbulence (one that does not affect the turbulence generated in the stable layer next to cloud top) is needed. Such a method may help to increase entrainment and bring the ADHOC simulation of temperature and moisture closer to that of the LES simulation and observations discussed in the next few sections. I will refer to this problem in the proceeding discussion as the "weak turbulence problem".

As a final note, I would like to mention the high sensitivity of the model results to "fixed" large-scale and surface forcing; something that 4 of the 5 simulated cases use to varying degrees (all except the SHEBA/FIRE case). It appears that "rigid" forcing does not allow the model to fully adjust to the evolving dynamic and thermodynamic changes in the boundary layer[6]. As a result, the PBL turbulence evolves in a somewhat unnatural way. Fig. 18 shows an example of this effect from the ATEX simulation (Section IV-C-3). As a sensitivity study, I ran the ATEX case with "rigid" values corresponding to a fixed mixed layer depth of 1500 m and fixed surface layer air properties corresponding to a transfer coefficient of 1.39×10^{-3} (Dunckel et al., 1974). The effect making the forcing "rigid" is significant, especially in the case of the radiative forcing. The difference between allowing the radiative cooling to depend on the height and quantity of liquid water in the boundary layer and forcing a prescribed radiative cooling profile significantly affects the amount of liquid water and the magnitude of the turbulent fluxes and variances. In addition, it also significantly influences the height of the PBL top. This problem is most evident in the BOMEX results (Section IV-C-2b). However, it also plays a role in the other cases as well. I will refer to it, when appropriate in each case discussions in this chapter, where applicable.

In Sections IV-B through IV-E, I compare the ADHOC results to both observations and those simulated by LES models. In order to help interpret the differences between ADHOC and LES, I briefly review the fundamental aspects of LES models in the next section.

---

6. Here, "rigid" forcing indicates that the values of the surface fluxes, radiation, horizontal advection, and vertical subsidence are all pre-set, and cannot evolve with the changing boundary layer; "semi-rigid" forcing refers to situations where the "forms" of the forcing are pre-set, but the actual values can change with the boundary layer evolution (e.g., the bulk aerodynamic formula for the surface flux is specified with a fixed drag coefficient, but the flux itself can change with the surface wind speed and properties; or the radiative forcing is a set function of the integrated liquid water path, but does not use a completely interactive radiation scheme).

Table 2: Model set-up and forcing for the cases discussed in Sections IV-B through IV-E

	WD	BOMEX	ATEX	ASTEX	ARCTIC
Surface sensible heat flux	Constant in time at 1.3×10^{-3} K m s^{-1}	Constant in time at 8×10^{-3} K m s^{-1}	Bulk aerodynamic formulae with fixed coefficients	Constant in time at 1×10^{-2} K m s^{-1}	Fully interactive: Louis (1979)
Surface latent heat flux	None	Constant in time at 5.2×10^{-5} m s^{-1}	Bulk aerodynamic formulae with fixed coefficients	Constant in time at 1×10^{-5} K m s^{-1}	Fully interactive: Louis (1979)
Radiative cooling	None	Prescribed function of height	Prescribed function of the liquid water path	Prescribed function of the liquid water path	Fully interactive: (Stephens and Gabriel, 1999)
Horizontal moisture advection	None	Prescribed function of height	Prescribed function of height	None	ECMWF-applied forcing
Horizontal temperature advection	None	None	Prescribed function of height	None	ECMWF-applied forcing
Subsidence	None	Prescribed function of height	Prescribed function of height	None	ECMWF-applied forcing
P_{sfc} (mb)	Not used	1015	1015	1029	Changing: interpolated ECMWF
T_{sfc} (K)	294	300.375	298	292.5	274
Timestep (seconds)	0.1	0.5	0.5	0.5	0.5
Grid spacing (m)	0.02	40	20	25	15
Length of simulation (hrs)	0.1	16	12	4	48
Number of levels	50	75	150	60	168
Time period shown in plots	Minute 6	Average over hours 12-16	Average over hours 10-12	Average over hours 3-4	12-hour averages

IV-A-1: LES models

LES modeling of turbulence in the atmospheric boundary layer was pioneered by Deardorff (1972). LES may represent the best approach to calculating the three-dimensional time-dependent structure of the atmospheric boundary layer. In contrast to the ensembled-averaged equations of HOC models, the LES equations incorporate true volume averaging. The volume averaging is sufficiently small such that the largest energy-containing eddies are resolved explicitly, at least away from the surface and inversion layers. This is of paramount importance, since turbulent flows tend to differ from one another mainly in their large-eddy structure, whereas the small scales in all turbulent flows tend to be statistically similar (Garrat, 1992). These smaller unresolved scales in LES models are parameterized with a sub-grid-scale model (SGS; see Fig. 13). The SGS turbulence parameterization typically used are an ensembled-averaged first or second-order closure scheme. For area-averaged turbulence statistics, the SGS-parameterized component must be added to the resolvable scale values to yield the total value at any given height. While the major strength of the LES approach is its ability to resolve many of the energy-containing eddies in the boundary layer, it is unfortunately impractical in large-scale models. LES models are seen as a middle ground between HOC, where all scales are parameterized, and direct numerical simulation (DNS), where all scales are resolved.

IV-B: Cloud-free convection

The term "cloud-free convection" can describe both pure, dry atmospheric convection and the convection of WD. In this study, we will use the term "dry convection" to represent both of these convective regimes, even though the latter is not really "dry". The statistics of free-convective flow are well known from observations (Willis and Deardorff, 1974) and LES (Moeng, 1984). Turbulence models have had much success simulating dry convection, provided they explicitly account for non-local transport (Section II-C-2) [e.g., transilient matrix models (Stull, 1984);

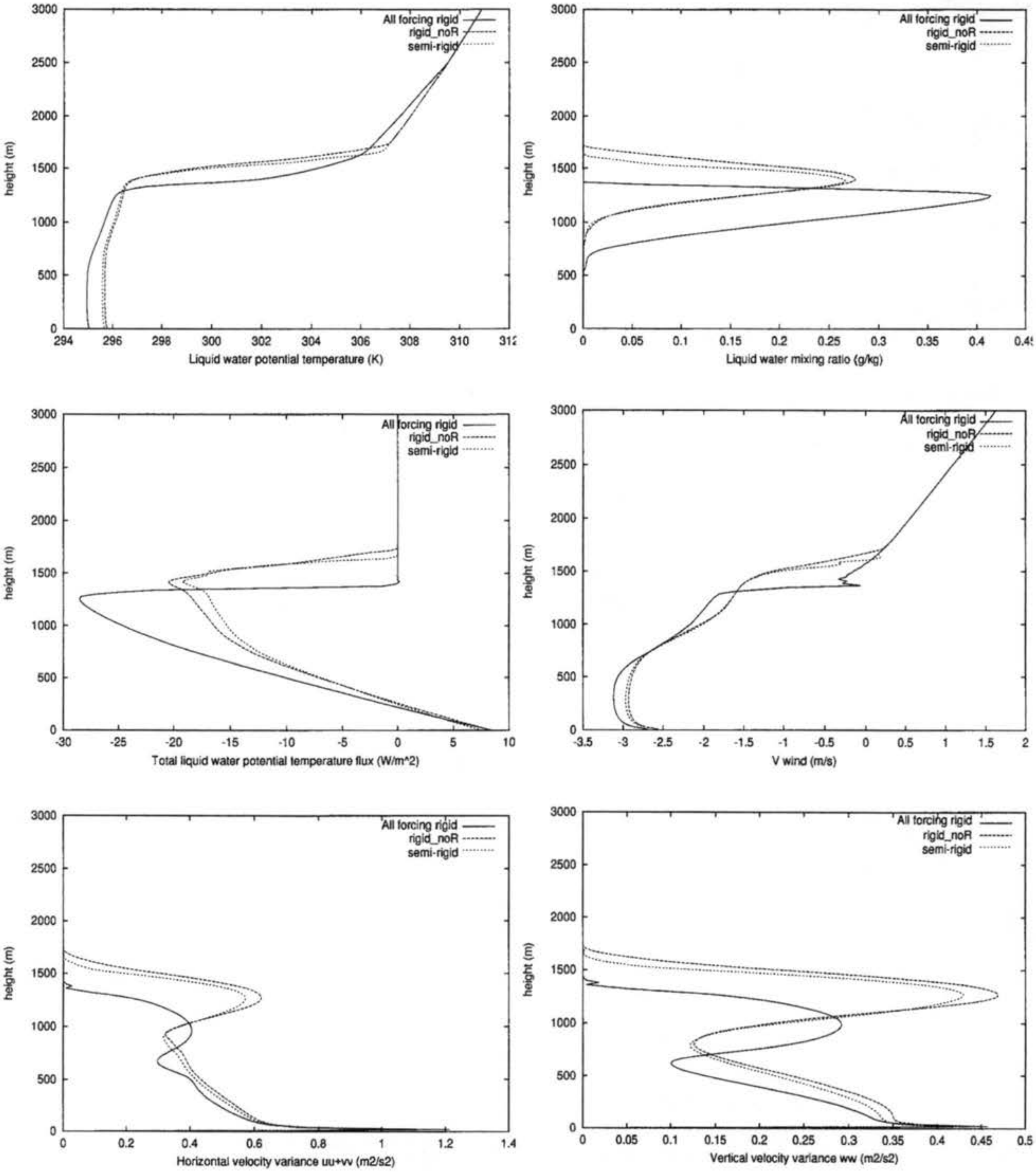

Figure 18: The effect of implementing "rigid" surface forcing in ATEX. "rigid" and "semi-rigid" are defined in the footnote on page 144; rigid_noR is the same as "rigid", with the exception that the radiation is "semi-rigid".

models with counter-gradient terms (Holtslag and Moeng, 1991); and mass-flux models (Wang and Albrecht, 1990)]. Dry convection can be described with two thermodynamic variables; potential temperature (or dry static energy) and water vapor mixing ratio (or specific humidity). Both are conserved in adiabatic motion. While moist convection can also be described with two variables (moist conservative ones, such as the liquid water potential temperature, the liquid water static energy, and total water mixing ratio), the phase change of water greatly complicates the thermodynamics (Section II-D-2). The scientific literature abounds with modeling studies of cloud-free convection. A comprehensive review of these studies was described in Section II-D-1 for HOC models and Section II-E-1 for mass-flux models.

Below, I show the ADHOC results from WD (Willis and Deardorff, 1974). I compare these results to well-known profiles of pure convection in the atmospheric boundary layer. In order to represent the physics of a cloud-free convective boundary layer, the model needs to represent the following:

- a mean state that is well-mixed below the PBL top;
- a positive heat flux that linearly decreases with height in the mixed layer and a negative heat flux representing entrainment at the PBL top;
- a vertical velocity variance that is a maximum in the low-to-mid boundary layer;
- relatively small horizontal velocity variances with maxima both near the surface and the boundary-layer top; and
- a temperature variance with maxima both at the surface (where heat is input) and near the PBL top (where entrainment is occurring).

I will examine the model results of this case, focusing on these features, in Section IV-B-1a. In the next section, I will describe the actual experiment and the case-specific parameters and forcing that I used in the simulation.

IV-B-1: Willis-Deardorff laboratory convection experiment

In the Willis-Deardorff laboratory convection experiment, a water chamber was heated at its lower boundary and the resulting convective flow was studied. The horizontal dimensions of the chamber were 114 cm by 122 cm and the depth was 76 cm. While this is not a typical aspect ratio for convection in the atmosphere, the normalized statistics of convection in this tank are representative of those in the atmosphere (Willis and Deardorff, 1974). The Reynolds number in the tank is approximately 4000 (also considerably less than that of the atmosphere).

The model is run for 6 minutes with a timestep of 0.1 seconds. As initial conditions, we prescribe a uniform temperature of 21°C in the lowest 50 cm capped by an overlying stable layer with a lapse rate of 0.16 K cm^{-1}. Higher-order correlations are assumed to be zero throughout the layer, except at the surface where we apply surface layer similarity theory ($\overline{w'w'w'}$ is zero everywhere). The only external forcing is a constant heat flux of 0.0013 K m s^{-1} which we apply at the surface. In the surface layer, the variances of the vertical velocity and temperature are estimated according to the free convection surface-layer similarity relations (Wyngaard and Coté, 1971):

$$\overline{w'w'} = a_1 u_f^2 , \qquad u_f = (\alpha g Q_o z)^{1/3} , \tag{4.2}$$

and

$$\overline{T'T'} = a_2 T_f^2 , \qquad T_f = \frac{Q_o}{u_f} ; \tag{4.3}$$

where $\alpha = 2.3x10^{-4}$ K^{-1} is the coefficient of thermal expansion for water, $a_1 = a_2 = 1.8$, Q_o is the applied surface heat flux, and $g = 9.8$ m s^{-1}.

The horizontal velocity variances in the surface layer are assumed to scale with the convective velocity scale (Deardorff, 1970) according to

$$\overline{u'u'} = \overline{v'v'} = a_3 w_*^2 , \qquad w_* = (\alpha g Q_o z_i)^{1/3} ; \tag{4.4}$$

where z_i is the mixed-layer depth and $a_3 = 0.2$. The mixed-layer depth is taken as the height where the heat flux is smallest. At the upper boundary, we set all higher-order terms to zero. We ran the simulation for 6 minutes with a timestep of 0.1 seconds and a grid spacing of 2 cm.

IV-B-1a: Results and discussion

The results from the ADHOC simulation of the WD laboratory convection experiment are shown in Figures 19-23. In Fig. 19, the simulated temperature profiles are compared to those of the actual experiment, as well as to those of André et al., 1976 [A76; I chose to use this study for comparative purposes because, to my knowledge, no other third-oder closure study has simulated this experiment; Canuto et al. (1994) simulated the revised WD experiment (Deardorff and Willis, 1985)]. Profiles of the mean temperature are plotted at indicated intervals in order to gain a sense of the entrainment rate.

Overall, ADHOC is able to capture the effects of the well-developed mixed layer and the entrainment of warmer water through turbulence at the boundary-layer (BL) top. The entrainment rate is well represented. This can be shown with the following simple analysis: The rate of change with height of the convective mixed layer (entrainment velocity; $\frac{\partial z_i}{\partial t}$) is a good indicator of the entrainment rate. We can non-dimensionalize $\frac{\partial z_i}{\partial t}$ if we divide by the convective velocity scale, w^* (Eq. 4.4). The value of this non-dimensional entrainment parameter in is 0.024 for ADHOC.

These values are in particularly good agreement with those of WD (0.023) and A76 (0.025). It is interesting to note that, without the inclusion of a SPS parameterization (see Section III-I; Fig. 12), the non-dimensional mixed-layer growth is 0.011. This further highlights the benefits of including SPS effects in the model.

The ADHOC temperature profiles in Fig. 19 highlight a potential weakness of the model. Near the surface, the simulated temperature profile is not as well-mixed as it is in the actual WD experiment, or in other simulations of pure convection (Canuto et al., 1994; André et al., 1978; Wang and Albrecht, 1990). However, the results of A76, while well mixed, sharply transition to an unstable layer near the surface. ADHOC is able to better incorporate the surface heating into the mixed layer through the use of an SPS model (Fig. 12). Despite this improvement, there is a need for additional surface mixing, which is related to the pressure-dissipation problem discussed in Section IV-A and shown in Fig. 17.

Figure 20 shows the turbulent heat flux, non-dimensionalized by the imposed surface heat flux, Q_0, as a function of the dimensionless height z/z_i. Overall, the agreement between ADHOC and the results of both A76 and WD is good. It appears as if the minimum heat flux is higher in ADHOC than in A76 and WD. However, z_i is defined in ADHOC as the height of the minimum heat flux. Thus, this will always occur at $z = z_i$. A76 and WD defined z_i as the height where the cooling of the initial temperature distribution is a maximum. In general, this occurs slightly below z_i. It also appears as if ADHOC is unable to smooth out the transition between the mixed layer and the overlying stable air. This is both an artifact of the manner in which I define z_i and the fact that I am plotting values at given heights and "connecting the dots" with straight lines. It is interesting to note that the magnitude of the negative heat flux near the inversion is highly sensitive to the pressure constant (Fig. 17).

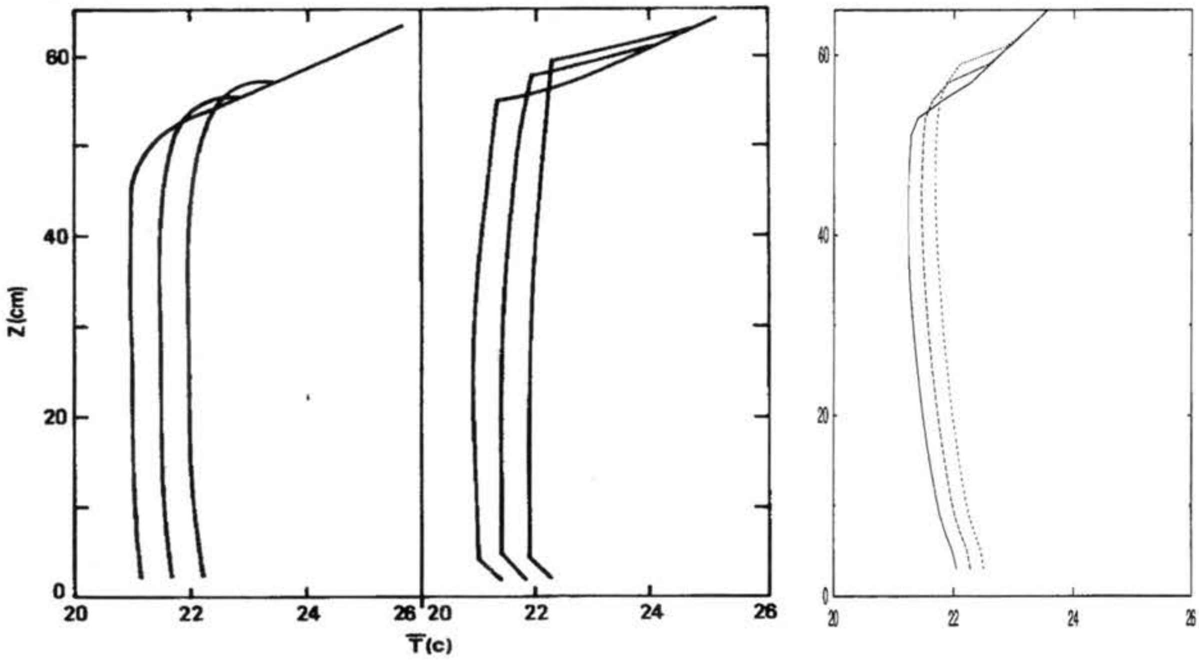

Figure 19: Evolution of mean temperature (in °C). Left: WD; middle: A76; Right: ADHOC. The three selected curves are the profiles at 150, 255, and 360 seconds (from left to right) after the beginning of the experiment.

In Figures 21-22, I show the ADHOC-simulated profiles of the horizontal and vertical velocity variances ($\overline{u'u'} + \overline{v'v'}$ and $\overline{w'w'}$ respectively) as well as those of A76 and WD. The gross shape of the ADHOC profiles is correct, but there are clearly differences. In the horizontal velocity variance profiles, the surface and the lower half of the mixed layer are well-represented, as well as the eventual drop-off to zero just above z_i. However, in between, ADHOC appears unable to mix $\overline{u'u'} + \overline{v'v'}$ high enough into the mixed layer. The likely "culprit" here is the manner in which the model handles momentum transport relative to transport of the thermodynamic variables (see Section IV-A).

If surface heating is responsible for momentum transport, then $\overline{u'u'} + \overline{v'v'}$ will not be as well-mixed as the thermodynamic variables (here, temperature). The contribution of this effect to

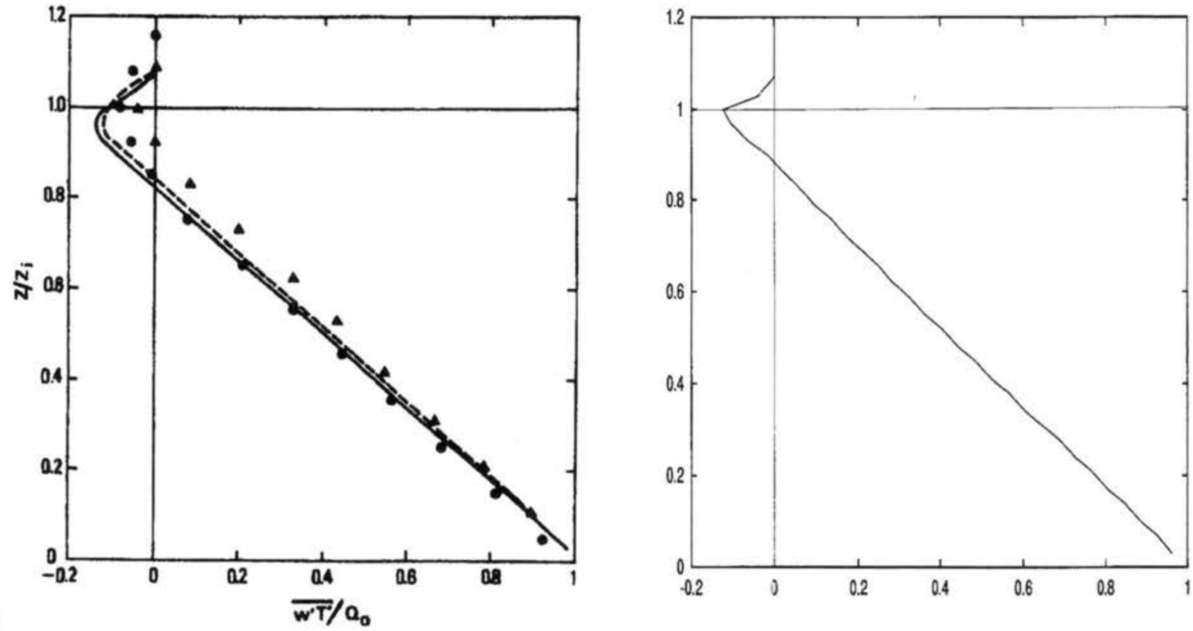

Figure 20: Vertical profiles of dimensionless heat flux. Left: A76, solid line; WD, dashed line. Triangles and circles are for runs done with a steeper inversion lapse rate; Right: ADHOC.

the problem is further implicated by the values of the momentum variances themselves, which appear to be too high in the lower half of the BL for ADHOC (if transport processes were acting in an efficient manner, the excess of $\overline{u'u'} + \overline{v'v'}$ in the lower half of the BL would be transported to the upper half, thereby reducing the horizontal velocity variance in the lower half of the BL). Other second-order closure models have had a similar problem [see Canuto et al. (1994), Fig. 24]. I believe that the incorporation of momentum into the ADHOC framework will significantly help this problem.

However, the lack of mixing may not be the whole story. Over time, non-local mixing can occur indirectly through other terms in turbulence equations (e.g., gradient production terms). In addition, part of the reason why $\overline{u'u'} + \overline{v'v'}$ should be able to sustain a large value near the BL top is its continuous feeding by the pressure terms (Sections II-C-1 and III-H). As discussed in Section IV-A, the relationship between pressure, dissipation, and entrainment at the BL top may not be handled in an accurate manner. It is suggested in Section IV-A that an "ADHOC-consistent" method to handle the pressure terms would help with this problem. A possible method to do this is discussed in Appendix B.

As a final note, the same problem with the pressure terms does not seem to occur at the surface where a similar pressure redistribution of momentum should occur (there is in fact a maximum in the horizontal velocity variance near the surface; Fig. 21). This is a result of surface layer similarity relations which are used to diagnose the velocity variances in the lowest layer (Eq. 4.4), circumventing the pressure terms.

Figure 22 shows the corresponding results for the vertical velocity variances. The shape of this curve agrees with the both WD and A76. In addition, the maximum value of the non-dimensional vertical velocity variance is close to 0.4 in all three cases. However, the maximum occurs at approximately $z = 0.3z_i$, where in WD and A76 it occurs at approximately $z = 0.55z_i$. Observations in the atmosphere show that the value should be approximately $0.3z_i$ (Wyngaard and Coté 1971; Lenschow and Stephens, 1980; Therry and Lecarreré, 1983). WD suggest that the higher value in the convective tank may be due to the limited width-to-height ratio of the laboratory model. A follow-up experiment to WD was done in 1985 (Deardorff and Willis, 1985) in which the aspect ratio was increased. These results show the height the maximum $\overline{w'w'}$ to be located near $z = 0.4z_i$.

Finally, I show plots of the TKE and heat flux budgets non-dimensionalized by $\frac{w^{*3}}{z_i}$ (Fig. 23) and $\frac{w^*\theta^{*2}}{z_i}$ (Fig. 24) respectively. In Fig. 23, only the three terms of the TKE budget which

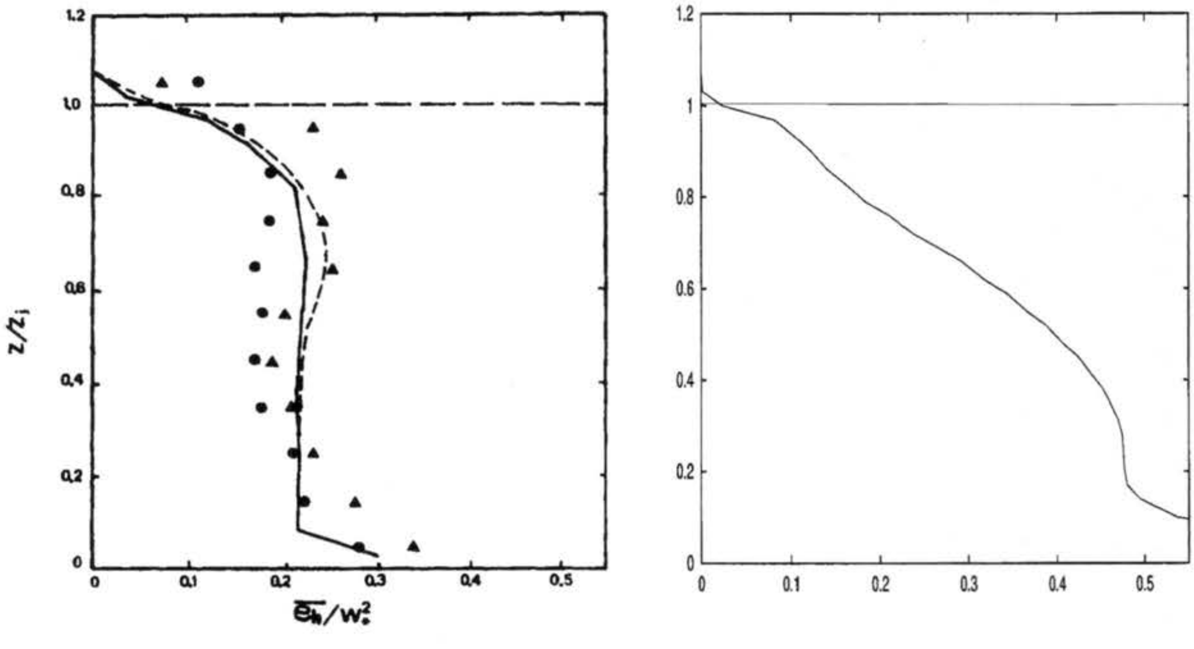

Figure 21: Vertical profiles of dimensionless horizontal velocity variance (e_h = uu+vv). Left: A76 and WD (symbols as in Fig. 20); Right: ADHOC.

have the largest contribution are displayed for ADHOC (buoyancy, turbulent transport, and dissipation); the shear production terms are zero in this experiment. The magnitudes and shapes of these three curves agree well with those of A76 and LES (not shown). In the lower half of the BL, transport and dissipation remove the buoyancy-produced TKE. In the middle of the boundary layer, where the TKE is the strongest, the dissipation is most active. Here, the transport term changes sign where it ceases to remove TKE and begins to deposit it. In the inversion layer, the positive turbulent transport balances the dissipation, negative production due to the conversion of kinetic energy into potential energy, and pressure transport.

Two notable differences are the location of the dissipation maximum and the shape of the transport profile near the inversion. In ADHOC, the height of the maximum dissipation is significantly lower than in A76. This is a direct result of the higher TKE in the ADHOC simulations in the lower half of the BL (discussed above; Figs. 21-22). The sharp point in the transport is more

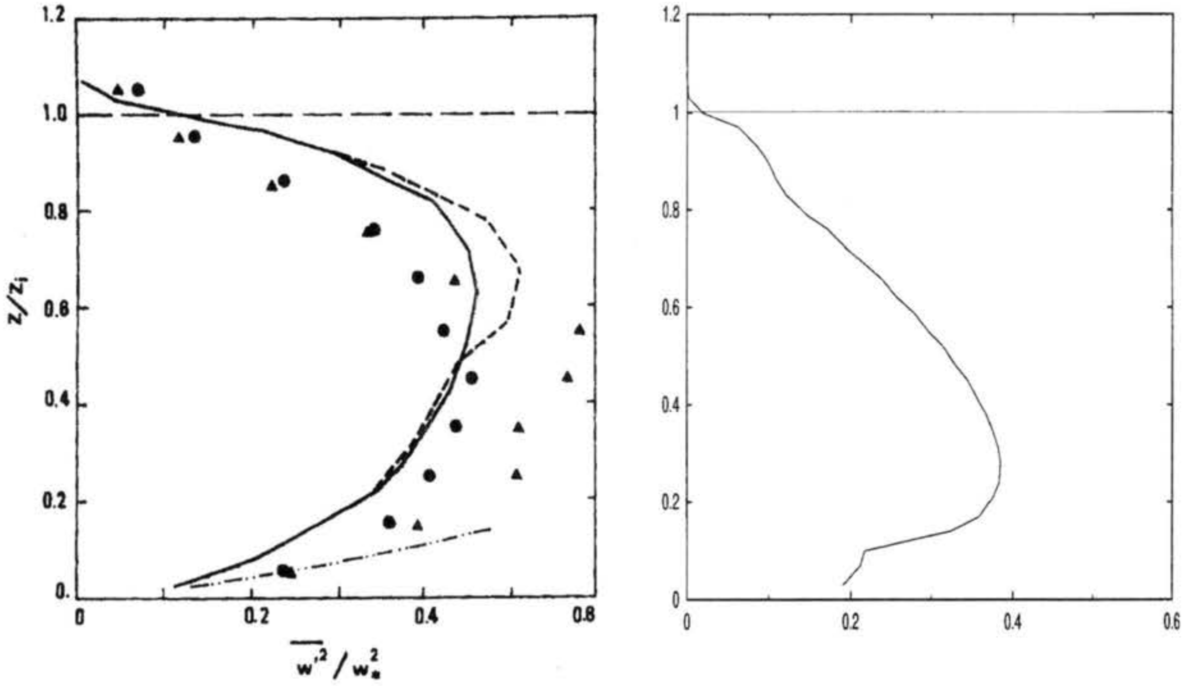

Figure 22: Vertical profiles of dimensionless vertical velocity variance. Left: A76 and WD (symbols as in Fig. 13); Right: ADHOC.

difficult to explain. It is likely related to the fact that these transport terms are a combination of local and non-local transport. As mentioned in Section IV-A, the vertical transport of horizontal momentum ($\overline{w'u'u'}$ and $\overline{w'v'v'}$) in ADHOC is "diffusive" in nature (see Eq. 3.144), while the vertical transport of vertical momentum ($\overline{w'w'w'}$) is "advective" (see Section III-A-1a). In order to form a total TKE transport for the purposes of this comparison, "apples and oranges" had to be combined. Once again, I believe that, with the eventual incorporation of momentum into the "ADHOC framework", these problems will be alleviated.

In Figure 24, I compare the non-dimensional heat-flux budget simulated by ADHOC to that of the LES results of Moeng and Wyngaard (1989). The results compare quite favorably. In the lower half on the BL, we see that both buoyancy and gradient production act to increase the heat flux, while transport and pressure both act to remove it. ADHOC has an additional sink,

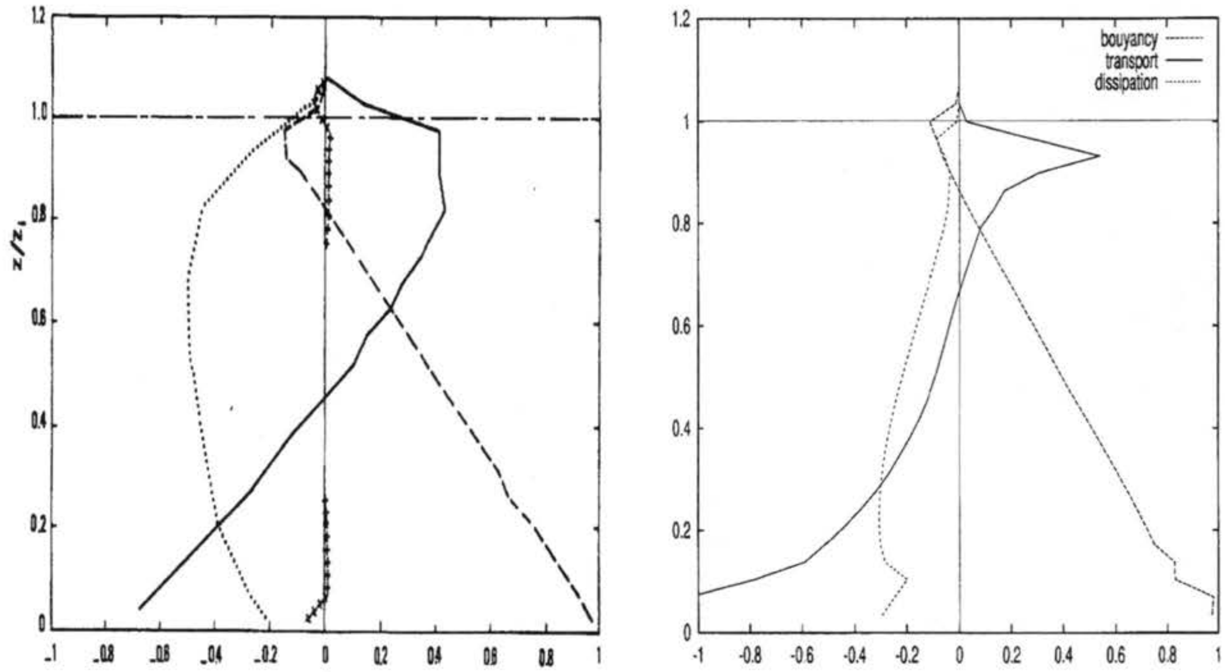

Figure 23: Dimensionless turbulence kinetic energy budget. Left: A76 (solid line, turbulent transport; dotted line, viscous dissipation; dashed line, buoyancy); right: ADHOC (lines are as marked).

which is dissipation. The flux dissipation term is neglected most LES simulations, as well as in HOC studies (I believe this is not a valid assumption; see Section IV-A).

There a few important differences here. First, the roles of gradient production and buoyancy appear to be reversed with gradient production being the dominant producer of TKE in ADHOC, verses buoyancy is in the LES. The reason for this relates to the ability of the models to produce a well-mixed layer. In the LES, the gradient of temperature is very close to zero in the mixed layer; thus, the gradient production term is small. As discussed, in ADHOC, the boundary layer is not as well-mixed as it should be. There is a set amount of heat that is input into this simulated convective system. This energy must be distributed among production components of the turbulent heat flux budget. The negative gradient of the temperature in the ADHOC simulations causes much of this energy to appear through the gradient production term, leaving less for buoyancy. On the other hand, the lack of a significant temperature gradient in the LES puts all the burden of production on the buoyancy term. Thus, the relative roles of these two processes are reversed between the LES and ADHOC.

On the destruction side of the lower half of the boundary layer, we see that the pressure effect is larger than the turbulent transport in both simulations for most of the lower part of the BL. As the surface is approached (in ADHOC), however, the pressure effect increases a bit, while the transport continues to decrease (not seen in the LES simulations). This is a direct result of the inability of ADHOC to accurately separate out the dissipation part of the pressure effect (discussed in Section IV-A). Due to this problem, a comparison with the LES pressure terms should only be made in a qualitative sense.

Finally, near the inversion, the LES results show a large contribution from the buoyancy term, which is balanced by pressure effects and gradient *production* (which is actually a "destruction" term in the stable layers of the lower inversion; see Eq. A.11). With the exception of the turbulent transport term, ADHOC is unable to capture the magnitude of these effects. In WD, there are no buoyancy contributions which arise from moisture differences (as they do in air). Thus, the buoyancy term in the heat flux equations (in WD) is directly proportional to the variance of temperature. The temperature variance should be a maximum in the inversion due to the entrainment of anomalously warm air from above. Thus, the buoyancy term should be large there as well. It is the buoyancy term that drives the heat-flux-budget profiles in the inversion; as warm air is entrained and the buoyancy increases, the pressure and transport terms must respond to keep the layer in balance. The gradient production term also responds as the entrainment of warm air alters the temperature gradient.

Thus, the insufficient heat-flux-budget terms must be due to an inadequate generation of temperature variance through entrainment. In fact, this is true; the temperature variance in ADHOC in the inversion is an order of magnitude less than that simulated by LES (not shown).

The reasons for this relate to the sensitivity of the model to small changes in the pressure-term constant (see Fig. 17). A small change in this constant is enough to change the temperature variance at cloud top and create stronger buoyancy. This sensitivity is due to the complex problems involved with the handling of pressure, dissipation, and entrainment near the inversion in ADHOC (discussed in Section IV-A). In the current simulation, the overall "dissipation effect" was too large because of this problem. I believe the increase in dissipation was sufficient to inhibit the production of temperature variance in the inversion. Once again, the inclusion of a pressure parameterization which is consistent with the ADHOC framework of ADHOC may greatly help with this problem (see Appendix B). In the WD simulations, this problem does not affect the overall results, since the terms of the heat flux budget sum to zero for both ADHOC and LES.

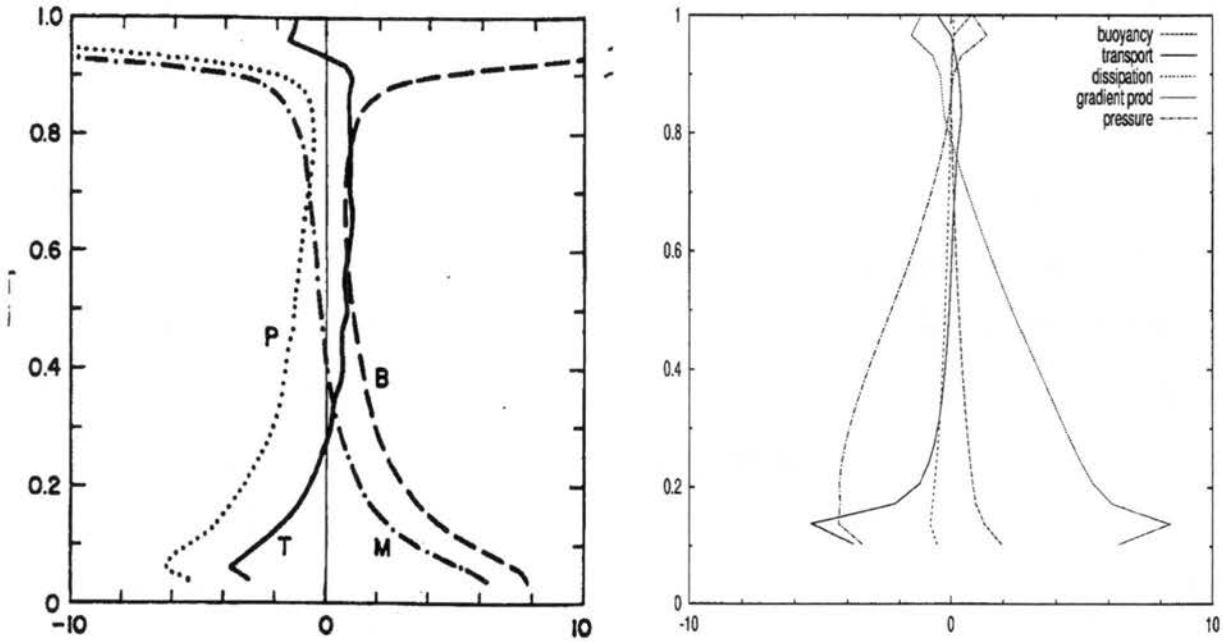

Figure 24: Dimensionless heat flux budget: Left: Moeng and Wyngaard's (1989) LES study of the convective boundary layer (B, buoyancy; M, gradient production; T, turbulent transport; P, pressure effect); right: ADHOC (lines as marked).

IV-B-1b: Summary of WD simulation

The WD case is one of pure "cloud-free" surface-driven convection. It is perhaps one of the least complicated and most understood turbulence regimes. Because the physics of this type of turbulence is well-understood (from LES models and observations), it is a good example to study in order to understand various strengths and shortcomings of a given model. In simulating WD with ADHOC, I gained some valuable insight in this regard.

In general the physics of a convective regime are well-represented with this hybrid MFC/ HOC model (ADHOC). One thing which I learned early on was that an SPS scheme was needed in conjunction with the mass-flux part of the model, so that small-scale eddies (such as those near the surface and near the inversion) could be better represented (Fig 12). In addition, the degree of homogeneity in the mixed layer is highly sensitive to the choice of a pressure constant (Fig. 17). In ADHOC, this is related to the problem discussed in Section IV-A, in which the dissipation and the pressure may overlap in function, giving rise to a dissipation rate which is too strong. The same problem does not occur at the surface when the turbulence is diagnosed with surface layer similarity.

Another thing which I learned about ADHOC was that it does not represent momentum transport well in convective regimes. I realized that simultaneously treating the transport of the horizontal momentum variance in a "local" manner and the vertical momentum variance in a "non-local" manner will not allow the horizontal momentum, generated near the surface and near the inversion, to efficiently mix into the middle of the PBL, where it is observed to exist.

In general, the turbulence statistics in a regime of surface-driven pure convection are well-represented with the ADHOC approach. The results here suggest that the inclusion of an "ADHOC-consistent" pressure parameterization and the incorporation of the momentum terms into the mass-flux framework will improve the solution and make it more robust (i.e., less sensitive to small changes such as pressure constants). In the next four sections, I will apply ADHOC to much more complicated regimes involving clouds. As we will see, the simple lessons that we learned here will help us analyze and better-understand the cloudy results. I will begin the discussion with the trade-wind regime, and then move on to stratocumulus and Arctic stratus.

IV-C: Trade-wind cumulus

The presence of trade-wind cumuli significantly intensifies the plume-scale atmospheric dynamics. The convective mixing of heat and moisture associated with these clouds increases the surface evaporation. This surface moisture source is transported downstream by the Hadley circulation and eventually serves as fuel for deep cumulus (Cu) convection in the intertropical convergence zone (ITCZ; Nitta, 1975; Yanai et. al., 1976). These deep Cu clouds are responsible for the energy transport needed to balance the export of potential energy in the outflow regions of the convection. This whole process is "fueled" by trade-wind Cu. Thus, in order to accurately represent large-scale dynamics in GCMs, we must first be able to accurately parameterize the effects of trade-wind Cu.

Locally, the effects of the trade-wind Cu are also important. In the subtropics, the environmental sounding is conditionally unstable, but only through a shallow layer. This promotes the development of shallow (often non-precipitating) clouds. Although Cu clouds in this regime are shallow, they are pivotal in maintaining the trade-wind inversion against the large-scale subsidence in the descending branch of the subtropical Hadley circulation (Riehl and Malkus, 1958). Deeper Cu activity, which is found near the ITCZ, is suppressed by subsidence in the trade-wind regime.

As warm, dry air descends across the trade-wind inversion, Cu clouds cool and moisten it. This cooling is produced by a combination of radiative cooling near cloud tops and evaporative cooling from liquid water deposited in the trade-wind inversion by the shallow Cu. Non-precipitating Cu clouds in this region (observed during BOMEX) transport water upwards and heat downwards through both condensation and the upward transport and evaporation of liquid water (Betts, 1973). While these processes act to destabilize and deepen the layer, the drying and warming due to large-scale subsidence balances the destabilization and allows a quasi-steady state to form. While shallow Cu clouds do transport heat, they provide no net source of heat if they do not precipitate (condensed water gets reevaporated within the layer). Radiative cooling in this system balances the total effect of adiabatic warming and the surface heat flux; the latter is quite small (Betts, 1975).

Observations show that trade-wind cumulus clouds have a three-layered structure: a subcloud mixed layer, a cloud layer, and a thin slightly stable layer between the two. The subcloud layer is typically well-mixed while the cloud layer is conditionally unstable (Fig. 26). A fourth layer (the trade-wind inversion) lies above the cloud layer. Unlike stratocumulus clouds, cumulus clouds exist in a dry, stably stratified environment, and their surrounding air (or environment) is non-turbulent. Modeling of the trade-wind Cu regime is complicated by these properties.

Despite the importance of the trade-wind Cu regime for the large scale dynamics, only a few schemes in operation in large-scale models treat shallow convection as part of a more general convection scheme [Tiedtke (1989), currently used in the ECMWF and Gregory and Rowntree (1990), operational in the U.K. Meteorological Office]. The cumulus parameterization of Arakawa and Schubert (1974) is technically able to represent these clouds; however, the number of clouds it produces is dependent on the number of vertical levels, which in GCMs is quite small in the boundary layer. Thus, in practice, the Arakawa-Schubert parameterization does not produce enough shallow clouds to fully represent this regime.

In most GCMs, shallow convection is ignored (Chapter I). The impact of including the trade-wind regime in convection schemes has been demonstrated by Tiedtke (1988). The main results were an increase in the surface evaporation above subtropical oceans by as much as 50 W m^{-2} to values more representative of those observed. Precipitation was enhanced by up to 10 mm day^{-1} in the ITCZ and there was a corresponding increase in the intensity of the Hadley circulation. This resulted in subtropical anticyclones that were stronger and more realistic. The necessity of accurately including the effect of the trade-wind Cu regime in large-scale models is clear from this study.

A number of detailed models have been used in attempts to simulate the trade-wind boundary layer (TWBL). Three-dimensional (3-D) LES models (Somméria, 1976; Cuijpers and Duynkerke, 1993; Schumann and Moeng, 1991) resolve Cu updrafts explicitly; two-dimensional (2-D) cloud ensemble models (Krueger, 1988; Krueger and Bergeron, 1994) cover a mesoscale domain; one-dimensional (1-D) HOC models make use of sub-grid scale condensation schemes (Bougeault, 1981a,b); and mixed-layer or "bulk" models (Betts, 1973; Albrecht, 1979) in which the boundary layer is typically one layer, and the turbulent fluxes in the PBL are computed from only the surface flux and the entrainment rate (for a detailed review of the simulation of trade-wind cumuli by HOC and mass-flux models, see Sections II-D-2b and II-E-1 respectively).

Although boundary layers containing Cu clouds are difficult to model, LES have had much success. Somméria (1976), using a 3-D LES, performed the first successful simulation of the TWBL. Although he noted several deficiencies, he was able to simulate in a realistic manner the Puerto Rico Field Experiment's observations (Pennell and LeMone, 1974). Later, Asai and Nakamura developed a 2-D version of this model and successfully applied it using data from the Air Mass Transformation Experiment (AMTEX). Recently, Siebesma and Cuijpers (1995) successful applied LES to the trade-wind Cu regime studied in the Barbados Oceanographic and Meteorological Experiment (BOMEX).

As discussed in Section II-E-1, previous models which have used MFC have been unable to address certain key issues of the trade-wind Cu regime. This is due to the fact that most mass-flux models employ first-order turbulence-closure schemes, which do not contain the necessary information to represent key processes in this regime (e.g., entrainment; see Sections II-E-1 and II-D for details). With ADHOC, we do not have the same limitations as previous mass-flux models because the equations contain additional information; those of the higher-moment statistics. In Sections IV-C-2b and IV-C-3b, I show results from simulations of two different trade-wind Cu cases; BOMEX and ATEX respectively. The setup for these simulations is that outlined by the Global Energy and Water Cycle Experiment Cloud System Studies (GCSS; Browning, 1994) boundary-layer workshops IV and V. In brief Sections preceding these (IV-C-2a and IV-C-3a), I will briefly review the meteorological conditions during these field projects, outline the initial conditions and the prescribed forcing for the simulations, and discuss the results. Before I progress to the results however, it is instructive to examine in more detail one final characteristic of trade-wind cumulus clouds, that of their differing updraft area fractions.

IV-C-1: What determines the updraft area fraction in the Trades?

Once of the biggest challenges in modeling the trade-wind regime is properly representing the updraft area fraction, σ. The trade-wind regime is a transition region between very narrow, energetic updrafts (and broad, non-turbulent downdrafts; $\sigma << 1$), which are found in tropical Cu clouds, and the more stratified mid-latitude Sc clouds (with their turbulent, saturated downdrafts; $\sigma > 0.5$). In BOMEX, the observed cloud fraction was near 20%, while in ATEX, it was closer to 50%. Despite this difference however, both are considered trade-wind cumulus cases. The questions that should be answered are: What determines the updraft are fraction in these regimes, and can ADHOC reproduce these conditions for BOMEX and ATEX?

The factors which determine the updraft area fraction in any regime are not clear. A couple of studies, however, have attempted to answer this question. Bjerknes (1938) proposed a very simple explanation to explain why σ becomes small in the tropics. He began his explanation from the equations

$$\frac{\partial T_{cld}}{\partial t} = w_{cld}(\Gamma - \Gamma_m) \tag{4.5}$$

and

$$\frac{\partial T_{env}}{\partial t} = w_{env}(\Gamma - \Gamma_d) \;; \tag{4.6}$$

where T is the temperature, Γ is the actual lapse rate, Γ_d is the dry adiabatic lapse rate, Γ_m is the moist adiabatic lapse rate, and the subscripts "*env*" and "*cld*" represent the environmental and cloud air respectively (or alternatively, the subsiding and rising motion respectively). With the use of Eq. 3.1 (the analogous version for $\bar{w}$), Bjerknes derived the following expression for the time rate of change of the buoyancy of a parcel of air:

$$\frac{\partial}{\partial t}(T_{cld} - T_{env}) = \bar{w}(\Gamma_d - \Gamma_m) + (w_{cld} - w_{env})[(1-\sigma)(\Gamma - \Gamma_m) + \sigma(\Gamma - \Gamma_d)] \;. \tag{4.7}$$

In a conditionally unstable sounding ($\Gamma_d > \Gamma > \Gamma_m$), the only term which can decrease the buoyancy in (4.7) is the last term. Thus, when $\sigma << 1$, the buoyancy will be as large as possible. Buoyancy in the saturated updrafts of a conditionally unstable regime will increase as the vertical velocity increases, while the it will decrease with increasing vertical motion in the unsaturated downdrafts. In other words, the larger w_{up} and the smaller w_{dn}, the greater the convection. Large w_{up} and small w_{dn} are both favored by small σ according to (4.7).

A similar result was found using a very different approach by Randall (1987). He derived an expression for the buoyancy and liquid water fluxes in partly cloudy layers (e.g., most trade-wind cumulus regimes), without using lapse rates in the analysis. The partly-cloudy buoyancy flux equation obtained by Randall (1987), which was derived using a straight forward application of a mass-flux model, can be written as

$$\overline{w's'_v} = (1-\sigma)(\overline{w's'_v})_{cld} + \sigma(\overline{w's'_v})_{env} + M_c[1-(1+\delta)\varepsilon]L_v\tilde{l} \ , \tag{4.8}$$

where $\delta = 0.608$, $\varepsilon = (C_pT)/L_v$, $C_p = 1004\,\mathrm{J\,kg^{-1}\,K^{-1}}$, $L_v = 2.52x10^{-6}\,\mathrm{J\,kg^{-1}}$, and $\tilde{l}$ is the amount of liquid water that would have to be isobarically evaporated into the mean state to bring it to saturation. This expression shows that the contribution of the positive buoyancy flux in the cloud to the mean buoyancy flux is largest when σ is smallest; the same result that Bjerknes found with an analysis of lapse rates.

With both this discussion and that of Section IV-C in mind, we are now ready to examine the ADHOC results of two very different trade-wind cumulus cases; BOMEX and ATEX.

IV-C-2: BOMEX

BOMEX took place 22-30 June 1969 near Barbados. It was designed to study the atmospheric trade-wind regime and its associated cloudiness. During the study, the conditions evolved from an "undisturbed" to a "disturbed" period (from the point of view of the large scale interaction with the Cu convection). The "undisturbed" period (22-26 June 1969) was characterized by downward motion below 500 mb, an apparent heat sink and moisture source[7] near the top of the inversion (located near 800 mb), and a substantial small-scale eddy moisture flux confined below the inversion. The heat budget during this phase was dominated by radiative cooling and a surface sensible heat flux. Approximately 2/3 of the sensible heat input at the surface was lost through radiation and the rest heated up the mixed layer. The sensible heat flux at the top of the mixed layer is small during the "undisturbed" period. The moisture budget during this period is dominated by a balance between the incoming surface latent heat flux and the moisture flux out of the mixed-layer top. Less than 10% of this flux is used to moisten the mixed layer. During this period, cloud fraction was approximately 20%. The disturbed period (27-28 June 1969) came as a mid-level trough passed through and weakened the inversion. This disturbance induced low-level convergence and upward motion at low levels and a heat flux from the Cu convection which extended to 500 mb.

IV-C-2a: GCSS BOMEX case

The GCSS (GEWEX Cloud System Studies) Boundary Layer Cloud working group aims to improve physical parameterizations of clouds and other boundary layer processes, and their interactions. To achieve this, the GCSS group designs intercomparison studies between observational or laboratory case studies, and a wide variety of boundary-layer models. The BOMEX GCSS trade-wind cumulus case was set up by Pier Siebesma of the Royal Netherlands Meteorological Institute (KNMI; http://www.knmi.nl/~siebesma/bomex.html). For this intercomparison study, the BOMEX undisturbed period from 22-26 June was chosen for the following reasons: there were no mesoscale complications; there were no transitions from/to or remains of stratocumulus (Sc); the clouds were non-precipitating; and observations show that the small-scale turbulence in the clouds was in quasi-steady state with the large-scale forcing.

Ideally, it would have been best to initialize the profiles of the thermodynamic and dynamic variables with the average values observed during the 5-day undisturbed period and run

---

[7]. The "apparent" moisture and heat sources and sinks refer to any process other than large-scale advection that contributes to the heating or moistening of the cumulus cloud layer. Observations show that the sum of the local tendency and large-scale advective terms are not equal to zero for these clouds. Thus, we conclude that a source or sink must exist. Because it is difficult to observe the sources and sinks directly, we deduce that they are there from the large-scale budgets; hence the term "apparent". This terminology was first used by Yanai et. al., 1973.

the model using the diagnosed large-scale forcing. However, this was not feasible since the temporal and spatial variations of the fields are such that an actual inversion, such as appears on most individual soundings, is not found in the mean soundings (Nitta and Esbensen 1974). Therefore, a mean profile over a shorter period was selected from the BOMEX Rawinsonde Atlas (1975). In this sounding, a well-defined steady state with a strong inversion was present. Four important forcings for the run were prescribed (see Table 2); large-scale subsidence (one typical of a large part of the trade-wind regime), radiative cooling, large-scale advective drying below 500 m (no temperature advection), and surface sensible and latent heat fluxes (8×10^{-3} K m s^{-1} and 5.2×10^{-5} m s^{-1} respectively). In addition, a surface pressure of 1015 mb and surface temperature of 300.375 K were prescribed. Figures 25-26 show the prescribed forcing and mean state initial profiles (for a summary of the model set-up and forcing, see Table 2).

For this simulation, I use the "case-specified" grid resolution of 40 m and a timestep of 0.5 seconds. I run the model for 16 hours and time-average the fields for the last four hours. It is these time-averaged fields that are shown in Figs. 27-36. In these figures, the results are compared with both observational data (where available) and LES results. The observations include data from rawinsondes and the large-scale heat and moisture budgets deduced by Holland and Rasmusson (1973), Nitta and Esbensen (1974), and Esbensen (1978). One weak point of BOMEX is that there is little cloud data available. Thus, the main intercomparison with observations are limited to averaged properties of the mean state and various turbulent fluxes. To supplement the observations, I do a systematic intercomparison of the ADHOC and LES simulations. The LES models used for comparison in this study are University of California, Los Angeles (UCLA), the University of Washington (UW); the Royal Netherlands Meteorological Institute (KNMI), the National Center for Atmospheric Research (NCAR), and the Max Planck Institute in Hamburg, Germany (MPI).

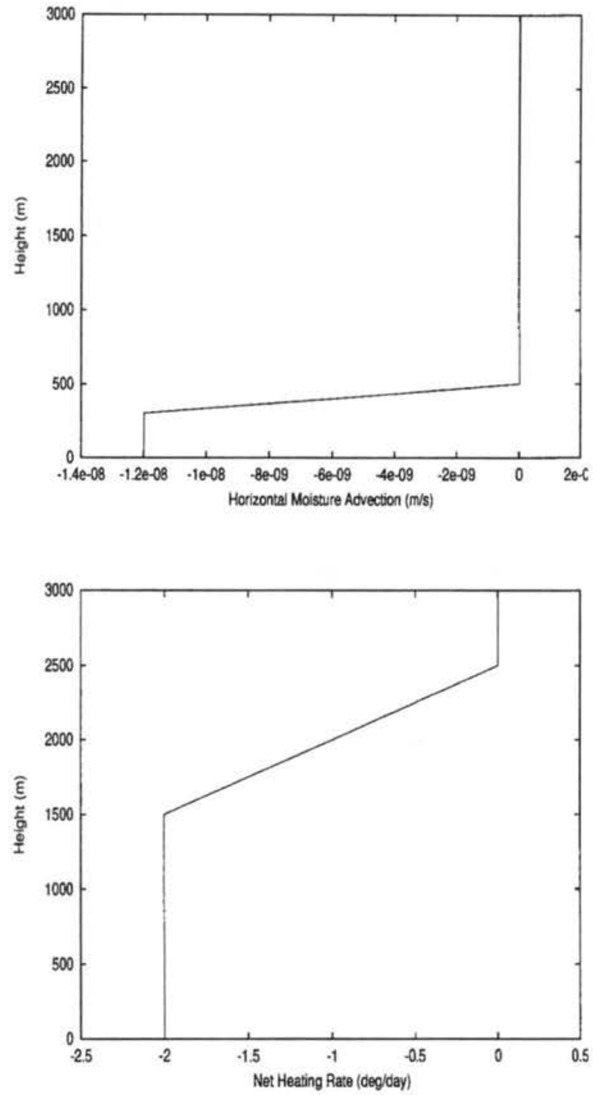

Figure 25: Initial prescribed forcing and winds for the BOMEX GCSS case. Top left: horizontal moisture advection; top right: subsidence velocity; bottom left: net radiative heating rate (negative is cooling); bottom right: zonal winds, dashed line is the mean wind and solid line is the geostrophic wind. The meridional mean and geostrophic winds are initially set to zero.

IV-C-2b: Results and discussion

In this section, I will show results of the mean state, turbulent fluxes, momentum variances, and various aspects of the TKE budget from BOMEX. Observations are shown where

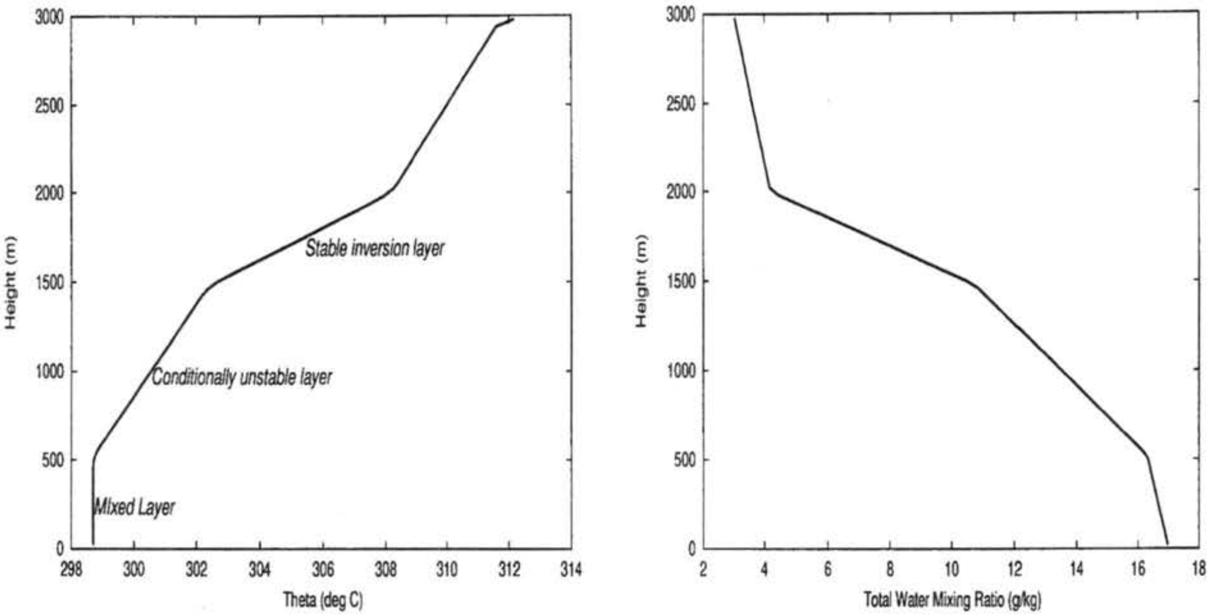

Figure 26: Initial profiles of the liquid water potential temperature (left) and total water mixing ratio (right) for BOMEX. The three-layered structure of trade-wind cumuli are so marked.

available. It is important to keep in mind that a comparison of ADHOC with observations must only be viewed in qualitative sense. The BOMEX GCSS case is highly "idealized"; the large-scale and surface forcing are constant and cannot adjust to the evolving dynamic and thermodynamic fields (see Table 2). In the "real atmosphere", the system obviously adjusts. Thus, by comparing this idealized case to observations, I look in particular for the model to represent the "shape" of the profiles, rather than the actual values which are highly tied to the observed forcing. In addition, an important aspect of this case is that all the forcing is completely "rigid" (see footnote, page 144 and Table 2 on page 145), even the height at which the radiative forcing is applied. As I discussed in Section IV-A, this significantly affects the results (Fig. 18). Many of the differences seen in this simulation are a direct result of this, as well as some of the other problems discussed in Section IV-A.

Figures 27-30 are profiles of the simulated and observed mean state. Overall, ADHOC is able to represent the observed wind, temperature, and moisture profiles observed during BOMEX. A comparison of the winds with observations (Fig. 27) shows that ADHOC adjusts to the initial wind profile (Fig. 25) in a manner that is consistent with observed winds. The meridional wind (V) has the wrong sign above the surface layer, but its magnitude is small and relatively insignificant. LES models are also unable to reproduce the sign of the meridional wind (Fig. 28); thus, this is likely an artifact of the GCSS idealized forcing and initial conditions (Figs. 25-26). The zonal component of the wind (U) looks quite similar to the observations in both shape and magnitude; the notable exception being that the maximum wind occurs at a lower height in the observations than in the ADHOC simulation. In ADHOC, the height of the maximum U wind corresponds to the cloud-top level, where vertical velocity is quickly converted to horizontal velocity (via the pressure terms; see Section II-C-1). The observed U wind maximum is located roughly at cloud-base height. LES simulations support the zonal wind peak location simulated by ADHOC (Fig. 28).

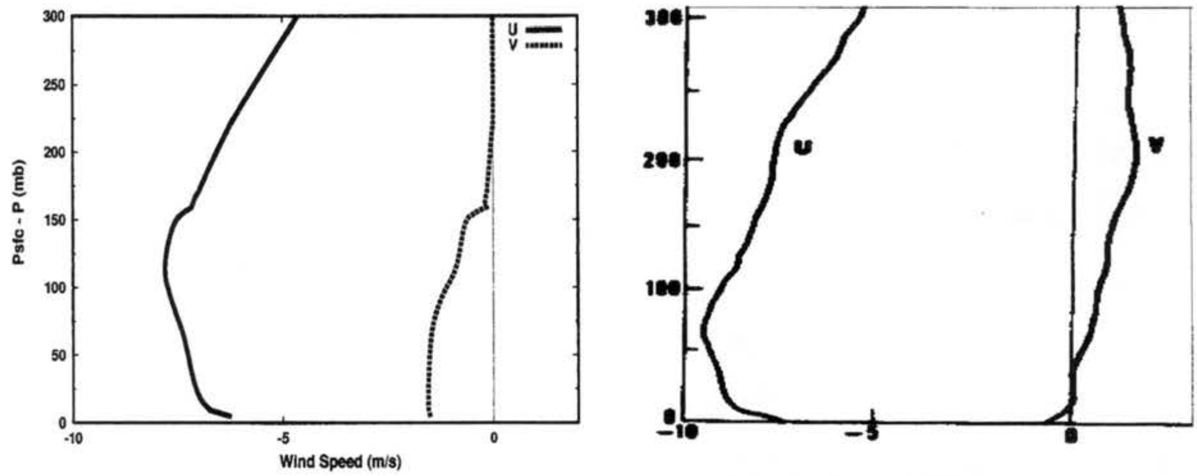

Figure 27: Comparison of the simulated mean winds (left) with BOMEX observations (right). The BOMEX observations are from Holland and Rasmusson (1973).

Figure 28 is a comparison of the steady state winds simulated by ADHOC and by various

LES models. ADHOC represents the zonal wind nicely, but produces an "over-active" meridional wind throughout the PBL. It is difficult to say why this occurs. The meridional wind equation consists of a coriolis term, a flux divergence term (transport), and a vertical advection term (subsidence) (Eq. A.2). Due to the fact that the geostrophic wind is prescribed, and the zonal wind component agrees with LES, the coriolis force is not responsible for this discrepancy. In addition, the vertical advection is "rigid" with a prescribed subsidence profile. Thus, the culprit must be the transport term. A comparison of the meridional wind fluxes ($\overline{w'v'}$) between ADHOC and LES (not shown) show that ADHOC does in fact produce fluxes which are too large. The reason for this likely relates to both the "ADHOC-inconsistent" manner in which the momentum terms are handled and the "rigid" BOMEX large-scale and surface forcing (Section IV-A; Fig. 18; Table 2 on page 145). I believe that the eventual incorporation of the momentum terms into the ADHOC framework will help with this problem.

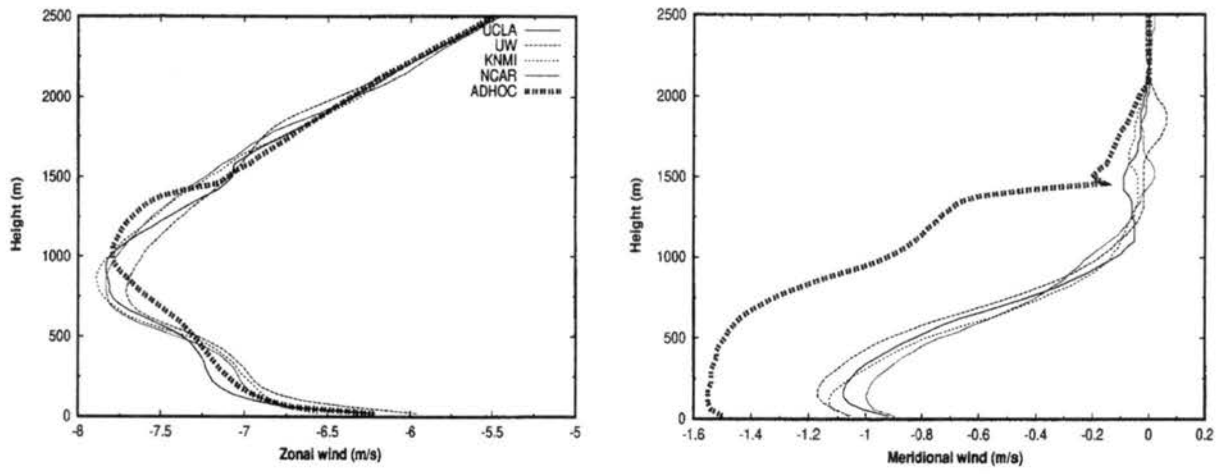

Figure 28: Comparison between ADHOC and LES simulations of the BOMEX zonal (left) and meridional (right) mean winds. The darkest line is ADHOC, while all other lines are the indicated LES models.

The thermodynamic quantities are completely "ADHOC-compatible" with the exception of the pressure terms. Figures 29-30 show a comparison of the observed dry static energy and total water mixing ratio with those simulated by ADHOC. ADHOC nicely captures the "3-layer" structure of this profile; the well-mixed layer, the conditionally unstable cloud layer, and the inversion layer (Fig. 26). However, the model is too "cold" by a nearly-constant amount throughout the PBL. Since the LES-simulated dry static energy agrees with ADHOC (not shown), this must be related to the specifics of GCSS setup for this simulation (e.g., the fact that the sea-surface temperature is set to a constant value of 300.375 K).

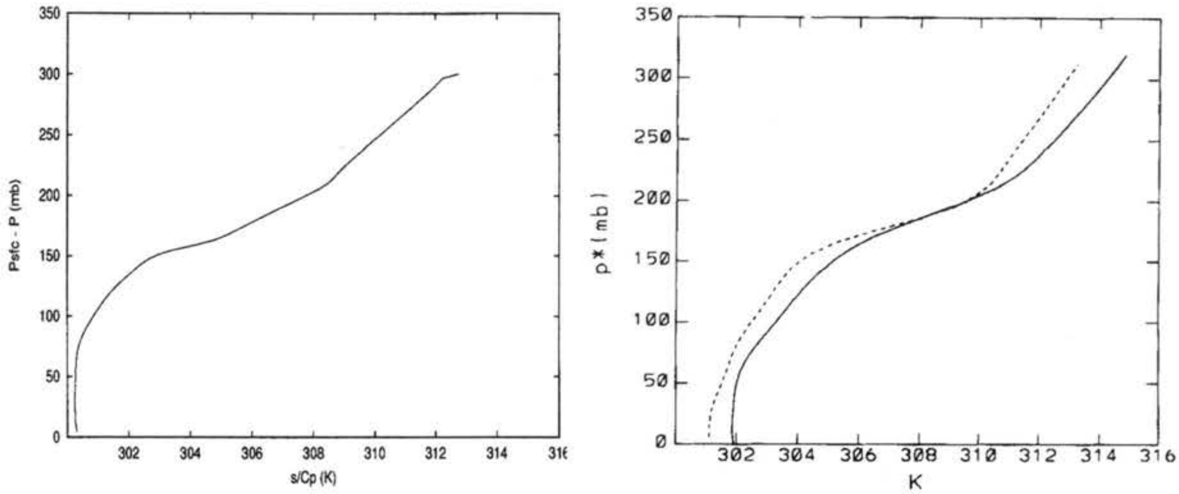

Figure 29: Comparison of the simulated dry static energy (left) with BOMEX observations (right, solid line). The dotted line on the right is from the 2-D cloud resolving model simulations of Krueger and Bergeron (1994).

Figure 31 shows comparisons between the ADHOC and LES simulated mean liquid water potential temperature and liquid and vapor mixing ratios. While the shapes are well-represented, the mixed layer is slightly too warm and too dry; the cloud layer is slightly too cold and too wet; and the lower part of the inversion is again slightly too warm and too dry. It is not clear to me why this is so. For the GCSS BOMEX case, most of the 1-D models produced similar results (http://www.knmi.nl/~siebesma/bomex.html). A possible reason is the "rigid" forcing prescribed in BOMEX. Figure 18 shows that (for ATEX), when radiative forcing is "rigid", the cloud layer is

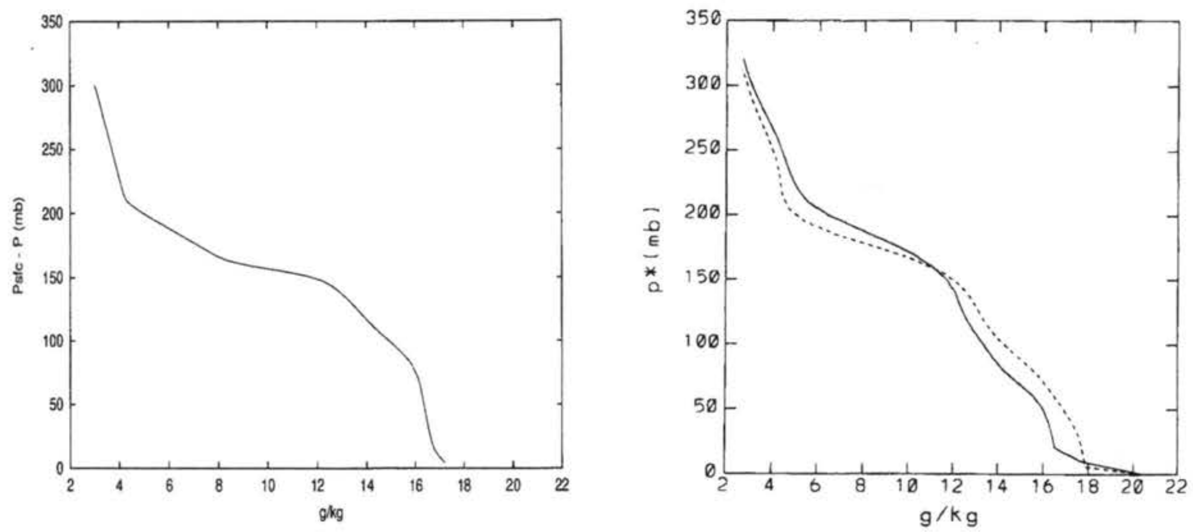

Figure 30: Comparison of the simulated total water mixing ratio (left) with BOMEX observations (right, solid line). The dotted line on the right is from the 2-D cloud resolving model simulations of Krueger and Bergeron (1994).

cooler and the inversion layer is warmer. While these results were from ATEX, they suggest that a similar mechanism could be affecting the BOMEX results as well.

Solely within the context of the 1-D turbulence equations, however, there are many possible explanations for why this would occur. These explanations range from direct effects such as the flux profiles having an incorrect slope (perhaps caused by equation constants which are not "tuned" specifically for this case), to less tangible feedback effects. For example, a cloud layer which is too moist and too cold may be caused by inefficient entrainment. If true, the effect may be further reinforced by the following feedback process: Entrainment at cloud top gives an upward moisture flux because the entrained air is drier than air in the PBL. Inefficient entrainment would thus lead to less entrainment drying, which would support a smaller upward moisture flux at all levels. This smaller upward moisture flux makes the buoyancy less strong which makes the turbulence weaker. Weaker turbulence, in turn, makes the entrainment weaker, and thus, the layer will not dry out as quickly. Many other possible feedback mechanism such as this exist because the turbulence equations are highly coupled.

However, with the BOMEX forcing so "rigid", there are few ways for the PBL to "express" itself and initiate these feedbacks (regardless of the manner in which the PBL evolves, the surface and large-scale forcing remain the same). Thus, the only manner through which the PBL can adjust itself in the BOMEX simulation is through the entrainment process. When the PBL prescribed forcing is too large, the turbulence increases; thus, entrainment should increase, and the PBL should grow to accommodate the additional energy. Likewise, when the forcing is too small, entrainment is not initiated and the PBL should not grow. In this highly idealized case, entrainment is the "boss" of the PBL. With this in mind, a PBL top which is too cold and too moist must be explained by inefficient entrainment (for this case). The reason for the inefficient entrainment is related to the manner in which I handle turbulence at the PBL top. This is discussed in great length in Section IV-A. I believe that both the "pressure-dissipation problem" and the "weak turbulence problem" both contribute to this problem. Thus, I believe that an "ADHOC-consistent" manner of handling the pressure terms and a better method for extinguishing artificial turbulence (one that does not affect the turbulence generated in the stable layer next to cloud top) is needed to bring the ADHOC simulation of temperature and moisture closer to that of the LES simulation.

Before moving on to the discussion of the fluxes, I would like to mention the liquid water mixing ratio in the cloud, which seems unrealistically large (Fig. 31). Another artifact of 1-D models in this simulation is that they produce clouds which are too wet. At the GCSS BOMEX intercomparison workshop, I learned that most 1-D models produced clouds with liquid water mixing ratios from 5-10 times larger than those simulated by LES. I believe this is caused by the imposed "rigid" forcing (see liquid water mixing ratio plot in Fig. 18). In ADHOC, however, the value is closer to 15 (Fig. 31). I believe that the additional difference in ADHOC is due to the reasons discussed above; the fact that cloud-top turbulence may be artificially killed by imposing condition (4.1), and that overly-active dissipation at the PBL top may render the entrainment process (which would dry the out the cloud layer) inefficient (Section IV-A). However, there may be another explanation which contributes as well: Sensitivity studies performed with the model show that, when the surface fluxes are *not* prescribed, the evolution of the cloud is highly dependent on the surface transfer coefficient. Perhaps the prescribed forcing in the idealized case setup is analogous to the use of a transfer coefficient which is too large. In this simulation, I am able to decrease the liquid water content in the cloud by manually setting the transfer coefficient to smaller values than those implied by the prescribed forcing. This is supported by the observational analysis of Ching (1975). For example, the transfer coefficients implied by the surface forcing are on the order of 2×10^{-3} (of course this depends on the simulated surface-layer air temperature). Observations show that this value should be approximately 1.3×10^{-3} (Ching, 1975).

Flux intercomparisons may give us more insight into the ADHOC-LES differences in the mean-state. Figures 32-34 show the fluxes simulated by ADHOC, along with those simulated by LES and observed (where available). Figure 32 shows that ADHOC is able to simulate the shape of the observed moist static energy flux profile. Near the surface, there is a little "dip" in the simulated flux. This is due to omission of the SPS fluxes from these plots. The addition of the SPS contribution to the moist static energy flux smooths out this "dip". The flux profile has a constant slope below cloud base, indicating that the layer is well-mixed. In general, the flux is too small, but is tied to the prescribed surface flux which is set to approximately 160 W m^{-2}.

Figure 33 depicts the observed and simulated fluxes of water vapor, liquid water, and virtual and dry static energies. They are placed on one plot to show their relative magnitudes. ADHOC nicely represents the shape of these profiles, as well as the relative magnitudes of the fluxes themselves. The sensible heat flux is downward, with a maximum at cloud base in both the

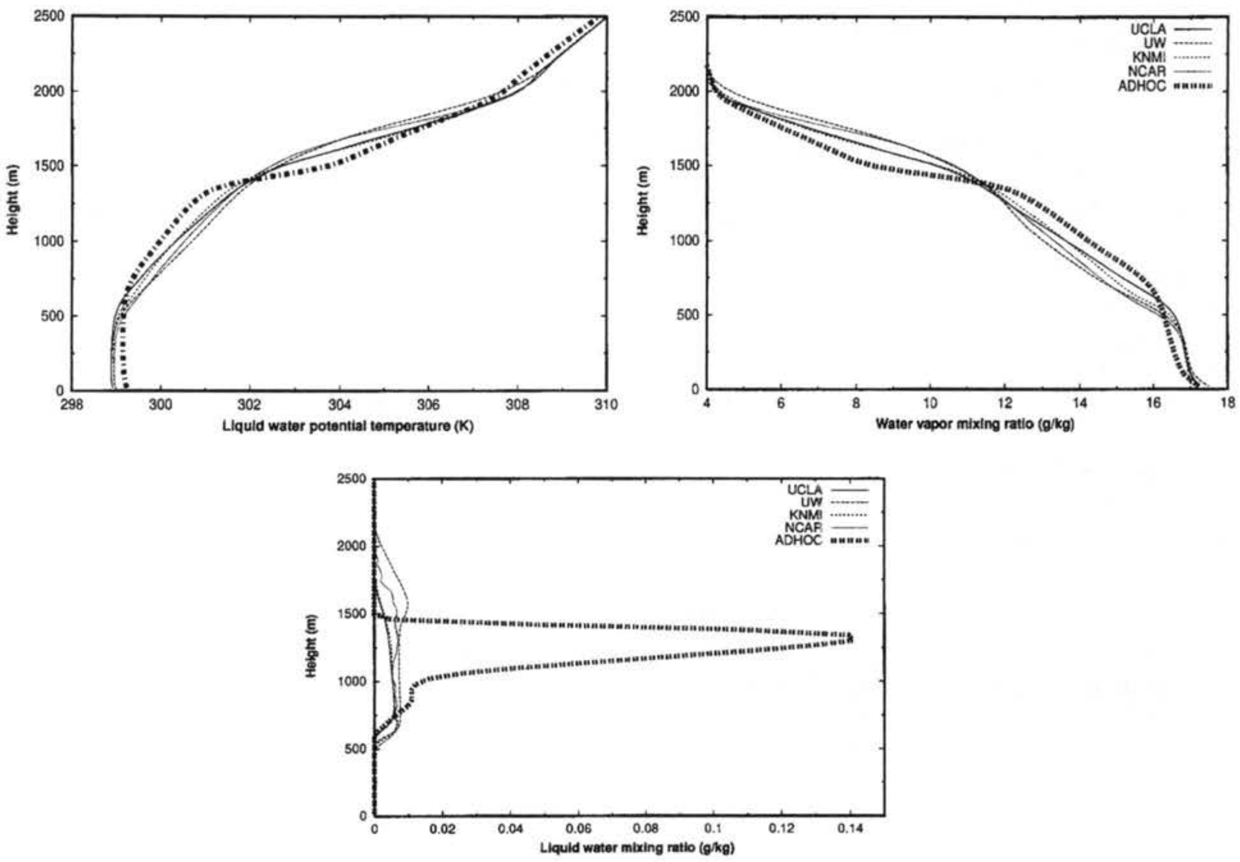

Figure 31: Comparison between ADHOC and LES simulations of the BOMEX liquid water potential temperature (top, left) and water vapor mixing ratio (top, right) and liquid water mixing ratio (bottom). The darkest line is ADHOC, while all other lines are the indicated LES models.

observations and the simulation. The profiles of the virtual and dry static energies are parallel below the cloud, but merge together as cloud top is approached. In ADHOC, the two are practically the same value in the upper-cloud layer. This means that the effects of buoyancy are no longer felt there (i.e., the increase in buoyancy due to large amounts of water vapor is offset by the decrease due to liquid water). The liquid water flux is non-zero starting at cloud base and increases to its maximum value just below cloud top. This increase at cloud top is not observed and likely has to do with the inefficient entrainment drying discussed above. It is interesting that, the buoyancy flux also shows a maximum near cloud top despite the large value of the liquid

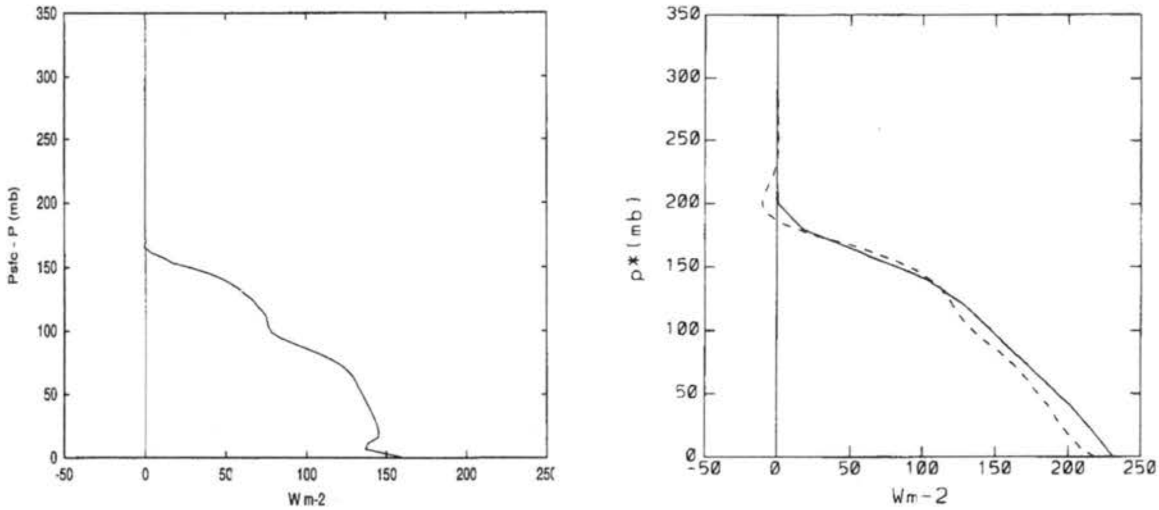

Figure 32: Comparison of the simulated moist static energy flux (left) with BOMEX observations (right, solid line). The dotted line on the right is from the 2-D cloud resolving model simulations of Krueger and Bergeron, 1994.

water loading there. It is clear that the maximum in the sensible heat flux which occurs at this height outweighs the liquid water loading effect on the virtual static energy flux. The maximum in the sensible heat flux is a results of the condensational heating.

We now switch our attention to look at the magnitudes of these fluxes (as opposed to just their shape) by comparing the BOMEX simulation directly with LES. Figure 34 shows the ADHOC and LES results for the fluxes of momentum, total water, liquid water, and liquid water potential temperature. In all cases, ADHOC nicely captures the magnitude of these fluxes. The fluxes depicted are comprised of the sum of the large scale and the SPS contributions. In general, the main differences between the two simulations reside in the upper boundary layer. There are three likely contributors to the disagreement: inefficient entrainment due to "pressure-dissipation problem" (Section IV-A); the "rigid" forcing problem (Fig. 18; footnote on page 144); and the "weak turbulence problem".

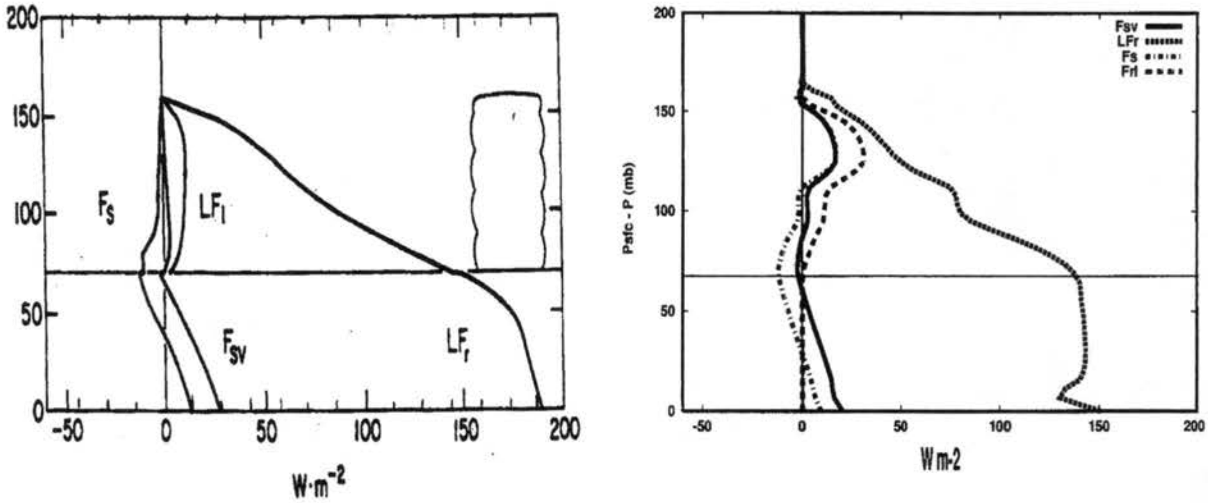

Figure 33: Comparison of the BOMEX-simulated (right) and observed (left) fluxes of dry static energy (Fs), virtual dry static energy (Fsv), total water (Fr), and liquid water (Fl). The observed profiles are from Esbensen (1978).

While inefficient entrainment is likely the cause of the thermodynamic fluxes being too small near the cloud top, the sharp decrease in the liquid-water flux may represent additional problems associated with enforcing condition (4.1). However, it is quite encouraging that the maximum liquid water fluxes of ADHOC and the LES are quite close in magnitude. Since the liquid water mixing ratio is too high, but the liquid water flux is not, the difference between the updraft and downdraft liquid water mixing ratios must be correct (Eq. 2.2). Due to the close agreement between ADHOC and LES in the lower half of the boundary layer, it appears as if a better treatment of turbulence at cloud top (which would allow the boundary layer to grow and fluxes to extend higher) may bring the results closer together in the cloud layer as well. A large part of this problem would be solved by removing the "rigid" forcing and by implementing an "ADHOC-consistent" method to handle the pressure terms (Appendix B).

Finally, Figures 35-36 relate to the TKE; Fig. 35 shows the horizontal and vertical velocity

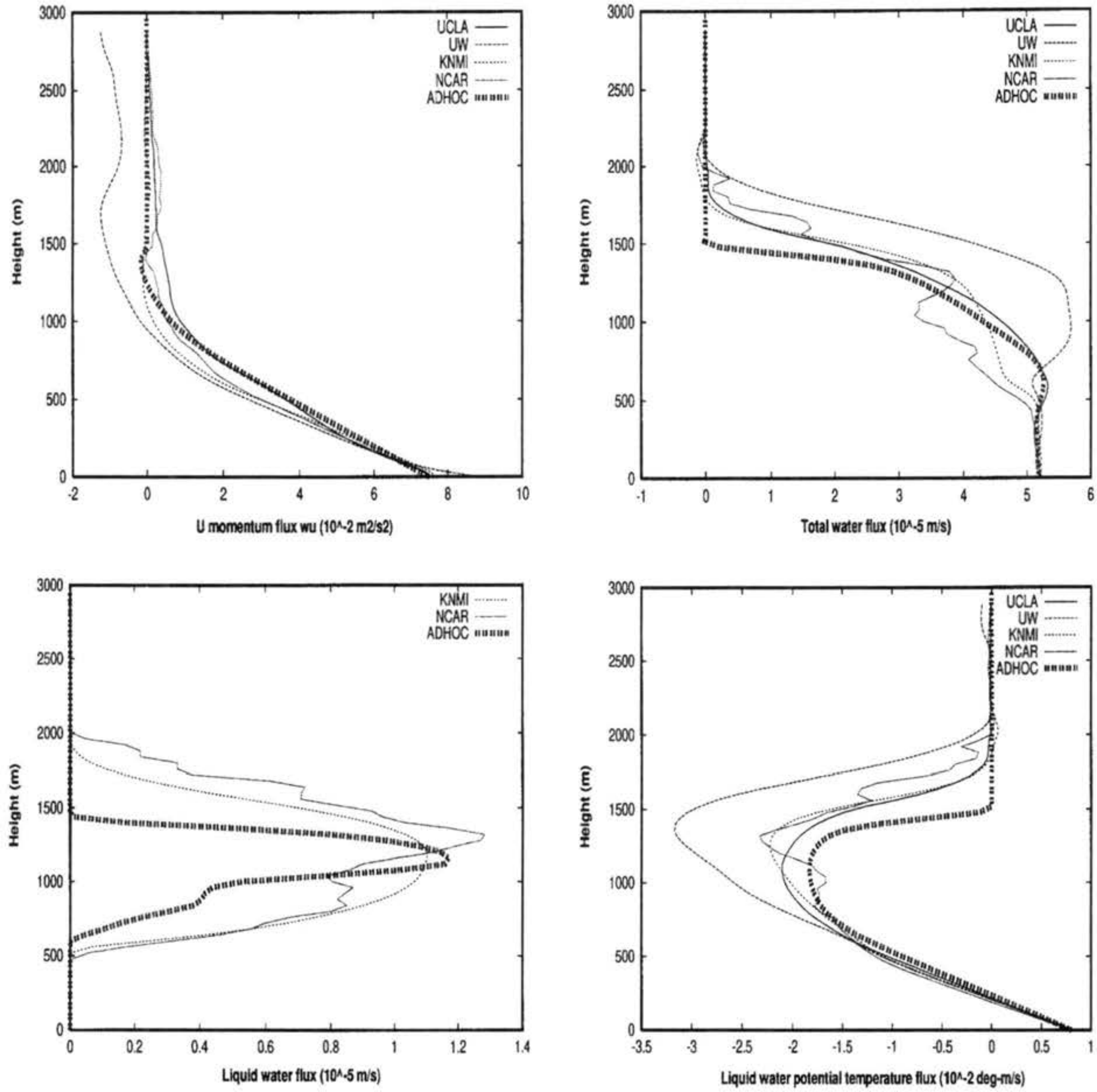

Figure 34: Comparison between ADHOC and LES simulations of the BOMEX zonal momentum flux (top, left); total water flux (top, right); liquid water flux (bottom, left); and liquid water potential temperature flux (bottom, right). The darkest line is ADHOC, while all other lines are the indicated LES models.

variances and Fig. 36 shows the terms which comprise the TKE (total variance) budget. The vertical velocity variance ($\overline{w'w'}$) plot shows quite nicely the combined effects of inefficient entrainment (due to the pressure-dissipation problem discussed in Section IV-A) and the "rigid" forcing. For example, in Fig. 18, $\overline{w'w'}$ is inhibited from rising beyond a certain level if the forcing is "rigid" in ATEX; this is quite similar to what we see in the $\overline{w'w'}$ plot for BOMEX (Fig. 35). The momentum variances in the LES slowly taper off to zero above cloud top (part of this may be due to gravity waves), while they sharply drop to zero directly at cloud top in ADHOC. A more accurate incorporation of the effects of entrainment would help make this transition smoother and bring the results closer to those of LES models. This would likely result if the surface forcing was not "rigid" (Fig. 15; footnote on page 144) and the "dissipation-pressure problem" (Section IV-A) was resolved with an "ADHOC-consistent" handling of the pressure terms. To some degree, the "weak turbulence problem" could also be playing a role.

In the PBL, both the ADHOC and LES models show a double peak in the horizontal and vertical momentum variances. This is expected as turbulence should be large near the surface, where it is generated by surface fluxes, and in the cloud, where it is generated by latent heat release and cloud top radiative cooling. ADHOC is able to simulate this physically realistic feature of the boundary layer. In addition, both indicate that, overall, $\overline{w'w'}$ is larger than $\overline{u'u'} + \overline{v'v'}$ and that the double peaks in $\overline{u'u'} + \overline{v'v'}$ are closer in magnitude than the double peaks in $\overline{w'w'}$. In the LES results, the lower peak is actually comprised of two narrower peaks, while in the ADHOC results, the lower peak resembles the two narrow LES peaks connected together (with no minimum in between). I am not sure why the LES produces this result, but it occurs in all four LES simulation, and thus appears to be a robust feature. A possible cause for the lack of this feature in ADHOC may be the inconsistent treatment of the pressure terms at the surface (see Section IV-A).

The lower height of the upper peak in ADHOC is also a combined result of the pressure problem and the "rigid" forcing, as is the smaller magnitude of ADHOC peak in $\overline{u'u'} + \overline{v'v'}$. The latter difference may be an indicator that specifically the "return-to-isotropy part" of the pressure term (Sections II-C-1 and III-H) is the culprit near cloud top, since all three components of the velocity variance are similar or "isotropic" in magnitude.

As an interesting addition, I included a comparison plot of the skewness of the vertical velocity in Figure 35. The LES models indicate a positive skewness (updraft area fraction less than 1/2; Eq. 2.9) throughout the PBL. The skewness reaches a maximum in the middle of the cloud with a secondary maximum just below the cloud. In the atmosphere, thermals which rise from the surface contain different amounts of energy and thus, stop at different levels. Thus, in the convective PBL, we would expect to find less and less updrafts the higher that we look; less updrafts area indicates a smaller σ and a larger (positive) skewness. This is simulated nicely by the LES. At cloud base, one would expect to see a slight decrease in the skewness as latent heat release initiates some additional updrafts. This is also nicely depicted in the LES. Finally, the fact that the skewness is never negative is indicative of the fact that cloud-top radiative cooling is not an important forcing mechanism in the LES simulations [cloud-top cooling initiates narrow downdrafts and negative skewness (Eq. 3.7) in the same manner that surface heating initiates narrow updrafts and positive skewness (Randall, 1980)].

The skewness simulated by ADHOC is quite different than that simulated by LES, although it is not as bad as it appears. Near the surface, the skewness increases in a similar manner to the LES skewness. However, it is important to keep in mind that the cloud in ADHOC is (1) narrower (with cloud base occurring higher and cloud top occurring lower); and (2) wetter. Thus, we would expect the relative minimum in the skewness (which occurs due to cloud base latent heating) to be higher and more pronounced in the boundary layer. This is exactly what we see; the minimum occurs near the ADHOC cloud base and appears to be a more prominent feature in the profile. The skewness increases again in the cloud, but never reaches values as large as those in the LES. This is likely due to a combination of (1) the fact that more latent heat is released in the wetter ADHOC cloud (insuring that most thermals reach cloud top) and (2) the fact that the skewness is slightly negative at cloud top indicating that cloud top radiative cooling may be counteracting the increase in skewness that would otherwise occur.

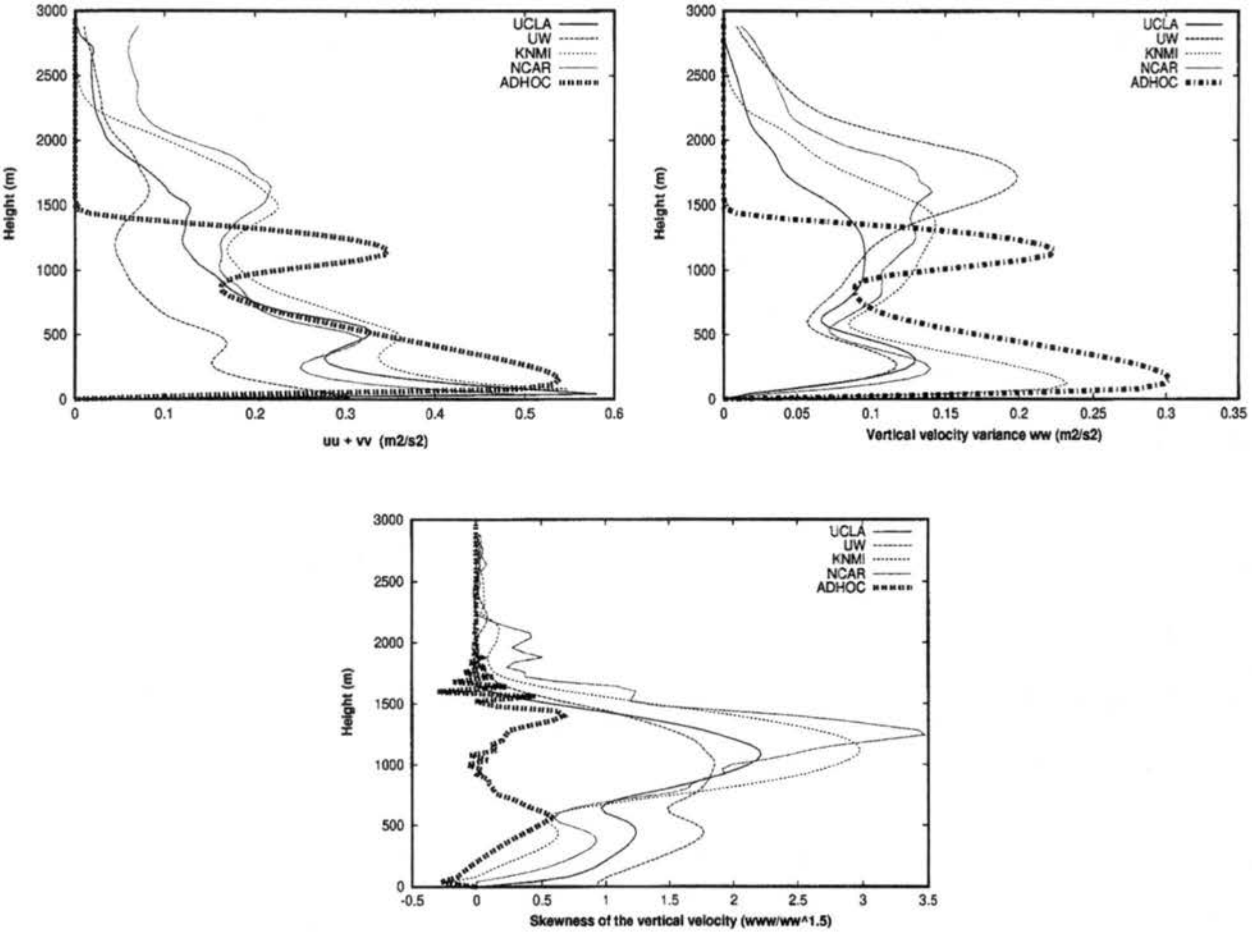

Figure 35: Comparison between ADHOC and LES simulations of the BOMEX horizontal velocity variance (top, left); vertical velocity variance (top, right); and skewness of the vertical velocity (bottom). The darkest line is ADHOC, while all other lines are the indicated LES models.

The final BOMEX comparison plots that I will show are the TKE budget profiles (Fig. 36).

These types of plots (budget study plots) give us insight into the relative importance of the mechanisms which comprise the turbulence. Figure 36 shows profiles of the buoyancy and shear production, as well as the turbulent transport and the dissipation of the total TKE. The differences between ADHOC and LES here are related to (1) the differences in the location of the cloud; and (2) the inefficient cloud-top entrainment previously discussed: The ADHOC-simulated buoyancy has the right shape and magnitude, but is large over a narrower range than the LES; the shear term has the correct shape, only the maximum that occurs at cloud base is higher in ADHOC than in the LES; the turbulent transport shows the export of TKE from the surface to the subcloud layer and from cloud base to cloud top (TKE is basically transported out of regions where it is produced); and the dissipation is largest where the TKE is largest.

I will leave a summary of the results of BOMEX until after ATEX is discussed in the next section. The results are more physically interesting in the context of both trade-wind regimes analyzed together. ATEX is different than BOMEX in subtle, but physically important ways. It is also a GCSS-designed case; one whose forcing is only "semi-rigid" (see footnote, page 144; Table 2 on page 145). As you will see, ADHOC is better able to simulate this regime for reasons that will explained in detail in the next section.

IV-C-3: ATEX

ATEX was also designed to increase our understanding of the trade-wind Cu regime and its effects on the large scale circulation (Augstein et al., 1973). The experiment took place in the Northeast Atlantic trades in February of 1969. ATEX is an "upstream" version of BOMEX; the trade inversion is much stronger and the mixed layer is somewhat deeper than what was observed during BOMEX, and cloud fractions were close to 50%. In contrast to BOMEX, the cloud and mixed layers are significantly cooler, but only slightly drier (the cloud layer has a much higher relative humidity). The sounding is nearly saturated at the base of the trade inversion.

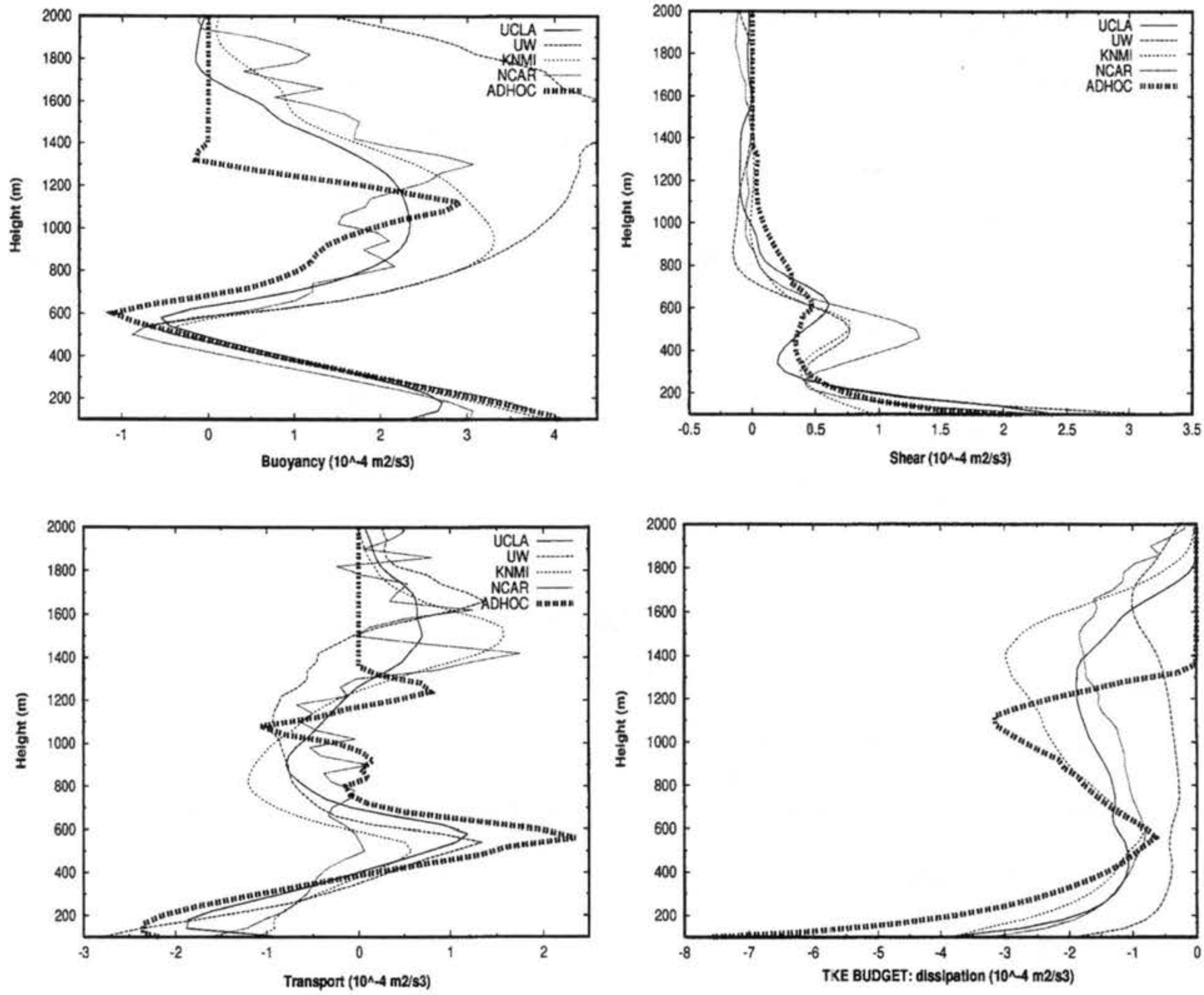

Figure 36: Comparison between ADHOC and LES simulations of the TKE budget for BOMEX. Top left, buoyancy; top right, shear; bottom left, turbulent transport; bottom right, dissipation. The darkest line is ADHOC, while all other lines are the indicated LES models.

For purposes of analysis the experiment is usually divided into two parts. The first period consisted of a "nearly classical" trade-wind situation with remarkably steady NE winds below the trade inversion, and generally suppressed conditions with no precipitation. During this period, the lowest 500 m temperature gradient was dry adiabatic and the humidity was well-mixed. The second period of ATEX was more disturbed, with the northern fringes of the ITCZ overlapping the southern portion of the study area. During this period a few cumulonimbi were observed. The current analysis, and most of the literature, is based on the first period.

IV-C-3a: ATEX GCSS case

The ATEX GCSS case was setup by Bjorn Stevens of the University of California at Los Angeles (UCLA; http://www.asp.ucar.edu/~bstevens/atex/overview.html). It was based on the relatively undisturbed period of ATEX. The composite sounding that is used is based on five days of observations. The sounding (provided by Bruce Albrecht of the University of Miami) was constructed by identifying the transition layer and the trade-inversion in individual soundings and then preserving the jumps across these layers in the averaging process. A nice feature of the sounding constructed in this manner is that the lifting condensation level of surface air tends to coincide with the middle of the transition layer. Geostrophic and initial mean winds were inferred from the data presented in Fig. 4 of Augstein et al. (1973). The surface pressure was set to 1015 mb also following Augstein et al. (1973), while the SST was specified at 298 K following Albrecht (1991). The imposed forcing includes the surface fluxes (specified using bulk aerodynamic formulae with fixed coefficients), the radiative cooling rate (based in the liquid water path), the advective tendencies of water and potential temperature, and the large-scale subsidence rate (Fig. 38). None of this forcing was applied until 1.5 hours into the simulation. The forcing is less "rigid" for the ATEX GCSS case than it was for BOMEX (see Table 2 on page 145). Here, the models are given some freedom to adjust to the evolution of the boundary layer. In BOMEX, forcing was prescribed and held constant, while in ATEX, only the "form" of the forcing is prescribed; the actual forcing itself is a function of the PBL depth, which evolves during the simulation. This is true for the surface forcing, subsidence, advective tendencies, and radiative cooling. This is more typical of the real atmosphere, in that the boundary-layer evolution depends strongly on feedbacks with the surface and large-scale forcing.

Figure 37 shows the initialized mean state for the ATEX simulation and Fig. 38 shows the large-scale forcing that would be applied for a PBL-top height of 1000 m. Due to the sparsity and uncertainty of the observational record, considerable freedom was exercised in specifying the large-scale conditions. To insure that the radiative cooling and subsidence warming above the inversion canceled identically, both were "faded" to zero above the height of the simulated inversion. In addition, a constant mixing ratio was specified above the trade inversion to insure that the properties of the free atmosphere would be unchanging as a result of large-scale processes, even for very long integrations.

Subsidence velocities at the trade inversion were selected based on preliminary runs to insure that the trade-inversion did not rise to rapidly. Observations showed a height variation of about 10% between the divergence at the surface and at 500 m. Brummer et al. (1974) cite values of divergence between 4.5×10^{-6} and 7.9×10^{-6} sec^{-1}. Preliminary tests indicated that the larger values of divergence tended to too rapidly shallow the cloud layer, hence the large scale subsidence velocity at the height of the inversion was specified as 6.5 mm sec^{-1}, corresponding to a divergence of 4.6×10^{-6} sec^{-1} at 1400 m. The horizontal advective tendencies were chosen from Wagner (1975). The large-scale temperature forcing is a combination of the clear-air radiative forcing and the advective forcing. None of the large-scale forcing was applied until 90 minutes into the simulation to insure that the turbulence had time to "spin up" (Table 2).

For this simulation, I use the "case-specified" grid resolution of 20 m and a timestep of 0.5 seconds. I run the model for 12 hours and time-average the fields for the last two hours. It is these time-averaged fields that are shown in Figs. 39-46. The ADHOC results are compared with observations (where available) and LES models. The LES models used in this study include UCLA, MPI, KNMI, and West Virginia University (WVU). For more details on the case specifics, the reader is referred to the ATEX web page, http://www.asp.ucar.edu/~bstevens/atex/overview.html.

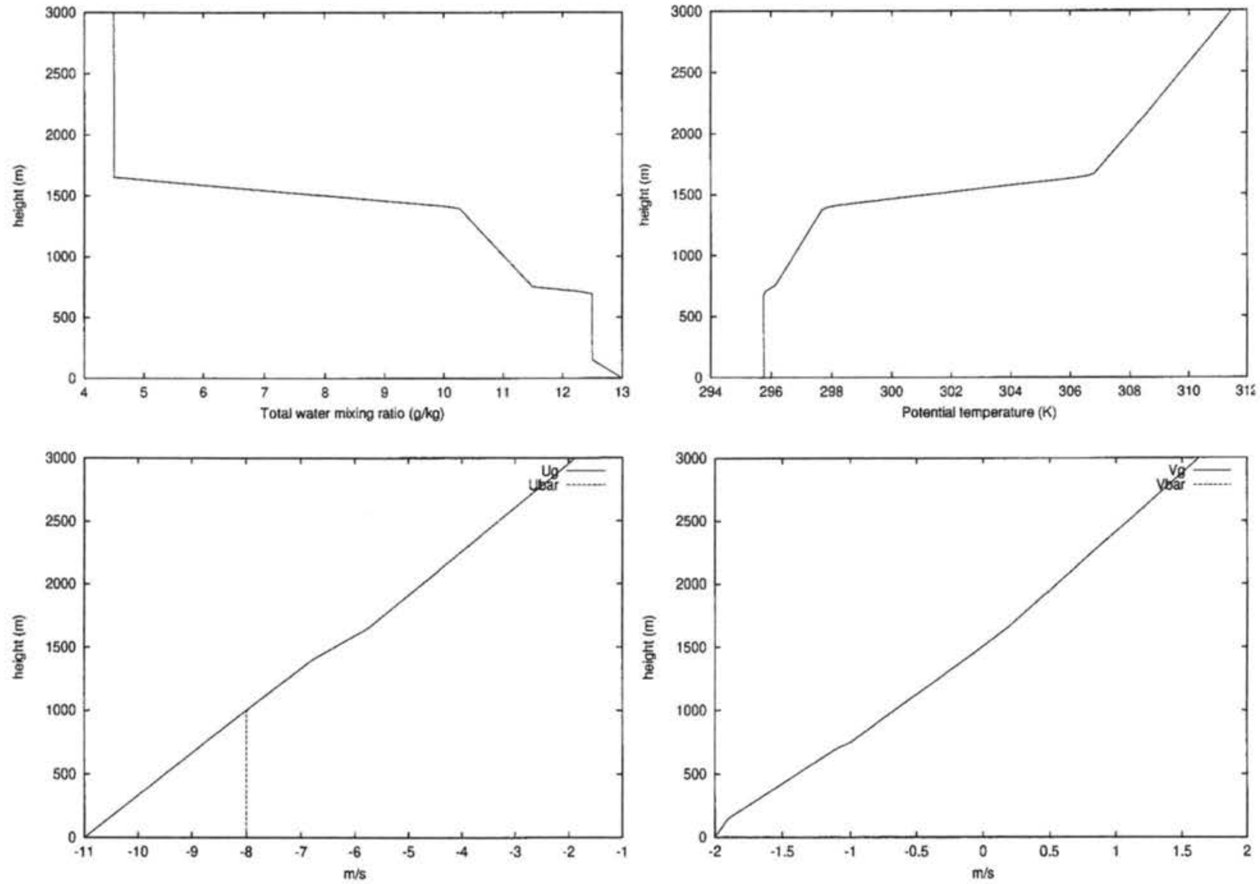

Figure 37: Initial profiles for ATEX. Top left, total water mixing ratio; top right, potential temperature; bottom left, mean and geostrophic zonal wind; bottom right, mean and geostrophic meridional wind.

IV-C-3b: Results and discussion

Overall, the ADHOC simulation of ATEX agrees better with LES than does in BOMEX simulation. The reasons for this partly relate to the less "rigid" large-scale and surface forcing in the ATEX GCSS setup. As discussed, the ATEX GCSS prescribed large-scale forcing depends on the height of the PBL and the surface forcing depends on the surface layer air properties. In BOMEX, both of these are completely "rigid". Thus, in ATEX, as the dynamics and thermodynamics of the boundary layer evolve, the large-scale and surface forcing have the freedom to

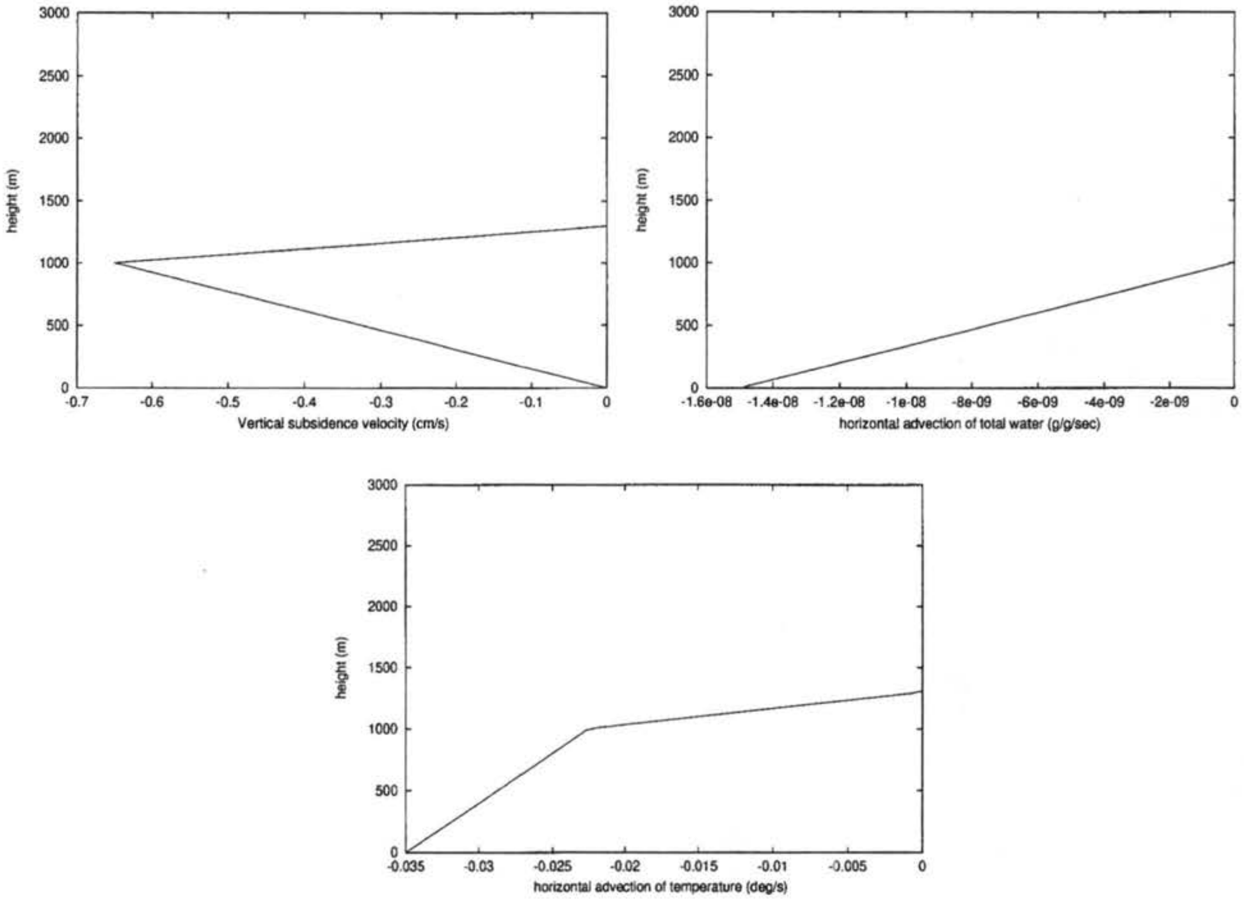

Figure 38: Prescribed forcing for a PBL-top height of 1000 m in the ATEX simulation. There is a low-level drying (top, right) and cooling (bottom) due to advection and a subsidence velocity (top, left) which is a maximum at the location of the PBL top.

adjust to the changing conditions (see Table 2 on page 145). This adjustment helps prevent an unrealistic distribution of turbulence (Fig. 18). Throughout the discussion of the results in this section, I will refer to this sensitivity run.

In Fig. 39, I show a comparison of the ADHOC-simulated winds with both LES and observations. As in BOMEX, the observation comparison must be viewed only in a qualitative sense as the magnitude of the simulated quantities is "tied" to the prescribed forcing. The top half of Fig. 39 shows that the simulated relative magnitudes of the zonal (U) and meridional (V) components of the wind agree with observations. The shapes of these curves are qualitatively similar as well, especially for the V wind. The winds simulated by LES agree with ADHOC quite nicely, especially the U component. The V wind is slightly underpredicted by ADHOC near the surface and slightly overpredicted near the inversion. It is not apparent why this is the case.

Figure 40 shows a comparison of the simulated and observed total water mixing ratio and dry static energy. Both the shapes and magnitudes of the ADHOC-simulated fields agree well with the observed conditions, even the presence of a "wiggle" in the transition region between the well-mixed layer and the conditionally unstable cloud layer. The "3-layered" structure of the trade-wind boundary layer is nicely represented here (Section IV-C).

Some important differences between these thermodynamic profiles and those of BOMEX should be pointed out (Figs. 29-30). First of all, the trade-wind inversion is nearly 3 times stronger in ATEX than in BOMEX; secondly, the mixed layer is somewhat deeper; and thirdly, the conditionally unstable layers are significantly cooler, but only slightly drier. All three differences reflect the more "upstream" nature of ATEX compared with BOMEX. As a result of these differences, we would expect that the entrainment rate (in the absence of radiative cooling) is less in ATEX due to a decrease in the surface forcing (colder SSTs) and an increase in the energy required to entrain the more stable inversion air. Less entrainment should lead to moister downdrafts and higher cloud fractions. In the BOMEX results (Section IV-C-2b), many of the problems were attributed to inefficient entrainment and "rigid" forcing. If this was in fact the case, then I would expect the decreased role of entrainment in ATEX, as well as the more liberal large-scale and surface forcing, to make the LES and ADHOC simulations more similar. The one thing which could offset this is if the increased cloud fraction generates stronger cloud-top radiative cooling which helps increase the ATEX entrainment rate. We will explore this point in the next few plots.

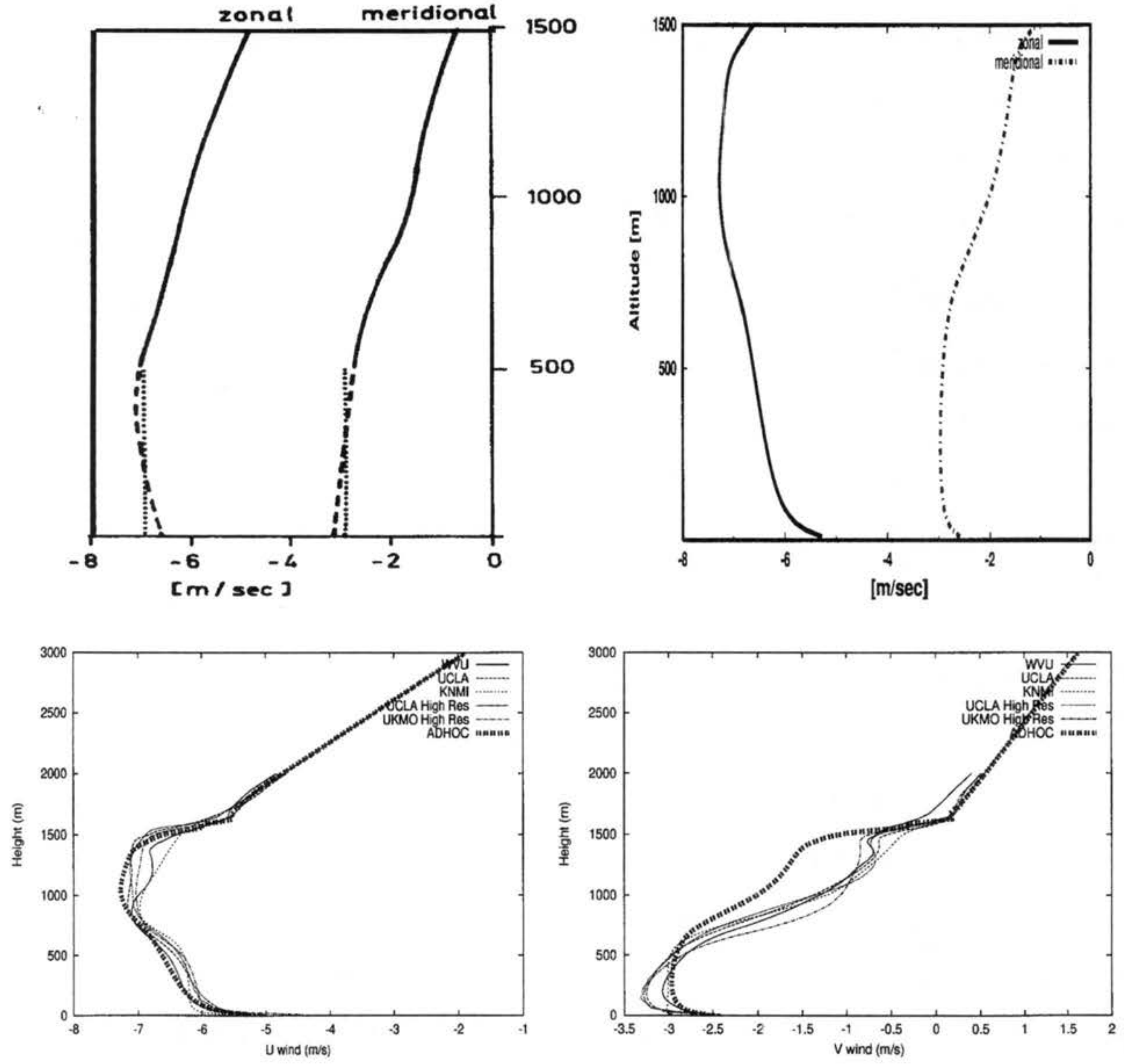

Figure 39: Intercomparison between observed and simulated zonal and meridional winds. Top left, observed winds form Brummer et al., 1974; top right, ADHOC-simulated winds; bottom left, LES and ADHOC zonal winds; bottom right, LES and ADHOC meridional winds. In the bottom row, the dark curve is from ADHOC and the other curves are the LES models indicated.

In Fig. 41, I compare the simulated ADHOC and LES total and liquid water mixing ratios, and the liquid water potential temperature. Here, ADHOC agrees with LES better than it did in BOMEX for all three fields. In fact, the only notable differences are that the ADHOC results are

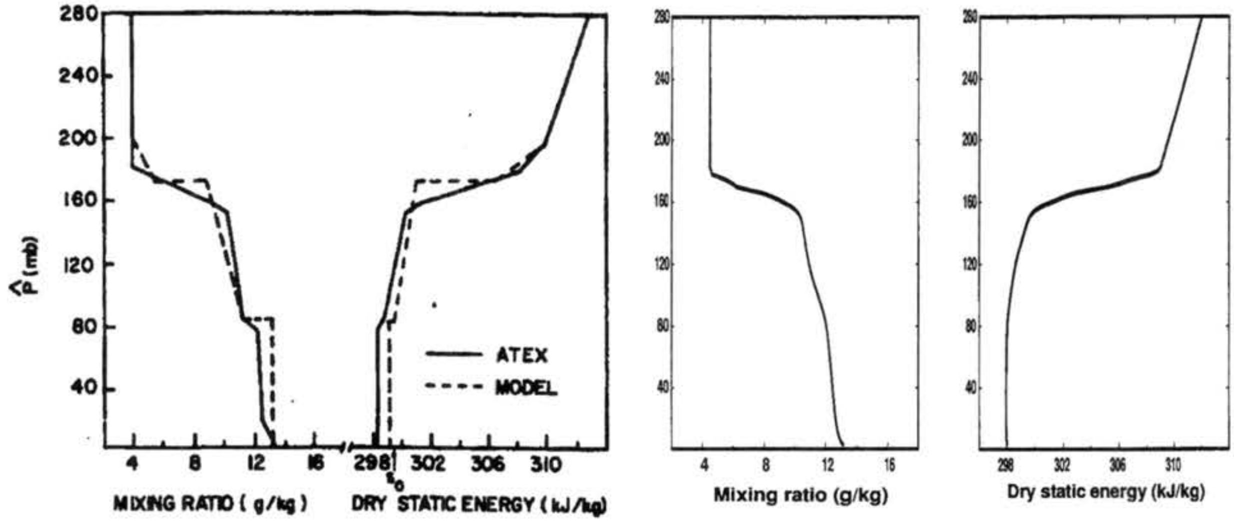

Figure 40: Comparison of the simulated and observed dry static energy and total water mixing ratio for ATEX. The top, left is the observed fields from Augstein et al., 1973; the middle and the right are the simulated mixing ratio and dry static energy.

wetter in the cloud layer (but still in the ballpark), colder near the inversion, and drier near the surface. In BOMEX, the liquid water mixing ratio was 15 times that of the LES. Here, it actually agrees with the UKMO high resolution LES run and is only a little greater than twice the other LES models. This supports my earlier conjecture that inefficient entrainment and "rigid" forcing (due to the reasons discussed in Section IV-A) will affect the ATEX results to a lesser extent than they do the BOMEX results.

Wetter clouds induce stronger radiative cooling. Thus, the cooler simulated temperatures near the inversion can be attributed to increased radiative cooling due to the wetter cloud. If the cloud-top cooling was able to initiate entrainment, the warming due to entrainment would help to bring the ADHOC results closer to those of the LES. The reason for the drier surface involves a "chicken and egg" explanation. In Fig. 42, we see that both the sensible and latent heat fluxes diagnosed by ADHOC are less than those diagnosed by the LES. We also see that the fluxes start out higher (within 20 W m^{-2} of 3 LES models), and then quickly decrease approximately one hour into the simulation, around the time that the cloud first forms (the LES models do not show such a drop). Initially, the PBL simulated by ADHOC gets wetter slightly slower than that of the LES models. As the PBL moistens, the latent heat flux at the surface should decrease (negative feedback). When PBL gets moist enough, a cloud forms. This occurs in both the ADHOC and LES simulations. However, here is where the evolution of ADHOC diverges. In the LES, cloud-top entrainment dries out the PBL so that the latent heat flux can remain relatively constant in the PBL. In ADHOC, the inefficient entrainment does not allow this to happen and the latent heat flux drops further. The decrease in the surface latent heat flux is seen by a mixed layer which is too dry in Fig. 41.

I now move away from the mean state fields and analyze the fluxes. Figure 43 shows the observed mean and ADHOC-simulated liquid water static energy (Eq. 3.137) and total water fluxes. The imposed constraints on the surface forcing (Table 2) are responsible for the lower total water flux (discussed above). However, the shapes of these profiles, including the magnitude and slope of the flux change across the inversion is well-simulated by ADHOC. ADHOC is clearly capturing the structure of the trade-wind-cumulus PBL in ATEX.

In Fig. 44, I compare the ADHOC fluxes to those simulated by LES. In all cases, the agreement is good. In the case of the liquid water flux, this seems odd given the fact that the cloud is so much wetter in the ADHOC results. The flux, however is proportional to the liquid water difference between the updraft and downdraft (Eq. 2.2). Thus, if both the updraft and downdraft liquid water mixing ratios are too moist, the flux could still be accurate. Experimental evidence suggests that the "tophat" breakdown of the fluxes only represents approximately 60% of the total flux (see Section III-I). However, in this case, ADHOC must respond to the applied forcing and thus the fluxes are accurate. I believe that in ADHOC, the fluxes represent the 100% of the fluxes, and the updraft/downdraft profiles adjust to accommodate this.

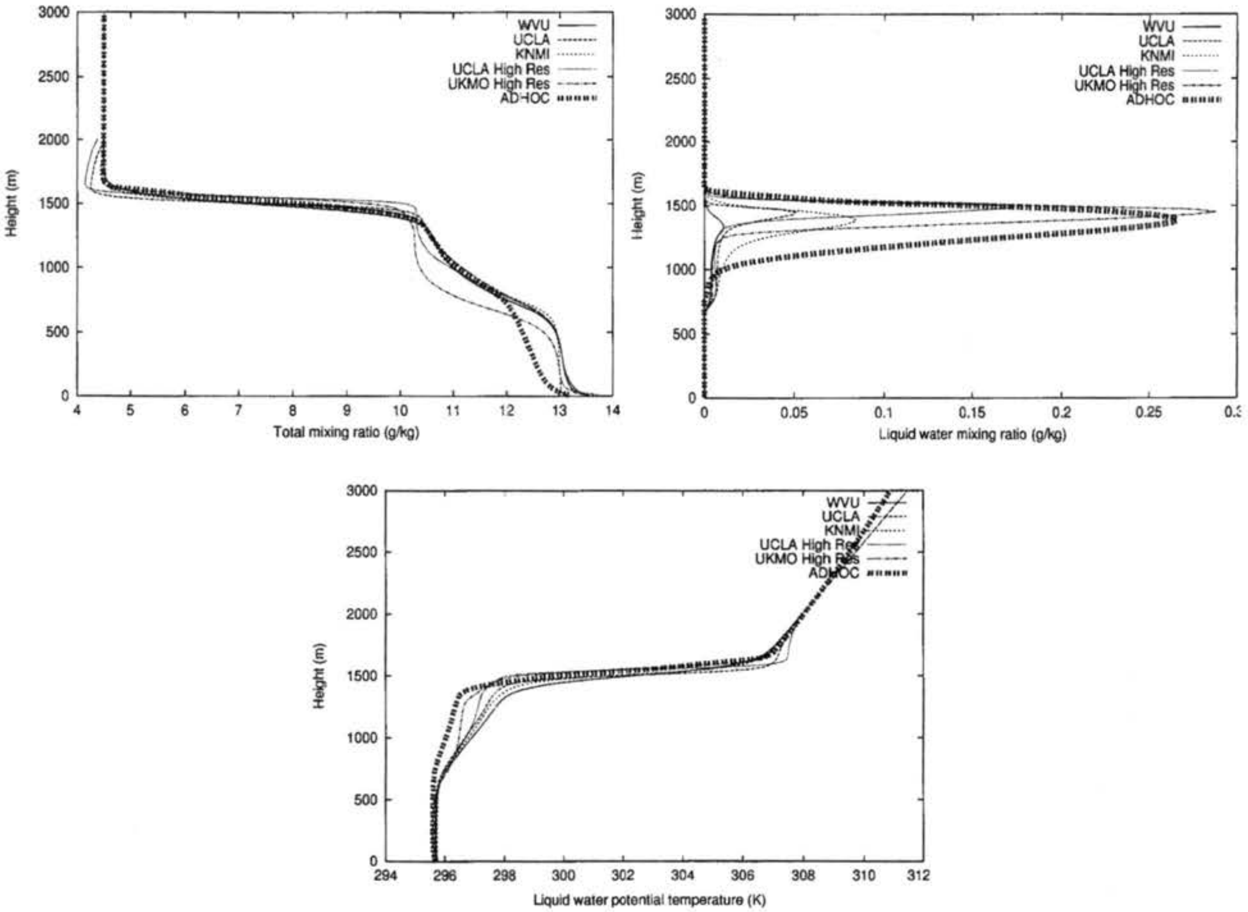

Figure 41: Comparison of the simulated ADHOC mean fields with LES for ATEX. Top left, total water mixing ratio; top right, liquid water mixing ratio; bottom, liquid water potential temperature. The darkest line is the ADHOC results.

The other three fluxes compared in Fig. 44 (zonal momentum, total water and liquid water potential temperature, θ_l) blend nicely with the LES results as well. Near the inversion layer, the absolute value of the slope of the θ_l flux becomes steeper. This is a direct result of the gradient production term in this equation (see Eq. A.11, second term on the right-hand side). We saw in Fig. 41 that θ_l is cooler than the LES sounding near the inversion. Thus, the gradient of θ_l is less

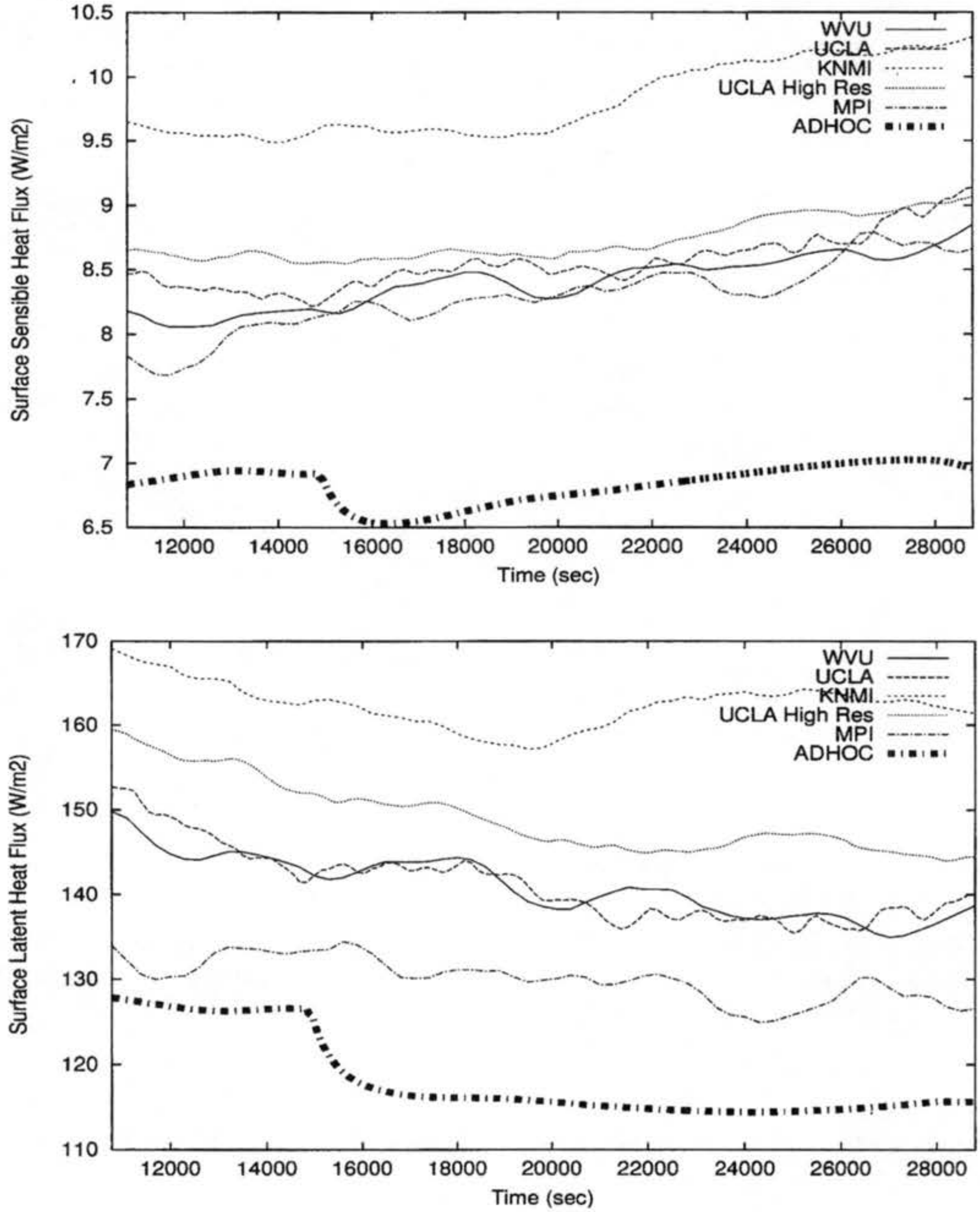

Figure 42: Time evolution of the simulated ATEX sensible and latent heat fluxes of the ADHOC and LES models. Top, sensible heat flux; bottom, latent heat flux. The darkest line is the ADHOC results.

steep, and the gradient production of the flux $\overline{w'\theta_l'}$ is smaller. The same argument can be used for

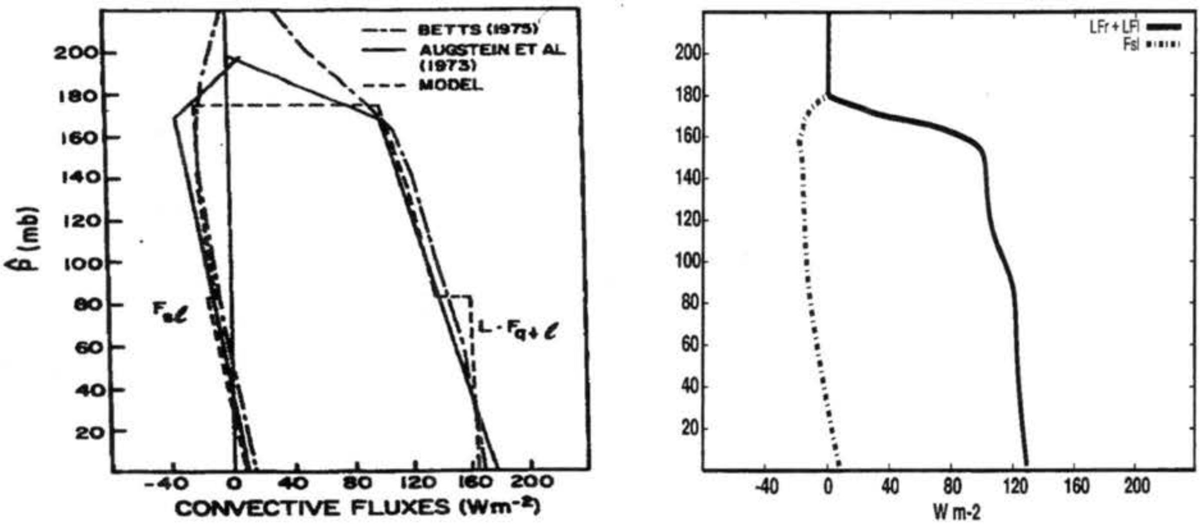

Figure 43: Comparison of the simulated (left) and observed (right) liquid water static energy and total water fluxes from ATEX.

the larger slope of the total water flux in Fig. 44.

Before analyzing the variances and the TKE budget from ATEX, I would like to draw some analogies with the BOMEX fluxes. In BOMEX, the fluxes also agreed nicely with the LES simulations in magnitude, but the profiles were somewhat compressed (Fig. 34). In the lower part of the PBL, the ADHOC and LES (BOMEX) results nicely follow each other. As the cloud and inversion layers are approached, the solutions diverge; the ADHOC fluxes are smaller and tend to zero lower. As discussed, inefficient entrainment in ADHOC, linked to the pressure terms and the "rigid" forcing (Section IV-A), prevented the boundary layer from growing and the fluxes from extending to higher levels. We do not see this same problem in ATEX. The physics of the "upstream" nature of the case dictate that the entrainment contribution from PBL turbulence will be less (in the absence of radiative cooling), because the surface is cooler and the inversion is stronger. The results of these flux intercomparisons support this notion. Inefficient entrainment is an issue in both cases, but because entrainment should be smaller in ATEX anyway, the turbulent fluxes near the inversion in ATEX better agree with LES than they do in the corresponding BOMEX simulations.

Finally, I would like to finish the discussion of ATEX by comparing the momentum vari-

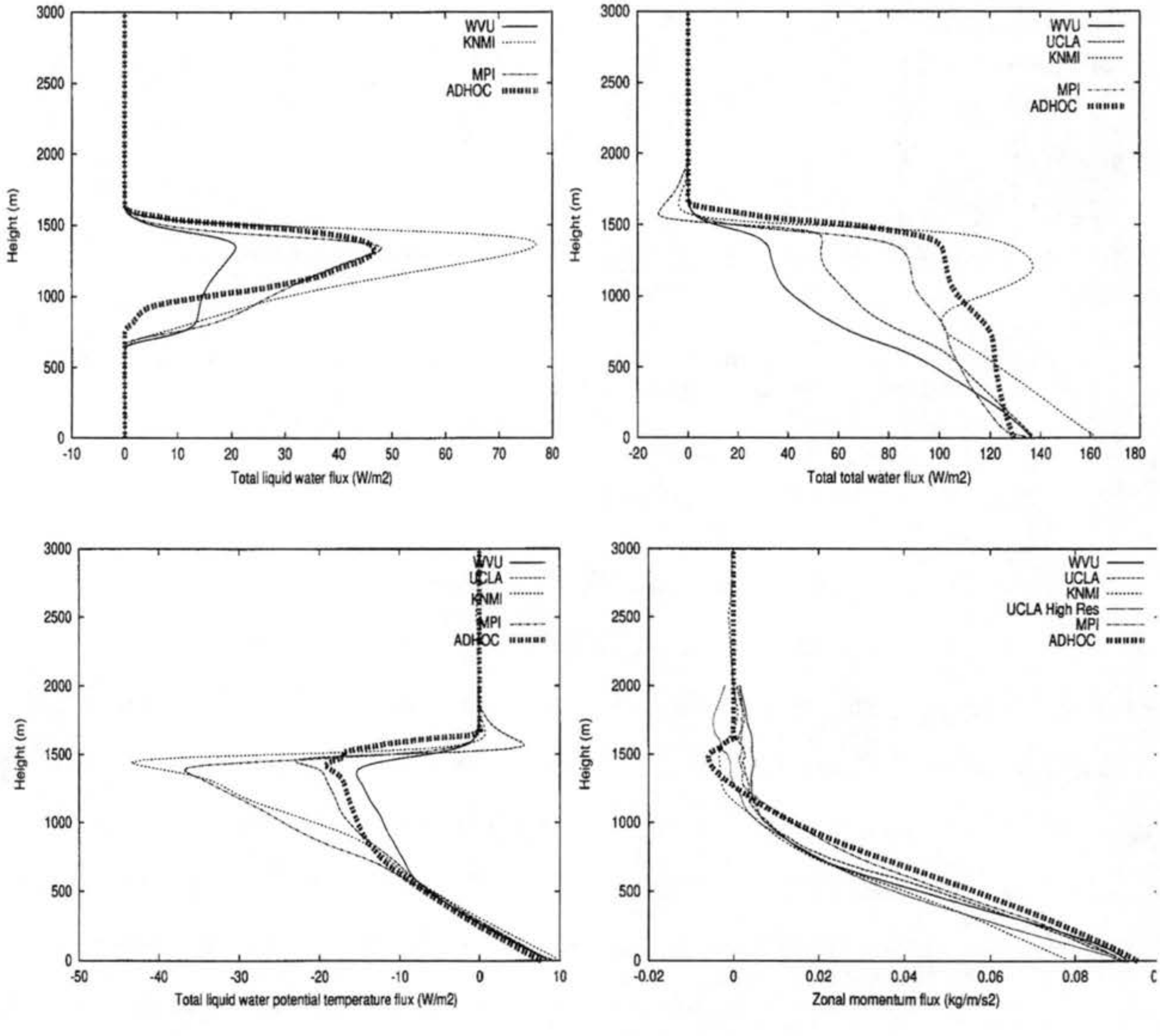

Figure 44: Comparison of the ADHOC and LES simulated fluxes for ATEX. Top left, liquid water flux; top right, total water flux; bottom left, liquid water potential temperature flux; bottom right, zonal momentum flux. The darkest line is ADHOC.

ances and the TKE budget. They are perhaps the "worst" feature of the ADHOC results. The horizontal momentum variances agree nicely with that of the LES. There is a maximum at the surface, where the pressure terms are active, and a secondary maximum near cloud top. However, the vertical momentum variances are not as nicely correlated. $\overline{w'w'}$ resembles that in the LES in shape, but is significantly larger in the inversion and near the surface. I suggest the following mechanism to explain this discrepancy: As discussed, too much liquid water is simulated by ADHOC (Fig. 41). Because the radiative cooling in ATEX is allowed to adjust to the amount of liquid water present, it too will be too large (not shown). This overly-active cloud-top radiative cooling drives a large buoyancy flux in the cloud (Fig. 46), which in turn creates too much $\overline{w'w'}$. However, due to condition (4.1) and the extreme stability of the inversion layer in ATEX, the large $\overline{w'w'}$ is unable to generate entrainment, something which can act to reduce $\overline{w'w'}$ [8]. The air thus descends, pushing the wet cloudy air into the subcloud layer. This air then evaporates, cools further and continues down to the surface where the secondary maximum in $\overline{w'w'}$ is observed. If the entrainment was not inhibited for the reasons discussed, I believe it would act to decrease $\overline{w'w'}$ in the cloud and prevent this process from occurring. In that situation, the surface $\overline{w'w'}$ would only be due to the surface sensible and latent heat effects as it is in the LES simulations.

In the ADHOC profiles, we also see that the three components of the velocity variance are almost equal (provided we assume that $\overline{u'u'}$ and $\overline{v'v'}$ contribute equally to the horizontal momentum variance). As was the case in BOMEX, this appears to be due to an overly-active "return-to-

[8]. A more active inversion-layer entrainment would decrease $\overline{w'w'}$ through the following mechanism: In a partly cloudy layer (such as this one), the potential temperature increases upwards. When air is entrained, we are forcing air to go down dry, against a stable stratification. The buoyancy force works against this. As a result, making air go down dry-adiabatically against a stable stratification tends to make the buoyancy term of the $\overline{w'w'}$ equation smaller, or even negative, because work must be done. Thus, for given liquid water potential temperature and total water mixing ratio fluxes, the buoyancy term will be smaller and $\overline{w'w'}$ will decrease.

isotropy" pressure contribution (see BOMEX discussion; Section IV-C-2b). At the inversion base, we would not expect the turbulence to be isotropic; $\overline{w'w'}$ must go to zero, and $\overline{u'u'}$ and $\overline{v'v'}$ must increase (through the total pressure effect) to accommodate the sudden drop in $\overline{w'w'}$. Thus, I would expect the other parts of the pressure term to be more active than the "return-to-isotropy" contribution (Section IV-C-2b). In the LES simulations, we see that the total pressure effect is well-represented; near the PBL top, $\overline{w'w'}$ is in fact much smaller than either $\overline{u'u'}$ or $\overline{v'v'}$. However, in the ADHOC simulation, an overly-active "return-to-isotropy" is unable to accommodate that aspect of the turbulence. The problem occurs at all levels of the PBL. As discussed, the implementation of an "ADHOC-consistent" pressure parameterization will likely alleviate these types of problems (Appendix B).

An interesting artifact of the ATEX inversion strength being 3 times larger than that of BOMEX is that the pressure terms must be more active in ATEX near this level. It is difficult for air impinging on the inversion to penetrate the extremely stable stratification of the ATEX inversion; thus, this impinging air must almost be entirely converted into horizontal momentum (or dissipated). In BOMEX, the requirement is not as strong since the inversion layer can more easily be penetrated. As a results of this, we see that the magnitudes of the horizontal velocity variances in BOMEX are, in general, smaller than in ATEX (near the inversion).

Finally, we look at a comparison of the TKE budgets for ADHOC and LES (Fig. 46). The shape and magnitude of the profiles is quite good despite the fact that the variances that comprise the TKE do not agree with LES all that well (Fig. 45). The major differences here relate to the overly-large value of $\overline{w'w'}$ discussed above. For example, the dissipation term is too large over the same heights where $\overline{w'w'}$ is too large. In addition, we see a larger negative peak in the transport term at the level, where the transport term reacts to remove the large $\overline{w'w'}$. The shear terms match

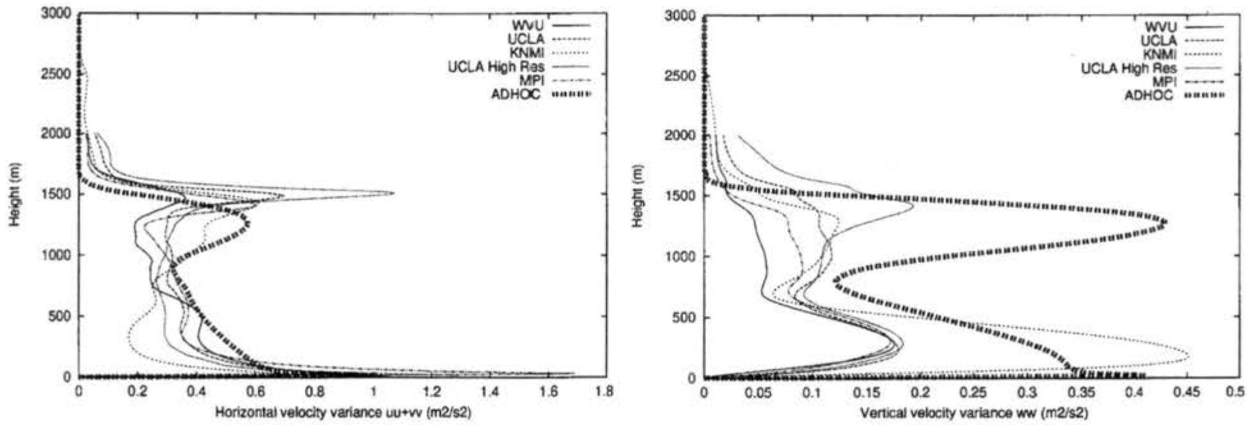

Figure 45: Comparison of the ADHOC- and LES-simulated momentum variances for ATEX. Left, total horizontal variance (uu + vv); right, vertical velocity variance (ww). The darkest line is ADHOC.

the LES well, as they are not related to $\overline{w'w'}$. Finally, the buoyancy term is big here for reasons discussed above. In BOMEX, the TKE budget profiles seem to match better than they do here. This is due to the fact that the radiative cooling is "rigid", and thus is not allowed to accommodate the overly large liquid water in the BOMEX cloud.

IV-C-4: Comparison of the BOMEX and ATEX simulations

BOMEX and ATEX are both considered trade-wind cumulus regimes. However, there are obvious differences between the two. In Sections IV-C-2b and IV-C-3b, I have compared the results of these simulations to LES models, and at times made comparisons between BOMEX and ATEX. However, these comparisons were mostly done from the LES comparison perspective (e.g., why ATEX agrees with LES better than BOMEX, etc.). From a purely "ADHOC" perspective, it would be interesting to examine how ADHOC distinguishes between these two similar regimes. If the ultimate goal is to incorporate a model of this sort into a large-scale model, it will be its ability to distinguish between small, but physically important differences in cloudy regimes that will determine its success. Some interesting questions with regard to this are:

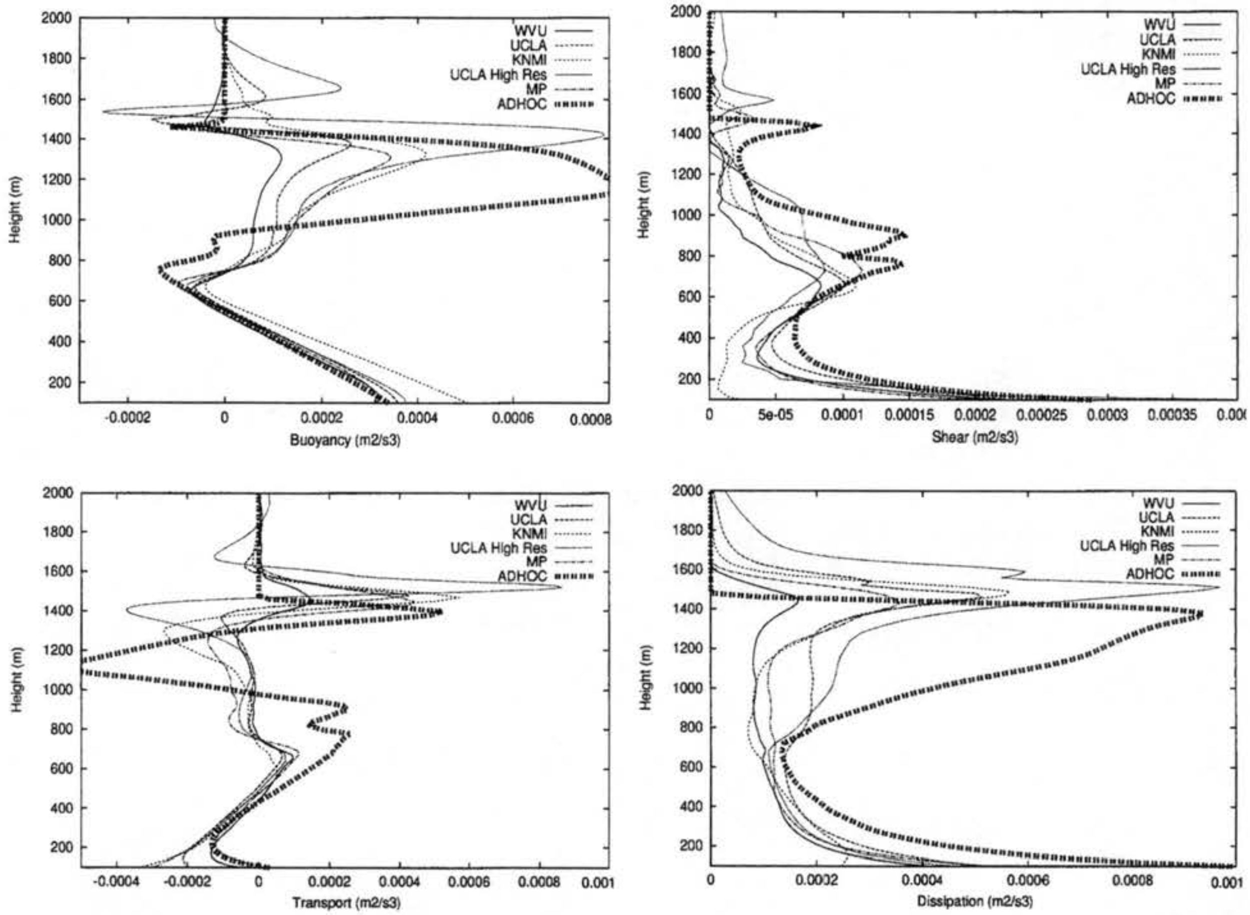

Figure 46: Comparison of the simulated ADHOC TKE budgets with LES for ATEX. Top left, buoyancy; top right, shear; bottom left, turbulent transport; bottom right, dissipation. The darkest line is ADHOC.

- Can ADHOC produce both the higher cloud fractions associated with ATEX and the lower cloud fractions associated with BOMEX? If so, what factors control the cloud fractions in the trades?

- How do the lateral mass exchange relations developed for ADHOC differ for BOMEX and ATEX? Do these differences reflect the fact that ATEX is a more upstream setting with a more humid cloud layer?

- Do the difference in properties between updrafts and downdrafts in BOMEX and ATEX reflect the different environmental settings of these two cases?

Before we discuss these questions, I'd like to review some of the important differences between these two cases, both from a physical standpoint and from a simulation standpoint. Physically, the differences are related to the fact that ATEX is an "upstream" version of BOMEX; there is a stronger inversion, a deeper mixed layer, cloud fractions are near 50% (as opposed to 20% in BOMEX), and it has cooler but only slightly drier mixed and cloud layers. The SSTs in ATEX were almost 3 K colder than in BOMEX and the inversion strength was approximately 3 times stronger. The colder SSTs and steeper inversion indicate that surface forcing and entrainment (respectively) should play lesser roles in ATEX. However, the increased radiative cooling due to the higher cloud fractions may help drive additional entrainment and counteract the latter effect.

That is what "should" happen from a physical standpoint. From the simulation standpoint, the differences make a direct comparison quite difficult. First of all, the "rigid" forcing in BOMEX changed the results significantly. Secondly, the grid resolution in BOMEX is twice that in ATEX (see Table 2 on page 145). The ATEX web page (see Section IV-C-3a) indicates that the results of the simulations vary significantly when the grid resolution is changed. This effect is thus an unknown in comparing the two simulations. Thirdly and perhaps most importantly, entrainment was inefficient in both cases due to a problem involving the handling of the pressure terms (see Section IV-A).

Natural differences in these cases should evolve as a result of the surface forcing, the simulated entrainment rate, and the large-scale forcing. The large-scale forcing is prescribed with observations in both BOMEX and ATEX; thus, it will naturally try and force the model in a manner which highlights the differences between the two regimes. The surface forcing should do this as well. However, the surface forcing is "rigid" in BOMEX, and thus cannot evolve in sync with the boundary layer dynamics and thermodynamics. This "rigid" forcing, which is not a factor in ATEX, was shown to significantly affect the results (Fig. 18). Entrainment is an important process in determining the boundary-layer evolution; and, as we saw in the last two sections, the entrainment was not accurately represented.

With all this in mind, I will make some general comparisons, but in order to fully test ADHOC's ability to represent subtle changes in the trade-wind regime, a more case-consistent setup must be used (e.g., both cases must have the same "form" of the forcing, the same grid resolution, etc.). In addition, I believe that, until the pressure problem discussed in Section IV-A is solved (through the use of a "ADHOC-consistent" pressure parameterization), a comparison of regimes (such as BOMEX and ATEX) which depend on subtle changes taking place in the entrainment zone is impossible.

In a general sense, let's see if the model is able to simulate the lower cloud fractions in BOMEX as compared to ATEX. In the context of ADHOC, this is analogous to having relatively drier downdrafts. In other words, if the cloud fraction is approximately 20% in BOMEX and 50% in ATEX, the downdrafts in BOMEX should be a lot drier relative to the updrafts than in ATEX. In the same vane as this, the updraft area, σ, should be closer to 0.5 in ATEX than it is in BOMEX. To make a qualitative comparison of these two cases, I will use these two simple tests. I will leave a more in depth comparison for the future, when the cases being analyzed are set up in more compatible manner, and the pressure and momentum problems have been addressed (see Section IV-A).

Figure 47 shows the percentage decrease of the downdraft liquid water mixing ratio as compared to that of the updraft (e.g., $(r_{L_{up}} - r_{L_{dn}})/r_{L_{up}}$) and the updraft area fraction. We see that the BOMEX simulation does in fact produce narrower updrafts, especially in the cloud (which extends from about 700 -1400 m in these simulations). In addition, the downdraft liquid water mixing ratio in the bulk of the cloud is also wetter in ATEX than it is in BOMEX (in this figure, a value of unity indicates that the updraft is completely dry. The lower the number, the wetter the downdraft relative to the updraft). These two results are a good indication that, despite the entrainment problems at the inversion, the PBL turbulence is trying to represent some of the physical differences between these regimes.

In the next section, I will discuss a very different case, that of stratocumulus. We will see that ADHOC in its current version is more suited to this regime than it is to the trade-wind regime.

IV-D: Marine stratocumulus

Marine stratocumulus (MSc) are globally important from both radiative and dynamical standpoints. These low-level marine clouds are significant modulators of the earth's radiation budget (Hartman et al., 1992). They increase the overall albedo because they are more reflective than the underlying ocean, but they have little effect on the longwave radiation emitted to space. Satellites show that the net cloud forcing by MSc can locally be as large as -100 W m^{-2}, and globally is approximately -17 W m^{-2} during the northern hemisphere summer (Ramanathan, 1989; Harrison et al., 1990). In addition, Slingo (1990) showed that modest changes in low-cloud amount, liquid water content, or droplet size in MSc could cause climatically significant changes in the global radiation budget.

From a dynamical standpoint, MSc can significantly modify the tropical general circulation (Tiedtke et al., 1988). They are found in the subtropics, upstream of trade-wind Cu. The MSc-topped boundary layer (ScTBL) differs from the TWBL in that the inversion strength is stronger and the sea surface temperatures (SST) are cooler. In both the undisturbed and disturbed trade-wind regime, the role of cloud processes is to cool and moisten the upper part of the PBL. This creates and maintains the trade-wind inversion and provides a moist environment for the deep convective clouds. Although seldom associated with disturbances, clouds in the MSc regime also behave in this manner (Hanson, 1981). While both the Marine ScTBL and the TWBL modify the large-scale circulation by maintaining the trade-wind inversion, the physical mechanisms are

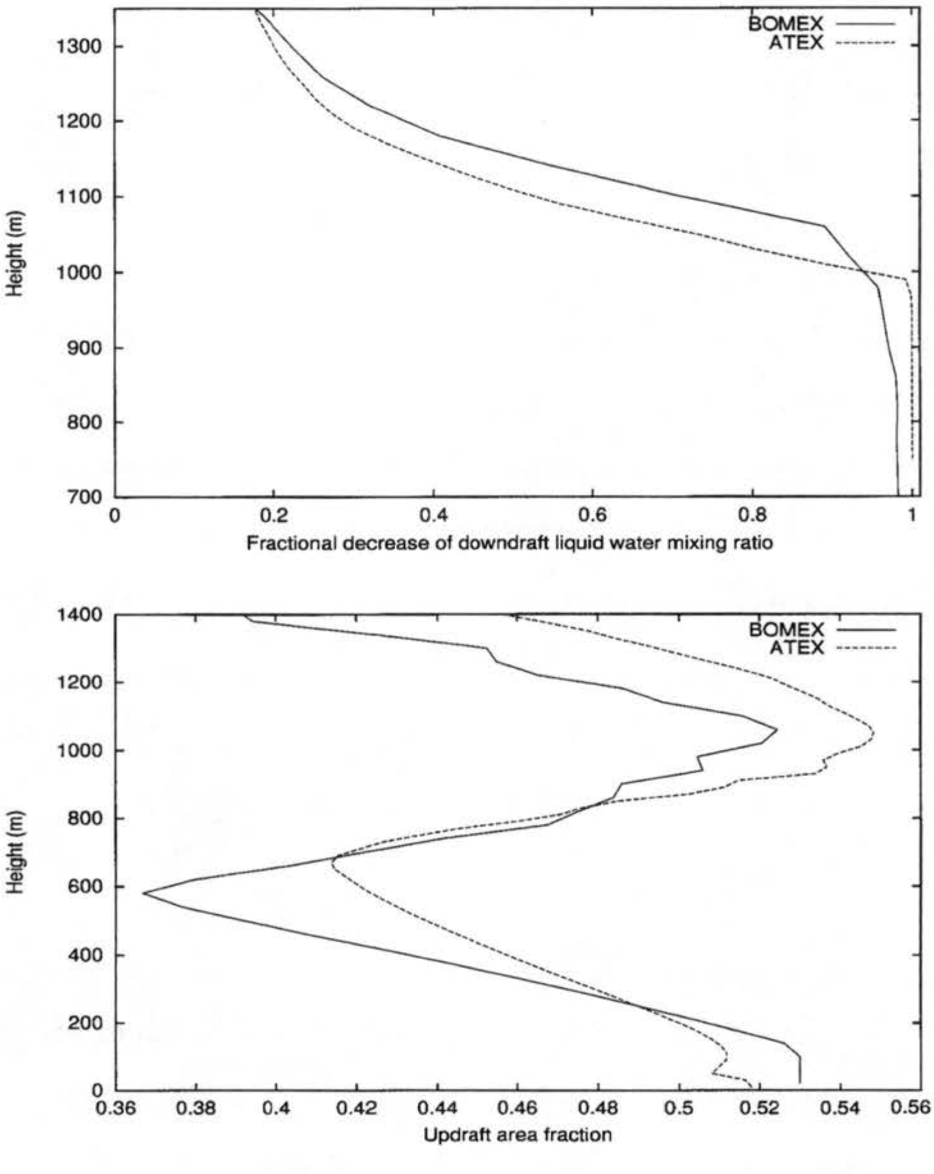

Figure 47: The percentage decrease of the downdraft liquid water mixing ratio relative to the updraft (top) and the updraft area fraction (bottom) for both ATEX and BOMEX.

different between these two regimes. In the MSc regime, all cloud-layer motions occur under saturated conditions, while in the trades, the subsiding motions are associated with unsaturated conditions. In addition, a ScTBL is turbulent throughout the entire layer while the Cu regime is only turbulent in the cloud; the region between the clouds being rather quiescent.

The turbulent/convective dynamics of Sc are driven primarily by radiative cooling of air parcels near cloud top (Lilly, 1968; Duynkerke et al., 1995; Nicholls, 1984;1989). This cooling drives sinking motion and boundary-layer convection. This convective circulation, which may be enhanced by surface heat fluxes when the surface temperature is high, results in a well-mixed boundary layer. If the boundary layer is not decoupled, (Nicholls, 1984) conserved variables such as the equivalent potential temperature or total water mixing ratio are nearly constant with height (they may deviate from this constant value near the inversion base and near the surface).

Another critical factor in the dynamics of these clouds is their large cloud-top entrainment rates. Some aircraft measurements suggest that the entrainment rate in cloud-topped boundary layers is about an order of magnitude larger than in the dry convective PBL (Nicholls and Turton, 1986; Duynkerke et al., 1995). The cloud-top cooling driven by radiation drives turbulence, and this turbulence drives the entrainment of air from above the cloud. This entrainment injects warmer, drier air into the cloud top, thereby causing droplets to evaporate. This can lead to even more cooling and more turbulence. It has been proposed that this process, called cloud-top entrainment instability (CTEI; Chapter I; Lilly, 1968; Deardorff, 1980; Randall, 1980; Siems et al., 1990), can eventually lead to the breakup of the cloud deck (see Chapter I). Clearly, the crux of accurately simulating these radiatively and dynamically important clouds is the proper representation of the entrainment process. Other processes which play a role in the ScTBL include latent and sensible heat fluxes from the surface, drizzle and its possible evaporation below the cloud, and solar absorption in the cloud layer. The latter two of these lead to "decoupling" of the subcloud and cloud layers (see Chapter I for a discussion of decoupling; Brost et al. 1982; Nicholls, 1984; Wang and Wang, 1994; Betts, 1990).

Most numerical investigations of the STBL have evolved from Lilly's (1968) mixed-layer approach. A detailed review of previous attempts to model the MSc has been discussed in Section II-D-2a for HOC models and Section II-E-1 for mass-flux models. The current model has advantages over both standard HOC (in that it is able to handle non-local transport) and previous mass-flux models (in that it has knowledge of higher-moment statistics). Both of these advantages should allow a better representation of MSc than either a HOC or mass-flux model could alone. I performed simulations with ADHOC of a MSc case from ASTEX using the computational design outlined by the GCSS Boundary-Layer Workshop III (http://www.fys.ruu.nl/~wwwimau/ASTEX/astexcomp.html).

IV-D-1: ASTEX

ASTEX took place 1-28 June 1992 over the northeastern Atlantic Ocean (Albrecht et al., 1995). One of its principal goals was to characterize the evolution of cloudiness and vertical structure in a marine boundary layer (MBL) as it moves over a warmer surface (Bretherton and Pincus, 1995). MSc form in regions where the ocean is relatively colder than the lower troposphere. The fractional area covered by these clouds is relatively large (up to 100%). This is in great contrast to the trade-wind Cu regime discussed in Section II-D-2b, where the SSTs are warmer and the cloud fraction is smaller. Two factors combined to make the ASTEX area an attractive place to examine MBL cloudiness. First, the relatively steady northerly trade flow in this region minimizes the effects of day-to-day variability in the MBL. Secondly, climatology suggests that we should typically see a substantial decrease in MBL cloud cover within an air mass as it advects southward over the warmer ocean (Bretherton and Pincus, 1995; Krueger, 1995).

The aim of the field project was to understand the *transition* from Sc to Cu in the subtropics. To this end, the observations were designed to determine how the transition was effected by 1) CTEI, 2) diurnal decoupling and clearing due to solar absorption, 3) patchy drizzle and a transition to horizontally inhomogeneous clouds through decoupling, 4) mesoscale variability in cloud thickness associated mesoscale circulations, and 5) episodic strong subsidence which can push the inversion below the lifting condensation level. A key result which emerged from ASTEX was the critical role that decoupling plays in the "stratus-to-cumulus" transition (see Chapter I). Consequently, we must examine solar absorption in clouds, drizzle, and the general deepening of the boundary layer (which all play important roles in decoupling) if we hope to understand this transition and accurately parameterize it in large-scale models.

IV-D-1a: ASTEX GCSS case

The ASTEX GCSS case (http://www.fys.ruu.nl/~wwwimau/ASTEX/astexcomp.html) was designed using the data from the first ASTEX Lagrangian (L1) study which too place from 12-14 June 1992. It is a 3-hour simulation which begins at 0400 UTC on 13 June 1992. During this time, the Azores high was well established and the winds were NNE at 10 m s-1. Sc with sustained drizzle was observed throughout the time period. Since many models (including ADHOC) do not have explicit microphysics schemes, GCSS cases were designed both with and without drizzle. In this simulation, I used the "no-drizzle" setup described below.

During L1, extensive aircraft measurements were taken (de Roode and Duynkerke, 1997). One of these aircraft, the NCAR Electra, flew during the times represented in this simulation (Flight RF06). In the next section, I will compare the ADHOC results for this case to these aircraft measurements, as well as to LES results.

The prescribed forcing includes the following: large-scale subsidence (shown in Fig. 48), longwave radiative cooling (profiles diagnosed as functions of the liquid water path; a typical one for this simulation is shown in Fig. 52), and surface sensible and latent heat fluxes (10^{-2} K m s^{-1} and 10^{-5} m s^{-1} respectively). In addition, the surface pressure (1029 mb) and temperature (292.5 K) were prescribed and held constant (not a typical Lagrangian specification but the assumption is that they do not change much in three hours). The initial mean conditions were chosen to be representative of the atmospheric conditions at ASTEX on the 13 June 1969 (Fig. 48). For more information on the case-specifics, consult the web page (note that large-scale horizontal advection was not prescribed since the case is designed to be Lagrangian; Table 2 on page 145).

The prescribed initial conditions and subsidence forcing which are shown in Fig. 48 are different from those of the BOMEX and ATEX trade-wind regimes (Figs. 26, 37). In general, the ScTBL is characterized by colder SSTs, colder and drier surface air properties, and weaker latent heat fluxes (Table 2). Due to weaker surface fluxes, the cloud-top inversion in the ScTBL occurs at a lower height (650 m in ASTEX verses 1300 m in ATEX). The strength of the inversion (defined as the jump in potential temperature divided by the height over which the "jump" occurs) is similar for ATEX and ASTEX. This is reflective of the fact that ASTEX is not a "classic" ScTBL (e.g., Sc which form off the coast of California), but is more representative of a "transitional" regime in between the TWBL and the "classic" ScTBL (this is discussed in more detail below).

The "classic" ScTBL has more in common with WD than it does with BOMEX or ATEX, regardless of the cloud effects. In fact, from a "turbulence" standpoint, the "classic" ScTBL and WD profiles are virtually identical (shape-wise; e.g., the mean states are both well-mixed, the flux profiles are linear, the vertical velocity variances are parabolic with a maxima in the middle of the boundary layer, etc.). However, because ASTEX is a "transitional" regime between that of the TWBL and the "classic" ScTBL, we often see characteristics of both these regimes in the ASTEX simulations (and observations). I will refer to this fact many times in the discussions of the ADHOC results in the next section.

As a final note about ASTEX, I'd like to mention another key issue which came up in the trade-wind cumulus GCSS BOMEX and ATEX simulations; that of "rigid" forcing. In BOMEX, the radiative, surface, and large-scale forcing was completely "rigid" so that the only manner in which the boundary layer could "express" itself was through the entrainment process (see Section IV-C-2b). In ATEX, the forcing was only "semi-rigid" (see footnote, page 144); the magnitude of the actual forcing at each level depended on the PBL height, the surface air properties, and the liquid water content. In this respect, the ATEX simulations were more realistic, because the boundary layer was able to evolve in manner consistent with the turbulence generated within it. In the ASTEX GCSS case, we have a mix between these two approaches. Here, the surface forcing and the subsidence profile is "rigid", but the radiative forcing is allowed to evolve with the quantity and distribution of liquid water (see Table 2 on page 145). As we saw in Fig. 18, rigidly applying the radiative forcing is very limiting in the context of a realistic boundary-layer evolution. Thus, as we will see in the next section, this was not a significant problem in the ASTEX simulation.

In the ADHOC results discussed in the next section, I used a grid resolution is 25 m, and a timestep is 0.5 seconds. I ran the model for 3 hours and time averaged fields during the last hour. It is these time averages that appear in the plots below. The LES models which I used for the intercomparisons include the Institute for Marine and Atmospheric Research Utrecht in the Netherlands, NCAR, and WVU. For more information on the case specifics, the reader should consult the web page (see top of this section).

IV-D-1b: Results and discussion

In this section, I will compare ADHOC with both aircraft measurements and LES models. In general, ADHOC is able to represent the ScTBL better than the TWBL (many of the problems discussed in Section IV-A do not affect the ASTEX simulation as severely). I will refer to both BOMEX and ATEX where applicable, to point out and suggest explanations for these differences. In addition, I will compare the turbulence statistics of ASTEX to those of WD and ATEX to show how this regime resembles the "transitional" nature between the TWBL the "classic" ScTBL (WD is used as a proxy for the latter since the shapes of the turbulence profiles for conservative variables are similar in both).

Figure 49 shows a comparison of the zonal and meridional mean winds simulated by

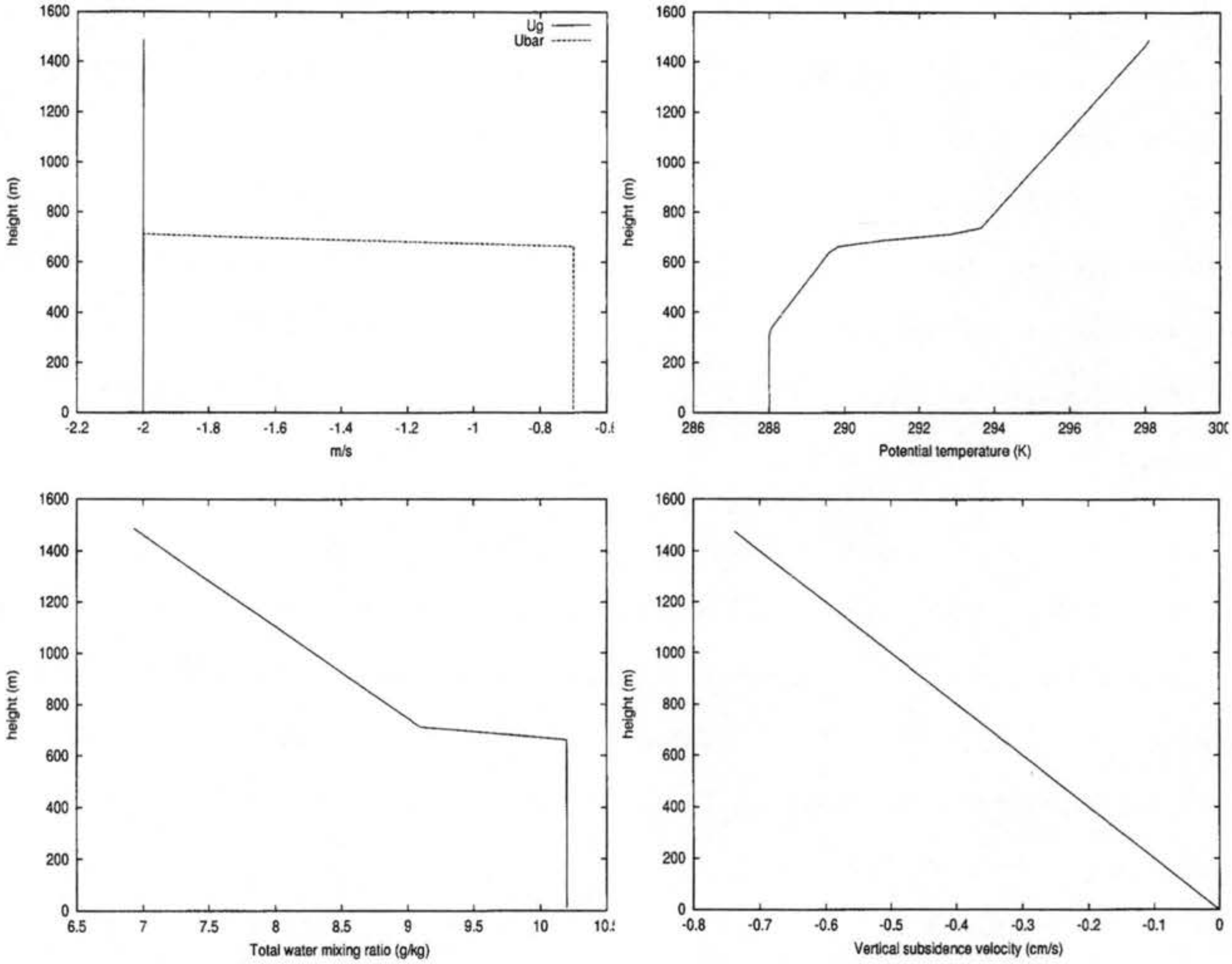

Figure 48: Initial mean state profiles for ASTEX. Top left, zonal mean and geostrophic zonal (the meridional mean and geostrophic winds are set to 10 m/s at all heights); top right, potential temperature; bottom left, total water mixing ratio; bottom right, vertical subsidence velocity. The subsidence velocity does not change throughout the simulation. No horizontal advection is prescribed.

ADHOC and LES. In general, ADHOC is able to represent the shape and magnitude of these profiles, especially that of the zonal wind. However, ADHOC slightly overpredicts the meridional wind near the inversion and a underpredicts it near the surface. While the actual magnitude (and likely effect) of the difference is not extremely significant (less than 3% for all heights), I can still narrow down the reason why it might occur. It is unlikely that the coriolis term in this equations is involved since the coriolis term in the meridional wind equation is a function of the difference of

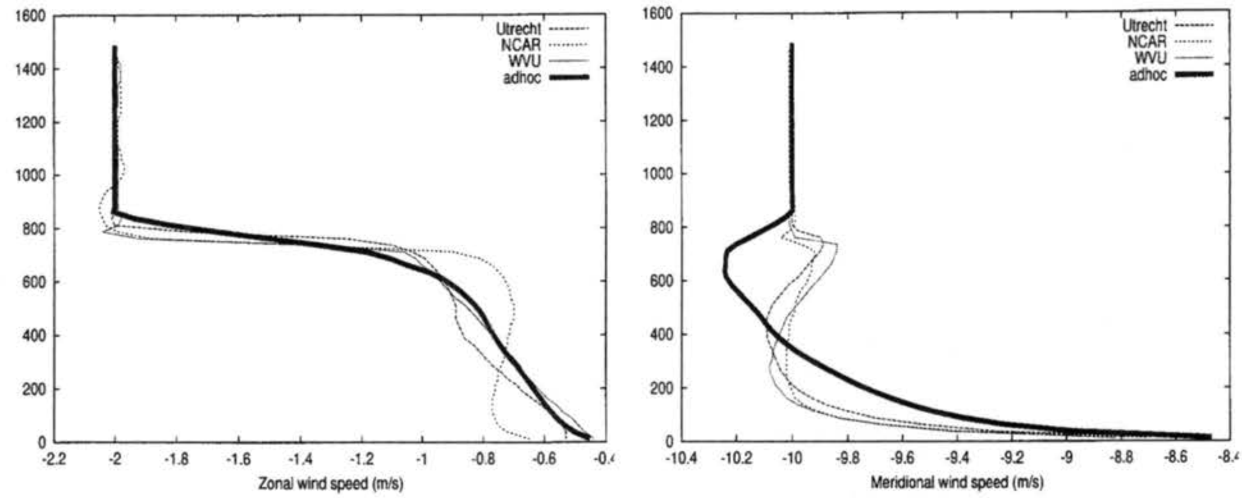

Figure 49: Comparison between the simulated ADHOC and LES mean winds in ASTEX. The darkest line is the ADHOC results.

the mean and geostrophic zonal winds [the former of which agrees with LES (Fig. 49) and the latter of which is prescribed; Eq. A.2]; likewise, it cannot be a result of vertical subsidence (this is also prescribed). The only term left is the momentum flux (transport) term. The shape of the profile would indicate that meridional momentum is being transported too quickly out of the lower half of the PBL up toward the inversion. This can only happen if the meridional momentum flux, $\overline{w'v'}$, is (1) too large near the surface or (2) too small near the inversion; both regions where the pressure terms are most active. Due to the known problems (see Section IV-A) with the pressure terms, it is not surprising that they likely play a role in this difference.

In Fig. 50, I show a comparison among the mean-state quantities (liquid and water vapor mixing ratios, and the equivalent and virtual potential temperatures) simulated by ADHOC, simulated by LES, and observed with aircraft. In general, ADHOC agrees with the aircraft observations quite nicely. In fact, the ADHOC profiles seem to agree with observations better than those of the LES models (e.g., the liquid water mixing ratio). In the plot of liquid water mixing ratio, ADHOC produces less liquid water than all of the LES models shown. This is also shown in Table 3, where the integrated liquid water path in ADHOC is less than that simulated by LES. Since the liquid water in a ScTBL is mainly determined by processes which occur at cloud top (see Section IV-D), this discrepancy likely reflects a difference between the amount of entrainment drying simulated by ADHOC and LES. We see in Table 3 that ADHOC is in fact, entraining faster than the LES models (I will come back to this point below, when I analyze the fluxes). Despite the ADHOC/LES differences, aircraft observations distinctly show that the maximum liquid water mixing ratio recorded was approximately 0.42 g kg^{-1}. Thus, ADHOC seems to be able to capture the observed evolution of this cloud layer. Interestingly enough, previous ADHOC problems concerning inefficient entrainment [such as those found with BOMEX and to a lesser extent, ATEX (Sections IV-C-2b and IV-C-3b respectively)] do not seem to have an effect in this case. The reasons for this are also discussed in detail below.

Figure 51 shows the mean state liquid water potential temperature ($\overline{\theta_L}$) and potential temperature flux ($\overline{w'\theta'_L}$). In general, the boundary layer is a little warmer than that simulated by LES near the surface. In addition, the inversion in the ADHOC results is not as "sharp" as that simulated by the LES models. The flux, $\overline{w'\theta'_L}$, has some scatter, even among the LES results. In general, this flux should be linear (or close to linear; other factors such as horizontal advection and subsidence can alter its shape) in the sub-cloud layer of a ScTBL, reflective of the fact that $\overline{\theta_L}$ is well-mixed there. In both the LES models and ADHOC, we see that this slope is, in fact, linear. Thus, while ADHOC does not strictly agree with the results of the LES models (as far as the magnitude of $\overline{w'\theta'_L}$), it is representing the "physics" of this regime by simulating a relatively linear flux profile in the sub-cloud layer.

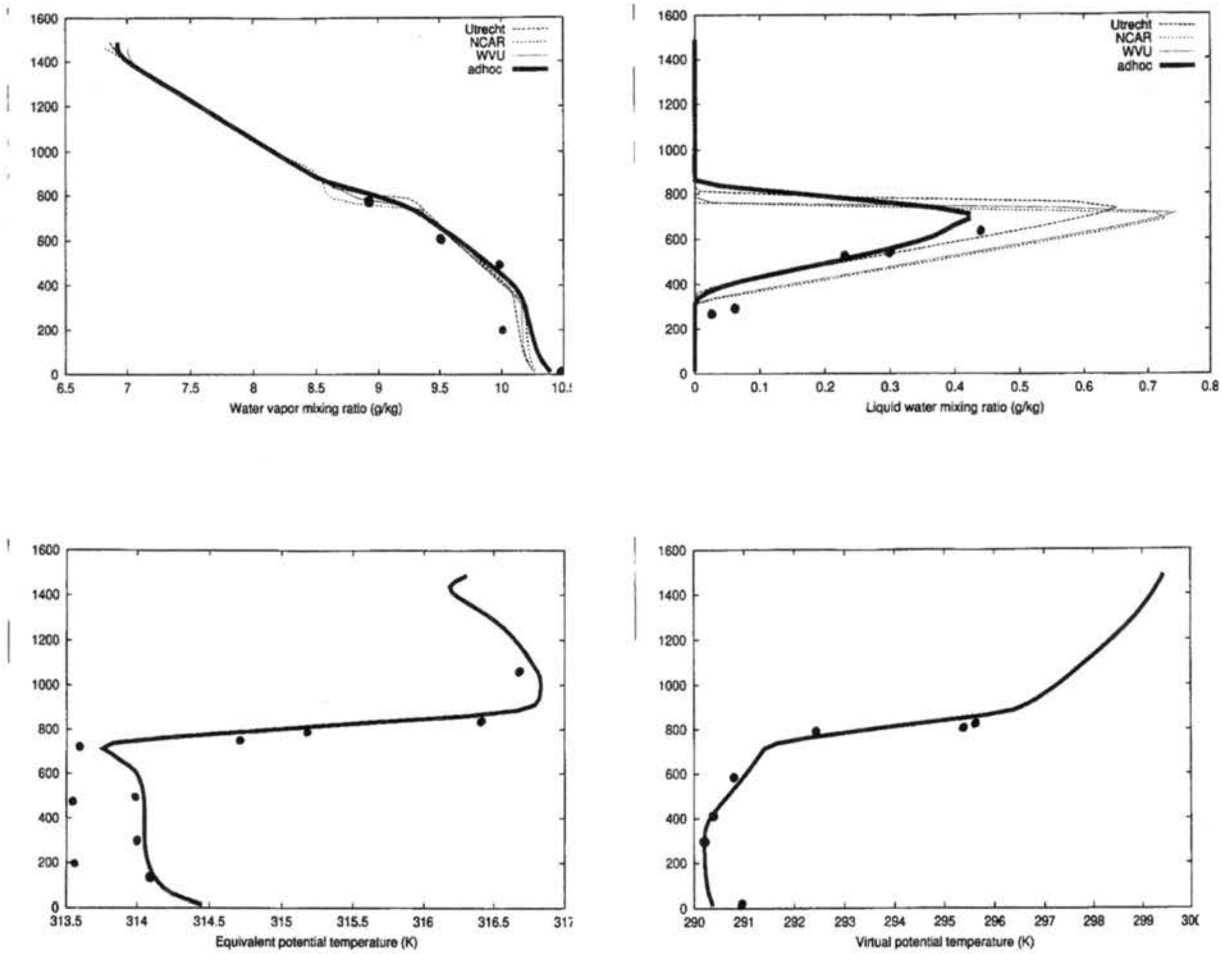

Figure 50: Comparison of the simulated mean state profiles for ASTEX with observations and with those simulated by LES (where available). The darkest curves is ADHOC, the lighter curves are the indicated LES, and the dots are observations from the NCAR electra as analyzed by de Roode and Duynkerke (1997): Top left, water vapor mixing ratio; top right, liquid water mixing ratio; bottom left, equivalent potential temperature; bottom right, virtual potential temperature.

It is important to note here that the cloud-layer profile of $\overline{\theta_L}$ is not well-mixed as one would expect it to be in a "typical" Sc regime. This is reflective of the fact that, in the ASTEX region, we find a more "transitional" type of boundary layer. In a classic ScTBL, we would expect the cloud and sub-cloud layers to both be well-mixed. ASTEX is really a cross between this "classic" ScTBL and the TWBL of BOMEX and ATEX. Thus, it is not surprising that some characteristics of ASTEX resemble both regimes. The slope of $\overline{\theta_L}$ is one such characteristic, which distinctly shows the transitional nature of this case; the existence of the slope is a TWBL characteristic, but the magnitude of the slope is a cross between a well-mixed (vertical) profile and the slopes seen in BOMEX and ATEX (Figs. 31 and 41 respectively).

At the top of the cloud layer in ASTEX, we would expect a jump in $\overline{w'\theta'_L}$ due to the strong radiative cooling which is occurring there. We see this "jump" in the LES models, but not in ADHOC. This is an indication that either (1) radiative cooling is not as strong in the ADHOC simulations as it is in the LES, (2) entrainment warming is overly efficient in the ADHOC simulation and it partially cancels the effect of radiative cooling, or (3) a combination of both of these is occurring. Figure 52, which depicts profiles of the radiative flux simulated by both ADHOC and LES, distinctly shows the radiative cooling rate in ADHOC is less than that of the LES (the radiative cooling rate is calculated by taking the vertical divergence of the radiative flux, which shown in that figure; this turns out to be approximately -28 K day^{-1} for ADHOC and -64 K day^{-1} for the averaged LES models, both over a 50 m interval). In addition, Table 3 shows that the entrainment rate in ADHOC is comparable to that simulated by LES. Thus, not only is the radiative cooling smaller, the *modulation* due to entrainment warming is larger (larger in a relative sense; i.e., for a given amount of radiative cooling, there is more entrainment warming).

These effects combine to make the inversion in ADHOC less "sharp" (by "sharp" I mean that the inversion layer is thicker than that simulated by the LES models, since the temperature and humidity jumps occur over a larger vertical distance). This is seen in both of the plots in Fig 51. While this explains why the inversion layer is not as strong, it directly highlights a contradiction in the ADHOC results; although significantly less cooling is occurring at cloud top, the entrainment rate and the average height of the PBL top are comparable between the LES and

ADHOC (see Table 3). Thus, it appears as though, in this simulation, radiative cooling is *overly* efficient at driving entrainment; the exact opposite conclusion which was found for BOMEX (and also, to a lesser extent, ATEX). In BOMEX, the inefficient entrainment was attributed to the "rigid" forcing, the overly active dissipation, and inconsistent pressure terms. In ATEX, the extremely stable inversion inhibited turbulent entrainment, despite a fairly large cloud-top radiative cooling rate, which was caused by the presence of too much liquid water (Fig. 41).

It was not 100% clear, however, why the radiative cooling in ATEX was unable to sustain adequate entrainment. Here, in ASTEX, we see *overly* efficient entrainment in the presence of "not enough" radiative cooling. This makes the ATEX results even less clear. In ASTEX, the inversion strength is even stronger than in ATEX, while they both have a similar radiative cooling rate. What factors control the differences in the way these two regimes process the radiative cooling which results in ASTEX being able to entrain inversion air, while ATEX cannot? There are many possible explanations for this. I will describe the two that I believe play a large role; one of them is physical, while the other is an unfortunate artifact of the model numerics.

From a physical standpoint, other processes can occur at cloud top, besides radiative cooling and entrainment warming. A big difference between ASTEX and ATEX, with regard to cloud top, is the updraft/downdraft liquid water differences. In ATEX, the downdraft is 20-80% drier than the updraft (depending on the location in the cloud; see Fig. 47). In ASTEX, the two quantities are virtually the same (corresponding to a constant value of unity in Fig. 47). Dry downdrafts adiabatically warm. Moist downdrafts warm as they descend, but the cooling due to the evaporation of liquid water tends to dominate the warming; only when the liquid water is zero, will the parcel continuously warm along the dry adiabat. I suggest this as a possible explanation for the difference in entrainment between ATEX and ASTEX. The additional cooling generated from the evaporation of liquid water in the downdrafts generates enough additional turbulence that entrainment can be maintained. It may very well be that, in the absence of this effect, the entrainment in

ASTEX would be inefficient as well.

If evaporative cooling was the major driving force in the generation of entrainment in ADHOC, then we would expect that the drier the downdrafts, the more inefficient the entrainment. Of all the cases simulated, BOMEX has the driest downdrafts. It was also shown to have the biggest problem with entrainment (see Section IV-C-2b). While this supports my conjecture, it is not concrete, given the other problems discussed with the BOMEX simulation. As a final note, another mechanism which may play a role in initiation of entrainment in ASTEX is the proposed CTEI mechanism, which involves the evaporation of liquid water specifically at cloud top due to entrainment (see Chapter I).

While all this may be true, there may be another factor which contributes; one that is related to the numerics of the model itself. The best way to show this is with a time series plot of $\overline{w'w'}$ (or any other higher-order statistic). It is important to remember that the profile plots shown in this thesis are time-averaged. Thus, in general, "oscillations" of any sort will be smoothed out (if they show up at all). It would, in principle, be easy to overlook problems if this was the only method used to analyze of the performance of the model. Here, I will show an example of how this can occur.

Figure 53 shows a time series of $\overline{w'w'}$ for ASTEX, ATEX, and BOMEX. We see that the ASTEX boundary layer evolves in a nice, smooth manner. As the cloud-top radiatively cools, it generates turbulence, which drives entrainment, and the boundary layer grows. In the BOMEX case, we see something very strange occurring. We see "pulses" of energy which appear to form near cloud base and propagate upwards, while in between these pulses, we see that the turbulence dies to near zero. In a time-averaged sense, the cloud is only entraining half the time. The "pulsing" in the ATEX simulation is somewhere in between that of BOMEX and ASTEX (i.e., the turbulence "pulses", but not as often). This "pulsing" appears to grow stronger the closer we get to the "pure" cumulus regime [i.e., the updraft area fraction is smallest (largest) and the downdrafts are driest (wettest) in BOMEX (ASTEX); ATEX is in the middle in all cases].

As discussed, the occurrence of the "pulsing" does not explicitly show up in the time-averaged plots. However, it still affects the results. I am suggesting here that, an additional reason why the overall entrainment is lower in ATEX than it should be (despite radiative cooling rates which are comparable to ASTEX) is that it is really only occurring half of the time. In a time-averaged sense, the "non-pulsing" periods decrease the entrainment. The reason why this "pulsing" occurs is not all together clear. However, it is a very common problem in turbulence closure models which are used to simulate the cumulus regime (Steve Krueger; Chris Bretherton, personal communication). The problem is likely associated with a stability cycle, initiated by clouds with a small updraft areas. This can be explained as follows: The top of the sub-cloud layer moistens and eventually generates a positive buoyancy flux; hence, this air gets mixed into the next layer up. This process continues layer-by-layer until the inversion is reached, leaving behind it a wake which is too dry to allow a significant cloud fraction. Then, the sub-cloud layer "recharges" again due to dry turbulence, moistening its top until the cycle begins again (Chris Bretherton, personal communication).

Many of the remaining ASTEX results can be explained in part by referencing the above discussion of the factors which affect entrainment in ADHOC. However, additional information is also provided in these figures. In Fig. 54, I show the fluxes of the zonal and meridional momentum, and the liquid and total water mixing ratios; in Fig. 55, I compare the total water and virtual static energy fluxes to aircraft observations. The major differences between the ADHOC and LES fluxes appear near the inversion for the thermodynamic variables. This supports my earlier discussion, which can be summarized as follows: A radiative cooling rate, which was too small, coupled with comparatively large entrainment warming, produced an inversion which was weaker than that produced by the LES simulations. The simulated momentum fluxes near the inversion corre-

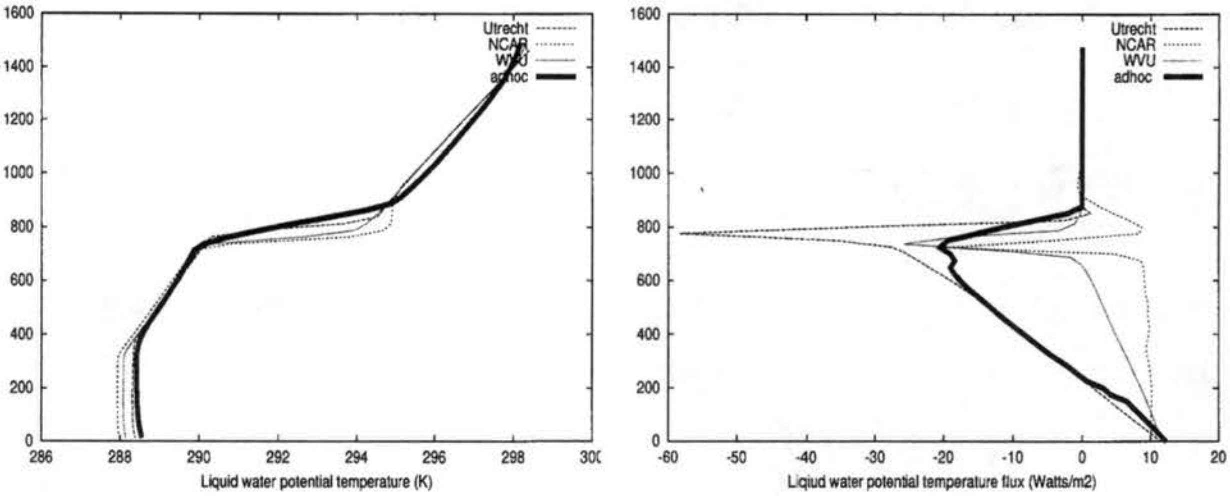

Figure 51: Comparison of the simulated mean liquid water potential temperature (left) and potential temperature flux (right) for ASTEX with that of LES. The darkest line is ADHOC and the lighter lines are the indicated LES models.

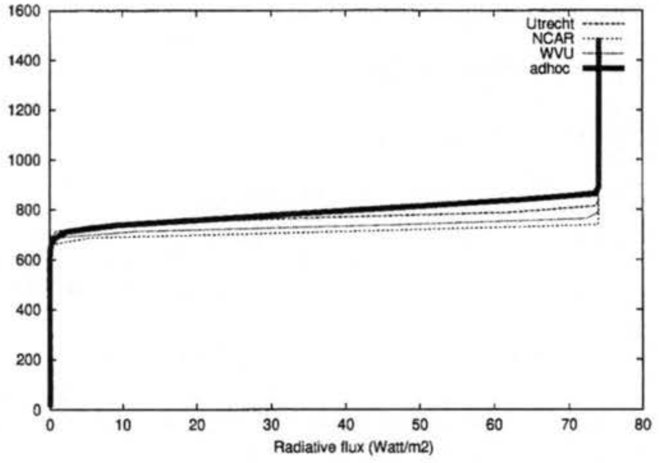

Figure 52: Comparison of the simulated radiative fluxes for ASTEX with those of LES. The darkest line is ADHOC and the lighter lines are the indicated LES models. These fluxes are computed strictly as a function of the integrated liquid water path.

spond quite well to those of the LES models.

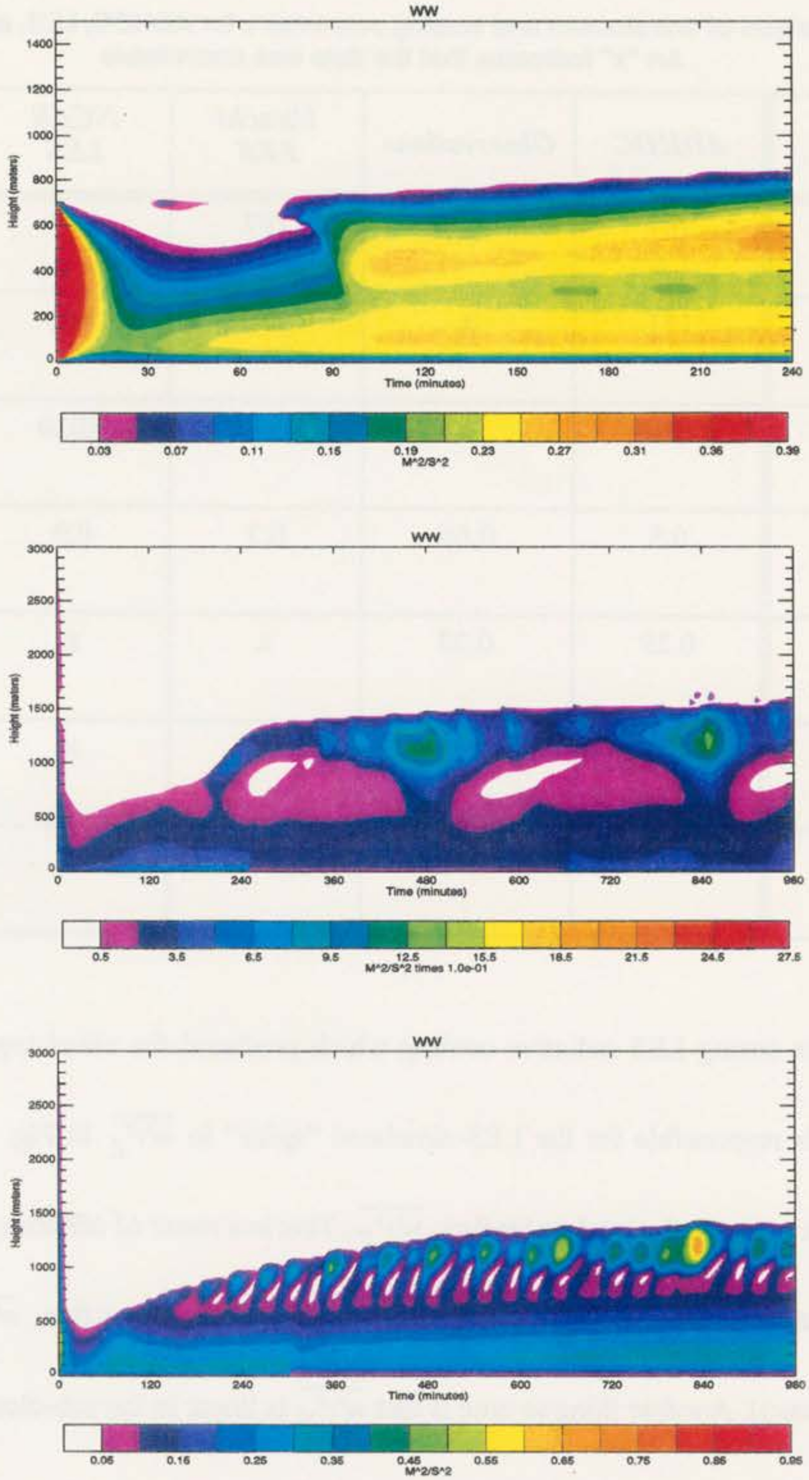

Figure 53: Time series of the evolution of $\overline{w'w'}$ for ASTEX (top) and ATEX (middle) and BOMEX (bottom).

Table 3: Comparison of entrainment and scaling parameters for ADHOC, LES, and observations. An "x" indicates that the data was unavailable

	ADHOC	*Observations*	*Utrecht LES*	*NCAR LES*	*UKMO LES*
Zi (m)	767	x	797	747	759
Integrated LWP ($g\ m^{-2}$)	151	x	176	182	177
We ($m\ s^{-1}$)	0.014	x	0.011	0.010	0.012
w ($m\ s^{-1}$)*	0.5	0.66	0.7	0.9	0.8
u ($m\ s^{-1}$)*	0.29	0.28	x	x	x
T (K)*	0.008	0.01	x	x	x
q ($g\ kg^{-1}$)*	0.022	0.027	x	x	x

The same strong LES radiative cooling which produced the cloud-top "spike" of $\overline{w'\theta'_L}$ (Fig. 51), also is responsible for the LES-simulated "spike" in $\overline{w'r'_L}$ in Fig. 54. Note that this "spike" does not occur in the total water flux, $\overline{w'r'_T}$. This is a result of offsetting "spikes" (similar in magnitude but opposite in sign) between $\overline{w'r'_L}$ and the water vapor flux, $\overline{w'r'_v}$ (the latter flux profile is not shown). Another thing to note is that $\overline{w'r'_T}$ is linear in the sub-cloud layer (similar to $\overline{w'\theta'_L}$; Fig. 51), reflecting the well-mixed mean state of this layer.

Before moving on to the discussion of the variances and the TKE budget, I would like to do a brief comparison of the ADHOC flux results with observations. Figure 55 shows $\overline{w'r'_T}$ and the virtual static energy flux, $\overline{w's'_v}$, simulated by ADHOC and observed with aircraft. There is much scatter in these plots. Overall, it appears as if the shape and magnitude of $\overline{w's'_v}$ in the observations is well-represented by ADHOC, while the magnitude of the simulated $\overline{w'r'_T}$ is too strong. In Fig. 54, we saw that $\overline{w'r'_T}$ simulated by ADHOC resided on the "high" end of the LES results. In the lower half of the boundary layer, the LES and ADHOC-simulated total water fluxes agree quite well (with the exception of the NCAR LES). They begin to diverge around the level of cloud base. It is thus not too surprising that the simulated *in-cloud* fluxes are larger in ADHOC than they should be; entrainment not only warms, but it also dries. The larger drying which occurs in the ADHOC simulation is directly responsible for a larger upward moisture flux; one that is needed to replenish the loss and maintain a steady state. If we refer back to Fig. 51, we see the same effect on $\overline{w'\theta'_L}$; the ADHOC-simulated flux resides on the *low* end of that simulated by the LES models (the warming at cloud top reducing the heat flux, even making it negative).

The profile of $\overline{w's'_v}$, simulated by ADHOC, is more typical of a TWBL, where the surface and the cloud layer are almost decoupled (the virtual static energy flux is negative between the two). This is almost identical to the shape simulated in the ATEX case (Fig. 46). However, the magnitude of the negative flux is much smaller percentage-wise (compared with the magnitude of the surface flux) in ASTEX than in ATEX. This reflects the transition away from the TWBL regime, toward the more "classic" ScTBL. The observations clearly support the simulated ADHOC profile.

For the final ASTEX analysis, I will examine the simulated velocity variances and TKE

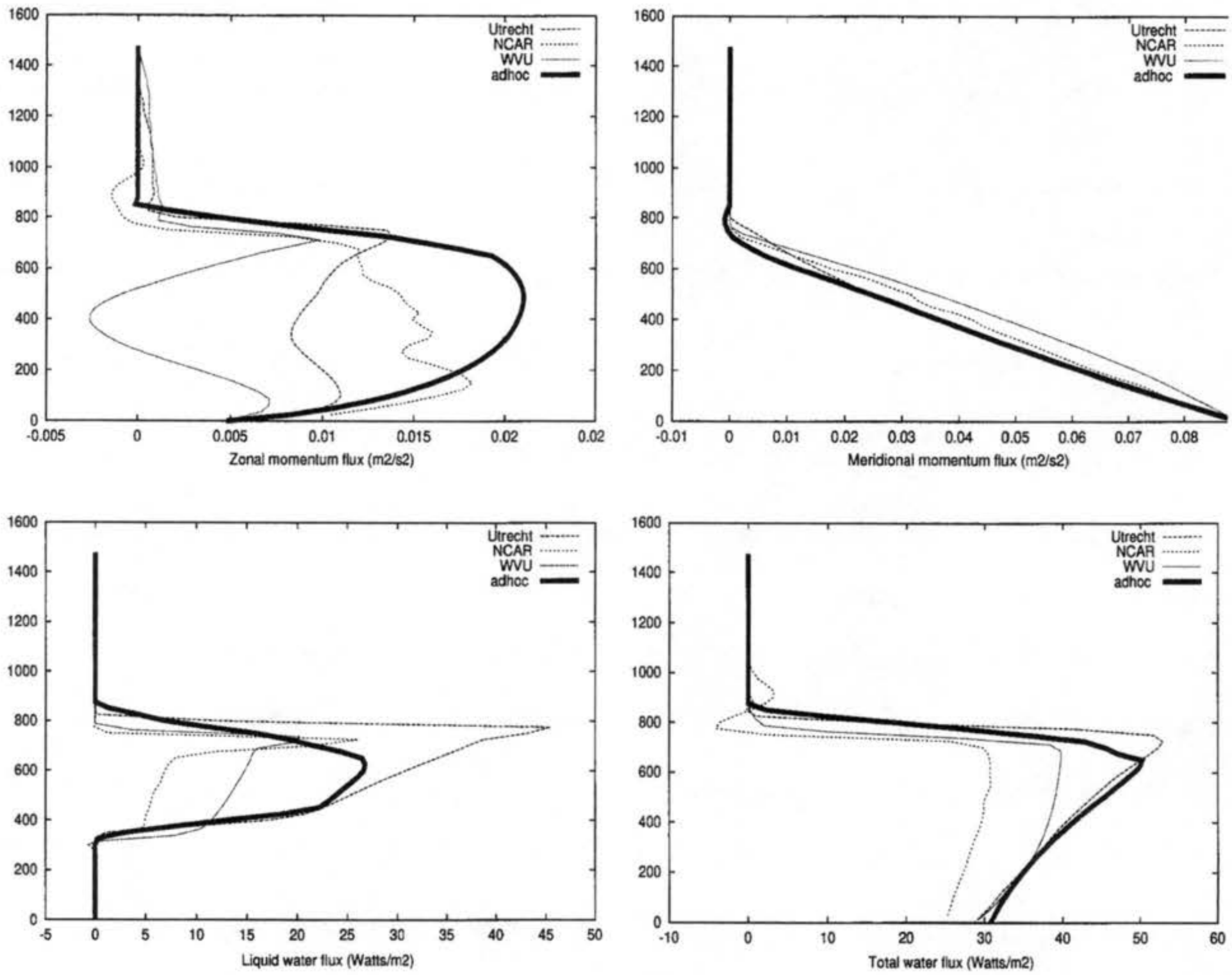

Figure 54: Comparison of the ADHOC- and LES-simulated fluxes for ASTEX: zonal momentum (top, left); meridional momentum (top, right); liquid water (bottom, left); total water (bottom, right). The darkest line is ADHOC and the lighter lines are the indicated LES models.

budget profiles and compare them to those of LES and observations (Figs. 56-57). The ADHOC results for the horizontal momentum variance ($\overline{u'u'} + \overline{v'v'}$) are quite different than those simulated by LES, especially near the inversion and near the surface. The simulated vertical velocity variance ($\overline{w'w'}$) is also significantly different than that of two of the LES models, with the largest difference being in the center of the PBL. However, $\overline{w'w'}$ simulated by ADHOC agrees quite nicely with the observations and with the Utrecht LES (the latter only in the upper boundary layer).

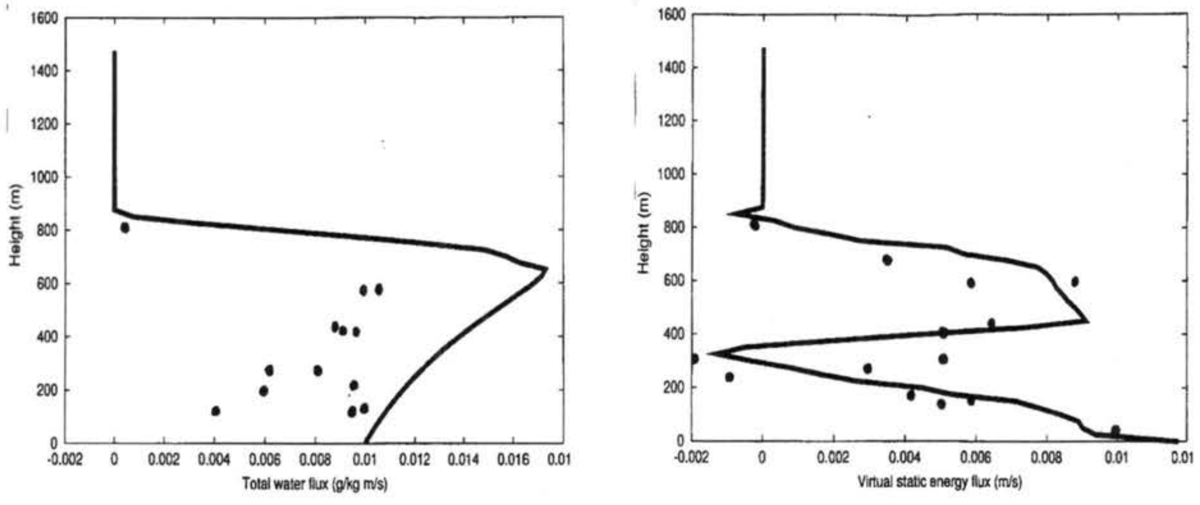

Figure 55: Comparison of the ADHOC-simulated fluxes of total water and virtual static energy with those observed by aircraft. The darkest line is ADHOC, the lighter lines are the indicated LES models, and the dots are aircraft observations from the NCAR electra as analyzed by de Roode and Duynkerke (1997).

Here is where the observations and ADHOC both show that the ASTEX regime has some TWBL characteristics, but that they are more "transitional" in nature than BOMEX and ATEX. The profile of $\overline{w'w'}$ in both BOMEX and ATEX has two distinct maximum (one in the cloud and one in the sub-cloud), with a significant minimum in between (Fig, 35 and 45 respectively). The maximum near the surface forms as a result of the surface sensible and latent heat fluxes, while the maximum in the cloud forms due to a combination of latent heat release at cloud base and radiative cooling at cloud top. In a "classic" ScTBL, however, the cloud-top radiative cooling is so strong that it is able to mix the entire boundary layer (the surface fluxes are also weak in the "classic" ScTBL; thus, they do not provide any resistance to mixing from above). The turbulence statistics in the "classic" ScTBL are more typical of a free convection (such as those of the WD boundary layer). In a free-convective well-mixed boundary layer, there is only a single peak in $\overline{w'w'}$ (Fig. 22).

What we see in ASTEX is a double peak, with a very small minimum in between. If we decrease that minimum a little, it becomes a TWBL profile, and if we increase it a little, it becomes a more "classic" ScTBL profile. This is a perfect example of the "transitional" nature of ASTEX. It is unclear to me why two of the LES models (NCAR and WVU) are producing profiles of $\overline{w'w'}$ which are more "free-convection" type of profiles. The Utrecht LES agrees with ADHOC in the cloud, and it also shows a hint of an additional peak in the sub-cloud layer. The observations strongly support the profile simulated by ADHOC.

The horizontal velocity variance profile simulated by ADHOC is not as encouraging however. It agrees nicely in the middle of the PBL, but is strongly at odds with that simulated by LES near the surface and near the inversion. A similar problem was observed in each of the other 3 cases discussed in this chapter. The reasons for the problem were discussed at length in each of the appropriate sections (WD, Section IV-B-1a; BOMEX, Section IV-C-2b; and ATEX, IV-C-2b). The basic point of those discussions is that the problem is related to (1) inconsistent handling of the pressure terms (the pressure terms are formulated with "conventional" HOC parameterizations and are not strictly compatible with the ADHOC approach; see Section III-H) and (2) the difference in the way that horizontal and vertical momentum are handled by ADHOC, particularly with regard to transport (the horizontal momentum terms still use "conventional" HOC equations; thus, they are currently not yet incorporated into the "ADHOC framework").

As a final note with regard to Fig. 56, I would like to comment that the skewness profiles simulated by ADHOC agree nicely with the observed skewness (bottom panel of Fig. 56), as well as the skewness simulated by LES. These profiles are physically realistic and tell us a significant amount about the regime we are representing. Near the surface, the skewness is close to zero, indicating that the updraft area fraction is approximately 1/2 (Eq. 3.7) (this is physically a result of the weak surface fluxes in ASTEX). At cloud top, the skewness is negative, indicating the presence of narrow downdrafts (this is physically a result of cloud-top radiative cooling). Finally, near cloud base, the skewness becomes positive, signaling the presence of condensational heating.

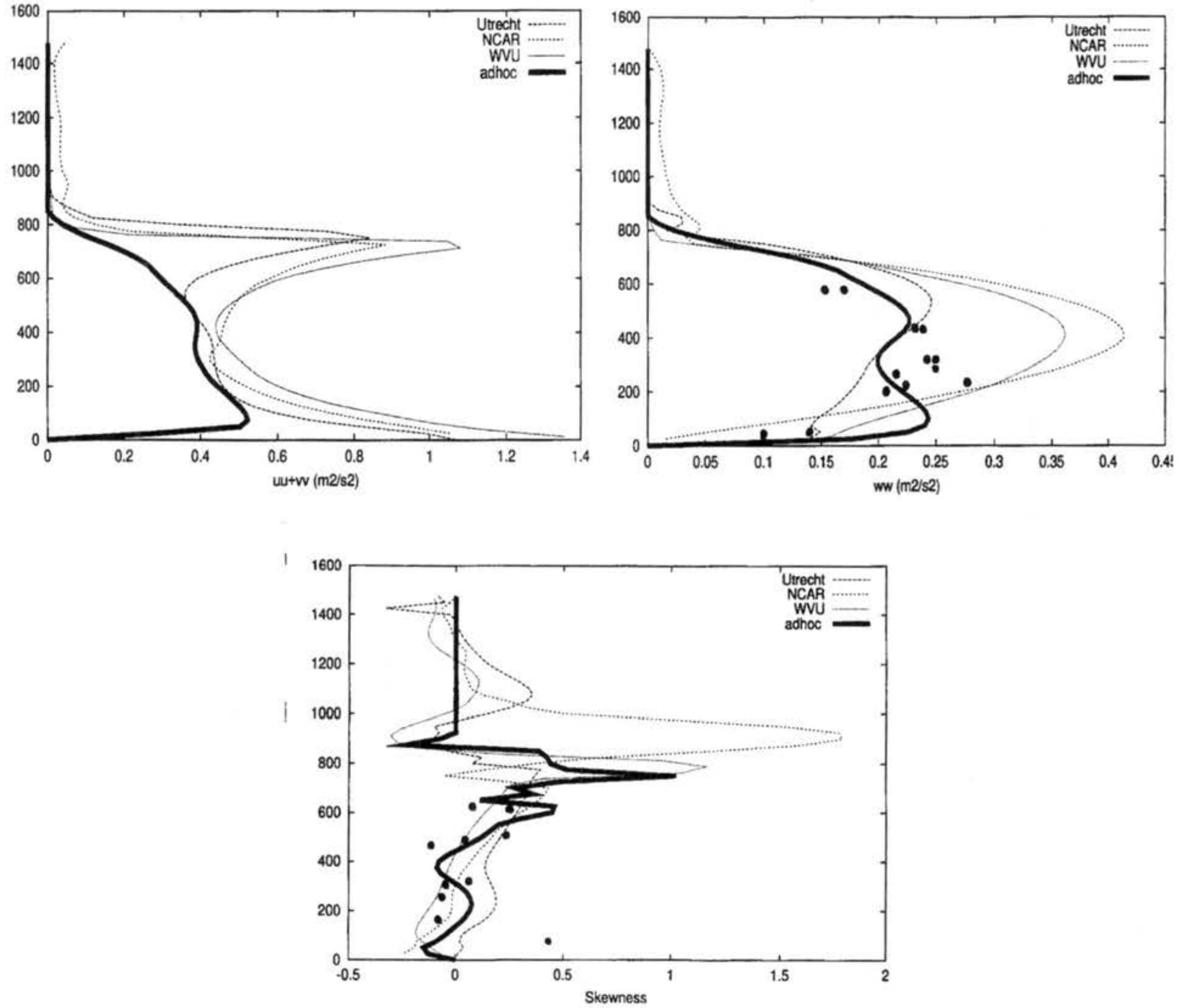

Figure 56: Comparison of the simulated velocity variances and skewness with those simulated by LES and observed. Top left, total horizontal variance; top right, vertical variance; bottom, skewness. The darkest line is ADHOC, the lighter lines are the indicated LES models, and the dots are aircraft observations from the NCAR electra as analyzed by de Roode and Duynkerke (1997).

As a final analysis for ASTEX, I compare the simulated ADHOC TKE budget profiles to those simulated by LES (Fig. 57). There is nothing much to add here, as far as new insight. We see that the largest difference occurs in the buoyancy profile. In the cloud layer, this difference is a direct result of the difference in the simulated radiative cooling between ADHOC and the LES models (Fig. 52). In the sub-cloud layer, the ADHOC-simulated buoyancy is reflective of a more "transitional" profile (one which we would see in between the TWBL and "classic" ScTBL regimes). The two LES models shown in this comparison, however, distinctly represent the turbulence in ASTEX in a manner similar to a "classic" ScTBL (see discussion of $\overline{w'w'}$ from Fig. 56). Much of this is explained above in the discussion of the virtual static energy flux (Fig. 55). Finally, while the difference between the LES and ADHOC-simulated buoyancy is significant, ADHOC closely resembles the observations (Fig. 55), while the LES do not. For the other simulated components of the TKE budget, the ADHOC and LES results agree quite nicely.

IV-D-1c: Summary of ASTEX simulation

The ASTEX region is considered a "transitional" region between the TWBL and the more "classic" ScTBL. The ASTEX field project was designed specifically to study the poorly-understood transition from Sc to Cu in the subtropics. Many of the simulated and observed fields described in the above section distinctly reflect the "transitional" nature of ASTEX, in that they simultaneously exhibit properties of both the TWBL and the "classic" ScTBL (e.g., $\overline{w'w'}$, $\overline{w's'}_v$, and $\overline{\theta_L}$).

The results of the ADHOC simulation of ASTEX were overall in excellent agreement with observations. Their agreement with LES, however, was not always as good. In particular, the ADHOC-simulated TKE buoyancy, vertical velocity variance, and mean liquid water mixing ratio agreed very nicely with the observed values, while they did not agree with those simulated by LES. It appears that ADHOC was able to capture the "TWBL part" of this transitional regime

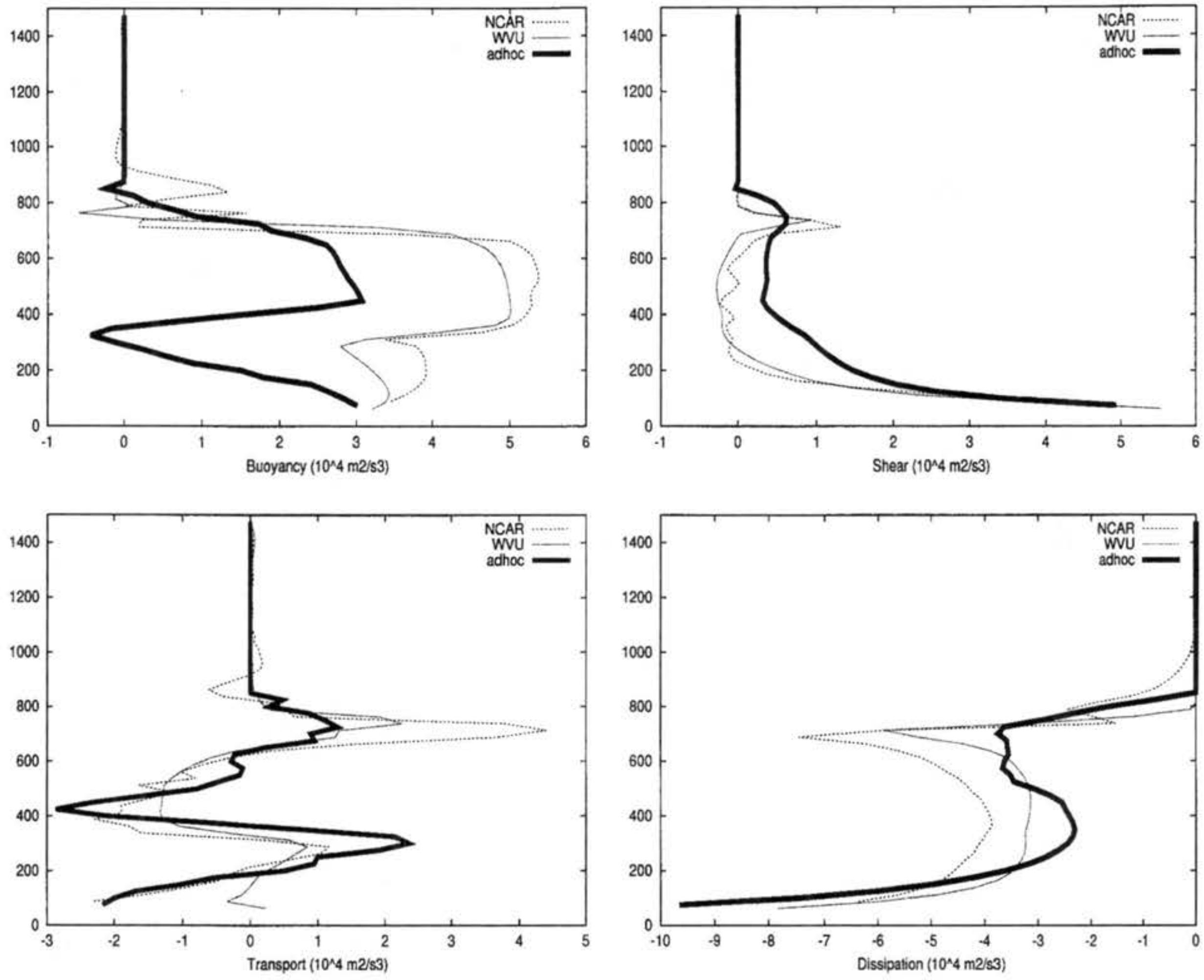

Figure 57: Comparison of the simulated ADHOC TKE budgets with LES for ASTEX. top left, buoyancy; top right, shear; bottom left, transport; bottom right, dissipation. The darkest line is ADHOC and the lighter lines are the indicated LES models.

very nicely, while some LES models had difficulty with this aspect. A good example of this is $\overline{w'w'}$ in Fig. 56. In this plot, ADHOC simulated a "double maximum", which is typical of the profile of $\overline{w'w'}$ in the TWBL. However, the relative minimum in between the two maxima was significantly smaller than that found in the TWBL, indicative of the fact it was not a "true" TWBL, but one in *transition* to the "classic" ScTBL regime. Two of the LES models simulated only a "single maximum" in $\overline{w'w'}$, which is typical of a "classic" ScTBL in the absence of any TWBL influence.

Anther significant difference between the ADHOC and LES simulations of ASTEX was the strength of the radiative cooling, which was much smaller in ADHOC. [this can be seen directly in the radiative flux profiles (Fig. 52) and indirectly in the cloud-top profiles of $\overline{w'\theta_L'}$ and $\overline{w'r_L'}$, where the LES results show a large "spike" and those of ADHOC do not (Figs. 51 and 54 respectively)]. The radiative cooling in the ASTEX GCSS case is a simple function of the integrated liquid water path, which was also smaller in the ADHOC simulations than it was in the LES results (Fig. 50). Due to the pivotal importance of radiative cooling in determining the strength of the downdraft and the subsequent magnitude of $\overline{w'w'}$, the ADHOC-simulated $\overline{w'w'}$ was also much less than that of LES. The ADHOC results are completely consistent with what one would expect with decreased radiative cooling. However, in spite of these ADHOC-LES differences, ADHOC agreed very well with the observed values, while the LES did not. Thus, I am inclined to believe that ADHOC is accurately representing the physics of this "transitional" regime.

The only major difference between the ADHOC simulation and the aircraft observations was that the total water flux in ADHOC was larger than that observed (Fig. 55). This was attributed to the large simulated entrainment drying at cloud top, which increased the upward moisture flux in the cloud. This was supported by Fig. 54, where the ADHOC-simulated $\overline{w'r'_T}$ is shown to reside on the high end of that simulated by LES. In this case, the LES agrees better with the observations than ADHOC does. What is interesting here is that the ADHOC-simulated profile of $\overline{w's'_v}$ agreed quite nicely with the observations, while the LES values were too small. This indicates to me that the ADHOC-simulated liquid water static energy flux ($\overline{w's'_L}$) must be smaller than that observed (so that it can balance the error in $\overline{w'r'_T}$ and produce an accurate $\overline{w's'_v}$); the same must be true for the LES-simulated $\overline{w's'_L}$, only for a different reason (so that it is consistent with the fact that its $\overline{w'r'_T}$ is correct, but its $\overline{w's'_v}$ is small). I could not find any observational data to support or refute this conjecture.

As a final note, Id like to discuss the benefits associated with simulating this ASTEX case. In the introduction section of chapter IV, I argued that I needed to analyze as many cases as possible because certain key physical issues are specific to one "type" of regime. The ASTEX simulation really highlighted this point. For example, if I had analyzed only WD, ATEX, and BOMEX for this thesis, one of my conclusions surely would have been that "entrainment is inefficient in ADHOC". I likely would have spent a great deal of time trying to "fix" that aspect of the model. However, with the addition of the ASTEX case, I learned that "entrainment is not inefficient in all situations". In fact, it can be *overly* efficient at times. This simulation allowed me to look at the problem in a new light. Instead of trying to "fix" the model (which is really a broad and obscure task), I simply analyzed the differences between the ASTEX and ATEX simulations and I gained new insight; the initiation of entrainment is highly dependent on the quantity of liquid water in the downdrafts; the moister the downdrafts, the more the entrainment. This pointed out the important role of evaporative cooling in the ADHOC simulations, and perhaps in the real atmosphere as well.

In the next section, I will examine yet another very different "type" of cloudy regime; that of Arctic stratus. I would expect many of the problems that I had in the more convective regimes to not be present in the stable Arctic stratus clouds. However, these clouds present new and different challenges. These new issues will be discussed and analyzed extensively Section IV-E below.

IV-E: Arctic Stratus

GCM simulations suggest that Arctic climate is sensitive to a doubling of tropospheric

CO_2 concentrations (Walsh and Crane, 1992). Simulations show a warming of 8-16°C in the Arctic winter compared to 1.5-4°C at lower latitudes (Houghton and Tourre, 1992). Prior to the 1997-1998 SHEBA/FIRE project, observations in the Arctic were scarce. Thus, we lack much of the knowledge necessary to accurately parameterize Arctic processes in GCMs, casting doubt on the simulated large temperature responses to CO_2 doubling. A major source this uncertainty is Arctic stratus clouds (ASC) and their associated feedbacks with the surface and the atmosphere (Walsh and Crane, 1992).

Currently, large discrepancies exist between GCM simulations and observed cloudiness in the Arctic (Lappen, 1996). Because the Arctic atmosphere is different both radiatively and thermodynamically, our understanding of cloud processes at lower latitudes does not apply here (McInnes and Curry, 1995). As a result, there is a big push in the modeling and observational communities to study Arctic stratus and develop "Arctic-specific" parameterizations. In order to do this, we need to better represent the mechanisms that form and dissipate these clouds, as well as the processes that sustain them. The latter includes their

- turbulent structure,
- microphysical interactions,
- radiative feedbacks, and
- interactions with the surface.

We must also understand how these processes in turn affect global climate.

Arctic stratus clouds are widespread and persistent. With cloud-fractional coverage typically ranging from 70-90% in summer (Herman and Goody, 1976), they play an important role in the surface radiation budget of the Arctic. These radiative effects (both shortwave and longwave) differ greatly from that of stratus clouds at lower latitudes; Curry and Ebert (1992) found that

ASC have an overall warming effect (except during a few weeks in summer), while at lower latitudes, stratus clouds cool the surface. Tsay et al. (1989) found that these clouds increase the downward longwave flux by 130 to 200 W m^{-2}.

The net radiative effects of ASCs on the surface is complicated by nonlinear interactions with the sea ice cover. The surface net flux depends on the state of the surface (relative amounts of ice, snow and open water) which is modulated by cloud cover (Ebert, 1984; Curry and Ebert, 1990). Clouds directly affect the surface temperature and albedo (Shine and Henderson-Sellers, 1985) and indirectly affect the stability of the atmospheric boundary layer through surface sensible and latent heat fluxes (Ebert, 1984). These non-linear feedbacks between the clouds and the surface make an assessment of cloud sensitivity over the Arctic more complex than in other areas of the globe (Curry et al., 1993). In addition, these feedback mechanisms are seasonally dependent, complicated by the low, persistent sun angles in the summer and the lack of solar radiation in the winter.

Small differences in the complex microphysical properties of ASCs also have a large effect on the radiative budget of the Arctic. Cloud optical depth has been shown to increase with increasing atmospheric temperatures, resulting in an enhanced net radiation flux at the surface. This so called "cloud-optical depth feedback" is positive in the Arctic (Curry et al., 1993), in contrast with the global result obtained by Somerville and Remer (1984). In addition, the Arctic may be a sink region for anthropogenic pollutants transported northward from mid-latitude sources (Barrie, 1986). This increase in aerosols has been hypothesized to make the cloud droplets smaller and more numerous (Curry et al., 1993), suppressing drizzle, increasing cloud optical depth, and slowing the breakup of ASCs (Curry, 1995). The results of calculations for the Arctic indicate that the response of the surface radiation fluxes to a decrease in drop size is complex, showing a decrease in summer and an increase in winter (Curry et al., 1993). Overall, we see that Arctic clouds do not provide a consistent negative feedback that would counteract the effects of global warming.

Curry et al. (1988) identified three main types of ASCs:

1. a cloud-topped mixed layer extending from the surface to the inversion base (likely formation mechanism: convection from cold air advecting over a relatively warm Arctic ocean);
2. a stable boundary layer with thin patchy clouds in numerous layers (likely formation mechanism: horizontal advection of warm, humid air into the colder Arctic basin)
3. a stable foggy boundary layer, surmounted by a cloud-topped mixed-layer (likely formation mechanism: a combination of advection and surface fluxes)

The underlying physical interactions that govern the behavior of ASCs are different for all three types, making their parameterization difficult. The simulation of these structures is further complicated by the frequent presence of multiple cloud layers, humidity inversions above cloud top, vertical in-cloud fluxes that are decoupled from the surface fluxes, and complex cloud microphysics (discussed above). This suggests models with sophisticated parameterizations are needed to accurately model this region.

Up to this point, only closure models have simulated the turbulent small-scale structure of Arctic stratus (for a detailed review of these studies, see Section II-D-2c). As far as mass-flux modeling is concerned, to my knowledge, there have been no attempts to use these parameterizations for Arctic stratus clouds (a discussion of why this is true is given in Section II-E-1). However, It should be stressed here that a mass-flux model may in fact add little to the simulation of ASCs. Typically, the Arctic cloudy boundary layer is shear-driven and level-four second-order closure models (without mass flux) are able to accurately simulate shear-driven boundary layers (Donaldson, 1971; Hanjalic and Launder, 1972). Thus, it is logical to wonder what the mass-flux part of this hybrid model could add to the simulation of ASCs. It is clear that it will not add anything to the shear-driven part of the turbulence because in the current model, momentum fluxes are handled with conventional HOC (see Part I of this paper, Section on momentum). However, in ASCs, turbulence acts to vertically redistribute the cloud thermodynamic properties. This vertical redistribution should be handled quite nicely with the mass-flux part of the model. In addition, it is this vertical redistribution of cloud properties that will ultimately determine the distribution of radiation within the cloud; something which has a critical impact on the regional and global effects of these clouds.

IV-E-1: SHEBA

The SHEBA field project took place from September 1997 to September 1998 on a drifting ice station, between 75N and 80N and between 143W and 166W. For atmospheric scientists, the goal of SHEBA was to extensively measure all facets of the Arctic atmosphere and surface in order to improve GCM's simulations of global climate. This motivation was fueled by the prediction of drastic climate change at high northern latitudes and by the stark differences in the magnitude of this change among different GCMs (see above). To this end, all aspects of the radiation, energy, and water budgets of the Arctic atmosphere and surface were measured throughout an entire annual cycle. For more detailed information about SHEBA, see the SHEBA web page, http://www.sheba.apl.washington.edu.

While the atmospheric component of the field project was designed to increase our understanding of Arctic climate for GCM parameterizations, the link from observations to large-scale models is huge. There are many steps in between. As a first step, we need to examine the data and understand the processes represented by the data. Then, we try to build parameterizations (or modify old ones) using our new insight. We test these new ideas in single-column or small-scale models in order to better isolate the process we are trying to understand. Only if the new parameterizations capture key elements of the physics do we attempt to implement them in large-scale models. ADHOC uses a new method to parameterize atmospheric turbulence and we seek to assess its performance in representing the physics of ASCs. It has shown great promise with tropical and subtropical clouds, but if it is to be used in a large-scale model, it must also perform adequately in high-latitudes.

IV-E-1a: July 23-25 SHEBA case

The synoptic conditions on July 23rd were as follows: a high occupied the Beaufort Sea and the SHEBA camp was on its western side in a southerly flow. A dense cloud mass covered the camp with a base between 4.5 and 5.0 km. This upper cloud showed two thick layers (from 4.5 to 6.5 km and from 7.0 to 10.5 km). The sounding showed a very thin but nearly saturated layer at 3 km with unsaturated conditions above and below this layer. The surface was saturated with fog and 1/2 mile visibility. The low level air (surface to 1.5 km) came from the eastern side of the Beaufort Sea, circling around the high pressure system. Higher altitude air came from the Canadian islands circling around the Beaufort Sea and crossing Alaska's north slope. At 9 km, the air came from the pole, circling around the western Arctic Ocean along the Siberian coast.

The surface fog layer, which was a few hundred meters thick is the subject of this ASC analysis. I chose to simulate this Arctic stratus case because of its simplicity; it is comprised of a single ice-free well-mixed layer with no significant precipitation fluxes [the current version of the model does not include a microphysics package and thus, cannot handle cloud ice or precipitation; it contains only a simple auto-conversion scheme which acts to prevent the buildup of unrealistic liquid water through some gravitational settling of condensate (Curry, 1983)]. Another reason for choosing this case is the availability of good observations (surface-based and aircraft) which can be used to assess the model's performance (many of these observations are not yet available; thus, a more detailed comparison with observations could not be done at this time).

We hope that ADHOC can reproduce the following characteristics of a single-layer liquid ASC (Curry, 1986):

1. The cloud layers themselves are well mixed. This mixing is not generally a result of surface fluxes, but is generated by the cloud itself from radiative cooling and latent heat release.
2. Because of the low sun angle, ASCs always show net cooling. The cloud infrared cooling is largest for clouds with higher liquid water content near cloud top. There is a net heating in the lower portion of the cloud that depends primarily on the difference in temperature between cloud base and the underlying surface.
3. Cloud-top entrainment does not penetrate beyond about 50m from cloud top (the entrainment effects are complicated in the presence of humidity inversions at cloud top.
4. The water fluxes near cloud base are negative or weakly positive, indicating that surface evaporation plays little role in maintaining the cloud. In the cloud interior, the total liquid water flux is as large as the water vapor flux.

For the ADHOC simulation of this case, I used a vertical resolutions of 15m. Sensitivity studies performed shows that grid resolution has a significant impact on the development of the turbulence and the evolution of the cloud (Section IV-E-1c; Fig. 64). The timestep was 0.5 seconds in both cases. The model was run for 2 days and 12-hour time averages were taken. While this seems like a long period to average, the cloud and turbulence properties changed very slowly for this case. Shorter time averages did not give any additional information about the evolution of this system.

The model was forced with the ECMWF horizontal advective tendencies for moisture and temperature; the ECMWF large-scale vertical velocities[9] (which were used to diagnose vertical advection terms); fully-interactive radiation [An important difference between this case and all the other cases described for this thesis is the use of an interactive radiation scheme (Stephens and Gabriel, 1999)]; and interactive surface fluxes (see Table 2 on page 145). The horizontal advective tendencies and the large-scale vertical velocity used in the 2-day simulation are shown in Fig. 58. This figure shows large-scale rising motion and a low-level moistening and warming throughout most of the lower the lower troposphere. The surface sensible and latent heat fluxes, which were small and played little role in the evolution of the cloud, were computed following Louis (1979). They remained fairly constant throughout the simulation; both being negative and less than 12 W m^{-2}. These values were close to those observed at SHEBA in July [approximately -2.4 W m^{-2} (sensible) and -1.3 W m^{-2} (latent); Ola Persson, personal communication]. However, there was one period of the simulation (between 18 and 36 hours) that these fluxes dropped to near -12 W m^{-2} and hovered there. This is 5-6 times larger than the observed values. I will discuss the reasons for this in detail in the next section.

There was no geostrophic wind data available, and thus, the geostrophic wind was set equal to the predicted wind at each timestep. The skin temperature was set to 274 K, which slightly warmer than the freezing temperature in July (due to surface melting). However, sensitivity studies, using a skin temperature of 271.35 K (the freezing point of sea water), were performed and are also shown in many of the figures. Finally, the surface pressure was interpolated from ECMWF analyses. During this 2-day simulation, the surface pressure remained between 1016 mb and 1019 mb. It decreased for about the first 12 hours and then steadily increased. For a summary of the model forcing and initial case set-up, see Table 2 on page 145).

[9.] This data was taken from the 12-35 hour forecasts of the ECMWF operational model. This forecast assimilated the twice-daily soundings and routine surface observations for the SHEBA ice camp into the model to help initialize each daily cycle. Overall, this suggests that the model wind and temperature fields are quite close to those observed at the SHEBA camp. However, the model is NOT for the exact camp location. Instead, it is for a model grid column that was in theory updated to remain near the SHEBA camp. For more information, see the web page, http://atmos.washington.edu/~breth/SHEBA/ECMWF.html.

IV-E-1b: Results and discussion

This analysis will be a little different than the previous four in this chapter for a number of reasons. This case was not a GCSS "controlled" run so there are no straightforward comparisons that can be made with other models (although a case such as this is currently being constructed). In addition, much of the SHEBA/FIRE observational data has not yet been processed. Thus, in many ways, the analysis of ADHOC below will depend on previous observations of Arctic stratus, although SHEBA/FIRE data is used, where available.

One previously analyzed case in particular had some aspects in common with the current case; the 28 June 1980 case from the Arctic Stratus Experiment in the Beaufort Sea (Curry et al., 1988). In this case, there was a surface fog layer, which extended to 250 m, surmounted by a cloud-topped mixed layer from 700-1000 m. The thermodynamic flux profiles were similar to the current case in magnitude and shape (Fig. 62). However, a significant difference between this case and the current one is that there were actually two cloud layers in the 28 June case, while in ADHOC there was only one. However, ADHOC did show a minimum in liquid water just above the surface (actually several days into the simulation, this minimum gradually became cloud-free). As we will see, this minimum was a sign of decoupling between the in-cloud and surface turbulence (as was the cloud-free region of 28 June 1980); and it was this decoupling that ultimately determined the structure of the thermodynamic fluxes; thus, the cases were actually quite similar. Anther big difference between the current case and the 28 June 1980 case is the height of cloud layers; thus, we try to compare the two cases in a relative manner (relative to the cloud location, not the actual heights).

In addition, since the properties of ASCs appear to be highly case-dependent, comparisons with previous cases need to be viewed in a "qualitative" manner only. For example, studies show that the development of ASCs is highly dependent on even subtle differences in their liquid water

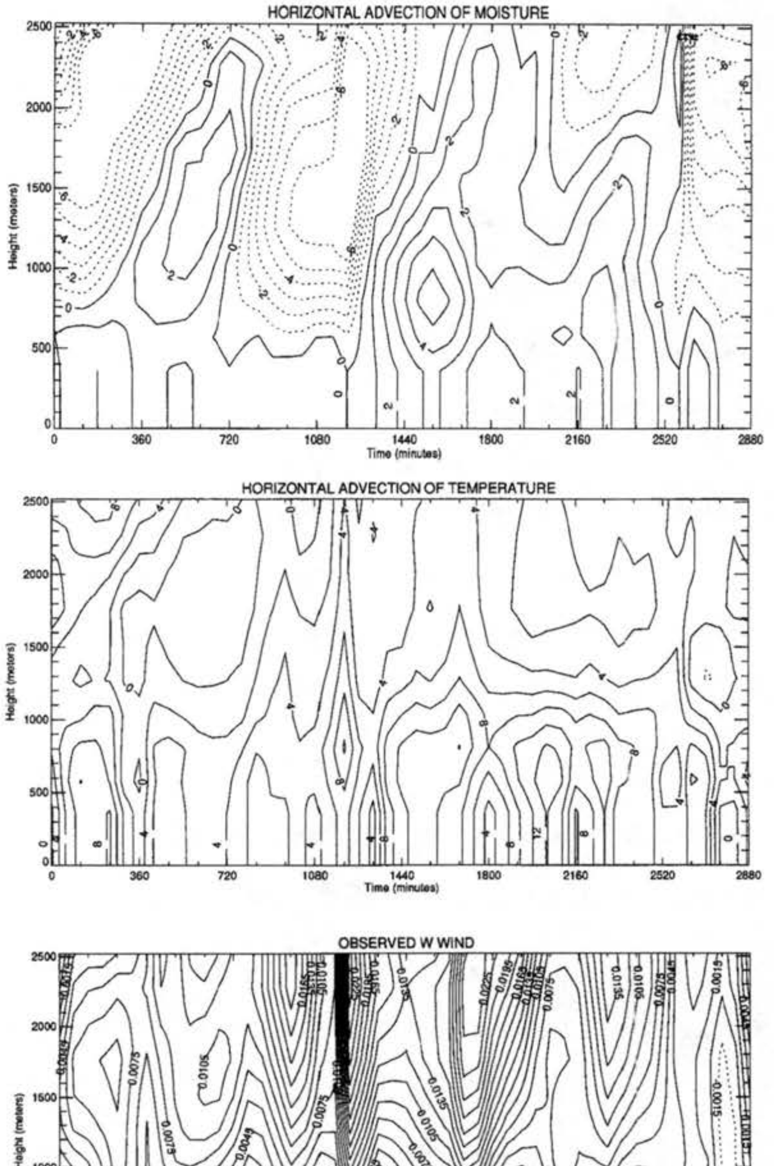

Figure 58: Time series of the horizontal advective forcing and subsidence for the 2-day ADHOC simulation. Top, advection of temperature (K day^{-1}); middle, advection of total water (g kg^{-1} day^{-1}); bottom subsidence velocity (m s^{-1}). Stippled regions indicate negative values.

content and microphysical properties (Curry et al. 1988; Curry and Ebert, 1992). There is not yet enough cloud data available for the July 23 SHEBA case to comment on its microphysical similarity with previously analyzed ASCs. In the figures in the remainder of this section, comparisons are made, where applicable, with the 28 June 1980 case. However, until cloud microphysical data is available for the July 23 SHEBA case, more quantitative comparisons are not possible. The eventual setup of the GCSS Arctic stratus case will be a very beneficial "post-thesis" analysis of these clouds.

Figure 59 shows a comparison of the evolution of the simulated temperature, mixing ratio, and relative humidity profiles with those measured using rawinsondes at SHEBA. The profiles are shown are for 3 different times (6, 18, and 30 hours into the run, corresponding to the times when rawinsonde data was available) and for 2 different initial skin temperatures (271.35 K and 274 K; discussed above). The profile which corresponds to the skin temperature of 274 K (green curves in Fig. 59) will be used in this discussion, since this is close to the "typical" July value at SHEBA. The profiles which correspond to 271 K are provided only for a reference, showing the sensitivity of the model to skin temperature. In general, this difference is not all that significant with regard to the shapes of the observed profiles. The overall biggest effects are in the simulated cloud-top height and the magnitude of the mean temperature and humidity in the cloud layer; the cooler skin temperature makes the cloud cooler and drier, but does not affect the relative humidity (RH) or the shape of the turbulence profiles (everything is just more "compressed"). With that said, I will not elaborate on the sensitivity study further, but will return to it in a later discussion in this section.

Overall, the simulated profiles are agree very nicely with the observations for all three fields. During the first 6 hours, the simulated and observed relative humidity in the lower part of the boundary layer is gradually increasing (see Fig. 60). By hour 6, the observations show a fog layer which extends to a height of 500 m, while the model is just beginning to reach saturation near 100 m (Fig. 59). This observed cloud is supported by the larger mixing ratios and colder temperatures measured by the rawinsondes between 200 m and 500 m. Since the simulated and observed temperatures are fairly close in value, the difference between the "nearly cloud-free" state in ADHOC and the foggy observed conditions is attributed to differences in the mixing ratio profiles.

Why doesn't ADHOC moisten as quickly as it should? At the beginning of the simulation (only 6 hours before this analysis), the model was initialized with rawinsonde observations (shown in Fig. 60). The difference between the initial mixing ratio profile and the one depicted for hour 6 in Fig. 59 is significant. Initially, the mixing ratio was virtually constant below 350 m at approximately 3.7 g kg^{-1}; above this, it increased to 4.4 g kg^{-1} at a height of 600 m. By hour 6 in the simulation, the mixing ratio in the surface-350 m layer increased to approximately 4.1 g kg^{-1}, while the value at 600 m moistened to 5.0 g kg^{-1}. Thus, we see that ADHOC is moistening at a fairly significant rate at lower levels in response to the forcing. The observations also begin with the mixing ratio profile depicted in Fig. 60. However, the observed profile moistens in a slightly different manner; it shows a moistening "burst" at approximately 500 m (from 3.7 g kg^{-1} to 6.9 g kg^{-1}). Above this, the moistening sharply decreases, while below this, the decrease is more gradual. Below 200 m, the simulated and observed mixing ratios are nearly the same again.

Thus, the question becomes, what is causing this burst of moistening in the 6 hours between the rawinsonde observations and why is it that ADHOC cannot reproduce this? The radiative effects between the surface and 500 m are fairly small, the vertical advection is weak (Fig. 58), and the surfaces fluxes are small and negative. The only factor remaining is the large-scale advective forcing. Fig. 58 shows that the advective forcing is moistening below 800 m. However, the advective tendencies are from the ECMWF analysis, which has a resolution of 25 mb (approximately 250 m). At that resolution, the ECMWF advective forcing has one or two grid points over the range of heights indicated by the moisture "burst"; thus, it is unable to properly resolve the "burst". In this case, the "burst" is severely under-represented. I believe this is why ADHOC did not form a cloud as quickly as the observations indicate that it should.

Twelve hours later, there is a cloud in both the ADHOC simulation and the observations, although the observations indicate a cloud-top height which is slightly higher than that simulated by ADHOC. There is a sharp decrease in the RH above cloud top in both profiles. At the surface, the observations show that the fog layer has lifted. However, ship reports from the Des Groseillier (the SHEBA ice breaker) indicate that no such lifting occurred. I believe this is a problem with the humidity sensor on the rawinsonde. From my experiences up at SHEBA, that was not an unusual occurrence in these extremely cold conditions.

The temperature profiles show exceptionally good agreement in the hour-18 profiles. The radiative cooling at cloud top is fairly large (Fig. 61), as indicated by the decrease of temperature with height in the cloud layer. In addition, we can see signs that entrainment at cloud top is active; in Fig. 60, the total water mixing ratio shows a positive "bump" near cloud top, indicating that entrainment *moistening* is active (note that this case has a humidity inversion at cloud top, so that entrainment actually acts to moisten the cloud layer; this common feature of ASC is something which is not seen in lower latitude clouds).

There is still a large discrepancy between the simulated and observed mixing ratio profiles between 300-600 m. As mentioned, we see that the cloud extends higher in the rawinsonde observations than it does in the ADHOC simulations, and that they both exhibit a sharp moisture decrease at cloud top. Thus, ADHOC is in the process of transitioning to much drier conditions at the same height where the observations indicate that the conditions are saturated. Above this (between 300-600m, at the level where the moisture "burst" appeared in the hour-6 profiles), it appears as though the differences between the observed and simulated mixing ratios are decreasing. During the 12 hours between the hour 6 and the hour 18 profiles, ADHOC moistened between 300-600 m, while the observations slightly dried. This trend continues through the hour 30 profile and will be discussed more below.

At hour 30, the ADHOC-simulated profiles still show a good resemblance to those measured by the rawinsondes. However, there are some significant differences. The observed temperature decreased between cloud top and 1500 m by approximately 1 K, while the simulated profiles actually increased at these levels nearly 2 K. In addition, the cloud-layer temperature in ADHOC also increased by the same 2 K, while that observed did not change. The fact that the entire ADHOC profile changed by approximately the same value is suspicious. For this case, there is no turbulent forcing (i.e., surface fluxes, radiation) which could cause a heating rate of 4 K day^{-1} in the cloud, and, even if there was, it could not explain the warming above the cloud. The large scale must be responsible for this.

In Fig. 58, we see that the horizontal temperature advection is largest in the simulation between hours 18 and 36. Ironically, it averages approximately 4 K day^{-1}; the exact rate of the observed temperature increase during this time. Thus, I conclude that the ECMWF advective tendencies are too strong, and not representative of the observed conditions. Other estimates of horizontal advective warming in the Beaufort region over the ice pack (in the absence of intense synoptic activity) are between zero and 1.4 K day^{-1} (Curry et al., 1988; Curry and Herman, 1985); significantly smaller than 4 K day^{-1} indicated by the ECMWF data for the current case. In addition, as discussed above, the simulated sensible heat fluxes are too large in magnitude (-12 W m^{-2} compared with an observed value of -2.4 W m^{-2}) during hours 18-36. This unrealistic advective warming of the air is enough to explain the discrepancy.

The difference between the simulated and observed mixing ratios at hour 6 decreased by hour 18 (discussed above), and has further decreased by hour 30. In fact, if one were to smooth out the noisy hour-30 observed mixing ratio profile, it would closely resemble that simulated by ADHOC. One should not be fooled by this agreement, however. Upon closer inspection, we can see that there are offsetting problems. First of all, in the 300-500 m height range, the observed mixing ratio has not significantly changed. Originally, we attributed under-resolved advective forcing to the difference between the simulated and observed mixing ratios at these levels. How is it that the ADHOC-simulated mixing ratio suddenly increases now, while that observed does not? The answer is the same as that discussed above to explain the temperature differences. The ECMWF advective moisture forcing in this case is too strong for the entire layer below 1000 m. In Fig. 58, we see that the largest moistening occurs between 300 m and 1000 m, during hours 22-30. A smaller but still significant moistening occurs between the surface and 300 m. In the 300-1000 m layer, the moistening averages approximately 3 g kg^{-1} day^{-1}. Other estimates of horizontal advective moistening in the Beaufort region over the ice pack (in the absence of intense synoptic activity) are between zero and 0.4 g kg^{-1} day^{-1} (Curry et al., 1988; Curry and Herman, 1985), an order of magnitude smaller than the 3 g kg^{-1} day^{-1} indicated by the ECMWF data for the current case. In addition, the ADHOC-simulated surface latent heat fluxes are (like the sensible heat fluxes) too large only during these hours of anomalous moistening (-10 W m^{-2} compared with an observed value of -1.3 W m^{-2}).

Thus, we see that both the advective warming and moistening are abnormally large during hours 18-36. As a result, the surface sensible and latent heat fluxes increase by factors of 5 and 10 respectively. While this is obviously an error, the evolution of the cloud is not significantly affected for two reasons:

1. There are offsetting problems near the entrainment region; just above the cloud top, the simulated moisture profiles are initially smaller than those observed, because the ECMWF gridded advective tendencies (which are used to force the model)

cannot properly resolve the observed forcing. However, the simulated moisture profiles by hour 30 are much closer to those observed at this level (although they are still too dry), because the ECMWF horizontal advective moistening is abnormally large over the entire lower boundary layer.

2. The errors at the surface are not as significant as they appear; while the magnitude of the surface fluxes is affected by the errors in the ECMWF horizontal advective forcing, the evolution of the cloud is highly dependent on cloud-top radiative cooling (for this case), and less (if at all) on the surface fluxes.

With this in mind, I would like to describe the evolution of the boundary layer purely from the perspective of the ADHOC equations. We know that (1) the simulated surface fluxes, which are directed downwards, are too large during hours 18-36; (2) the model produces a cloud layer which is too warm and too moist during the same period; and (3) the region above the cloud (the entrainment region) is too dry during the whole period (less so toward the end) and too warm during hours 18-36. How does the model evolve in response to these known errors? Does the evolution of the ADHOC fields make sense in light of these problems. In the next few pages, we will specifically address this. During this discussion, we will refer to other similar observed cases for comparison.

Figure 60 shows the evolution of the mean profiles of the meridional wind ($\overline{V}$), total and liquid water mixing ratios ($\overline{r_T}$ and $\overline{r_L}$ respectively), and liquid water potential temperature ($\overline{\theta_L}$). The initial profiles are also shown (the darkest line) for reference (note that the scale here is different than that in Fig. 59; only the most active lower boundary layer region is shown). The profile of $\overline{V}$ is initially well mixed. The magnitude at lower levels decreases due to the surface influence. The simulated $\overline{V}$ profile increases during the first 12 hours, and decreases rather steadily over the following 24 hours. As the magnitude of the wind evolves, the wind profile maintains its shape.

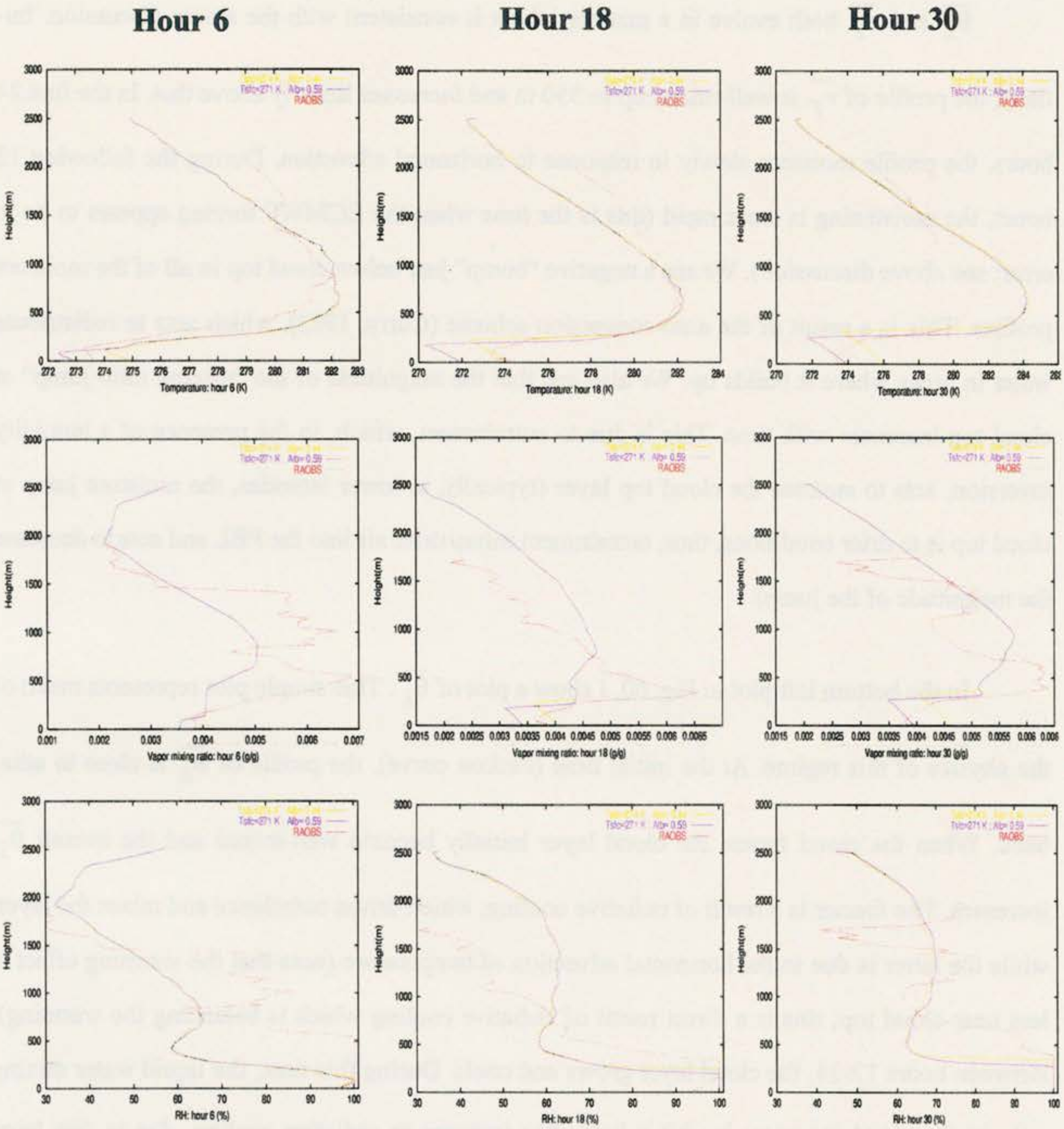

Figure 59: Comparison between simulated and observed temperature (top row), water vapor mixing ratio (middle row), and relative humidity (bottom row). The left column is for 6 hours into the simulation; the middle column is for 18 hours into the simulation; and the right column is for 30 hours into the simulation. The observations are from rawinsondes, which were launched at SHEBA. The two ADHOC runs are for skin temperatures of 271.35 K and 274 K, the latter of which is more "typical" for July at SHEBA.

$\overline{\theta_L}$ and $\overline{r_T}$ both evolve in a manner which is consistent with the above discussion. Initially, the profile of $\overline{r_T}$ is well-mixed up to 350 m and *increases* linearly above this. In the first 24 hours, the profile moistens slowly in response to horizontal advection. During the following 12 hours, the moistening is more rapid (this is the time when the ECMWF forcing appears to be in error; see above discussion). We see a negative "bump" just below cloud top in all of the moisture profiles. This is a result of the auto-conversion scheme (Curry, 1983), which acts to redistribute water in areas where it builds up. We also see that the magnitude of the "mixing ratio jump" at cloud top increases with time. This is due to entrainment, which, in the presence of a humidity inversion, acts to *moisten* the cloud top layer (typically, at lower latitudes, the moisture jump at cloud top is to drier conditions; thus, entrainment mixes drier air into the PBL and acts to decrease the magnitude of the jump).

In the bottom left plot in Fig. 60, I show a plot of $\overline{\theta_L}$. This simple plot represents much of the physics of this regime. At the initial time (darkest curve), the profile of $\overline{\theta_L}$ is close to adiabatic. When the cloud forms, the cloud layer initially become well-mixed and the overall $\overline{\theta_L}$ increases. The former is a result of radiative cooling, which drives turbulence and mixes the layer, while the latter is due to the horizontal advection of temperature (note that the warming effect is less near cloud top; this is a direct result of radiative cooling which is balancing the warming). Between hours 12-24, the cloud layer grows and cools. During this time, the liquid water mixing ratio in the cloud increases by 0.3 g kg^{-1}. The increase in radiative cooling, due to this large increase in $\overline{r_L}$, outweighs the warming due to horizontal advection.

During the subsequent 12 hours (hours 24-36), the "unrealistically large" ECMWF advective warming (see above discussion) is large enough to outweigh the radiative cooling. During this time, $\overline{r_L}$ increases less than 0.05 g kg^{-1}. Another interesting feature of the 24-36 hour $\overline{\theta_L}$ profile is that the layer from the surface to 150 m appears to not be as well mixed as the rest of the profile. What is occurring here is that the unrealistically large warming creates stronger-than-normal downward sensible and latent heat fluxes (see above discussion). This acts to cool the lower layers, decoupling them from the in-cloud turbulence. Thus, we see that ADHOC is responding in a manner which is physically consistent with the "unrealistic ECMWF" forcing.

As a final note, the magnitude of the liquid water mixing ratios simulated in this case are within the range of those previously observed in these types of ASCs [~0.1-0.3 g kg^{-1}, Tsay and Jayaweera (1984); ~0.35-0.5 g kg^{-1}, McInnes and Curry (1995); ~0.5 g kg^{-1}, Smith and Kao (1996)].

As discussed, the radiative forcing in this simulation is interactive, using the radiation scheme described by Stephens and Gabriel (1999). Figure 61 shows a time series of the shortwave (SW) and longwave (LW) radiation at the top of the atmosphere (TOA), as well as the net SW at the surface; also shown are the simulated time-averaged profiles of the SW, LW, and net heating/cooling rate during hours 24-36. The climatological averages for July, as reported by Curry and Ebert (1992), are also indicated. The most obvious feature in the SW plots is the diurnal cycle. The values of both the SW and LW fluxes reported by Curry and Ebert are close to those diagnosed in the presence of the cloud by the radiation code in ADHOC. This shows that the climatological averages include clouds most of the time. In fact, the reported cloud cover in the summer of the Arctic is near 90%, with the low cloud cover near 75% (Huschke, 1969).

The cloud forcing (SW, LW, or net) is defined as the difference in magnitude between the respective cloudy and clear-sky radiative fluxes. The simulated surface cloud forcing is -140 W m^{-2}, while the TOA SW cloud forcing is -110 W m^{-2}. Thus, the clouds act to cool the atmosphere,

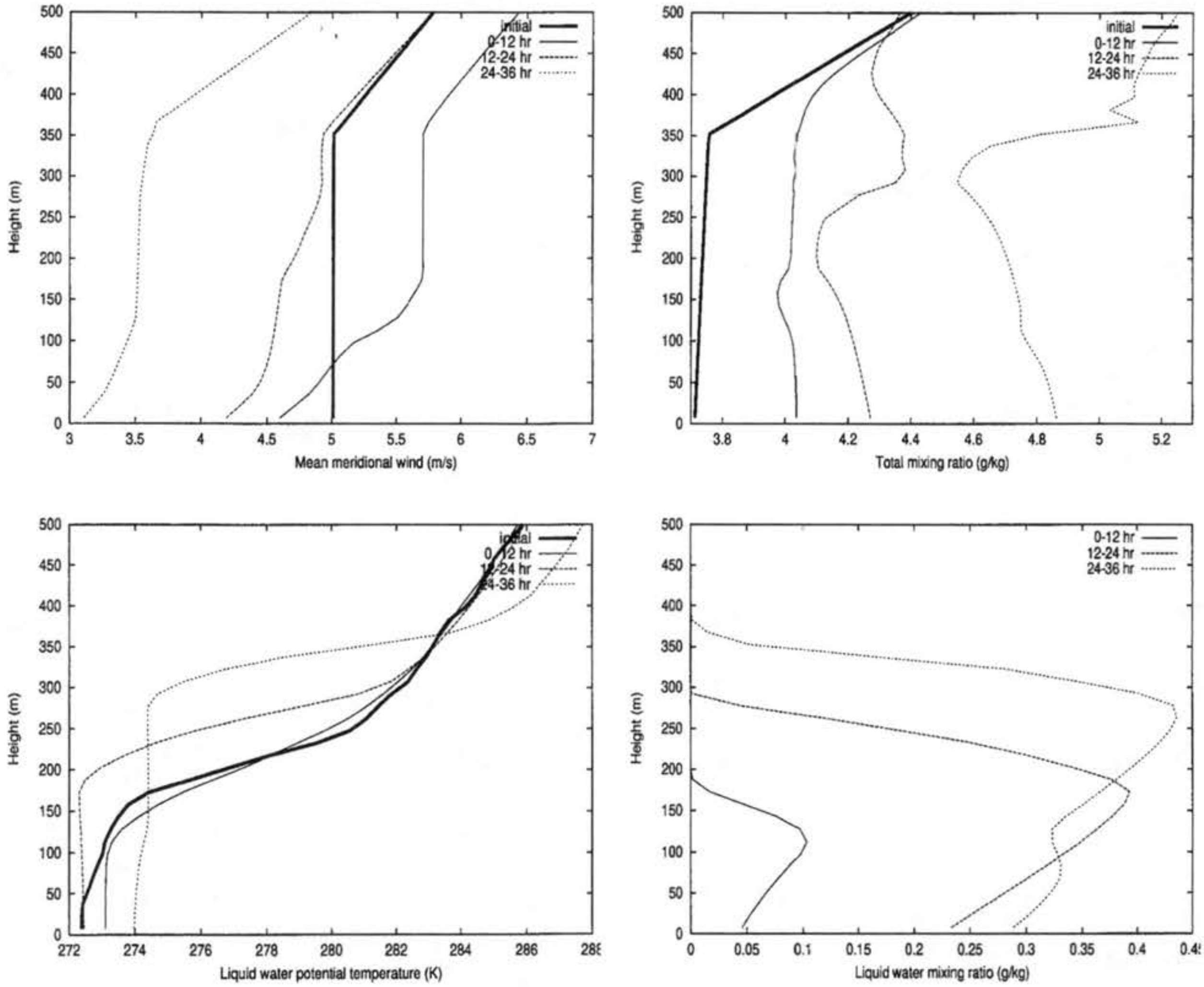

Figure 60: Profiles of the simulated mean meridional velocity (top, left); mean total water mixing ratio (top, right); mean liquid water potential temperature (bottom, left); and mean liquid water mixing ratio (bottom, right). The darkest line is the initial conditions. All other lines are averages for the period indicated.

with the surface cooling being larger than that at the TOA. Curry and Ebert (1992) found that climatologically, the actual cooling is slightly stronger at the TOA. However, the current study is one case, which I am comparing to a multi-year climatological average. In addition, these parameters are very sensitive to cloud microphysical properties, which I am not computing here (there is not microphysics package in ADHOC). The magnitude of the SW cloud forcing reported by Curry and Ebert (1992) is -100 W m^{-2} (surface) and -110 W m^{-2} (TOA), which is quite close to those simulated by ADHOC.

The simulated TOA LW forcing is also close to that reported by Curry and Ebert (270 W m^{-2}). There is a 3 W m^{-2} decrease in the TOA LW flux when the skin temperature is dropped to 271.35 K. While this is larger than that found for the SW fluxes, it still only represents 1% of the total.

The LW, SW, and net heating/cooling rate profiles are shown in the bottom, right panel of Fig. 61. We see that the net cloud-top radiative cooling averages approximately -35 K day^{-1} (divided between -46 K day^{-1} LW cooling and 11 K day^{-1} SW heating). This cooling, which occurs over a 50 m interval, is lower than that reported by McInnes and Curry (1995; -60 K day^{-1} over a 50 m interval) and Curry (1986; approximately -45 K day^{-1} over 50 m in their "deck 1" shown in Fig. 4). I believe that the reason for the difference is that the ADHOC cooling, shown in Fig. 61, is a 12-hour time-averaged rate. The cloud is growing over this 12-hour period and thus, the cloud top (the area of maximum cooling) only resides at a given height for part of the time. The time-averaged cooling in this case would be less than that found if we were to always measure the value at the cloud top itself. Following cloud top, the radiative cooling rate is near -60 K day^{-1} over 50 m, significantly larger than the time-averaged value.

As a final note, there is an small peak in the radiative cooling near the surface. As we discussed above, the liquid water mixing ratio increases near the surface due to an increase in the downward sensible and latent heat fluxes there (caused by unrealistic horizontal advection; see above discussion). This increase in the simulated liquid water (which can be seen in Fig. 60) is responsible for the small radiative cooling increase near the surface in Fig. 61.

In Fig. 62, I show the simulated fluxes of meridional momentum, total and liquid water,

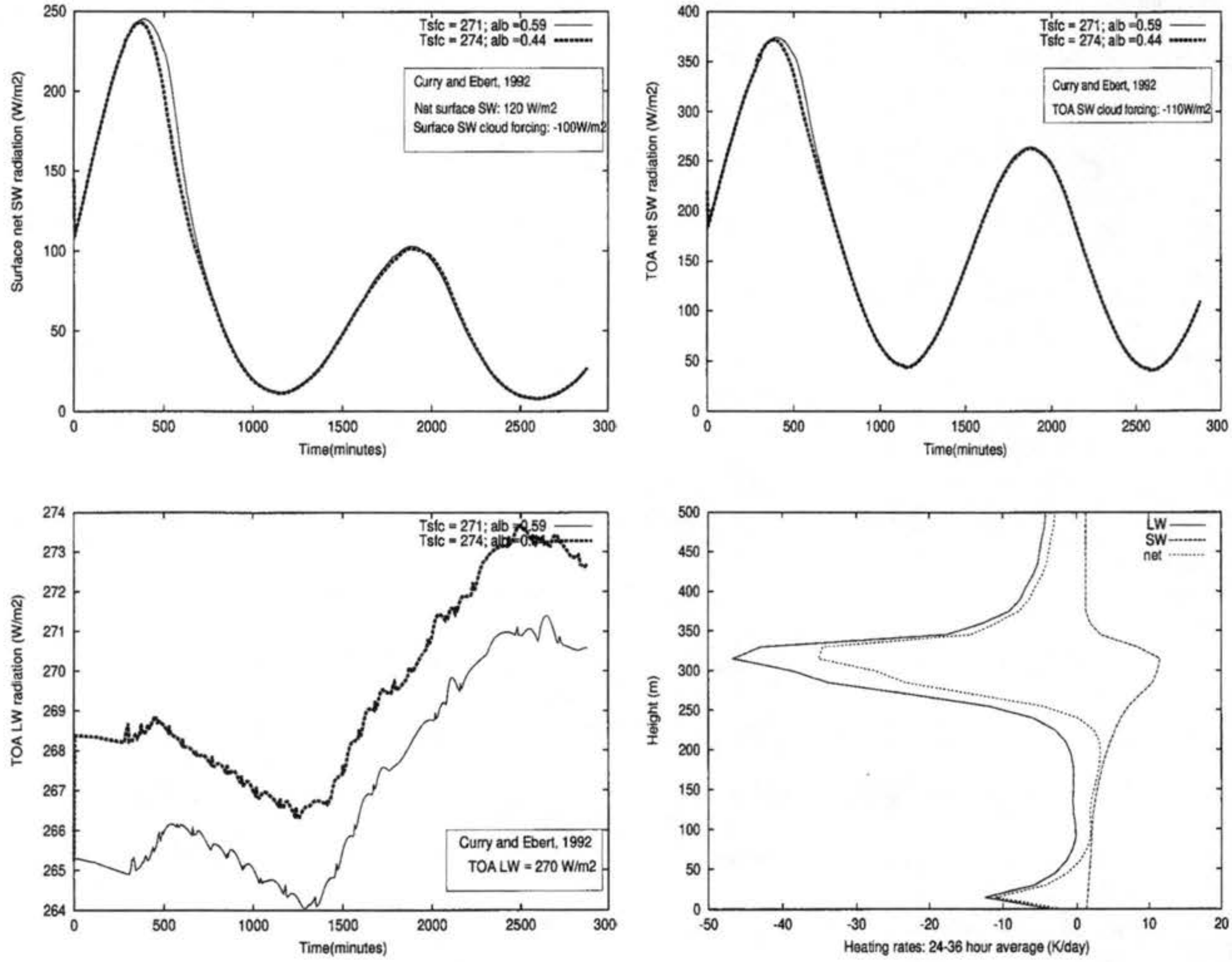

Figure 61: Time series of the radiative forcing, diagnosed using the radiation code of Stephens and Gabriel (1999). Top left, surface net SW radiation; top right, TOA net sw radiation; bottom left, TOA net LW radiation; bottom right, SW, LW, and net radiative heating rates. The values obtained by Curry and Ebert (1992) are indicated. The two ADHOC runs are for 271 K and 274 K (along with their appropriate albedos) as indicated. The darkest lines are for the more "typical" skin temperature and albedo in July.

and virtual potential temperatures. The momentum fluxes are smooth and evolve in a manner which is consistent with the growth of turbulence in the boundary layer. However, the momentum fluxes do not show even a slight peak at cloud top, as they should (this is reported my almost all other studies of ASC (e.g., Finger and Wendling, 1990; Curry et al., 1988; Smith and Kao, 1996). The problem here is related to the handling of horizontal momentum in ADHOC. This is discussed in great detail in Section IV-A, and thus, will not be discussed further here.

The potential temperature and total water fluxes are fairly typical for ASCs. Next to the corresponding ADHOC-simulated profiles in Fig. 62 are the simulated profiles from Smith and Kao (1996; SK96; lines) and the observations reported by Curry (1986; C86; circles). The ADHOC-simulated fluxes are amazingly similar to the profiles of SK96 and C86 in shape, and are within a reasonable range in magnitude[10]; especially considering the large differences that are found among ASCs.

The simulated virtual potential temperature fluxes are negative near the surface in ADHOC, as well as in the comparative plots. In ADHOC, right at the surface, we see a discontinuous jump to very large negative values. This is a direct result of the unrealistic advective warming (discussed above), and is not a problem with ADHOC. The simulated heat flux, in the absence of this unrealistic warming, is negative and continuous with the heat flux above this layer (as evidenced by the profile before the unrealistic warming begins; not shown). In general, the negative virtual heat flux indicates that the turbulence is not driven by buoyant production at the surface (this is supported by C86, who found that at most 10% of the cloud-top cooling is balanced by heat fluxes from below). The virtual heat flux increases with height in the cloud to a maximum at cloud top, showing the effects of condensation and radiative cooling. At cloud top, the heat flux decreases sharply with height, as a result of the strong radiative flux divergence which occurs in this layer (Fig. 61). The region of negative virtual heat flux corresponds to the entrainment of warm air into the boundary layer. These features are also indicated by the studies of SK96 and C86.

---

[10]. Note that the actual heights are not included on the Smith and Kao (1996) and Curry (1986) plots. The case represented by these plots is an ASC with a cloud top near 1000 m and a cloud base at approximately 500 m; from 250-500 m is a humid, but unsaturated layer, which transitions to a foggy layer between the surface and 250 m. Thus, the cloud heights do not correspond with those in the current case. The plots are provided for a "generic" shape-and-magnitude comparison to previously studied ASCs.

The ADHOC-simulated total water fluxes also agree nicely in shape and magnitude with those of SK96 and C86 (with the exception of the jump in the latent heat flux at the surface, which is related to the "anomalous advection" problem discussed numerous times). The stable, near surface region is characterized by a negative total moisture flux, which indicates that moisture is being removed from the atmosphere and deposited on the ice. This transport is like facilitated by the large near-surface momentum fluxes.

Above this, the simulated ADHOC moisture flux profile and those of SK96 and C86 all exhibit the same unusual feature; the flux, which is increasing upwards from the surface, transitions to a near vertical profile, and then resumes a positive slope. This feature in ADHOC is strongest during the 24-36 hour period, but can still be seen during the earlier 12-hour period. In SK96 and C86, the region over which this occurs is actually cloud-free, while in ADHOC it is not. However, this feature is an indicator that the surface and the cloud layers are decoupled (at least partially), which occurs in ADHOC, as well as in SK96 and C86. In addition, while this region is not cloud-free in the ADHOC simulation, the liquid water mixing ratio is a minimum there (Fig. 60). Thus, while the cloud structure is not similar (between ADHOC and SK96/C86) in this region, the feature is not necessarily associated with the cloud-free conditions. It is more an sign that the surface fluxes are decoupled from the in-cloud fluxes; which is indicated if the region is either cloud-free or characterized by a "liquid water minimum". As an interesting note, when the ADHOC run was extended to more than 2 days, the negative simulated heat and moisture fluxes near the surface eventually dried out the region above the surface fog layer (in ADHOC, this involved the cloud splitting into two layers); at that point the ADHOC simulation and that of SK96 and C86 were even more similar than they are here.

Above this feature, we see that the ADHOC-simulated total water flux and those of SK96 and C86 increase with height. At cloud top, the SK96 profiles show a small negative spike, while the ADHOC 24-36 hour profile does not. It is unclear why this occurs. My guess may be that it is related to entrainment, which dries in the SK96 (since humidity decreases with height above cloud top) and moistens in ADHOC (since humidity increases above cloud top). As a final note about the in-cloud fluxes, the shape and magnitude of the simulated liquid water fluxes in Fig. 62 are close that observed for ASC (Curry et al., 1988 reported approximately 7.5 W m^{-2}).

The last aspect of the turbulence in ASC that I will discuss is the variances and TKE budget profiles. They are shown in Fig. 63. There are a few problems with the vertical velocity variance, $\overline{w'w'}$. The magnitude of $\overline{w'w'}$ is similar to that reported by others [e.g., Smith and Kao, 1996; Finger and Wendling, 1990; Curry et al., 1988 (case 5)]. However, unlike the simulated $\overline{w'w'}$ profile in ADHOC, there is no maximum at the surface in these cases. The large negative sensible and latent heat fluxes at the surface should inhibit any production of $\overline{w'w'}$. In all the studies just mentioned, the horizontal velocity variances are a maximum near the surface (due to shear production) but the vertical velocity variances drop smoothly to zero. In ADHOC, at the lower boundary, $\overline{w'w'}$ is set to zero (surface level not shown in Fig. 63). However, directly above this layer, $\overline{w'w'}$ increases to a large value (0.2 m^2 s^{-2}). This problem relates to something I have discussed exhaustively in the previous sections in this chapter; the pressure terms. The shear terms generate horizontal velocity variance, and then an "over-active" return-to-isotropy term redistributes this variance equally among the 3 components ($\overline{u'u'}$, $\overline{v'v'}$, and $\overline{w'w'}$). The same problem is seen in the rest of the cloud layer in this simulation; in fact, $\overline{u'u'}$, and $\overline{v'v'}$ are indistinguishable in the upper cloud (see Sections II-C-1 and III-H for more information on the "return-to-isotropy" part of the pressure term; see Section IV-A for a discussion of its tendency to be inaccurate; and see Appendix B for a discussion of a possible approach to solving this pressure-related problem). Since enough has already been discussed with regard to this problem, I will not comment further on the near-surface velocity variances.

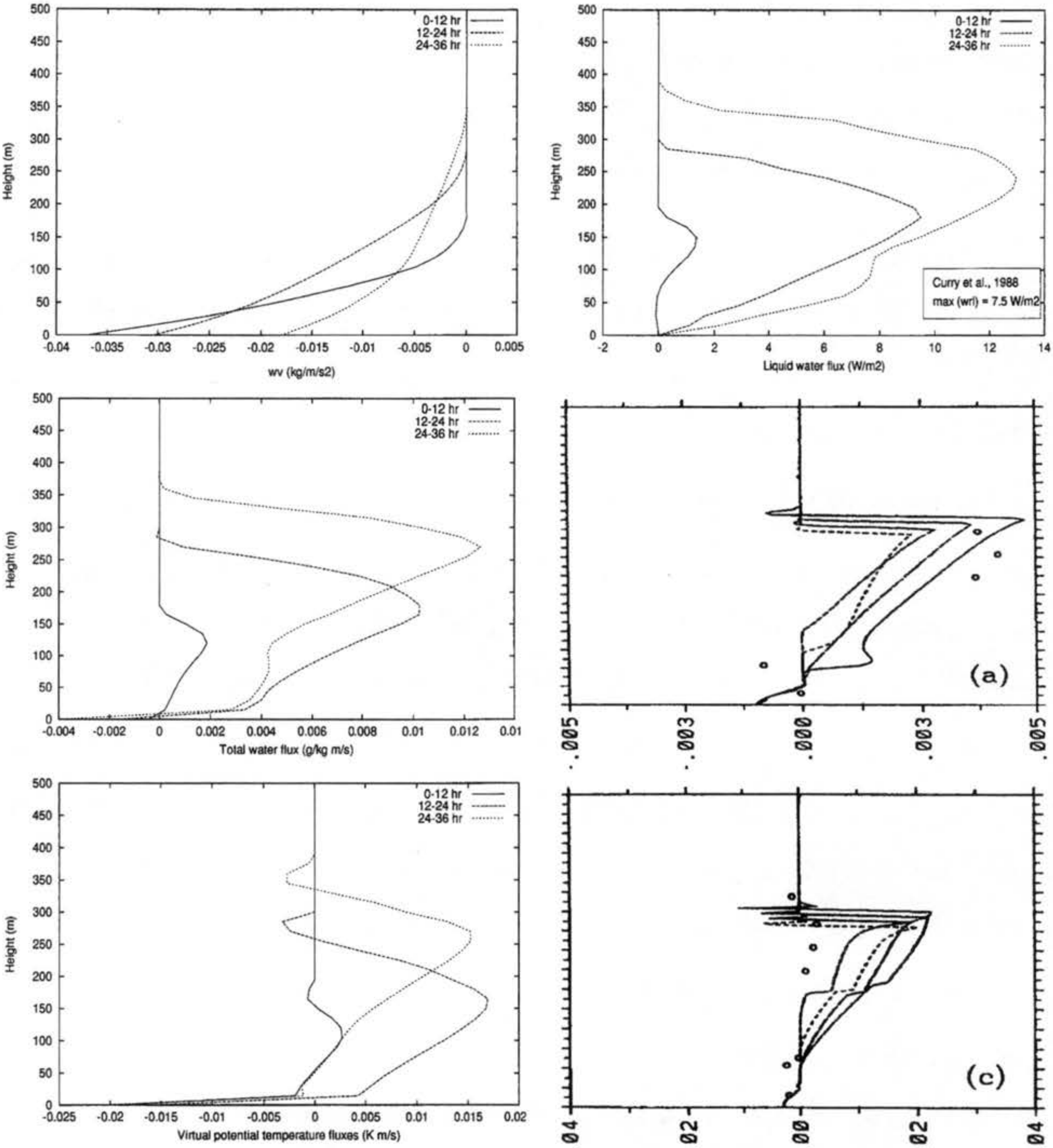

Figure 62: Flux profiles. Top left, simulated meridional momentum flux; top right, simulated liquid water flux; middle left, simulated total water flux; middle right, total water flux from Smith and Kao (1996; lines) and Curry (1986; circles); bottom left, simulated potential temperature fluxes; bottom right, virtual potential temperature from Smith and Kao (1996; lines) and Curry (1986; circles). Values from Curry et al. (1988) are also listed where applicable. The profiles are for the time-averaged periods indicated.

The TKE budget profile is shown in the bottom panel of Fig. 63. In reality, there is not all that much new information here. But, it is informative to see the relative contribution to the TKE in one plot. The buoyancy profile was explored extensively in the above discussion of the fluxes; specifically, $\overline{w'\theta'_v}$ (Fig. 62). In that section, the negative buoyancy flux at the surface was attributed to the downward sensible heat flux, which was caused by horizontal advection of warm air (at times too warm due to incorrect ECMWF forcing); the positive in-cloud buoyancy was attributed to cloud-top radiative cooling and in-cloud condensational warming; finally the negative at cloud top was a results of entrainment warming.

The shear was also mentioned in the discussion of the fluxes, and the conclusion was that shear is adequately represented at the surface, but is severely under-represented at cloud top. This was a result of inconsistencies between the ways in which the momentum and the thermodynamics variables are handled in ADHOC. Fig. 63 also shows the transport and the dissipation. The dissipation is simply largest where the TKE is largest; in the cloud (buoyancy) and near the surface (shear). Finally the transport term shows that the TKE is transported out of the cloud region where it is produced. Overall, the TKE budget is characterized by a balance between the buoyancy and dissipation in the cloud, and the shear and dissipation near the surface.

IV-E-1c: Sensitivity studies

The last aspect of this Arctic simulation that I would like to discuss is the result of a grid-resolution sensitivity test. Many different sensitivity tests have been performed in other Arctic simulations. Finger and Wendling (1990) found that when radiative processes are not considered, the turbulence at cloud top decreases by 90%, while that at the surface decreases by 23%. In this no radiation case, wind shear alone was not able to maintain an efficient turbulent exchange and the turbulent fluxes decreased to very low values. They also found that the addition of large-scale subsidence can prevent the cloud top from rising, but the simultaneous change in the turbulence

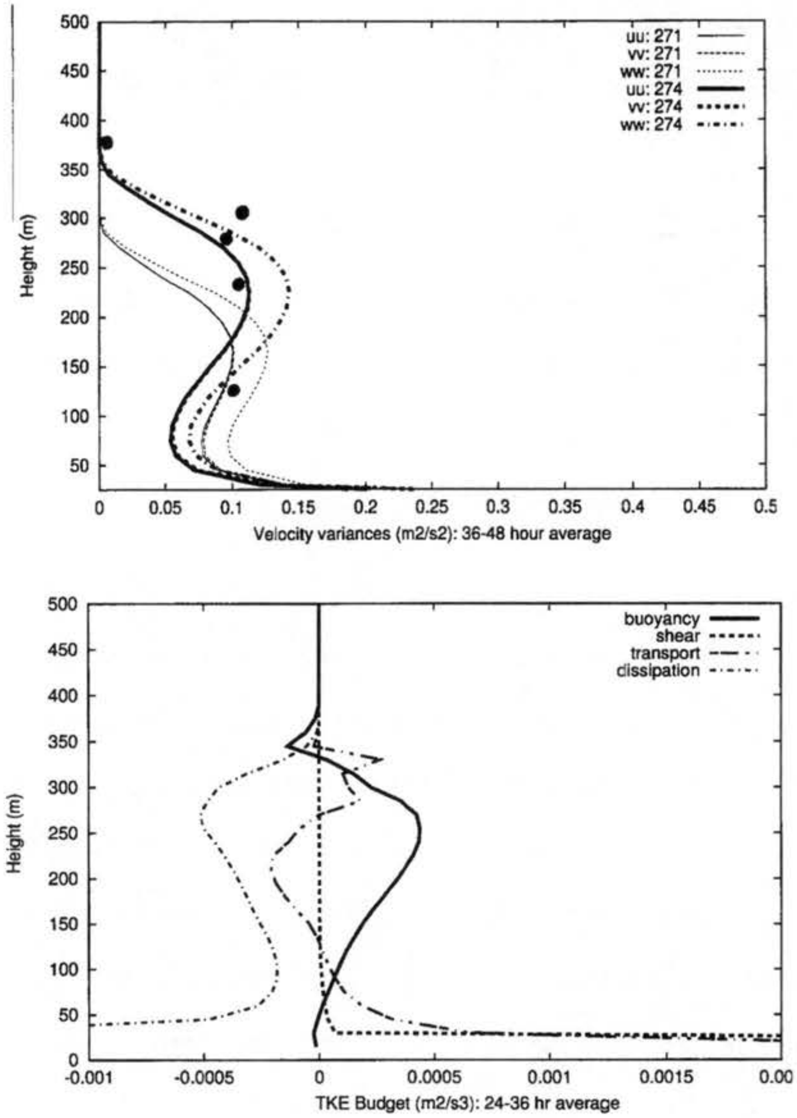

Figure 63: Profiles of the simulated horizontal and vertical velocity variances (top; for 2 different skin temperatures as indicated) and TKE budget (bottom). The dots are the observations of Curry et al., 1988 (scaled to match this cloud). The darkest line is the more "typical" skin temperature (274 K) for July.

structure, especially of the heat flux, causes the cloud-top boundary layer to cool faster than the case without subsidence.

McInnes and Curry (1995) also did a radiation and subsidence sensitivity study, as well as one for grid resolution. Their results were similar to those of Finger and Wendling (1990) for the radiation sensitivity. For the dependence on large-scale vertical motion, they found that uniform large-scale *ascent*, imposed on the boundary layer, leads to an elevation and thickening in the vertical extent of the two cloud layers (they had a double stratus deck in their simulations). They also found that uniform large-scale *descent* produces strong TKE, which eventually mixes out all the vertical gradients in the mean profiles, and leads to destruction of the cloud through evaporation. Finally, the grid resolution sensitivity test in which they performed showed that the optimal vertical resolution required by the model to most accurately model the observed features of the boundary layer was 25 m. They also found that a grid resolution of 200 m could still resolve many of the broad features.

I also performed sensitivity studies for the current case using ADHOC. These studies tested the sensitivity of the results to (1) gird resolution and (2) the surface skin temperature and albedo. In some of the plots in this section, I showed the simulated profiles obtained using skin temperatures of 274 K and 271 K (e.g., Figs. 59, 63). Along with these skin temperatures, I used surface albedos of 0.44 and 0.59 respectively. The albedo change by itself had little effect; however, the albedo change with the temperature change had a slightly larger effect. The main effect was that the colder skin temperature caused the turbulence to appear more "compressed", although the profiles retained their overall shape. The cloud in this SHEBA case originally formed by advection of warm, moist air over the cool ice. Thus, the colder skin temperature created a cloud more easily, but prevented it from growing due to the larger downward surface sensible and latent heat fluxes, which counteracted the warming due to advection. The overall result was that the turbulent and mean state profiles evolved in a similar manner as that with the warmer skin temperature, but the colder skin temperature stunted the height to which the turbulence grew.

The other sensitivity study done with ADHOC for this case was for grid resolution. I compared the results for resolutions of 15 m, 25 m, and 50 m. The result was that the simulated results drastically changed between 25 m and 50 m, while they hardly changed between 15 m and 25 m.

The results of this test (for 25 m and 50 m) are shown in Fig. 64 for the vertical velocity variance and the liquid water mixing ratio. The sensitivity of this case to the model resolution is significantly more severe than that reported by McInnes and Curry (1995). A simple doubling of the grid to only 50 m completely erases the turbulence and produces no cloud. It is unclear if the model itself is responsible for this sensitivity, but the case is surely involved. In reality, with a resolution of 50 m, the entire boundary layer only contains 6 or 7 grid points. This clearly not enough to resolve the detailed structure of the turbulence. McInnes and Curry reported that the broad feature of the ASC which they simulated were represented on a 200 m grid. The boundary-layer top in their simulation however, was 1300 m, while in the current case it is approximately 350 m. More ADHOC tests show that, in order to represent the "gross" structure of the current case, a minimum of 10 boundary layer grid points is needed (roughly 35 m resolution). In the case of McInnes and Curry, they require at least 6-7 grid points (roughly 200 m resolution).

It is clear from this study and that of McInnes and Curry that ample grid resolution is critical for the evolution of ASC. I tried similar tests with BOMEX and ATEX and found that the restrictions were significantly more liberal. Thus, the restrictions in the Arctic are likely related to the small boundary layer scales and the large static stability.

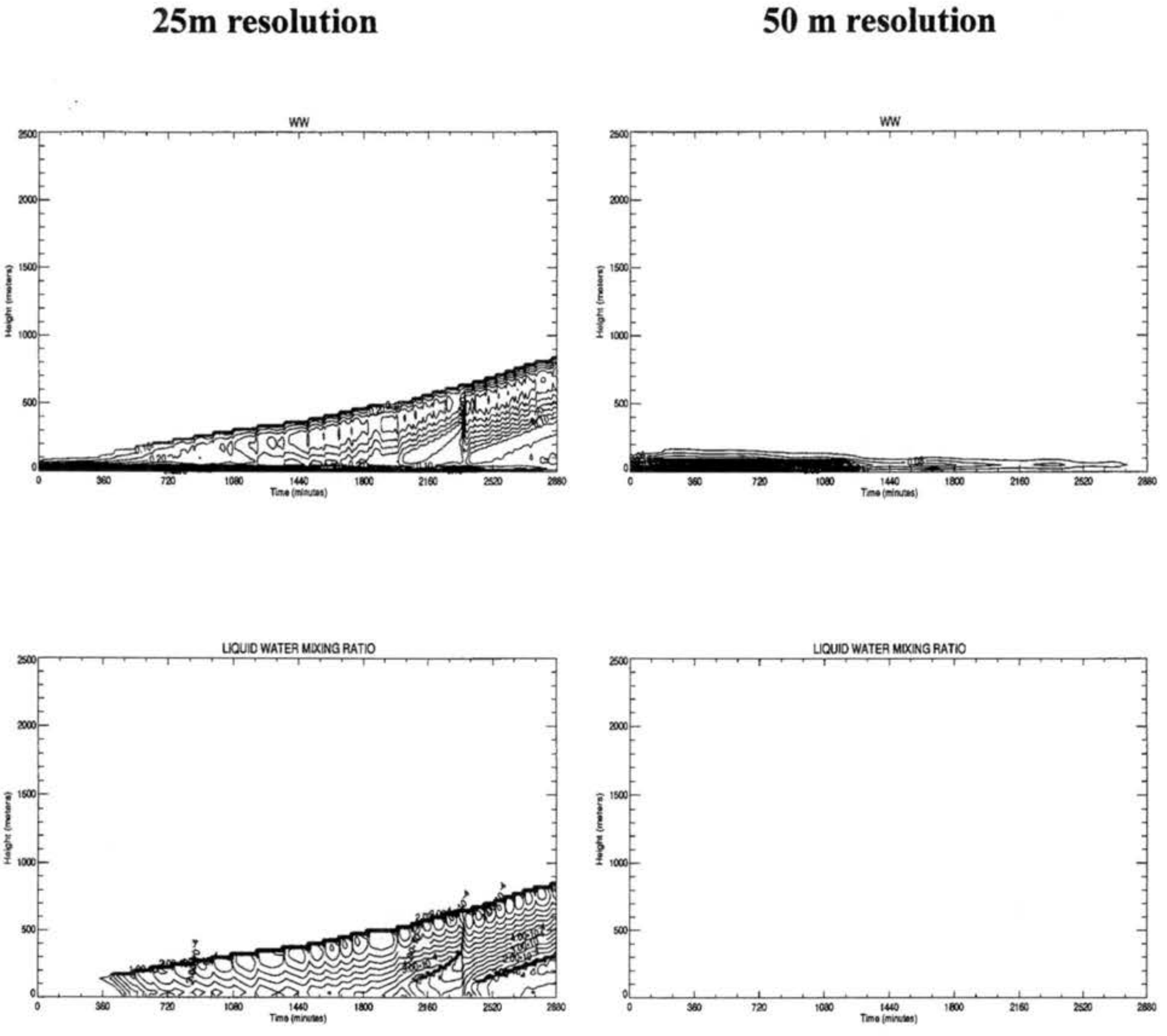

Figure 64: Simulated vertical velocity variances (top row) and liquid water mixing ratios (bottom row) for 2 different resolutions: left column, 25 m resolution; right column 50 m resolution.

IV-E-1d: Summary of SHEBA simulation

The SHEBA case that I chose to simulate to test ADHOC in the Arctic was a fairly simple liquid-only surface-based ASC, which encompassed many of the features that distinguish ASCs from stratus clouds at lower latitudes (e.g., a humidity inversion). It was difficult to obtain observational data from SHEBA to compare with the ADHOC simulations, as much of the data has not yet been processed. In addition, unlike other cases discussed in this thesis, this was not a case organized by the GCSS cloud-modeling group; thus, LES data for this case was also unavailable. The ADHOC results were compared with SHEBA rawinsonde and surface data (which were available) and, in a more qualitative manner, with previously simulated or observed ASCs in other regions of the Arctic.

In general, one does not associate a "mass-flux" or a "plume-type" model with ASCs, because these approaches are typically applied in situations where "non-local" transport plays a more dominant role (e.g., Cu, Sc). To my knowledge, no such model has ever been applied to the Arctic boundary layer, where shear production often dominates the TKE budget. However, despite this fact, ADHOC performed quite nicely. I was able to accurately simulate the development and subsequent evolution of the mean and turbulent state of an ASC, observed at SHEBA on 23 July 1998, in a manner which was also consistent with the development of these clouds in previous studies.

Aside from the ECMWF horizontal advective tendencies and the large-scale vertical motion field (which was small and directed upwards at most times), the forcing in ADHOC was allowed to interact and adjust to the development of the PBL through the radiation scheme of Stephens and Gabriel (1999) and the surface flux parameterization of Louis (1979). As we saw in the previously-discussed cases in this chapter (e.g., BOMEX, ATEX, ASTEX), the use of non-interactive radiation and surface flux parameterizations (i.e., using prescribed values) significantly inhibited the development of PBL turbulence, particularly the cloud-top entrainment. No such limitation was found in this simulation, further supporting the notion that interactive forcing schemes are critical for an accurate representation of turbulence in numerical models.

The simulated and observed cloud for the 23 July 1999 SHEBA/FIRE case formed as a result of the advection of warm, moist air over the relatively cold ice surface. The physics of this cloud evolved as follows: After the cloud formed, radiative cooling at cloud top produced turbulence, which mixed all but the lowest few layers (approximately 100 m) of the boundary layer. The boundary layer likely grew by a combination of 2 methods; turbulent entrainment, and "radiative encroachment" (entrainment caused by direct cooling of the capping inversion; Deardorff, 1981). It is difficult to separate these two processes; however, Curry (1986) found (by analyzing the thermodynamic profiles and microphysical properties of these cloud) that condensation due to radiative encroachment occurred most often in ASCs with humidity inversions (a mixing ratio which increases with height, as it does in the current case).

While the cloud top grew through the entrainment process, the surface gradually "decoupled" itself from the overlying in-cloud turbulence. This was a direct result of the continuous downward sensible and latent heat fluxes, which acted the cool the lowest layers. This effect was found to be particularly significant in this simulation, due to unrealistically large advective warming and moistening rates (4 K day^{-1} and 3 g kg^{-1} day^{-1} respectively) supplied by the ECMWF data, which were used to force the model (this occurred during hours 18-36 in the simulation). This decoupling was enough to split the cloud deck in two, although not during the initial 48 hours described in this section.

The cloud structure itself, although only a single layer, exhibited many of the same characteristics of a two-layered system (where one of the two layer is fog and the layers are within a few hundred meters of one another), especially that observed on 28 June 1980 in the Beaufort Sea

(Curry et al., 1988; Smith and Kao, 1996). Figure 62 shows that the buoyancy and total water fluxes in the 28 June 1980 and the current 23 July 1998 cases were strikingly similar, especially in the shape of the profiles. The similarity of this single-cloud-layered ASC to those with two layers was attributed to the "decoupling" which occurs in both cases between the in-cloud turbulence and the surface fluxes. In the current case, the liquid water mixing ratio exhibited a minimum just above the surface, while in the 28 June case, the region above the surface fog was cloud-free. However, both are indications of decoupling, which was the dominant factor in determining the evolution of the flux profiles. In addition, in a test case (not shown), I permitted the model to run for an additional two days. By the end of this simulation, the cloud in the current case split into two layers as well.

One important difference between the two cases was their boundary layer depths. In the 28 June case, the cloud extended to over 1 km, while in the current case, it was limited to approximately 400 m. In this regard, it was difficult to directly compare these two cases; thus, the comparisons were done in a relative sense (i.e., terms such as "half way between cloud base and cloud top" were used, as opposed to terms like "at 500 m"). While most previous studies of ASCs elaborate on the high degree of variability in these clouds (mostly due to differences in the liquid water content and distribution of cloud microphysics; Olsson et al., 1998; Curry et al., 1988; Curry, 1986), I showed that two very different clouds actually exhibit some properties which are quite similar. This may be an indication that the physical processes which determine the evolution of ASCs (either single of double layered) with surface fog layers, are similar (although perhaps only in the presence of surface/in-cloud turbulence decoupling).

Despite these encouraging aspects of the simulation, ADHOC was certainly not problem-free. The same problems which affected the results of cases previously discussed in this thesis, also occurred in this simulation; in particular, the problems with the pressure and momentum transport terms. This was particularly evident in the velocity variance profiles (Fig. 63). ADHOC is simply unable to (1) handle momentum transport into and out of the surface and cloud-top regions and (2) accurately determine pressure-induced momentum redistribution in these same regions. The reasons for this were discussed extensively in Section IV-A.

Finally, sensitivity tests performed showed that the model is highly sensitive to grid resolution. A doubling of the grid spacing from 25 m to 50 m was large enough to kill the turbulence and inhibit the initiation of the cloud (Fig. 64). A sensitivity study, in which the skin temperature and albedo were varied, showed that a 3 K lowering of the skin temperature acted to "compress" the turbulence in the boundary layer, despite the fact that the turbulent profiles retained their structure.

Despite the encouraging results discussed in this section, I believe that the inclusion of a microphysics package in the model would allow us to better represent the complex physical processes of ASCs, especially those with more complex structures than the current case. Evidence exists throughout the literature of the importance of the cloud microphysical structure on the local and global budgets of radiation, water, and energy (Herman, 1980; Curry, 1986; Curry and Ebert, 1992; Olsson et al., 1998; Pinto and Curry, 1997). Thus, if I truly hope to make the ADHOC approach applicable to all Arctic stratus clouds (as well as other lower latitude boundary-layer clouds where microphysics play a role), the inclusion of a microphysics regime is essential. Finally, I believe that the GCSS ASC intercomparison case, which is currently being constructed, will help greatly in pinpointing further weaknesses of the ADHOC approach as applied to this regime. I await this study for further Arctic-specific refinements.

Chapter V: Summary and conclusions

In this thesis, I have taken known "plume" equations describing the mean properties of updrafts and downdrafts and used the framework of RSM to derive a set of higher-order prognostic equations. This resulted in a combined MFC/HOC model whose equations are term-by-term consistent with the corresponding "conventional" HOC equations. The potential use of such an approach in large-scale models is wide-ranging. Currently, GCMs tend to poorly represent the effects of clouds (Randall et al., 1998) in multiple-cloud regimes. They conventionally distinguish between the boundary layer and the cumulus layer based on the assumption that they are physically distinct layers. However, this is not always the case. In addition, GCMs currently use separate schemes for PBL processes, shallow and deep cumulus convection, and stratiform clouds. Individually, these schemes sometimes work well in their respective areas, but often two or more or these regimes coexist (e.g., cumulus-under-stratus, stratocumulus "decoupling"). As discussed in Chapter III, these distinctions represent holes in our understanding. The current ADHOC approach may be the first step toward unifying the co-dependent cloud and boundary-layer processes in large-scale models.

Previous mass-flux models could not be universally applied to all cloud and boundary-layer processes because they lacked a physically-based method to determine σ and M_c. They worked quite well in "case-specific" simulations for which LES output or observations of these parameters were available. The framework of RSM helps to fill this gap by providing a method to diagnose σ and M_c for *any* situation in which $\overline{w'w'}$ and $\overline{w'w'w'}$ are known. One method for determining $\overline{w'w'}$ and $\overline{w'w'w'}$ would be to predict them with conventional HOC techniques. However, there is nothing to guarantee that the parameterizations in the HOC equation will be consistent with the tophat distributions assumed in the mass-flux model. Here, ADHOC fills in the missing link. The ADHOC equations are derived by integrating the prognostic equations over a tophat PDF, thus guaranteeing consistency with the mass-flux model. In addition, since all higher-moment statistics are derived from the same PDF, there are no realizability issues with this model.

The basic logic behind the ADHOC approach is described in Fig. 16 and can be summarized as follows:

1. Prognose $\overline{w'w'}$ and $\overline{w'w'w'}$ using the unified MFC/HOC equations (Eqs. 3.72, 3.85).
3. Use these prognosed values to diagnose σ and M_c (Eqs. 3.7, 3.8).
4. Predict any fluxes (e.g., Eq. 3.81).
5. Use the thermodynamic fluxes, along with M_c, to diagnose the properties of the updraft and downdrafts (Eq. 3.3).
6. Diagnose higher-order moments using the RSM formulations (Eqs. 3.3-3.6).
7. Calculate the SPS fluxes and the radiative forcing (done separately for the updraft and downdrafts).
8. Update the surface fluxes, diagnose the lateral mixing terms (E and D).

As I discussed above and in Section III-A-1b, a disadvantage of the mass-flux approach is that the tophat PDF cannot fully describe the statistics of the flow; it is an oversimplification to categorize all motion into 2 categories (Figs. 4-5). To make the approach more accurate, a broader PDF must be used to describe the motion. A nice aspect of the ADHOC approach is that it can be generalized quite easily to a more realistic PDF. We can do this as follows:

1. Assume a PDF shape.
2. Integrate the prognostic equations over the PDF to get a "plume" model.
3. Make mechanistic assumptions in the framework of the plume model (e.g., make

assumptions about the lateral mixing).

4. Derive higher-moment equations from the plume model.
5. Diagnose the parameters which describe the PDF shape from the predicted moments.

While this is the logic for generalizing the PDF, we can actually go from 1 to 4 directly for some of the terms. For example, in the current version of ADHOC, the thermodynamic variances are diagnosed directly from the PDF shape, as long as the fluxes of the respective variables are known (see Fig. 6).

One result that emerges from the plume/HOC equations is that the lateral mixing terms (E and D) are analogous to the dissipation terms in the corresponding "standard" HOC equations. Since length-scale and dissipation closures have been a thorn for HOC models, I propose a new method to determine the lateral mixing (and thus, the dissipation). I base this parameterization on the goal of making E large near the surface and D large near cloud base (Fig. 9). Since the size of the dissipation length scales (L_{up} and L_{down}) is limited by the PBL top and the surface respectively (Bougeault and André, 1986), I set E inversely proportional to L_{up} and D inversely proportional to L_{down} to achieve this goal. In addition, since the dissipation time scales of $\overline{w'w'w'}$ are likely to be different from those of the second-order terms [as evidenced by the different forms that E and D take in these equations (Eqs. 3.72; 3.85)], I propose a proportionality factor between the dissipation scales of the second and third moments. The proportionality factor that I choose is 2 and is based on the necessity to keep E and D positive, as well as the desire *not* to restrict the range of σ (Section III-G). As I showed in Chapter IV of this thesis, this formulation appears to be able to capture the physics of a variety of PBL regimes.

Another new feature of this model is the inclusion of the effects of SPS motion. Previous mass-flux models have typically been used in conjunction with a mixed-layer model (e.g., Wang and Albrecht, 1986) and thus have not been concerned with small-scale aspects of the flow. The ensemble-averaged statistics in conventional HOC models are supposed to encompass all scales of motion, also alleviating the need for a small-scale parameterization. In order to combine both these approaches so that the equations are consistent "scale-wise", I argue that there is a need to add small-eddy (subplume-scale) motions to the mass-flux equations to obtain realistic results in regions where the motions are inherently small (e.g., near the surface and the inversion). Another reason for the inclusion of a SPS model is the overwhelming evidence the representing fluxes with a "tophat" distribution (Eq. 2.2; Figs. 4-5) accounts for only about 60% of the total flux (Businger and Oncley, 1990; Young, 1988a; Schumann and Moeng, 1991; Wyngaard and Moeng, 1992; de Laat and Duynkerke, 1998). For this reason, a recent study by Petersen et al. (1999) showed that inclusion of these effects in mass-flux models is critical for accurately simulating the convective boundary layer (see Section III-I). Similar studies show a smaller percentage for variance and covariances. With the SPS scheme, I am able to account for the portion of the turbulent motion which is not represented with the "tophat" PDF.

In Section IV-B of this thesis, I showed that the addition of a SPS scheme greatly improved the simulations of the Willis-Deardorff convection experiment (shown graphically in Fig. 12). In addition, the ADHOC equations (derived in Chapter III) provide some quantitative justification for this. For example, in Eqs. (3.127) and (3.128), we see terms that represents the sources and sinks of h. These terms represent (among other things) the divergence of the SPS flux and the SPS contribution to the flux respectively. The SPS scheme that I use is based on that of Deardorff (1980).

In Chapter IV, I applied the ADHOC approach to 5 different boundary-layer regimes; pure convection (WD), trade-wind cumulus (BOMEX), upstream trade-wind cumulus (ATEX), marine stratocumulus (ASTEX), and Arctic stratus (SHEBA/FIRE). The motivation behind analyzing such a wide variety of cases was that the ultimate application of this type of approach is in a large-scale model, where regime-independence is critical for accuracy. In order to make this approach truly regime-independent, I will need to be aware of its strengths and weaknesses for as many physical situations as possible. Each of the 5 different cases analyzed provided new information which will help me to make the ADHOC approach more robust.

A couple universal weaknesses of ADHOC became apparent from these analyses:

(1) The handling of the pressure terms

This was the largest problem in the ADHOC simulations. It was visible in all 5 cases analyzed. The pressure terms which appear in the ADHOC equations are parameterized with a "conventional" HOC approach (Section III-H), even in the thermodynamic equations, where all other terms are consistent with both MFC and HOC. In "conventional" HOC, a dissipation-like form is assumed for the pressure terms in the flux equations, and the actual dissipation itself is neglected. As I discussed in Section IV-A, I believe that the dissipation in HOC models is incorrectly neglected and that these models rescue themselves by increasing the value of the constant in the pressure parameterization (the ADHOC equations clearly show that the dissipation term is not negligible). Thus, the pressure problem occurs because ADHOC naturally represents dissipation through the lateral mass exchange terms (Section III-G) and it additionally uses the HOC parameterization for the pressure terms (which likely includes dissipation; Section III-H). Thus, the effects of dissipation (of fluxes) in ADHOC is represented twice. The additional dissipation provided by this mechanism is enough the make cloud-top entrainment inefficient at times. This is shown in Fig. 17.

In light of the pressure-related problems seen in the 5 simulations discussed in Chapter IV, a possible "ADHOC-consistent" approach to modeling the pressure terms is proposed in Appendix B. The future direction of ADHOC's development is undoubtedly in the implementation of such a scheme. An approach such as that discussed in Appendix B is the final step in completely unifying MFC and HOC in the ADHOC model. I believe such a step will improve the results shown in Chapter IV significantly.

(2) The horizontal momentum terms

The horizontal momentum terms are not "ADHOC-compatible". This is especially problematic with regard to momentum transport. In the current version of ADHOC, I chose to use "conventional" HOC to prognose the momentum fluxes (the argument for doing this is that the success of the tophat approach depends in part on a strong correlation between the vertical velocity and any other variable; Figure 14 shows that horizontal and vertical momentum are not well-correlated in the convective boundary layer). This involved the use of a down-gradient assumption for the transport terms in the flux equations, an assumption which is applicable where "local" transport dominates. However, the evolution of the mean and turbulent thermodynamic state, as well as the vertical velocity statistics, are all determined within the "plume framework" of ADHOC. Imbedded in the ADHOC framework is the concept of "non-local" transport. Thus, the horizontal momentum terms are handled in a manner inconsistent with the other ADHOC variables. This inconsistency caused 2 major problems with the simulations.

The biggest problem was in the momentum variances, where the 3 components of the TKE (2 of which are determined with HOC and one of which is determined with the ADHOC approach) are intricately coupled through the pressure and dissipation terms. This often resulted in the pressure redistribution which was "overly efficient" (e.g., BOMEX; Section IV-C-2b, Fig. 35 and SHEBA/FIRE; Section IV-E-1b, Fig. 63). The second problem occurred with the momentum fluxes in convective regimes. Horizontal momentum could not be transported out of regions where it was produced as efficiently as the thermodynamic variables. This often resulted in horizontal momentum profiles which were in error (e.g., WD; IV-B-1a, Fig. 21).

(3) Stability issue for stable layer

The "stability issue" refers to the generation of artificial turbulence in stable layers. This occurred because the skewness (which is used to determine σ and M_c and thus all higher moments of the flow) is a ratio of two numbers ($\overline{w'w'}$ and $\overline{w'w'w'}$; Eq. 3.11), which are small in stable layers. The ratio of two small numbers is not always small and thus, unless limits are placed on these values, artificial turbulence can sometimes develop and create problems in stable layers. A problem occurs in situations where the turbulence grows very slowly. In these cases, imposed limits on the skewness can inhibit the development of turbulence.

(4) Sensitivity to the forcing

In all of the atmospheric cases simulated, the forcing was applied in a different manner. For BOMEX, ATEX, and ASTEX, the GCSS case setup was followed to facilitate comparison with other models. The forcing in each case can be summarized as follows (a complete description of the model forcing and initial set-up for each case is given in Table 2 on page 145):

- BOMEX: All forcing completely preset, even the heights at which the forcing is applied. The evolution of the boundary layer turbulence is not allowed to feed back and change the forcing.
- ATEX: All forcing was "semi-preset". In this case, the forms for the forcing were given but the surface forcing was allowed to change with the surface air properties; the large-scale forcing was allowed to change with the boundary-layer depth; and the radiative forcing was allowed to evolve with the integrated liquid water path
- ASTEX: Forcing was partly preset and partly "semi-preset". Here, the value for the

surface fluxes were not allowed to change. The radiative forcing was allowed to evolve with the liquid water path as in ATEX. There was no large-scale forcing because the case was assumed to be LaGrangian in nature.

- SHEBA: All forcing was completely interactive. A full radiation scheme and surface flux parameterization were used to determine the forcing as the flow evolved. The large-scale forcing was prescribed with the ECMWF advective tendencies, which evolved with the observed changes in the boundary layer.

These four cases thus represent four different ways to apply forcing in the boundary layer. We found one very limiting factor among all these methods; that of prescribing the radiative forcing, especially with preset heights as in BOMEX. A comparison of the effects of presetting the values of the radiative forcing and the heights at which it is applied, presetting the surface fluxes, and not presetting anything was shown in Fig. 18 for ATEX. In that figure, we saw that prescribing the radiation had significant effect on the results. Ideally, of course, it is best that the boundary layer forcing be completely interactive with the evolving turbulence.

In each of the 5 different cases, the AHDOC approach was analyzed to see if it could capture the specific physics of the regime. We can summarize the results of each simulation as follows:

(1) Willis Deardorff

The Willis-Deardorff experiment was one of pure convection, driven by surface heating (see Section IV-B-1). The physics of this regime were well-represented by ADHOC. The simulated mean state was well mixed, and the use of the SPS parameterization greatly helped with this result (Fig. 12); the heat flux was linear from the surface up through the entrainment zone, where it became negative in response to entrainment of the warmer water from above; the vertical velocity variance was parabolic in shape with a maximum in the lower to middle boundary layer, as a result of the vertical acceleration experienced by thermals as they rise. (this vertical motion is reduced due to drag, dilution with downdraft fluid, and the warm and stabilizing effect of entrainment; it also must be identically zero at the surface and near the inversion); the temperature variance was a maximum near the surface (where surface heating is being applied) and near the inversion (where entrainment is occurring). The only real problems with WD were in the horizontal velocity variances (where the momentum transport was unable to carry horizontal momentum high enough in the boundary layer; see above discussion) and a sensitivity to the pressure constant, related to the dissipation/pressure issue discussed above.

(2) BOMEX

BOMEX was a "classic" trade-wind (or shallow cumulus) case, where the cloud fractions were observed to be near 20%. Accurately parameterizing this regime is critical in GCMs (see Section IV-C). The TWBL has a three-layered structure: a sub-cloud mixed layer, a conditionally unstable cloud layer, and an absolutely stable inversion layer (Fig. 26). The evolution of trade-wind cumulus is highly dependent on processes which occur at or near cloud top (e.g., entrainment warming and drying, radiative cooling, and evaporative cooling), and to a smaller extent on surface fluxes. Thus, accurately representing these cloud-top processes is the key to modeling this regime. The large-scale environment surrounding these cloud is dominated by dry subsiding conditions. Thus, the simulation of this regime is complicated by dry downdrafts and a positively-skewed boundary layer.

Non-local transport is dominant in this regime and thus, one would expect that ADHOC would perform quite nicely. Mass-flux models were specifically designed to handle regimes which are positively skewed. Unfortunately, a true assessment of ADHOC is really not possible due to the manner in which the prescribed forcing was applied (see above list). The preset values of the radiative cooling, as well as the preset height at which it was applied stunted the natural evolution of the boundary layer. This case needs to be rerun with interactive radiation for a true comparison with the observed conditions, as well as to fully assess the applicability of the ADHOC approach to modeling this "classic" trade-wind regime.

However, I will review the findings of the simulation. Overall ADHOC was able to capture the 3-layered structure associated with this regime. The mean state profiles agreed nicely with observations and the other LES models. However, the mixed layer was slightly too warm and too dry, while the cloud layer was slightly too cold and too wet. This was attributed to inefficient entrainment which resulted from (1) the prescribed radiative forcing not matching the height of the cloud top in all cases and (2) inefficient pressure redistribution (discussed above). In this simulation, the simulated liquid water mixing ratio was 15 times larger than that simulated by LES. Other 1-D models which simulated this case experienced the same problem, although the effect was even larger in ADHOC. It is not clear why 1-D and 3-D LES models differ so greatly, but in ADHOC the additional liquid water (beyond the 1-D/3-D differences was a result of (1) inefficient entrainment drying and (2) the use of a transfer coefficient which was larger than that actually observed during BOMEX (the value of the transfer coefficient was tied to the prescribed surface fluxes).

The shape and magnitude of the simulated fluxes agree with both LES and observations as well. The biggest problem with the fluxes was that they represented a boundary layer whose inversion was too low (a result of the prescribed radiative forcing not matching the height of the cloud top in all cases and inefficient pressure redistribution in the inversion). The same was true for the velocity variances. The TKE budget exhibited nice agreement with that simulated by LES.

We see that despite the problems associated with the unusually rigid forcing and the pressure redistribution, ADHOC was still able to capture the shape and magnitude of the "typical" observed profiles of the TWBL. The differences were mostly found in the cloud layer where mean state was too warm and too wet and the fluxes did not extend high enough in the boundary layer (they were somewhat stunted). It is clear that a more liberal interactive forcing, as well as a new method to make the pressure terms "ADHOC-consistent" (Appendix B) would greatly improve the treatment of entrainment at cloud top. This would allow the cloud layer to warm and dry (bringing it closer to the observations) as well permit the fluxes to extend to higher heights (also in accord with the observations and LES simulations). Despite the problems, ADHOC was able to capture the overall physics of this regime.

(3) ATEX

ATEX was also a trade-wind cumulus case. However, it was physically distinct from BOMEX in that it occurred more "upstream", where the inversion is stronger (3x stronger), the mixed layer deeper, and the cloud fraction higher (~50%). Here, the difference between the moisture content in the updrafts and downdrafts was closer than it was in BOMEX (Fig. 47). As discussed, the ATEX forcing was more liberal than the other GCSS cases; it was allowed to evolve in response to the changing boundary-layer characteristics. The result of this was a decrease in the differences between the ADHOC and LES results. Another reason for this improved agreement was that the entrainment process was less critical to the evolution of this regime (because of the cooler SSTs and the stronger inversion). Thus, the two problems in BOMEX (the forcing and the pressure-related inefficient entrainment) were both minor issues in ATEX.

The simulated mean state profiles in ATEX, which also exhibit the 3-layered trade-wind structure, again agree with LES and observations. The cloud-layer in this case was slightly cooler and wetter than that simulated by LES, but nowhere near as wet as it was in BOMEX. The decreased role in ATEX of entrainment drying is evident by the closer agreement of ADHOC with the LES simulations. However, entrainment is not altogether absent from the ATEX regime; it just plays a more minor role. The cooler simulated temperature was associated with both increased radiative cooling due to the higher liquid water content and a decrease in the entrainment warming. Thus, we see that ATEX case still exhibited inefficient entrainment, but the overall effect of this problem was smaller.

In addition, the simulated humidity of the near-surface air was drier in ADHOC than it was in the LES simulations. This was traced to a feedback between the inefficient entrainment drying and the surface latent heat fluxes. This feedback occurred in ATEX because the surface fluxes were permitted to evolve with the changing surface air temperatures. In BOMEX, the value of the surface forcing was rigidly set, and thus no such feedback was allowed. Undoubtedly, if the surface fluxes in BOMEX were permitted to be interactive, a drying at the surface would have also occurred. This drying would likely have been larger than in BOMEX because the relationship of the feedback to inefficient entrainment (see Section IV-C-3b).

The agreement of the simulated fluxes between ADHOC and LES is excellent. As in BOMEX, the magnitude and shape of these simulated profiles agree with both LES and observations. However, the agreement in ATEX is better because the height of the inversion is also well-represented by these flux profiles. This is a result of the more liberal forcing (see list above) and the decreased role of entrainment.

The only real major problem in the ATEX simulations was the vertical velocity variance profiles. In ADHOC, the simulated $\overline{w'w'}$ had a shape which was "typical" of the TWBL (a double bump shape due to the separation of in-cloud and surface-generated buoyancy processes). This agreed with the LES models, but the magnitude of the "bumps", especially the one in the cloud, was twice what the LES simulated. I attributed that to 3 things: (1) an overly active "return-to-isotropy" parameterization; (2) too much radiative cooling due to the higher liquid water contents; and (3) a problem with the imposed restriction on $\overline{w'w'}$, which was instated to prevent artificial turbulence from being generated in stable layers (see above discussion and Eq. 4.1). The largest differences in the TKE budget were related to the differences in the $\overline{w'w'}$ field.

What we see overall is that ATEX is better represented than BOMEX in these simulations. The reason for this was associated with the more liberal interactive forcing in ATEX and the decreased role of entrainment, which is a documented problem in the current version of the model.

(4) ASTEX

Marine stratocumulus are globally important from both a radiative and dynamical standpoint. They reside in the region upstream of the trade-wind regime, where colder SSTs and stronger subsidence inversions prevail. The colder SSTs almost completely remove the role of surface fluxes in the evolution of PBL turbulence. Here, the downdrafts are almost always completely saturated, and the boundary layer is thoroughly well-mixed; the latter is an almost exclusive result of cloud top radiative processes.

Another factor which directly relates to these clouds is the large cloud-top entrainment rates; significantly larger than that in trade-wind cumulus clouds. This is caused by a number of factors, including the increased radiative cooling due to the uniformly saturated conditions, and the effects of evaporative cooling, which occurs as (1) dry air is entrained into the PBL and (2) liquid water in the downdrafts evaporates. Both these processes increase the downward convection, and helped to drive more entrainment. The ASTEX case itself was not a "classic" stratocumulus case; it was more of a transition case between the "classic" stratocumulus region upstream and the trade-wind region downstream. The ASTEX field project was designed specifically to study the poorly-understood transition from Sc to Cu in the subtropics. Many of the simulated and observed fields distinctly reflect the "transitional" nature of ASTEX, in that they simultaneously exhibit properties of both the TWBL and the "classic" ScTBL (e.g., $\overline{w'w'}$, $\overline{w's'_v}$, and $\overline{\theta_L}$).

The results of the ADHOC simulation of ASTEX were overall in excellent agreement with observations (for both the turbulent and mean state profiles). Their agreement with LES, however, was not always as good. In particular, the ADHOC-simulated TKE buoyancy, vertical velocity variance, and mean liquid water mixing ratio agreed very nicely with the observed values, while they did not agree with those simulated by LES. It appears that ADHOC was able to capture the "TWBL part" of this transitional regime very nicely, while some LES models had difficulty with this aspect. A good example of this is $\overline{w'w'}$ in Fig. 56. In this plot, ADHOC simulated a "double maximum", which is typical of the profile of $\overline{w'w'}$ in the TWBL. However, the relative minimum in between the two maxima was significantly smaller than that found in the TWBL, indicative of the fact it was not a "true" TWBL, but one in *transition* to the "classic" ScTBL regime. Two of the LES models simulated only a "single maximum" in $\overline{w'w'}$, which is typical of a "classic" ScTBL in the absence of any TWBL influence.

Anther significant difference between the ADHOC and LES simulations of ASTEX was the strength of the radiative cooling, which was much smaller in ADHOC. This brought up an apparent contradictory point, in which the radiative cooling was too small, but the entrainment was not. Thus, it appeared as if the entrainment was overly-efficient in ASTEX, in stark contrast to the conclusion reached for BOMEX and ATEX. This apparent contradiction was explained in terms of (1) the difference in physics between these two regimes and (2) a problem related to the numerics of the model.

The physical reason was as follows: In ATEX, the downdrafts are saturated and contain significantly more liquid water than in BOMEX. Thus, the liquid water in the downdrafts evaporates as it descends, cooling the cloud layer and forcing additional entrainment. This phenomenon could not take place in the drier downdrafts of ATEX and BOMEX. The numerical reason was related to a "pulsing" problem which occurred in regimes with drier downdrafts (regimes in which the boundary-layer turbulence was more skewed). This pulsing, which can be seen in Fig. 53, does not show up in the time-averaged profiles. It is a problem that is well-known in single-column turbulence models of cumulus clouds (Chris Bretherton, personal communication). The effect it has on entrainment is that the entrainment is only occurring during the pulses, about half of the time. Thus, in BOMEX (and ATEX to a lesser extent) the entrainment will naturally be inefficient. In ASTEX, where this "pulsing" is not present, entrainment is allowed to be realistically represented at all times.

The only major difference between the ADHOC simulation and the aircraft observations was that the total water flux in ADHOC was larger than that observed (Fig. 55). This was attributed to the large simulated entrainment drying at cloud top, which increased the upward moisture flux in the cloud. This was supported by Fig. 54, where the ADHOC-simulated $\overline{w'r'_T}$ is shown to reside on the high end of that simulated by LES. In this case, the LES agrees better with the observations than ADHOC does. However, overall, the results of the ADHOC-simulated mean state and turbulent profiles are in outstanding agreement with the observations; in fact, in most cases this agreement is better than that of the LES simulations. The mass-flux model, despite its known problem with the pressure and the horizontal momentum transport terms, is able to capture the physics of the ASTEX regime. This is encouraging from the perspective that the ultimate goal of the ADHOC approach is "regime independence", and the case which it simulates the best is a "transitional" case, in which characteristics of both "classic" stratocumulus and shallow trade-wind cumulus are both evident.

(5) SHEBA/FIRE

From a global perspective, Arctic stratus clouds are important to understand because they represent a major source of uncertainty in the extreme global warming predicted in the Arctic by GCMs. The processes thought to be relevant for the initiation, maintenance, and dissipation of these clouds include their turbulent structure, complex microphysics, and radiative and surface feedbacks. Curry et al. (1988) identified 3 main types of ASC clouds: a cloud-top mixed layer, which is surface based; a stable boundary layer with patchy clouds in numerous layers; and a stable foggy boundary layer, surmounted by a cloud-topped mixed layer. The underlying physical interactions that govern the behavior of ASCs are different for all three types, making their parameterization difficult. The simulation of these structures is further complicated by the presence quite often of multiple cloud layers, humidity inversions above cloud top, vertical in-cloud fluxes that are decoupled from the surface fluxes, and complex cloud microphysics (discussed above). The SHEBA case simulated for this thesis is a combination of the first and the third cloud types listed above.

The case I chose for this simulation was the 23 July 1998 SHEBA/FIRE case. This case was a surface fog which formed as a result of warm, moist advection over the colder ice. The process which acted to sustain this cloud was cloud radiative cooling. The eventual splitting of the cloud into two (after the time shown in these results) was a result of the strong cooling at lower levels, which was due to continuous downward surface sensible and latent heat fluxes. One of the biggest problems with this case was the ECMWF advective forcing which was believed to be anomalously large during hours 18-36 in the simulation (large here referring to both warming and moistening). The other forcing in this case, the radiation and the surface fluxes, was completely interactive with the evolving boundary layer. In this respect, this case was a true test of the ability of all aspects of ADHOC to communicate and evolve as a system.

This case was a true challenge for ADHOC, because the ASC regime is not specifically tailored for mass-flux-specific parameterizations. Thus, the if the "regime independent" goal were to break down for any of the cases, it would surely have been this one. However, interestingly enough, the results of this simulation actually agreed with the observations which were available at SHEBA, as well as with those of some previously studied ASCs.

The cloud structure itself, although only a single layer, exhibited many of the same characteristics of a two-layered system (where one of the two layer is fog and the layers are within a few hundred meters of one another), especially that observed on 28 June 1980 in the Beaufort Sea (Curry et al., 1988; Smith and Kao, 1996). In particular, the buoyancy and total water fluxes were strikingly similar, especially in the shape of the profiles. The similarity of this single-cloud-layered ASC to those with two layers was attributed to the "decoupling" which occurs in both cases between the in-cloud turbulence and the surface fluxes. In the current case, the liquid water mixing ratio exhibited a minimum just above the surface, while in the 28 June case, the region above the surface fog was cloud-free. However, both are indications of decoupling, which was the dominant factor in determining the evolution of the flux profiles. These similarities were seen despite the fact that in the 28 June case, the cloud extended to over 1 km, while in the current case, it was limited to approximately 400 m.

While most previous studies of ASCs elaborate on the high degree of variability in these clouds (mostly due to differences in the liquid water content and distribution of cloud microphysics; Olsson et al., 1998; Curry et al., 1988; Curry, 1986), I showed that two very different clouds actually exhibit some properties which are quite similar. This may be an indication that the physical processes which determine the evolution of ASCs (either single of double layered) with surface fog layers, are similar (although perhaps only in the presence of surface/in-cloud turbulence decoupling).

Despite these encouraging aspects of the simulation, ADHOC was certainly not problem-free. The same problems which affected the results of cases previously discussed in this thesis also occurred in this simulation. In particular, the problems with the pressure and momentum transport terms manifested themselves again. This was particularly evident in the velocity variance profiles (Fig. 63). The current version of ADHOC is simply unable to (1) handle momentum transport into and out of the surface and cloud-top regions and (2) accurately determine pressure-induced momentum redistribution in these same regions.

Finally, sensitivity tests performed showed that the model is highly sensitive to grid resolution. A doubling of the grid spacing from 25 m to 50 m was large enough to kill the turbulence and inhibit the initiation of the cloud (Fig. 64). A sensitivity study, in which the skin temperature and albedo were varied, showed that a 3 K lowering of the skin temperature acted to "compress" the turbulence in the boundary layer, despite the fact that the turbulent profiles retained their structure.

Despite the encouraging results discussed in this section, I believe that the inclusion of a microphysics package in the model would allow us to better represent the complex physical processes of ASCs, especially those with more complex structures than the current case. Evidence exists throughout the literature of the importance of the cloud microphysical structure on the local and global budgets of radiation, water, and energy (Herman, 1980; Curry, 1986; Curry and Ebert, 1992; Olsson et al., 1998; Pinto and Curry, 1997). Thus, if I truly hope to make the ADHOC approach applicable to all Arctic stratus clouds (as well as other lower latitude boundary-layer clouds where microphysics play a role), the inclusion of a microphysics parameterization is essential. Finally, I believe that the GCSS ASC intercomparison case, which is currently being constructed, will help greatly in pinpointing further weaknesses of the ADHOC approach as applied to this regime. I await this study for further Arctic-specific refinements.

V-A: Summation and Future Research

The goal of this thesis was to create a regime-independent turbulence model; one which could unify the traditional distinction between the cumulus layer and the boundary layer in GCMs, as well as one that could be used to describe all cloud- and boundary-layer physics within a single framework. I achieved that goal by unifying the equations of MFC and HOC into one internally-consistent system, which captures the individual physics of both parameterizations.

This new unified system of equations was derived in the following manner: Using (1) known "plume" equations describing the time evolution of the updraft and downdraft properties of the flow (e.g., Eqs. 3.15-3.16) and (2), a continuity equation which predicts the updraft area fraction σ (Eq. 3.67), I constructed prognostic equations for higher moments by algebraically manipulating these equations in order to predict these moments in a manner consistent with their mass-flux formulas. These new prognostic equations were shown to be term-by-term consistent with those in the HOC equations. In this way, I was able to combine these two very different methods for representing cloud and boundary-layer processes.

In order to make the two approaches completely consistent with one another, I added the following new parameterizations:

- A physically based method to determine the updraft area fraction (σ) and the convective mass flux (M_c)
- A new parameterization for the lateral mass exchange terms, which I showed was analogous to the dissipation terms of the HOC equations
- A subplume-scale model, which I showed had a significant impact in regions where the eddies are small (e.g., near the surface and near the inversion)
- A possible new approach for modeling the pressure terms (Appendix B).

I showed that a model implemented with this scheme can be used to simulate regimes as different as cloud-free convection, trade-wind cumulus, marine stratocumulus, and Arctic stratus.

By combining MFC and HOC, I have eliminated some of the shortcomings of both methods. For example, one of the weaknesses of previous mass-flux models was the lack of a physically-based method to determine σ and M_c. In the past, MFC has shown great promise in specific regimes where profiles of these two quantities are known apriori from either observation or LES studies, and where M_c is independent of species (e.g., water mixing ratio, temperature, chemical species etc.). Thus, prior to the current model, previously determined profiles of σ and M_c were input to mass-flux models, and \ were not allowed to change as the boundary-layer turbulence evolved. This is clearly not a physically correct assumption. In addition, no two regimes are exactly alike and thus, a given profile may not be representative of all boundary layers in that region. An example of this, which was shown in this thesis, are the trade-wind cumulus regimes of ATEX and BOMEX. The differences between the turbulent statistics in these regimes is large, and it is these turbulence statistics which physically must determine σ and M_c. Certainly the same profiles of σ and M_c cannot be used in both of these trade-wind regimes. The fact that ADHOC uses a physically-based method to determine these quantities makes the scheme more universally applicable and is a significant improvement of previous mass-flux models.

The ADHOC approach also eliminates some of the shortcomings of pure HOC models. For example, HOC is plagued by the large numbers of equations and closure assumptions that lead to inconsistencies. In addition, HOC has issues with realizability among higher moments. Suppose that we wish to know all the turbulent statistics up to the third-order moments in a HOC model that has two thermodynamic variables; we would need 51 equation to describe the turbulence (31 for the third-moments, 15 for the second moments, and 5 for the mean states). In a fully unified ADHOC model (one in which the momentum terms were mass-flux compatible), we would only need 11 (one for $\overline{w'w'w'}$, 4 for the fluxes, and 5 for the mean states). In addition, we could diagnose any higher-order moment that we wanted with the same number of equations, and we are guaranteed that all the moments are" realizable" (all higher moments are diagnosed from the same PDF, once the parameters of the updraft and downdraft are known; therefore they are always physically consistent with one another). The drastic reduction in the number of equations needed to describe the flow and the elimination of realizability issues are two distinct advantages of the current approach over "HOC only" models.

While the ADHOC approach is quite powerful, the perception that all motion can be broken down into one of two categories (an updraft and a downdraft) at any given height is a crude representation of reality. In most situations, there are many values of a given parameter at a given height. However, the approach itself can be generalized to include more categories by using a more realistic PDF (i.e., a plume model with more than two categories can easily be created using the same basic ideas put forth in the current tophat version). The "recipe" for deriving a plume model with a more realistic PDF can be viewed as follows:

1. Assume a PDF shape (here, I assumed a tophat distribution).
2. Integrate the prognostic equations over the PDF to get the "plume" model (here, I obtained equations for the updraft and downdraft quantities; in a model with more categories, there would be more equations).
3. Make mechanistic assumption in the framework of the plume model (e.g., parameterize E and D, apply radiation and microphysics separately to each category in the plume model, etc.).
4. Derive higher-moment equations from the plume model (e.g., Section III-E).
5. Diagnose the parameters describing the PDF shape from the predicted moments (here, I used $\overline{w'w'}$ and $\overline{w'w'w'}$ to diagnose σ and M_c).

The key to accurate climate simulations is the proper treatment of clouds over the globe and thus, some powerful implications for GCMs emerge from this "generalized PDF" approach. First, it provides a method to unify cloud and boundary-layer processes. As discussed in Chapter I, separate schemes are currently used in GCMs for the PBL, and deep and shallow cumulus clouds. This "separate scheme" approach makes GCMs unable to accurately represent the effect of clouds in either cloudy transition regions (e.g., stratocumulus "decoupling", "cumulus-under-stratus", and the "stratocumulus-to-cumulus transition), or in regions where clouds straddle the PBL/free atmosphere boundary. The hope is that, by broadening the tophat PDF to one that is more realistic, we can derive an even more accurate convection model. The ultimate goal of generalizing the ADHOC approach is a unified model which will completely bridge the gap between PBL and cumulus parameterizations in large-scale models.

The second powerful implication for GCMs is the fact that previous studies have shown that even simple forms of HOC (level 2.5 schemes) greatly improve the treatment of boundary-layer processes in global climate simulations (Miyakoda and Sirutis, 1977). Due to complexity, no scheme higher than level 2.5 has ever been used in a GCM. With the scheme that I propose, the additional complexity (and accuracy) introduced by prognosing the fluxes, $\overline{w'w'}$, and $\overline{w'w'w'}$, is offset by the simplicity of unifying cloud and boundary-layer parameterizations.

While my eventual goal for ADHOC is to incorporate it into a large-scale model, the current version of the model is not "GCM-ready" for several reasons. First of all, a grid resolution of 25 m (or less) and a timestep of 0.5 seconds (which are currently used in ADHOC) are not realistic for use in GCMs. This is an aspect of the model that will need to be altered if it is to be incorporated into the framework of a large-scale model. We must be able to represent turbulence in the PBL using much coarser resolution. In the middle of the PBL, coarser resolution is often all that is needed because the fields are smoothly varying in the vertical. However, near the surface and near the inversion, physically important turbulence-generating mechanisms occur on finer scales. In the few tens of meters near the surface, surface layer similarity can be used to diagnose the turbulence statistics, and thus fine resolution in a GCM in this region is not required. However, the PBL-top inversion must be adequately resolved to accurately represent the effects of clouds. One possible way to avoid high resolution in this region is to use a modified "sigma" coordinate (such as that used in the CSU GCM; Suarez et al., 1983). This is a stretched vertical coordinate in which the PBL top a layer edge. The use of ADHOC in a GCM with a stretched vertical coordinate would allow the inversion to be accurately represented. We would need an "ADHOC-consistent" method to calculate the physically important entrainment rate.

Apart from the resolution issue, other aspects of the model must be addressed before it is "GCM ready". While I believe that broadening the current tophat PDF to one which is more representative of the flow (as discussed above) will greatly improve the accuracy of the simulation, ADHOC may not quite be ready yet for this step. The simulations of the variety of regimes in this thesis highlighted several critical problems which need to be addressed before ADHOC is "ready" to incorporate a broader PDF. These changes (discussed below) will make the approach more internally consistent and robust, and should be attempted first with the simpler tophat PDF.

First, it was quite obvious that the manner in which the pressure terms are handled in ADHOC is both inconsistent with the spirit of the "plume approach" and inadequate. An "ADHOC-consistent" pressure parameterization must be used if we hope to capture the important contribution of these terms to the structure and evolution of the turbulent regime which we are trying to represent. Secondly, the momentum terms must be incorporated into the "ADHOC framework". While I originally argued that this may not be necessary, I now believe that, it is not only necessary, but critical for consistency with the evolution of other variables in the model. Since all the turbulence equations are highly coupled, one cannot hope to describe a regime with equations containing inconsistent (or ever contradictory) parameterizations. Only when all the terms in the equations are internally consistent, can the ADHOC approach be a confidently extended to a broader PDF. I believe that its eventual incorporation into a large-scale model also awaits these changes.

Appendices

Appendix A: Higher-moment equations

In the equations which follow, $\overline{(\ )}$ represents a mean quantity and $(\ )'$ represents a turbulent deviation from $\overline{(\ )}$.

A.1 Mean quantities

(A.1) $$\frac{\partial}{\partial t}\bar{u} = -\frac{\partial}{\partial z}\overline{w'u'} + f(\bar{v} - v_g) - \bar{w}\frac{\partial}{\partial t}\bar{u}$$

(A.2) $$\frac{\partial}{\partial t}\bar{v} = -\frac{\partial}{\partial z}\overline{w'v'} + -f(\bar{u} - u_g) - \bar{w}\frac{\partial}{\partial t}\bar{v}$$

(A.3) $$\frac{\partial}{\partial t}\bar{r}_t = -\frac{\partial}{\partial z}\overline{w'r_t'} - \underset{\sim}{V} \bullet \nabla\bar{r}_t - \bar{w}\frac{\partial}{\partial t}\bar{r}_t$$

(A.4) $$\frac{\partial}{\partial t}\bar{s}_L = -\frac{\partial}{\partial z}\overline{w's_L'} - \underset{\sim}{V} \bullet \nabla\bar{s}_L - \bar{w}\frac{\partial}{\partial t}\bar{s}_L + C_p\bar{R}$$

In Eqs. A.1-A.4, u, v, and w are respectively the zonal, meridional, and vertical components of the wind; r_t is the total water mixing ratio; u_g and v_g are respectively the zonal and meridional geostrophic wind velocities; $\underset{\sim}{V}$ is the total mean horizontal wind vector; R is the radiative cooling rate; s_L is the liquid water static energy defined as $s_L \equiv C_pT + gz - L_vr_l$; r_l is the liquid water mixing ratio, $g = 9.8\ \mathrm{m\ s^{-2}}$ is the acceleration due to gravity, T is the temperature in Kelvin, $C_p = 1004\ \mathrm{J\ kg^{-1}\ K^{-1}}$ is the heat capacity of air at constant pressure, $L_v = 2.52x10^6$ J $\mathrm{kg^{-1}}$ is the latent heat of vaporization of air, and z is the height in meters.

A.2 Higher moments

$$\text{(A.5)}\quad \frac{\partial}{\partial t}\overline{w'w'} = -\frac{1}{m}\frac{\partial}{\partial z}m\overline{w'w'w'} + 2\frac{g}{C_pT_o}\overline{w's_v'} - \frac{2}{m}\overline{\frac{\partial w'p'}{\partial z}} - 2\varepsilon$$

$$\text{(A.6)}\quad \frac{\partial}{\partial t}\overline{u'u'} = \frac{1}{m}\frac{\partial}{\partial z}m\overline{w'u'u'} - 2\overline{w'u'}\frac{\partial}{\partial z}\bar{u} - \frac{2}{m}\frac{\partial}{\partial z}\overline{u'p'} - 2\varepsilon$$

$$\text{(A.7)}\quad \frac{\partial}{\partial t}\overline{v'v'} = \frac{1}{m}\frac{\partial}{\partial z}m\overline{w'v'v'} - 2\overline{w'v'}\frac{\partial}{\partial z}\bar{v} - \frac{2}{m}\frac{\partial}{\partial z}\overline{v'p'} - 2\varepsilon$$

$$\text{(A.8)}\quad \frac{\partial}{\partial t}\overline{w'u'} = \frac{1}{m}\frac{\partial}{\partial z}m\overline{w'w'u'} - \overline{w'^2}\frac{\partial}{\partial z}\bar{u} + \frac{g}{C_pT_v}\overline{u's_v'} + \overline{\frac{p'}{m}\frac{\partial}{\partial z}u'} - 2\varepsilon_{wu}$$

$$\text{(A.9)}\quad \frac{\partial}{\partial t}\overline{w'v'} = \frac{1}{m}\frac{\partial}{\partial z}m\overline{w'w'v'} - \overline{w'^2}\frac{\partial}{\partial z}\bar{v} + \frac{g}{C_pT_v}\overline{v's_v'} + \overline{\frac{p'}{m}\frac{\partial}{\partial z}v'} - 2\varepsilon_{wv}$$

$$\text{(A.10)}\quad \frac{\partial}{\partial t}\overline{w'w'w'} = -\frac{1}{m}\frac{\partial}{\partial z}m\overline{w'w'w'w'} + \frac{3}{m}\overline{w'^2}\frac{\partial}{\partial z}\left(m\overline{w'^2}\right) + 3\frac{g}{C_pT_o}\overline{w'S_v'} - \overline{\frac{3}{m}w'^2\frac{\partial p'}{\partial z}} - \varepsilon_{www}$$

In Eqs. A.5 - A.9, ε is the total TKE dissipation rate; ε_x is the dissipation rate of any variable x; $s_v = C_pT_v + gZ$ is the virtual static energy; $T_v = T(1 + 0.61r_v - r_L)$ is the virtual temperature; z is the height; r_v is the water vapor mixing ratio; m is the density of the air; and p is the pressure.

$$\text{(A.11)}\quad \frac{\partial}{\partial t}\overline{w's_L'} = \frac{1}{m}\frac{\partial}{\partial z}m\overline{w'w's_L'} - \overline{w'^2}\frac{\partial}{\partial z}\bar{s}_L + \frac{g}{C_pT_v}\overline{s_L's_v'} + \overline{\frac{1}{m}p'\frac{\partial}{\partial z}s_L'} - 2\varepsilon_{ws_L}$$

$$\text{(A.12)}\quad \frac{\partial}{\partial t}\overline{u's_L'} = \frac{1}{m}\frac{\partial}{\partial z}m\overline{w'u's_L'} - \overline{w'u'}\frac{\partial}{\partial z}\bar{s}_L - \overline{w's_L'}\frac{\partial}{\partial z}\bar{u} - 2\varepsilon_{us_L}$$

$$\text{(A.13)}\quad \frac{\partial}{\partial t}\overline{v's_L'} = \frac{1}{m}\frac{\partial}{\partial z}m\overline{w'v's_L'} - \overline{w'v'}\frac{\partial}{\partial z}\bar{s}_L - \overline{w's_L'}\frac{\partial}{\partial z}\bar{v} - 2\varepsilon_{vs_L}$$

(A.14) $$\frac{\partial}{\partial t}\overline{s_L'^2} = \frac{\partial}{\partial z}\overline{w's_L'^2} - 2\overline{w's_L'}\frac{\partial}{\partial z}\overline{s}_L - 2\overline{s_L'\frac{\partial}{\partial z}R'} - 2\varepsilon_{s_L s_L}$$

(A.15) $$\frac{\partial}{\partial t}\overline{w'r_t'} = \frac{1}{m}\frac{\partial}{\partial z}m\overline{w'w'r'_t} - \overline{w'^2}\frac{\partial}{\partial z}\overline{r}_t + \frac{g}{C_p T_v}\overline{r_t's_v'} + \frac{1}{m}\overline{p'\frac{\partial}{\partial z}r_t'} - 2\varepsilon_{wr_t}$$

(A.16) $$\frac{\partial}{\partial t}\overline{u'r_r'} = \frac{1}{m}\frac{\partial}{\partial z}m\overline{w'u'r_t'} - \overline{w'u'}\frac{\partial}{\partial z}\overline{r}_t - \overline{w'r_t'}\frac{\partial}{\partial z}\overline{u} - 2\varepsilon_{ur_t}$$

(A.17) $$\frac{\partial}{\partial t}\overline{v'r_t'} = \frac{1}{m}\frac{\partial}{\partial z}m\overline{w'v'r_t'} - \overline{w'v'}\frac{\partial}{\partial z}\overline{r}_t - \overline{w'r_t'}\frac{\partial}{\partial z}\overline{v} - 2\varepsilon_{vr_t}$$

(A.18) $$\frac{\partial}{\partial t}\overline{r_t'^2} = \frac{\partial}{\partial z}\overline{w'r_t'^2} - 2\overline{w'r_t'}\frac{\partial}{\partial z}\overline{r}_t - 2\varepsilon_{r_t r_t}$$

(A.19) $$\frac{\partial}{\partial t}\overline{r_t's_L'} = \frac{\partial}{\partial z}\overline{w'r_t's_L'} - \overline{w'r_t'}\frac{\partial}{\partial z}\overline{s}_L - \overline{w's_L'}\frac{\partial}{\partial z}\overline{r}_t - 2\varepsilon_{r_t s_L}$$

Appendix B: A possible ADHOC approach for the pressure terms

In this appendix, I propose a possible "plume-type" approach for modeling the pressure terms in ADHOC; one which is compatible with the mass-flux decomposition used for all other terms in the ADHOC equations. An approach such as this will make the pressure terms completely consistent across all of the higher-moment equations, and should significantly improve the simulations (see Chapter IV).

The basic idea here is to create two equations for the two unknowns, p_{up} and p_{dn}. The first of these equations can be derived as follows: We assume that

$$\overline{\nabla \bullet \underset{\sim}{V}_H} << (\nabla \bullet \underset{\sim}{V})_{up,dn} \ , \tag{B.1}$$

where $\underset{\sim}{V}_H$ is the mean horizontal velocity vector and $(\nabla \bullet \underset{\sim}{V})_{up,dn}$ is divergence of either the updraft or downdraft mean horizontal velocity. Equation B.1 implies that

$$\frac{\partial}{\partial z}\overline{w} << \frac{\partial}{\partial z}(w_{up,dn}) \ , \tag{B.2}$$

where $\overline{w}$ is the mean vertical velocity and $w_{up,dn}$ is the vertical velocity of either the updraft or downdraft. Equation B.2, along with the fact that $\overline{w} = 0$ at the surface implies that $w \cong 0$ at all heights. This argument, which hold for all times, implies that

$$\frac{\partial}{\partial t}\overline{w} \cong 0 \tag{B.3}$$

at all heights.

We can write $\bar{w}$ as

$$\bar{w} = \sigma w_{up} + (1-\sigma) w_{dn} \ . \tag{B.4}$$

Plugging (B.4) into (B.3) gives

$$\frac{\partial}{\partial t}\bar{w} = \sigma \frac{\partial w_{up}}{\partial t} + (1-\sigma)\frac{\partial w_{dn}}{\partial t} + (w_{up} - w_{dn})\frac{\partial \sigma}{\partial z} \cong 0 \ . \tag{B.5}$$

We can write

$$\frac{\partial w_{up}}{\partial t} = \Pi_{up} + O_{up} \tag{B.6}$$

and

$$\frac{\partial w_{dn}}{\partial t} = \Pi_{dn} + O_{dn} \ , \tag{B.7}$$

where Π represents the pressure terms and O represents all other terms. Plugging (B.6), (B.7), and (3.67) into (B.5), we obtain an equation involving p_{up} and p_{dn};

$$\sigma \Pi_{up} + (1-\sigma)\Pi_{dn} = -\sigma O_{up} - (1-\sigma) O_{dn} - (w_{up} - w_{dn})\left(E - D - \frac{\partial M_c}{\partial z}\right) . \tag{B.8}$$

The forms of Π_{up} and Π_{dn} are $-\frac{1}{\rho}\left(\overline{\frac{\partial p}{\partial z}}\right)_{up}$ and $-\frac{1}{\rho}\left(\overline{\frac{\partial p}{\partial z}}\right)_{dn}$ respectively (as they would appear in the equations for w_{up} and w_{dn}). We need one more equation for p_{up} and p_{dn} to solve this system. To derive the second equation, we consider the volume integral of the vertical pressure gradient over a section of an updraft (or downdraft). The average of the vertical pressure gradient over the cross section of a plume has a contribution from the vertical derivative of the averaged pressure, and a second contribution from the rate of change of the cross-sectional area with height. The form of this second contribution depends on the geometry of the plume field. Consider an isolated plume with a circular cross section. Consider a horizontal "slice" through the plume, of thickness dz, and let the plume have radius $R(z)$. We want to compute the volume average (over the slice) of the vertical component of the pressure gradient. The starting point is the general expression for the gradient:

$$\int_V \nabla p \; dV = \int_S pn \;\; dS . \tag{B.9}$$

Here V is the volume that we are integrating over, S is its bounding surface, and n is the outward normal vector on S. Considering only the contributions to the vertical component of ∇p, which come from n_z, the vertical component of n, we can write

$$\int_V \frac{\partial p}{\partial z} \; dV = \langle \frac{\partial p}{\partial z} \rangle dV , \tag{B.10}$$

where the pointy brackets indicate a volume-average,

$$dV \cong \pi R^2(z) dz , \tag{B.11}$$

$$
\begin{aligned}
\int_S p n_z \; dS &= -\bar{p}(z)\pi R^2(z) + \left[\bar{p}(z) + \left(\frac{\partial}{\partial z}\bar{p}\right)dz\right]\left\{\pi\left[R(z) + \frac{\partial R}{\partial z}dz\right]^2\right\} \\
&\qquad -p_{\mathrm{edge}}\left\{\pi\left[R(z) + \frac{\partial R}{\partial z}dz\right]^2 - \pi R^2(z)\right\} \\
&\cong -\bar{p}(z)\pi R^2(z) + \bar{p}(z)\pi\left[R^2(z) + 2R\left(\frac{\partial R}{\partial z}dz\right)\right] + \left[\left(\frac{\partial}{\partial z}\bar{p}\right)dz\right]\pi R^2(z) \\
&\qquad -p_{\mathrm{edge}}\left[2\pi R(z)\frac{\partial R}{\partial z}dz\right] \ .
\end{aligned}
\tag{B.12}
$$

Here the overbar denotes a horizontal areal average, and the approximations involve dropping products of differentials. The p^i_{edge} term represents the contribution to the surface integral of the pressure along the tilted side of the updraft. It appears with a minus sign because if the plume radius is increasing upward, then the vertical component of the outward normal along the sloping plume edge points downward. Simplification of (B.12) yields

$$
\int_S p n_z \; dS \cong \left[\left(\frac{\partial}{\partial z}\bar{p}\right)dz\right]\pi R^2(z) + [\bar{p}(z) - p_{\mathrm{edge}}]2\pi R\left(\frac{\partial R}{\partial z}dz\right). \tag{B.13}
$$

Next, we substitute (B.10), (B.11), and (B.13) into (B.9), to obtain:

$$
\begin{aligned}
\langle\frac{\partial p}{\partial z}\rangle &= \frac{\left[\left(\frac{\partial}{\partial z}\bar{p}\right)dz\right]\pi R^2(z) + [\bar{p}(z) - p_{\mathrm{edge}}]2\pi R\left(\frac{\partial R}{\partial z}dz\right)}{\pi R^2(z)dz} \\
&= \left(\frac{\partial}{\partial z}\bar{p}\right) + [\bar{p}(z) - p_{\mathrm{edge}}]\frac{1}{\pi R^2(z)}\frac{\partial}{\partial z}[\pi R^2(z)] \ .
\end{aligned}
\tag{B.14}
$$

Finally, we identify the area of the "isolated plume" with area of the updrafts, and write

$$\overline{\left(\frac{\partial p}{\partial z}\right)}_{\text{up}} = \frac{\partial \bar{p}_{\text{up}}}{\partial z} + (\bar{p}_{\text{up}} - p_{\text{edge}})\left(\frac{1}{\sigma}\frac{\partial \sigma}{\partial z}\right). \tag{B.15}$$

This is equivalent to

$$\sigma\overline{\left(\frac{\partial p}{\partial z}\right)}_{\text{up}} = \sigma\frac{\partial \bar{p}_{\text{up}}}{\partial z} + (\bar{p}_{\text{up}} - p_{\text{edge}})\frac{\partial \sigma}{\partial z}. \tag{B.16}$$

We assume that

$$\bar{p} = \sigma\bar{p}_{\text{up}} + (1-\sigma)\bar{p}_{\text{dn}} \tag{B.17}$$

and

$$\begin{aligned} \overline{\left(\frac{\partial p}{\partial z}\right)} &= \frac{\partial}{\partial z}\bar{p} \\ &= \sigma\overline{\left(\frac{\partial p}{\partial z}\right)}_{\text{up}} + (1-\sigma)\overline{\left(\frac{\partial p}{\partial z}\right)}_{\text{dn}} \quad . \end{aligned} \tag{B.18}$$

Combining (B.16) - (B.18) gives

$$
\begin{aligned}
(1-\sigma)\overline{\left(\frac{\partial p}{\partial z}\right)}_{\mathrm{dn}} &= \overline{\left(\frac{\partial p}{\partial z}\right)} - \sigma\overline{\left(\frac{\partial p}{\partial z}\right)}_{\mathrm{up}} \\
&= \overline{\left(\frac{\partial p}{\partial z}\right)} - \left[\left(\sigma\frac{\partial \bar{p}_{\mathrm{up}}}{\partial z} + (\bar{p}_{\mathrm{up}} - p_{\mathrm{edge}})\frac{\partial \sigma}{\partial z}\right)\right] \\
&= \overline{\left(\frac{\partial p}{\partial z}\right)} - \sigma\frac{\partial}{\partial z}\left[\frac{\bar{p}-(1-\sigma)\bar{p}_{\mathrm{dn}}}{\sigma}\right] - \left[\frac{\bar{p}-(1-\sigma)\bar{p}_{\mathrm{dn}}}{\sigma} - p_{\mathrm{edge}}\right]\frac{\partial \sigma}{\partial z} \\
&= \overline{\left(\frac{\partial p}{\partial z}\right)} - \frac{\partial}{\partial z}\bar{p} + \frac{\bar{p}}{\sigma}\frac{\partial \sigma}{\partial z} + (1-\sigma)\frac{\partial \bar{p}_{\mathrm{dn}}}{\partial z} - \frac{\bar{p}_{\mathrm{dn}}}{\sigma}\frac{\partial \sigma}{\partial z} - \left[\frac{\bar{p}-(1-\sigma)\bar{p}_{\mathrm{dn}}}{\sigma} - p_{\mathrm{edge}}\right]\frac{\partial \sigma}{\partial z} \qquad \text{(B.19)} \\
&= (1-\sigma)\frac{\partial \bar{p}_{\mathrm{dn}}}{\partial z} - \frac{\bar{p}_{\mathrm{dn}}}{\sigma}\frac{\partial \sigma}{\partial z} + \left[\frac{(1-\sigma)\bar{p}_{\mathrm{dn}}}{\sigma} + p_{\mathrm{edge}}\right]\frac{\partial \sigma}{\partial z} \\
&= (1-\sigma)\frac{\partial \bar{p}_{\mathrm{dn}}}{\partial z} + (p_{\mathrm{edge}} - \bar{p}_{\mathrm{dn}})\frac{\partial \sigma}{\partial z} \\
&= (1-\sigma)\frac{\partial \bar{p}_{\mathrm{dn}}}{\partial z} - (p_{\mathrm{edge}} - \bar{p}_{\mathrm{dn}})\frac{\partial}{\partial z}(1-\sigma) \quad .
\end{aligned}
$$

This is equivalent to

$$
\overline{\left(\frac{\partial p}{\partial z}\right)}_{\mathrm{dn}} = \frac{\partial \bar{p}_{\mathrm{dn}}}{\partial z} - \frac{(p_{\mathrm{edge}} - \bar{p}_{\mathrm{dn}})}{(1-\sigma)}\frac{\partial}{\partial z}(1-\sigma). \qquad \text{(B.20)}
$$

For an array of linear updraft-downdraft pairs (rolls), one can derive an analogous expressions for

$$
\overline{\left(\frac{\partial p}{\partial z}\right)}_{up}.
$$

In order to obtain an "ADHOC-consistent" pressure parameterization (which is the goal of this exercise), we add (B.20) to the analogous updraft equation, and use the result, along with (B.8), to solve for Π_{up} and Π_{dn}. This theoretical approach is merely formulated in this thesis. In order to fully make the ADHOC equations internally consistent among themselves, as well as with HOC equations, I must incorporate a "plume-like" pressure parameterization, such as the one presented here into the model equations. The need for doing this was demonstrated several times in the results presented in Section IV.

The incorporation of these terms would take the exact form dictated by the HOC equations and thus, they would be completely consistent among all equations. For example, in Eqs. A.5-A.17 (with the exception of A.14), there is a term involving the vertical gradient of the perturbation pressure. The exact forms of the perturbation pressure gradient which appear in these equations can be written in term of $\left(\overline{\frac{\partial p}{\partial z}}\right)_{up}$ and $\left(\overline{\frac{\partial p}{\partial z}}\right)_{dn}$ (or analogously, Π_{up} and Π_{dn}). Thus, the values that we obtain for Π_{up} and Π_{dn} are directly used in each of the HOC/MFC equations, guaranteeing consistency among the pressure terms in all equations.

Appendix C: Finite-difference methods

The time-differencing scheme that I use varies from term to term. The following list summarizes the schemes used:

- The dissipation terms [as well as parameterized pressure terms that resemble dissipation (Section III-H) employ the backward-implicit scheme
- The transport terms are categorized and employ either a Euler forward, a tridiagonal backward implicit, or a semi-implicit/semi-forward scheme (explained further below)
- All other terms integrate forward in time with a second- or third-order Adams Bashforth scheme (set at run time).

The manner in which I chose the finite difference scheme for the transport terms is as follows: I use a simple Euler-forward timestep when the higher-order term is known and can be directly finite-differenced in space. For example, I use this scheme for the flux divergence term of the mean state equations (e.g., Eq. C.6) (Here, I know the flux because I predict it). I also use this method for the transport (third-moment) term of the flux equations (e.g., Eq. C.6) (In this case, I know the third-moment because I diagnose it using RSM); I use a tridiagonal backward-implicit scheme when the higher-order transport term is unknown [e.g., the transport term of the $\overline{w'u'}$ equation (Eq. C.5)]; and I use a semi-implicit/semi-forward scheme for the transport term in the $\overline{u'u'}$ and $\overline{v'v'}$ equations (e.g., Eq. C.3).

I use the latter scheme for the transport terms of the horizontal momentum variance equations due to the fact that the three momentum variance equations are "tied" to one another through the Rotta terms (Section II-C-1). Thus, in order to keep all the Rotta "dissipation-like" terms implicit, I solve all three components of the momentum variances simultaneously (Eqs. C.3-C.4). The problem of solving a matrix of three equations when two of them have tridiagonally-implicit terms is unnecessarily complex. A semi-implicit scheme is also stable in this case and it greatly simplifies the equations (S. Krueger, personal communication, 1998).

For the space differencing, I use a staggered grid (Fig. 15) such that the mean quantities and the triple moments are defined at the middle of the layers while the second and fourth moments are defined at the layer edges. This staggering allows the transport and diffusion terms to be finite-differenced without averaging (Krueger, 1985). Below, I show examples of the space finite differencing methods for $\overline{u'u'}$, $\overline{w'w'}$, $\overline{w'u'}$, $\overline{w's_L'}$, and $\overline{s_L}$, and $\overline{w'w'w'}$. In these equations, n is the timestep counter; l is model grid level where "half" levels refer to layer centers and "integer" levels refer to layer edges (Fig. 15); $[\ \ ]_{AB}$ refers to terms that use an Adams-Bashforth-weighted time scheme; dzm and dzt are the widths of the mean and turbulent grid levels respectively (see Fig. 15); And, $(\frown)$ is a vertical linearly interpolated value. For simplicity, the "primes" and "bars" have been left out.

$$\frac{{s_L}_{l+\frac{1}{2}}^{n+1}}{\delta t} = \frac{{s_L}_{l+\frac{1}{2}}^{n}}{\delta t} - \left[\frac{{ws_L}_{l+1}^{n} - {ws_L}_{l}^{n}}{dzt_{l+\frac{1}{2}}}\right] - \left[ww_l^n\left(\frac{\widehat{s}_{L_{l+1}}^{\,n} - \widehat{s}_{L_l}^{\,n}}{dzm_l}\right)\right]_{AB} + \left[F^n_{s_{L_l}}\right]_{AB} \tag{C.2}$$

$$\frac{ww_l^{n+1}}{\delta t} = \frac{ww_l^n}{\delta t} - \left[\frac{www_{l+\frac{1}{2}}^{n} - www_{l-\frac{1}{2}}^{n}}{dzm_l}\right] + \left[\frac{1}{3}C_1\frac{uu_l^{n+1}}{\tau} + \frac{1}{3}C_1\frac{vv_l^{n+1}}{\tau} - \frac{2}{3}C_1\frac{ww_l^{n+1}}{\tau}\right] \tag{C.3}$$

$$+\left[2\frac{g}{C_pT_0}ws_{v_l}^{n}\right]_{AB} + \left[P_{ww_l}^{n}\right]_{AB} + LME_{ww_l}^{n} + LMD_{ww_l}^{n}$$

$$\frac{uu_l^{n+1}}{\delta t} = \frac{uu_l^{n}}{\delta t} - \left[\frac{1}{dzm_l}\left\{\left[\widehat{K^n}_{l+\frac{1}{2}}\left(\frac{uu^n{}_{l+1} - uu_l^{n+1}}{dzt_{l+\frac{1}{2}}}\right)\right] - \left[\widehat{K^n}_{l-\frac{1}{2}}\left(\frac{uu_l^{n+1} - uu^n{}_{l-1}}{dzt_{l-\frac{1}{2}}}\right)\right]\right\}\right] \tag{C.4}$$

$$+\left[\frac{1}{3}C_1\frac{vv_l^{n+1}}{\tau} + \frac{1}{3}C_1\frac{ww_l^{n+1}}{\tau} - \left(1+\frac{2}{3}C_1\right)\frac{uu_l^{n+1}}{\tau}\right] - \left[2wu_l^n\left(\frac{U^n_{l+\frac{1}{2}} - U^n_{l-\frac{1}{2}}}{dzm_l}\right)\right]_{AB}$$

$$+\left[P^n_{uu_l}\right]_{AB}$$

$$\frac{wu_l^{n+1}}{\delta t} = \frac{wu_l^{n}}{\delta t} \tag{C.5}$$

$$-\left[\frac{1}{dzm_l}\left\{\left[\widehat{K^n}_{l+\frac{1}{2}}\left(\frac{wu^{n+1}_{l+1} - wu_l^{n+1}}{dzt_{l+\frac{1}{2}}}\right)\right] - \left[\widehat{K^n}_{l-\frac{1}{2}}\left(\frac{wu_l^{n+1} - wu^{n+1}_{l-1}}{dzt_{l-\frac{1}{2}}}\right)\right]\right\}\right]$$

$$-\left[C_4\frac{wu_l^{n+1}}{\tau}\right] - \left[(1-C_5)ww_l^n\left(\frac{U^n_{l+\frac{1}{2}} - U^n_{l-\frac{1}{2}}}{dzm_l}\right)\right]_{AB} + \left[(1-C_5)\left(\frac{g}{C_pT_0}(us_{v_l})^n\right)\right]_{AB}$$

$$\frac{ws_{L_l}^{n+1}}{\delta t} = \frac{ws_{L_l}^{n}}{\delta t} - \left[\frac{wws_L{}^n_{l+\frac{1}{2}} - wws_L{}^n_{l-\frac{1}{2}}}{dzm_l}\right] - \left[C_6\frac{ws_{L_l}^{n+1}}{\tau}\right] \tag{C.6}$$

$$+\left[(1-C_7)\frac{g}{C_pT_0}(s_Ls_{v_l})^n\right]_{AB} - \left[ww_l^n\left(\frac{s_L{}^n_{l+\frac{1}{2}} - s_L{}^n_{l-\frac{1}{2}}}{dzm_l}\right)\right]_{AB} + LME^n_{ws_{L_l}} + LMD^n_{ws_{L_l}}$$

$$\frac{www^{n+1}_{l+\frac{1}{2}}}{\delta t} = \frac{www^{n}_{l+\frac{1}{2}}}{\delta t} - \left[\frac{3}{2}\frac{(ww^{n}{}_{l+1} - ww^{n}{}_{l})^{2}}{dzt_{l+\frac{1}{2}}}\right] \tag{C.7}$$

$$-\left[C_8 \frac{www^{n+1}_{l+\frac{1}{2}}}{\tau}\right] + \left[3(1-C_{11})\frac{g}{C_p T_0} wws_{v_l}{}^{n}\right]_{AB} + \widehat{LME}^{\,n}_{www_l} + LMD^{\,n}_{www_l}$$

In the above finite difference equations, LME and LMD are the lateral mass entrainment and detrainment terms defined in Section III-G for their respective equations; $C_8 = 6.5$; $C_{11} = 0.4$, $C_7 = 0.4$; $C_6 = 4.85$; $C_1 = 2.0$; $C_4 = 4.5$; $C_5 = 0.0$; K is the eddy diffusivity for momentum; F_{s_L} is the sum of the radiative cooling and the horizontal advective forcing for the mean liquid water static energy; U is the mean zonal wind speed; P_{uu} and P_{ww} are the combined buoyancy and mean strain pressure effects for uu and ww respectively (Section II-C-1).

References

Abdella, K. and N. McFarlane, 1996: Parameterization of the surface-layer exchange coefficients for atmospheric models. *Bound.-Layer Meteor.*, **80**(3), 223-248.

Albrecht, B. A., 1979: A model of the thermodynamic structure of the trade-wind boundary-layer. Part I. Theoretical formulation and sensitivity tests. *J. Atmos. Sci.*, **36**, 73-89.

Albrecht, B. A., 1979: A model of the thermodynamic structure of the trade-wind boundary-layer. Part II. Applications. *J. Atmos. Sci.*, **36**, 90-98.

Albrecht, B. A., 1981: A parameterization of trade-wind cumulus cloud amounts. *J. Atmos. Sci.*, **38**, 97-105.

Albrecht, B. A., 1981: A parameterization of trade-wind cumulus cloud amounts. *J. Atmos. Sci.*, **38**, 97-105.

Albrecht, B. A., 1991: Fractional cloudiness and cloud-top entrainment instability. *J. Atmos. Sci.*, **48**(12), 1519-1525.

Albrecht, B. A., D. Johnson, W. H. Schubert, and A. S. Frisch, 1995: The Atlantic stratocumulus transition experiment--ASTEX. *Bull, of the Amer. Meteor. Soc.*, **76**(6), 889-904.

André, J. C., G. DeMoor, P. Lacarrere, and R. DuVachat, 1976a: Turbulence approximation for inhomogeneous flows: Part I. The clipping approximation. *J. Atmos. Sci.*, **33**, 476-481.

André, J. C., G. DeMoor, P. Lacarrere, and R. DuVachat, 1976b: Turbulence approximation for inhomogeneous flows: Part II. The numerical simulation of a penetrative convection experiment. *J. Atmos. Sci.*, **33**, 482-491.

André, J. C., G. DeMoor, P. Lacarrere, G. Therry, and R. DuVachat, 1978: Modeling the 24-hour evolution of the mean and turbulent structures of the planetary boundary layer. *J. Atmos. Sci.*, **35**(10), 1861-1883.

André, J. C., 1978: Modeling the 24-hour evolution of the mean and turbulent structures of the planetary boundary layer. *J. Atmos. Sci.*, **35**(10), 1861-1883.

Arakawa, A., 1969: Parameterization of cumulus convection. *Proc. WMO/IUGG Symp. Numerical Weather Prediction*, Tokyo, Japan Meteor. Agency. IV, 8, 1-6.

Arakawa, A., and W. H. Schubert, 1974: The interaction of a cumulus cloud ensemble with the large-scale environment, Part I. *J. Atmos. Sci.*, **31**, 674-701.

Augstein, E., H. Schmidt, and F. Ostapoff, 1973: The vertical structure of the atmospheric planetary boundary layer in undisturbed tradewinds over the Atlantic Ocean. *Bound.-Layer Meteor.*, **6**, 129-150.

Ball, F. K., 1960: Control of inversion height by surface heating. *Quart. J. Roy. Meteor. Soc.*, **86**, 483-494.

Barre, L. A., 1986: Arctic air pollution: an overview of current knowledge. *Atmos. Env.*, Special Issue, **20**(4): 643-663.

Batchelor, G. K., 1954: Heat convection and buoyancy effects in fluids. *Quart. J. Roy. Meteor. Soc.*, **80**, 339-358.

Bechtold, P., 1992: A model of marine boundary-layer cloudiness for mesoscale applications. *J.*

Atmos. Sci., **49**(18), 1723-1744.

Bechtold, P., 1995: Modeling of trade wind cumuli with a low-order turbulence model: toward a unified description of Cu and Sc clouds in meteorological models. *J. Atmos. Sci.*, **52**(4), 455-463.

Bechtold, P., S. K. Krueger, W. S. Lewellen, E. van Meijgaard, C.-H. Moeng, D. A. Randall, A. van Ulden, and S. Wang, 1996: Modeling a stratocumulus-topped PBL: intercomparison among different one-dimensional codes and with large eddy simulation. *J. Atmos. Sci.*, **77**(9), 2033-2042.

Beljaars, A. C. M., J. L. Walmsley, and P. A. Taylor, 1987: Modeling of turbulence over low hills and varying surface roughness. *Bound.-Layer Meteor.*, **41**(1/4), 203-215.

Benoit, R., 1976: A comprehensive parameterization of the atmospheric boundary-layer for general circulation models. Ph.D. dissertation, McGill University, and National Center for Atmospheric Research cooperative thesis No 39, 278pp.

Berkowicz, R., L. P. Prahm, and J.-F. Louis, 1979: Global 2-D spectral dispersion model. *World Meteorological Organization*, Geneva, WMO-No. 538, pp. 359-365.

Betts, A., 1973: Non-precipitating cumulus convection and its parameterization. *Quart. J. Roy. Meteor. Soc.*, **99**, 178-196.

Betts, A., 1975: Parametric interpretation of trade-wind cumulus budget studies. *J. Atmos. Sci.*, **32**(10), 1934-1945.

Betts, A., 1976: Modeling subcloud layer structure and interaction with a shallow cumulus layer.

J. Atmos. Sci., **33**(12), 2363-2382.

Betts, A., 1983: Thermodynamics of mixed stratocumulus layers. *J. Atmos. Sci.*, **40**, 2655-2670.

Betts, A., 1990: Diurnal variation of California coastal stratocumulus from two days of boundary layer soundings. *Tellus,* **42A**(2), 302-304.

Bhumralkar, C. M., 1975: A survey of parameterization techniques for the planetary boundary layer in atmospheric circulation models. Defense Advanced Research Agency R-1653-ARPA. ARPA order No. 189-1, 84pp.

Bjerknes, J., 1938: Saturated-adiabatic ascent of air through dry-adiabatically descending environment. *Quart. J. Roy. Meteor. Soc.*, **64**, 325-330.

Blackadar, A. K., 1962: The vertical distribution of wind and turbulent exchange in neutral atmospheres. *J. Geophys. Res.*, **67**, 3095-3102.

Blackadar, A. K., 1979: High-resolution models of the planetary boundary layer. *Advances in Environmental Science and Engineering*, Vol. 1, N.Y., Gordon and Breach Science Publishers, Incorporated, pp. 50-85.

Blanchet, J., 1970: Etude statistique d'un systeme fluide- Application a la meteorologie. *La meteorologie V,* **15**, 15-78.

Bougeault, P., 1981a: Modeling the trade wind cumulus boundary layer, Pt. 2, High-order one-dimensional model. *J. Atmos. Sci.*, **38**(11), 2414-2428.

Bougeault, P., 1981b: Modeling the trade wind cumulus boundary layer, Pt. 2, High-order one-dimensional model. *J. Atmos. Sci.*, **38**(11), 2429-2439.

Bougeault, P., 1982: Cloud-ensemble relations based on the gamma probability distribution for the higher-order models of the planetary boundary layer, *Atmos. Sci.*, **39**(12), 2691-2700.

Bougeault, P., and J. C. André, 1986: On the stability of the third-order turbulence closure for the modeling of the stratocumulus-topped boundary layer. *J. Atmos. Sci.*, **43**(15), 1574-1581.

Bretherton, C. S., and R. Pincus, 1995: Cloudiness and marine boundary layer dynamics in the ASTEX Lagrangian experiments. Part I: Synoptic setting and vertical structure. *J. Atmos. Sci.*, **52**(16), 2707-2723.

Brost, R. A., J. C. Wyngaard, and D. H. Lenschow, 1982: Marine stratocumulus layers, Pt. 2: Turbulence budgets. *J. Atmos. Sci.*, **39**, 818-836.

Browning, K. A., 1994: Survey of perceived priority issues in the parameterizations of cloud-related processes. *Quart. J. R. Met. Soc.*, **120**(5), 483-487.

Brummer, B., E. Augstein and H. Riehl, 1974: On the low-level wind structure in the Atlantic trade. *Quart. J. R. Met. Soc.*, **100**, 109-121.

Busch, N., O. Ebel, H. Kraus, and E. Schaller, 1982: The structure of the sub-polar inversion-capped ABL. *Arctic Meteorol. Geophys Biokl.*, **A.31**, 1-18.

Businger, J. A. and S. P. Oncley, 1990: Flux measurements with conditional sampling. *J. Atmos. and Ocean Technol.*, **7**, 349-352.

Canuto, V. M., 1992: Turbulent convection with overshooting: Reynolds stress approach. The

Astrophys. J., **392**, 218-232.

Canuto, V. M., F. Minotti, C. Ronchi, R. M. Ypma, and O. Zeman, 1994: Second-order closure PBL model with new third-order moments: comparison with LES data. *J. Atmos. Sci.*, **51**(12), 1605-1618.

Chatfield, R. B. and R. A. Brost, 1987: Two-stream model of the vertical transport of trace species in the convective boundary layer. *J. of Geophys. Res.*, **92**(D11), 13263-13276.

Chen, C., and W. R. Cotton, 1983: One-dimensional simulation of the stratocumulus-capped mixed layer. *Bound.-Layer Meteor.*, **25**(3), 289-321.

Ching, J. K. S., 1975: Determining the drag coefficient from vorticity, momentum, and mass budget analyses. *J. Atmos. Sci.*, **32**, 1898-1908.

Crow, S. C., 1968: Viscoelastic properties of fine-grained incompressible turbulence. *J. Fluid Mech.*, **33**, 1-20.

Cuijpers, J. W. M. and P. G. Duynkerke, 1993: Large eddy simulation of trade wind cumulus clouds. *J. Atmos. Sci.*, **50**(23), 3894-3908.

Curry, J. A., 1983: On the formation of continental polar air. *J. Atmos. Sci.*, **40**(9), 2278-2292.

Curry, J. A., 1986: Interactions among turbulence, radiation, and microphysics in Arctic stratus clouds. *J. Atmos. Sci.*, **43**(1), 90-106.

Curry, J. A., E. E. Ebert, and G. F. Herman, 1988: Mean and turbulence structure of the summertime Arctic cloudy boundary layer. *Quart. J. Roy. Meteor. Soc.*, **114**(481), 715-

746.

Curry J. A., and E. E. Ebert, 1990: Sensitivity of the thickness of Arctic sea ice to the optical properties of clouds. *Ann. Glac.*, **14**, 43-46.

Curry, J. A., and E. E. Ebert, 1992: Annual cycle of radiation fluxes over the Arctic Ocean: sensitivity to cloud optical properties. *J. Clim.*, **5**(11), 1267-1280.

Curry, J. A., J. L. Schramm, and E. E. Ebert, 1993: Impact of clouds on the surface radiation balance of the Arctic Ocean. *Meteor. and Atmos. Phys.*, **51**(3-4), 197-217.

Curry, J. A., 1995: Interactions among aerosols, clouds, and climate of the Arctic Ocean. *Science of the Total Environment*, **160-161**, 777-791.

Deardorff, J. W., 1966: The counter-gradient heat flux in the lower atmosphere and in the laboratory. *J. Atmos. Sci.*, **23**, 503-506.

Deardorff, J. W., 1970: Convective velocity and temperature scales for the unstable planetary boundary layer and for Rayleigh convection. *J. Atmos. Sci.*, **27**, 1211-1213.

Deardorff, J. W., 1972: Numerical investigation of neutral and unstable planetary boundary layers. *J. Atmos. Sci.*, **29**, 91-115.

Deardorff, J. W., 1973: Three-dimensional numerical modeling of the planetary boundary layer. *Workshop on Micrometeorology*, D. A. Haugen, Ed., Boston, Amer. Met. Soc., 271-311.

Deardorff, J. W., 1976: Usefulness of the liquid water potential temperature in a shallow cloud model. *J. Appl. Meteorol.*, **15**, 98-102.

Deardorff, J. W., 1980: Cloud top entrainment instability. *J. Atmos. Sci.*, **37**(1), 131-147.

Deardorff, J. W., 1980: Stratocumulus-capped mixed layers derived from a three-dimensional model. *Bound.-Layer Meteor.*, **18**(4), 495-527.

Deardorff, J. W., 1981: On the distribution of mean radiative cooling at the top of a stratocumulus-capped mixed layer. *Quart. J. Roy. Meteor. Soc.*, **107**, 191-202

Deardorff, J. W., and G. E. Willis, 1985: Further results from a laboratory model of the convective boundary layer. *Bound.-Layer Meteor.*, **32**, 205-236.

de Laat, A. T. J. and P. G. Duynkerke, 1998: Analysis of ASTEX-stratocumulus observational data using mass-flux approach. *Bound.-Layer Meteor.*, **86**(1), 63-87.

de Roode, S. R. and P. G. Duynkerke, 1997: Observed Lagrangian transition of stratocumulus into cumulus during ASTEX: mean state and turbulence structure. *J. Atmos. Sci.*, **54**(17), 2157-2173.

Deterling, H. W., and D. Etling, 1985: Application of the E-ε turbulence model to the atmospheric boundary layer. *Bound.-Layer Meteor.*, **33**(2), 113-133.

Ding, P., and D. A. Randall, 1998: A cumulus parameterization with multiple cloud base levels. *J. of Geophys. Res.*, **103**(D10), 11341-11353.

Donaldson, C., 1971: Calculation of turbulent shear flows for atmospheric and vortex motions.

AIAA J., **10**, 4-12.

Donaldson, C., 1973: Construction of a dynamic model of the production of atmospheric turbulence and the dispersal of atmospheric pollutants. *Workshop on micrometeorology*, D. A. Haugen, ed., Amer. Meteorol. Soc., Boston, 313-392.

Dunckel, M., J. Hasse, L. Krugermeyer, D. Schriever, and J. Wucknitz, 1974: Turbulent fluxes of momentum, heat, and water vapor in the atmosphere surface layer at sea during ATEX. *Bound.-Layer Meteor.*, **6**, 81-106.

Duynkerke, P. G., H. Q. Zhang, and P. J. Jonker, 1995: Microphysical and turbulent structure of nocturnal stratocumulus as observed during ASTEX. *J. Atmos. Sci.*, **52**, 2763-2777.

Ebert, E. E., 1984: Radiative interaction between Arctic sea ice and boundary layer stratus. M. S. thesis, University of Wisconsin-- Madison, 180pp.

Esbensen, S., 1978: Bulk thermodynamic effects and properties of small tropical cumuli. *J. Atmos. Sci.*, **35**, 826-837.

Fiedler, B. H., 1984: Integral closure model for the vertical turbulent flux of a scalar in a mixed layer. *J. Atmos. Sci.*, **41**(4), 674-680.

Finger, J. E., and H. Schmidt, 1986: On the efficiency of different higher order turbulence models simulating the convective boundary layer. *Contr. to Atmos. Phys.*, **59**(4), 505-517.

Finger, J. E., and P. Wendling, 1990: Turbulence structure of Arctic stratus clouds derived from measurements and calculations. *J. Atmos. Sci.*, **47**(11), 1351-1373.

Frisch, A. S., D. H. Lenschow, C. W. Fairall, W. H. Schubert, and J. S. Gibson, 1995: Doppler radar measurements of turbulence in marine stratiform cloud during ASTEX. *J. Atmos. Sci.*, **52**(16), 2800-2808.

Forkel, R. and P. Wendling, 1986: A numerical study of the formation of Arctic stratus clouds with consideration of absorbing aerosol particles. *Meteor. Rundsch.*, **59**, 74-79.

Garrat, J. R., 1992: *The Atmospheric Boundary Layer.* Cambridge University Press, New York, New York, 316pp.

Greenhut, G. K., S. Khalsa, and J. Singh, 1982: Updraft and downdraft events in the atmospheric boundary layer over the equatorial Pacific Ocean. *J. Atmos. Sci.*, **39**(8), 1803-1818.

Greenhut, G. K., and S. Khalsa, 1987: Convective elements in the marine atmospheric boundary layer, Pt. 1, Conditional sampling statistics. *J. Appl. Clim. and Met.*, **26**(7), 813-822.

Gregory, D. and P. R. Rowntree, 1990: A mass-flux convection scheme with representation of cloud ensemble characteristics and stability-dependent closure. *Mon. Wea. Rev.*, **118**(7), 1483-1506.

Hack, J. J., 1994: Parameterization of moist convection in the NCAR Community Climate Model (CCM2). *J. Geophys. Res.*, **99**, 5551-5568.

Hanjalic, K., and B. E. Launder, 1972: A Reynolds stress model of turbulence and its application to thin shear flows, *J. Fluid. Mech.*, **52**(4), 609-638.

Hanson, H. P., 1981: On mixing by trade-wind cumuli. *J. Atmos. Sci.*, **38**(5), 1003-1014.

Hartman, D. L., M. E. Ockert-Bell, and M. L. Michelsen, 1992: The effect of cloud type on earth's energy balance. *J. Clim.*, **5**, 1281-1304.

Harrison, E. F., F. P. Minnis, B. R. Barkstrom, V. Ramanathan, R. D. Cess, and G. G. Gibson, 1990: Seasonal variation of cloud radiative forcing derived from the earth's radiation budget experiment. *J Geophys. Res.*, **95**, 18687-18703.

Helfand, H. M., and J. C. Labraga, 1988: Design of a non-singular level 2.5 second-order closure model for the prediction of atmospheric turbulence. *J. Atmos. Sci.*, **45**(2), 113-132

Herman, G. F., and R. Goody, 1976: Formation and persistence of summertime Arctic clouds. *J. Atmos. Sci.*, **33**(8), 1537-1553.

Herman, G. F., 1980: Thermal radiation in Arctic stratus clouds. *Quart. J. Roy. Meteor. Soc.*, **106**(450), 771-780.

Heymsfield, A. J., P. N. Johnson, and J. E. Dye, 1978: Observations of moist adiabatic ascent in Northeast Colorado cumulus congestus clouds. *J. Atmos. Sci.*, **35**, 1689-1703.

Holland, J. Z., and E. M. Rasmusson, 1973: Measurements of the atmospheric mass, energy, and momentum budgets over a 500-kilometer square of tropical ocean. *Mon. Wea. Rev.*, **101**(1), 44-55.

Holton, J. R., 1973: A one-dimensional cumulus model including pressure perturbations. *Mon. Wea. Rev.*, **101**(3), 201-205.

Holtslag, A. A. M., and B. A. Boville, 1993: Local versus nonlocal boundary-layer diffusion in a global climate model. *J. Clim.*, **6**, 1825-1842.

Holtslag, A. A. M. and C.-H. Moeng, 1991: Eddy diffusivity and countergradient transport in the convective atmospheric boundary layer. *J. Atmos. Sci.*, **48**(14), 1690-1698.

Houghton, R. W., and Y. M. Tourre, 1992: Characteristics of low-frequency sea surface temperature fluctuations in the tropical Atlantic. *J. Clim.*, **5**(7), 765-771.

Huschke, R. E., 1969: Arctic cloud statistics from "air-calibrated" surface weather observations. The Rand Corp., RM-6173-PR, 79pp.

Kain, J. S., and J. M. Fritsch, 1990: A one-dimensional entraining/detraining plume model and its application in convective parameterization. *J. Atmos. Sci.*, **47**(23), 2784-2802.

Keller, L. V., and A. A. Friedman, 1924: Differentialgleichung fur die turbulente bewengung einer kompressiblen flussigkeit. *Proc 1st Intern. Congr. Appl. Mech.*, Delft, 395-405.

Kiehl, T. J., J. J. Hack, G. B. Bonan, B. A. Boville, B. P. Briegleb, D. L. Williamson, and P. J. Rasch, 1996: Description of the NCAR Community Climate Model (CCM3). *NCAR Technical Note TN-420+STR,* National Center for Atmospheric Research, Boulder, Colorado, 152pp.

Khalsa, S. J. S., and G. K. Greenhut, 1985: Conditional sampling of updrafts and downdrafts in the marine atmospheric boundary layer. *J. Atmos. Sci.*, **42**(23), 2550-2562.

Kolmogorov, A. N., 1941: Energy dissipation in locally isotropic turbulence. *Doklady AN SSSR*, **32**(1), 19-21.

Kolmogorov, A. N., 1942: Equations of turbulent motion of an incompressible fluid. *Izvestiya AN SSSR, Ser. fiz.*, **6**(1-2), 56-58.

Krueger, S. K., 1985: Numerical simulation of tropical cumulus clouds and their interaction with the subcloud layer. Ph.D. thesis, University of California, Los Angeles, 205pp.

Krueger, S. K., 1988: Numerical simulation of tropical cumulus clouds and their interaction with the subcloud layer. *J. Atmos. Sci.*, **45**(16), 2221-2250.

Krueger, S. K., and A. Bergeron, 1994: Modeling the trade cumulus boundary layer. *Atmos. Res.*, **33**(1-4), 169-192.

Krueger, S. K., G. T. McLean, and Q. Fu, 1995: Numerical simulation of the stratus-to-cumulus transition in the subtropical marine boundary layer. Part I: Boundary-layer structure. *J. Atmos. Sci.*, **52**(16), 2839-2850.

Langland, R. H., and C.-S. Liou, 1996: Implementation of an E-ε parameterization of vertical subgrid-scale mixing in a regional model. *Mon. Wea. Rev.*, **124**(5), 905-918.

Lappen, C.-L., 1996: Comparison of the simulated arctic climate of the CSU GCM with observations. Atmospheric Science Paper No. 614, Colorado State University, 38pp.

Launder, B. E., 1975: On the effects of a gravitational field on the turbulent transport of heat and momentum. *J. Fluid Mech.*, **67**(3), 569-581.

Launder, B. E., G. J. Reece, and W. Rodi, 1975: Progress in the development of a Reynolds stress turbulent closure. *J. Fluid Mech.*, **52**, 609-638.

Lenshow, D. H., and P. L. Stephens, 1980: Role of thermals in the convective boundary layer. *Bound.-Layer Meteor.*, **19**(4), 509-532.

Lenshow, D. H., J. C. Wyngaard, and W. T. Pennell, 1980: Mean field and second moment budgets in a baroclinic, convective boundary layer. *J. Atmos. Sci.*, **37**, 1313-1326.

Lewellen W. S., and M. E. Teske, 1976: Second-order closure modeling of diffusion in the atmospheric boundary layer. *Bound.-Layer Meteor.*, **10**(1), 69-90.

Lilly, D. K., 1967: The representation of small-scale turbulence in numerical simulation experiments. *Proc. IBM Sci. Comput. Symp. Environmental Sci.*, Thomas J. Watson Research Center, Yorktown Heights, New York, 195-210.

Lilly, D. K., 1968: Models of cloud-topped mixed layers under a strong inversion. *Quart. J. Roy. Meteor. Soc.*, **94**, 292-309.

Lin, C., and A. Arakawa, 1997a: The macroscopic entrainment processes of simulated cumulus ensemble. Part I: Entrainment sources. *J. Atmos. Sci.*, **58**(4), 1027-1043.

Lin, C., and A. Arakawa, 1997b:The macroscopic entrainment processes of simulated cumulus ensemble. Part II: Testing the entraining-plume model. *J. Atmos. Sci.*, **58**(4), 1044-1053.

Lorenz, E. N., 1963: Deterministic non-periodic flow. *J. Atmos. Sci.*, **20**, 130-141.

Louis, J.-F., 1979: Parametric model of vertical eddy fluxes in the atmosphere. *Bound.-Layer Meteor.*, **17**(2), 187-202.

Lumley, J. L., and B. Khajeh Nouri, 1973: Modeling homogeneous deformation of turbulence. *Pennsylvania State University, Dept. Aeron. Rep.*

Lumley, J. L., and B. Khajeh Nouri, 1974: Computational modeling of turbulent transport. *Adv.*

Geophys., Vol. 18a, Academic Press, pp 169-192.

Lumley, J. L., 1978: Computational modeling of turbulent flows. *Advances in Applied Mechanics*, vol. 18, New York Academic Press, New York, pp. 123-176.

Mailhot, J. and R. Benoit, 1982: Finite-element model of the atmospheric boundary layer suitable for use with numerical weather prediction models. *J. Atmos. Sci.*, **39**(10), 2249-2266.

McBean, G. A., and J. A. Elliot, 1975: Vertical transports of kinetic energy by turbulence and pressure in the boundary layer. *J. Atmos. Sci.*, **32**(4), 753-766.

McInnes, K. L., and J. A. Curry, 1995: Modeling the mean and turbulent structure of the summertime Arctic cloudy boundary layer. *Bound.-Layer Meteor.*, **73**(1-2), 125-143.

Mellor, G. L., 1973: Analytic prediction of the properties of stratified planetary surface layers. *J. Atmos. Sci.*, **30**, 1061-1069.

Mellor, G. L., and T. Yamada, 1974: A hierarchy of turbulence closure models for planetary boundary layers. *J. Atmos. Sci.*, **31**, 1791-1806.

Mellor, G. L., and T. Yamada, 1982: Development of a turbulence closure model for geophysical fluid problems. *Rev. of Geophys. and space Phys.*, **20**(4), 851-875.

Millionshchikov, M., 1941: On the theory of homogeneous and isotropic turbulence. *C. R. Acad. Sci. URSS*, **32**, 615-618.

Miyakoda, K., and J. Sirutis, 1977: Comparative integrations of global models with various parameterized processes of subgrid-scale vertical transports: description of the parameterizations. *Contr. to Atmos. Phys.*, Oxford, **50**(4): 445-487.

Moeng, C.-H., and A. Arakawa, 1980: Numerical study of a marine subtropical stratus cloud layer and its stability. *J. Atmos. Sci.*, **37**(2), 2661-2676.

Moeng, C.-H., 1984: A large-eddy-simulation for the study of planetary boundary-layer turbulence. *J. Atmos. Sci.*, **41**(13), 2052-2062.

Moeng, C.-H., and D. A. Randall, 1984: Problems in simulating the stratocumulus-topped boundary layer with a third-order closure model. *J. Atmos. Sci.*, **41**(9), 1588-1600.

Moeng, C.-H., and J. C. Wyngaard, 1989: Evaluation of turbulent transport and dissipation closures in second-order modeling. *J. Atmos. Sci.*, **46**, 2311-2330.

Monin, A. S., and A. M. Obukhov, 1954: Basic laws of turbulent mixing in the atmosphere near the ground. *Tr. Akad. Nauk SSSR Geofiz. Inst.*, **24**(151), 163-187.

Morton, B. R., 1957: Buoyant plumes in a moist atmosphere. *J. Fluid Mech.*, **2**, 127-144.

Naot, D., A. Shavit, and M. Wolfshtein, 1973: Two-point correlation model and the redistribution of Reynolds stresses. *Phys. of Fluids*, **16**(6), 738-743.

Nicholls S. and M. A. Lemone, 1980: Fair weather boundary layer in GATE: the relationship of subcloud fluxes and structure to the distribution and enhancement of cumulus clouds. *J. Atmos. Sci.*, **37**(9), 2051-2067.

Nicholls S., 1984: Dynamics of stratocumulus: aircraft observations and comparisons with a mixed layer model. *Quart. J. R. Met. Soc.*, **110**(466), 783-820.

Nicholls S., and J. D. Turton, 1986: Observational study of the structure of stratiform cloud sheets: Pt. 2, Entrainment. *Quart. J. R. Met. Soc.*, **112**(472), 461-480.

Nicholls, S., 1989: The structure of radiatively-driven convection in stratocumulus. *Quart. J. R. Met. Soc.*, **115**, 487-511.

Nieuwstadt, F. T. M., and R. Brost, 1986: Decay of convective turbulence. *J. Atmos. Sci.*, **43,** 532-546.

Nitta, T., and S. Esbensen, 1974: Heat and moisture budget analyses using BOMEX data. *Mon. Wea. Rev.*, **102**(1), 17-28.

Nitta, T., 1975: Observational determination of cloud mass flux distributions. *J. Atmos. Sci.*, **32**, 73-91.

Ogura, Y., 1962a: A consequence of the zero-fourth accumulant approximation. *J. Fluid Mech.*, **13**, 369-375.

Ogura, Y., 1962b: Energy transport in isotropic turbulent flow. *J. Geophys. Res.*, **67**, 3143-3149.

Oliver, D. A., W. S. Lewellen, and G. G. Williamson, 1978: Interaction between turbulent and radiative transport in the development of fog and low-level stratus. *J. Atmos. Sci.*, **35**(2), 301-316.

Olsson, P. Q., J. Y. Harrington, G. Feingold, W. R. Cotton, and S. M. Kreidenweis, 1998: Exploratory cloud-resolving simulations of boundary-layer Arctic stratus clouds. Part I:

Warm-season clouds. *Atmos. Res.*, **47-48**, 573-597.

Orszag, S. A., 1970: Analytical theory of turbulence. *J. Fluid Mech.*, **41**, 383-386.

Ooyama, K., 1971: A theory on parameterization of cumulus clouds. *J. Meteor. Soc. Japan*, **49** (special issue), 744-856.

Paluch, I. R., and D. H. Lenschow, 1991: Stratiform cloud formation in the marine boundary layer. *J. Atmos. Sci.*, **48**(19), 2141-2158.

Penc, R. S., and B. Albrecht, 1987: Parametric representation of heat and moisture fluxes in cloud-topped mixed layers. *Bound.-Layer Meteor.*, **38**(3), 225-248.

Pennel, W. T., and M. A. Lemone, 1974: Experimental study of turbulence structure in the fair-weather trade wind boundary layer. *J. Atmos. Sci.*, **31**(5), 1308-1323.

Petersen, A. C., C. Beets, H, van Dop, and P. G. Duynkerke, 1999: Mass-flux characteristics of reactive scalars in the convective boundary layer. *J. Atmos. Sci.*, **56**(1), 37-56.

Pielke, R. A., and Y. Mahrer, 1975: Representation of the heated planetary boundary layer in mesoscale models with coarse vertical resolution. *J. Atmos. Sci.*, **32**(12), 2288-2308.

Pinto, J. O., and J. A. Curry, 1997: Role of radiative transfer in the modeled mesoscale development of summertime arctic stratus. *J. Geophys. Res.*, **102**(D12), 13861-13872.

Prandtl, L., 1925: Bericht uber untersuchgen zur ausgebildeten turbulenz, *Zs. angew. Math. Mech.*, **5**(2), 136-139.

Ramanathan, V., 1989: Cloud-radiative forcing and climate: results from the Earth Radiation

Budget Experiment. *Science*, **243**(4887), 57-63.

Randall, D. A., 1976: The interaction of the planetary boundary-layer with large-scale circulations. Ph.D. thesis, University of California, Los Angeles, 247pp.

Randall, D. A., 1980: Conditional instability of the first kind upside-down. *J. Atmos. Sci.*, **37**(1), 125-130.

Randall, D. A., and M. J. Suarez, 1984: On the dynamics of stratocumulus formation and dissipation. *J. Atmos. Sci.*, **41**(20), 3052-3057.

Randall, D. A., J. A. Abeles, and T. G. Corsetti, 1985: Seasonal simulations of the planetary boundary layer and boundary-layer stratocumulus clouds with a general circulation model. *J. Atmos. Sci.*, **41**(7), 641-675.

Randall, D. A., 1987: Turbulent fluxes of liquid water and buoyancy in partly cloudy layers. *J. Atmos. Sci.*, **44**(5), 850-858.

Randall, D. A., Q. Shao, and C.-H. Moeng, 1992: A second-order bulk boundary-layer model. *J. Atmos. Sci.*, **49**, 1903-1923.

Randall, D. A., and D.-M. Pan, 1993: Implementation of the Arakawa-Schubert parameterization with a prognostic closure. *The Representation of Cumulus Convection in Numerical Models*. K.A. Emanuel and D.J. Raymond (eds.), Meteorological Monographs, Vol. 24, No. 46, American Meteorological Society, Boston, MA, 137-144.

Randall, D. A., 1995: Parameterizing Fractional Cloudiness Produced by Cumulus Detrainment. Paper presented at the *Workshop on Microphysics in GCMs*, Kananaskis, Alberta, Canada, May 23-25, 1995. WMO/TD-No. 713, 1-16.

Randall, D. A., Q. Shao, and M. Branson, 1998: Representation of clear and cloudy boundary layers in climate models. *Clear and Cloud Boundary Layers*. A. A. M. Holtslag and P. G. Duynkerke (eds.), Royal Netherlands Academy of Arts and Sciences, Amsterdam, pp. 305-322.

Raymond, D. J., 1979: A two-scale model of moist, non-precipitating convection. *J. Atmos. Sci.*, **36**, 816-831.

Raymond, D. J., and M. Wilkening, 1982: Flow and mixing in New Mexico mountain cumuli. *J. Atmos. Sci.*, **39**, 2211-2228.

Raymond, D. J., and A. M. Blyth, 1986: A stochastic mixing model for nonprecipitating cumulus convection. *J. Atmos. Sci.*, **43**(22), 2708-2718.

Reynolds, O., 1894: On the dynamical theory of incompressible viscous fluids and the determination of the criterion. *Phil. Roy. Trans. Soc. London*, **186**, 123-161.

Richardson, L. F., 1922: *Weather Prediction by Numerical Process*. Cambridge University Press.

Riehl, H., and J. S. Malkus, 1958: On the heat balance in the equatorial trough zone. *Geopshysica*, **6**, 503-537.

Rotta, J. C., 1951a: Statistische Theorie Nichthomogener Turbulenz 1. *Z. Phys.*, **129**, 547-572.

Rotta, J. C., 1951b: Statistische Theorie Nichthomogener Turbulenz 2. *Z. Phys.*, **131**, 51-77.

Schubert, W. H., 1979: Marine stratocumulus convection, Pt. 1, Governing equations and horizontally homogeneous solutions. *J. Atmos. Sci.*, **36**(7), 1286-1307.

Schumann and C.-H. Moeng, 1991a: Plume fluxes in clear and cloudy convective boundary layers. *J. Atmos. Sci.*, **48**(15), 1746-1757.

Schumann and C.-H. Moeng, 1991b: Plume budgets in clear and cloudy convective boundary layers. *J. Atmos. Sci.*, **48**(15), 1758-1770.

Scorer, R. S., 1957: Experiments on convective isolated masses of buoyant fluid. *J. Fluid Mech.*, **2**, 583-594.

Shine, K. P., and A. Henderson-Sellers, 1985: The sensitivity of a thermodynamic sea ice model to changes in surface albedo parameterization. *J. Geophys. Res.*, **90**, 2243- 2250.

Siebesma, A. P., and J. W. M. Cuijpers, 1995: Evaluation of parametric assumptions for shallow cumulus convection. *J. Atmos. Sci.*, **52**(6), 650-666.

Siebesma, A. P., and A. A. M. Holtslag, 1996: Model impacts of entrainment and detrainment rates in shallow cumulus convection. *J. Atmos. Sci.*, **53**(16), 2354-2364.

Siems S. T., C. S. Bretherton, M. B. Baker, S. Shy, and R. E. Breidenthal, 1990: Buoyancy reversal and cloud-top entrainment instability. *Quart. J. R. Met. Soc.*, **116**(493), 705-739.

Simpson J., R. H. Simpson, D. A. Andrews, and M. A. Eaton, 1965: Experimental cumulus dynamics. *Rev. Geophys.*, **3**, 387-431.

Simpson J., and V. Wiggert, 1969: Models of precipitating cumulus towers. *Mon. Wea. Rev.*, **97**, 471-489.

Simpson J., 1971: On cumulus entrainment and one-dimensional models. *J. Atmos. Sci.*, **28**, 449-455.

Slingo, A., 1990: Sensitivity of the Earth's radiation budget to changes in low clouds. *Nature*, **343**(6253), 49-51.

Smagorinski, J., 1963: General circulation experiments with the primitive equations. *Mon. Wea. Rev.*, **91**, 99-165.

Smith, W. S., and C.-Y. J. Kao, 1996: Numerical simulation of observed Arctic stratus clouds using a second-order turbulence closure model. *J. Appl. Meteor.*, **35**, 47-59.

Somerville, R. C. J., and L. A. Remer, 1984: Cloud optical thickness feedbacks in the CO_2 climate problem. *J. Geophys. Res.*, **89**(D6), 9668-9672.

Somméria, G., 1976: Three-dimensional simulation of turbulent processes in an undisturbed trade wind boundary layer. *J. Atmos. Sci.*, **33**(2), 216-241.

Somméria, G., and J. W. Deardorff, 1977: Subgrid-scale condensation in models of non-precipitating clouds. *J. Atmos. Sci.*, **34**, 344-355.

Squire, P., 1958: Penetrative downdraughts in cumuli. *Tellus*, **10**, 381-389.

Squire, P., and J. S. Turner, 1962: An entraining jet model for cumulonimbus updraughts. *Tellus*, **4**, 422-434.

Stephens, G., and P. Gabriel, 1999: Parameterization of atmospheric radiative transfer I: Validity of simple models. In preparation for submission, Colorado State University, Fort Collins CO.

Stommel, H., 1947: Entrainment of air into a cumulus cloud. *J. Meteor.*, **4**, 91-94.

Stull, R. B., 1984: Transilient turbulence theory, Pt. 1, Concept of eddy mixing across finite distances. *J. Atmos. Sci.*, **41**(23), 3351-3367.

Stull, R. B., 1988: *An Introduction to Boundary Layer Meteorology*. Kluwer Academic Publishers Group, Dordrecht, The Netherlands, 666pp.

Suarez, M. J., A. Arakawa, and D. A. Randall, 1983: The parameterization of the planetary boundary layer in the UCLA general circulation model: Formulation and results. *Mon. Wea. Rev.*, **111**(11), 2225-2243.

Sun, W.-Y., and Y. Ogura, 1980: Modeling the evolution of the convective planetary boundary layer. *J. Atmos. Sci.*, **37**(7), 1558-1572.

Taylor, G. I., 1921: Diffusion by continuous movements. *Proc. London Math. Soc.*, **20**(2), 196-211.

Taylor, G. I., 1935: Statistical theory of turbulence I-III. *Proc. Roy. Soc. London*, **A151**(874), 465-478.

Taylor, G. R., and M. B. Baker, 1991: Entrainment and detrainment in cumulus clouds. *J. Atmos. Sci.*, **48**(1), 112-121.

Telford, J. W., 1975: Turbulence, entrainment, and mixing in cloud dynamics. *Pure Appl.*

Geophys., **113**, 1067-1084.

Therry, G., and P. Lecarreré, 1983: Improving the eddy kinetic energy model for planetary boundary layer description. *Bound.-Layer Meteor.*, **25**(1), 63-88.

Tiedtke, M., 1988: Parameterization of cumulus convection in large-scale models. *Physically-Based Modeling and Simulation of Climate and Climate Change*, M. Schlesinger, Ed. D. Reidel, 375-431.

Tiedtke, M., 1989: A comprehensive mass-flux scheme for cumulus parameterization in large-scale models. *Mon. Wea. Rev.*, **117**, 1779-1800.

Troen, I., and L. Mahrt, 1986: A simple model of the atmospheric boundary layer: Sensitivity to surface evaporation. *Bound.-Layer Meteor.*, **37**, 129-148.

Tsay, S.-C., K. Stamnes, and K. Jayaweera, 1984: Physical characteristics of Arctic stratus clouds. *J. Appl. Meteorol.*, **23**, 584-596.

Tsay, S.-C., K. Stamnes, and K. Jayaweera, 1989: Radiative energy budget in the cloudy and hazy Arctic. *J. Atmos. Sci.*, **46**(7), 1002-1018.

Turner, J. S., 1973: *Boundary Effects in Fluids*. Cambridge University Press, 337pp.

Turton, J. D., and S. Nicholls, 1987: Study of the diurnal variation of stratocumulus using a multiple mixed-layer model. *Quart. J. R. Met. Soc.*, **113**(477), 969-1009.

Wagner, V., 1975: Relationship between the tropospheric circulation and energetic processes within the Hadley circulation over the Atlantic Ocean. Ber. Inst. Radiometeor. and

Maritime Meteor., Universtat Hamburg, No 26, 83pp.

Walsh, J. E., and R. G. Crane, 1992: A comparison of GCM simulations of Arctic climate. *Geophys. Res. Let.*, **19**(1), 29-32.

Wang, S., and B. Albrecht, 1986: Stratocumulus model with an internal circulation. *J. Atmos. Sci.*, **43**(21), 2374-2391.

Wang, S., and B. Albrecht, 1990: A mean gradient of the convective boundary-layer. *J. Atmos. Sci.*, **47**(1), 126-138.

Wang, S., and Q. Wang, 1994: Roles of drizzle in a one-dimensional third-order turbulence closure model of the nocturnal stratus-topped marine boundary layer. *J. Atmos. Sci.*, **51**(11), 1559-1576.

Warner, J., 1970: On steady-state one-dimensional models of cumulus convection. *J. Atmos. Sci.*, **27**, 1035-1040.

Warner, J., 1971: Corrigendum. *J. Atmos. Sci.*, **28**, 1099.

Weinstock, J., 1987: Turbulence field generated by a linear gravity wave. *J. Atmos. Sci.*, **44**(2), 410-420.

Wieghardt, K., 1945: Uber die turbulente stromung in rohr und langs der platte. *Zs. agnew. Math. Mech.*, **24**(4), 294-296.

Willis, G. E., and J. W. Deardorff, 1974: Laboratory model of the unstable planetary boundary layer. *J. Atmos. Sci.*, **31**(5), 1297-1307.

Wu, X., and M. Yanai, 1994: Effects of vertical wind shear on the cumulus transport of momentum: Observations and parameterizations. *J. Atmos. Sci.*, **51**(12), 1640-1660.

Wyngaard, J. C., and O. R. Coté, 1971: The budget of turbulent kinetic energy and temperature variance in the atmospheric surface layer. *J. Atmos. Sci.*, **28**, 190-201.

Wyngaard, J. C., and O. R. Coté, 1974: The evolution of a convective planetary boundary layer. *Bound.-Layer Meteor.*, **7**, 289-308.

Wyngaard, J. C., O. R. Coté, and K. S. Rao, 1974: Modeling the atmospheric boundary layer. *Advances in Geophys.*, Vol. 18A, Academic Press, 193-211.

Wyngaard, J. C., 1978: Temperature-humidity covariance budget in the convective boundary layer. *J. Atmos. Sci.*, **35**(1), 47-58.

Wyngaard, J. C. and J. C. Weil, 1991: Transport asymmetry in skewed turbulence. *Phys. Fluids*, **3**(1), 155-161.

Wyngaard, J. C. and C.-H. Moeng, 1992: Parameterizing turbulent diffusion through the joint probability density. *Bound.-Layer Meteor.*, **60**, 1-13.

Yamada, T. and G. Mellor, 1975: A simulation of the Wangara atmospheric boundary layer data. *J. Atmos. Sci.*, **32**, 2309-2329.

Yanai, M., Esbensen, S., and J. Chou, 1973: Determination of bulk properties of tropical cloud clusters from large scale heat and moisture budgets. *J. Atmos. Sci.*, **30**, 611-627.

Yanai, M., J. H. Chu, T. E.Stark, and T. Nitta, 1976: Response of deep and shallow tropical marine cumuli to large-scale processes. *J. Atmos. Sci.*, **33**, 976-991.

Yau, M. K., 1979: Perturbation pressure and cumulus convection. *J. Atmos. Sci.*, **36**, 690-694.

Young, G. S., 1988a: Turbulence structure of the convective boundary layer, Pt. 1, Variability of normalized turbulence statistics. *J. Atmos. Sci.*, **45**(4), 719-726.

Young, G. S., 1988b: Turbulence structure of the convective boundary layer, Pt. 2, Phoenix 78 aircraft observations of thermals and their environment. *J. Atmos. Sci.*, **45**(4), 727-735.

Zeman, O., and J. J. Lumley, 1976: Modeling buoyancy driven mixed layers. *J. Atmos. Sci.*, **33**(10), 1974-1988.

Zeman, O., 1981: Progress in the modeling of planetary boundary layers. *Annul Reviews in Fluid mechanics*, Vol. 13, Annual Reviews, 253-272.

Zhang, D., and R. A. Anthes, 1982: High-resolution model of the planetary boundary layer: sensitivity tests and comparisons with SESAME-79 data. *J. Appl. Meteor.*, **21**(11): 1594-1609.

Zhang, G. J., and H.-R. Cho, 1991a: Parameterization of the vertical transport of momentum by cumulus clouds. Part I: Theory. *J. Atmos. Sci.*, **48**, 1483-1492.

Zhang, G. J., and H.-R. Cho, 1991b: Parameterization of the vertical transport of momentum by cumulus clouds. Part II: Application. *J. Atmos. Sci.*, **48**, 2448-2457.

Zhang, G. J., and N. A. McFarlane, 1995: Sensitivity of climate simulations to the parameterization of cumulus convection in the Canadian Climate Center general circulation model. *Atmos. and Oceans*, **33**, 407-446.